On the oxidation of high-temperature alloys, and its role in failure of thermal barrier coatings

by

Kaspar Andreas Loeffel

Dipl. Ing. ETH, Swiss Federal Institute of Technology Zurich (2007)

Submitted to the Department of Mechanical Engineering
in partial fulfillment of the requirements for the degree of

Doctor of Philosophy

at the

Massachusetts Institute of Technology

February 2013

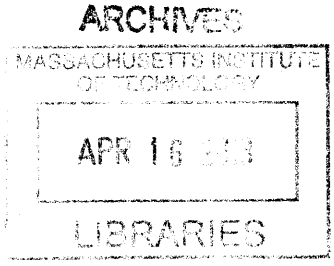

Author .....
Department of Mechanical Engineering
September 25, 2012

Certified by .....
Lallit Anand
Warren and Towneley Rohsenow Professor of Mechanical Engineering
Thesis Supervisor

Accepted by .....
David E. Hardt
Chairman, Department Committee on Graduate Students

On the oxidation of high-temperature alloys, and its role in failure of thermal barrier coatings

by

Kaspar Andreas Loeffel

Submitted to the Department of Mechanical Engineering
on September 25, 2012, in partial fulfillment of the
requirements for the degree of
Doctor of Philosophy

Abstract

Thermal barrier coating (TBC) systems are applied to superalloy turbine blades to provide thermal insulation and oxidation protection. A TBC system consists of (a) an outer oxide layer that imparts thermal insulation, and (b) a metallic layer that affords oxidation protection for the substrate through the formation of a second, protective oxide layer. This slow oxidation of the metallic layer controls the mechanical integrity of the TBC system since it is accompanied by a large, anisotropic volumetric change on the order of 30 percent. To describe this coupled process at the microscale, in this thesis we formulate a continuum-level, chemo-thermo-mechanically coupled, thermodynamically-consistent theory which integrates (a) diffusion of oxygen, (b) oxidation with accompanying anisotropic volume change, (c) thermo-elasto-viscoplastic deformations that may be locally large, and (d) transient heat conduction. We numerically implement our theory in an implicit finite-element program, and calibrate the material parameters in our theory for an FeCrAlY alloy experimentally studied in the literature. We simulate the high-temperature oxidation of FeCrAlY, and show that our theory is capable of reproducing with reasonable accuracy the oxide thickness evolution with time at different temperatures, the shape distortion of the specimens, as well as the development of large compressive residual stresses in the protective surface oxide which forms.

For the consideration of failure of thermal-barrier-coated components at the macroscale, a limitation of this type of model is that numerical simulations become challenging due to the sub-micron resolution of the required mesh. In a second part of this thesis, we therefore present a framework that facilitates macroscopic simulations by noting that the macroscopic effect of oxidation is simply to degrade some mechanical properties in the TBC system. In this framework oxidation is thus not modeled explicitly, but only indirectly manifested by affecting failure-related material parameters. We implement this model in an explicit finite-element program, apply it to a plasma-sprayed TBC system, and calibrate the material parameters. We then show that the model is capable of predicting with reasonable accuracy the load at which crack initiation occurs in a notched four-point bend test experimentally studied in the literature, as well as the overall qualitative load-displacement behavior in this test.

Thesis Supervisor: Lallit Anand
Title: Warren and Towneley Rohsenow Professor of Mechanical Engineering

Acknowledgments

First, I would like to express my sincere gratitude to my advisor, Prof. Lallit Anand, for his support and guidance over the past years. I know that his dedication to the field of Mechanics and Materials and his encouragement to pursue impeccable standards will be an inspiration to me throughout my career. The support of the members of my thesis committee, Prof. Chris Schuh, Prof. Franz-Josef Ulm, and Prof. Ahmed Ghoniem, has also been of central importance, and I am very thankful for their constant encouragement and very valuable input. Furthermore, I thank Prof. Zuhair Gasem and Prof. Khaled Al-Athel from the King Fahd University for Petroleum and Minerals in Dhahran, Saudi Arabia, for the collaboration.

Many thanks go to Ray Hardin, Leslie Regan, Joan Kravit, and Pierce Hayward, whose assistance I have greatly appreciated. I also extend my sincere thanks to my current and former lab mates Dr. Shawn Chester, Dr. Haowen Liu, Dr. David Henann, Claudio Di Leo, Mary Cookson, and Dr. Vikas Srivastava for being great colleagues and friends. The frequent fruitful discussions we have had have been very valuable to my work.

Financial support from the King Fahd University of Petroleum and Minerals in Dhahran, Saudi Arabia, through the Center for Clean Water and Clean Energy at MIT and KFUPM under project number R9-CE-0, and from NSF (CMMI Award No. 019646-001) is also gratefully acknowledged.

Contents

List of Figures

List of Tables

Chapter 1

Introduction to this thesis

1.1 Thermal barrier coating systems

Turbine inlet temperatures in the gas path of modern high-performance gas turbines operate at temperatures up to around 1400 °C. In the high-temperature regions of the turbine, special high-melting-point nickel-based superalloy blades and vanes are used, which retain strength and resist oxidation and hot corrosion at extreme temperatures. These superalloys melt around 1300 °C, which means that the blades (and vanes) closest to the combustor may be operating in gas-path temperatures which exceed their melting point, and the blades must therefore be *cooled* to acceptable service temperatures around 1050 °C (a homologous temperature of about 0.8) in order to maintain integrity. Accordingly, modern turbine blades subjected to the hottest gas flows take the form of elaborate single-crystal superalloy investment castings that contain intricate internal passages and surface-hole patterns, which are necessary to channel and direct cooling air within the blade, as well as over its exterior surfaces. After casting, the exposed surface of a high-temperature turbine blade is also typically coated with a *thermal barrier coating (TBC) system* which acts as a thermal insulator and oxidation inhibitor, and serves to increase the life of the blade. The current generation of TBC systems can accommodate surface temperatures up to about 1275 °C. A TBC system consists of two layers: (a) a metallic layer, or *bond coat*, deposited on the superalloy — the bond coat is typically an alloy based on Ni(Al) with various additions (such as Cr, Co, Pt, Y, and Hf); and (b) an yttria-stabilized-zirconia (YSZ) *top coat* deposited on the bond coat [41]. Each of these layers has a thickness on the order of 200 microns; the top coat imparts thermal insulation, while the bond coat affords oxidation protection for the base alloy through the formation of a second oxide, primarily α-Al_2O_3, as well as plastic accommodation of misfit strains [40, 80]. A coated turbine blade, along with a schematic of the cross section, is shown in Fig. 1-1.

One of the problems limiting the use of TBC systems is their long-term durability. It is the *oxidation of the bond coat* that is the intrinsic mechanism controlling the long-term stability and mechanical integrity of a TBC system, combined with the associated time-dependent deformation and degradation processes in the multi-layered system [40]. The product of bond coat oxidation is the α-Al_2O_3 layer, which is commonly known as the *thermally grown oxide* (TGO), and has a thickness on the order of 10 microns after prolonged high-temperature

exposure. The formation of the TGO is associated with a large *volumetric change* on the order of 30 percent, and when this volumetric change is combined with the effects of property mismatch, especially since the former are constrained by the material surrounding the TGO, large local stresses can develop. The location and magnitude of these stresses strongly depend on the thickness and morphology of the TGO layer, and also the fact that the volumetric expansion has an *associated preferred direction*, which at the microstructural level may be associated with grain-boundaries in the oxide which lie perpendicular to the oxide-metal interface [26, 102, 103]. These stresses eventually lead to the nucleation of microcracks at or near the interfaces in the TBC system. Finally, failure will occur likely by debonding either at the top-coat/TGO interface, or the TGO/bond-coat interface [40, 96, 97].

1.2 Modeling of high-temperature metal oxidation

In order to gain an understanding of the overall degradation and failure process of the TBC system *on the microscale*, due to the central role of bond-coat oxidation in TBC system mechanics, it is clear that a *constitutive model for high-temperature metal oxidation* is needed that describes the coupled phenomena of (a) diffusion (which is necessary for the oxidation to occur), (b) oxidation with accompanying permanent and anisotropic volume change (i.e. *swelling*), and (c) thermo-elasto-viscoplastic deformations that may be locally large. In addition, since it is the purpose of the TBC system to impart a temperature gradient, transient heat conduction may also have to be taken into account.

Major contributions to modeling of high-temperature oxidation, within the context of TBC systems, have been made over the past 15 years by the groups of Evans and Hutchinson and their co-workers [cf., e.g., 8, 9, 39, 50, 60, 62, 86], and Busso and co-workers [cf., e.g., 15, 16, 18, 43]. However, to the best of the author's knowledge, a theory and a corresponding numerical simulation capability for metal oxidation that explicitly includes and couples (a) modeling of the diffusion of oxygen, (b) oxidation accompanied by anisotropic swelling, (c) elastic-viscoplastic deformation of the oxide and the base material, and (d) transient heat conduction, is still lacking. It is a main objective of this thesis to develop a constitutive theory and corresponding numerical implementation that fulfill this need. Further, and importantly, most previous chemo-mechanically coupled theories for oxidation have been formulated in the small-deformation context. The deformations associated with metal oxidation may involve *locally large strains and rotations*, though; the theory presented here is therefore formulated within a rigorous finite-deformation framework.

1.3 Modeling of degradation and failure in macroscopic thermal-barrier-coated components

While a model of the strongly coupled phenomena associated with bond-coat oxidation is a central requisite to understanding the degradation and failure process of a TBC system on the *microscale*, its limitation lies in the fact that when one is interested in modeling the degradation and failure of a *macroscopic* part like an entire turbine blade, simulations quickly become computationally extremely challenging due to the very fine discretization

(i.e. the large amount of finite elements) needed to resolve the small thickness of the TGO – on the order of 10 microns – and the associated imperfections on the same order.

In a second part of this thesis, the goal is therefore to present a framework that facilitates the simulation of degradation and failure of a *macroscopic* component. To this end, we note that the *macroscopic* manifestation of the oxidation process is simply that it *causes a change in the resistance of the TBC system to spallation failure* as a function of time at high temperature (the *dwell time*). For this reason, we adopt a description of the thermal-barrier-coated component in which *we do not explicitly model oxidation; rather, we assume that oxidation is manifested only indirectly by changing the resistance of the TBC system to spallation.* With such an approach, the very fine mesh required by explicitly modeling oxidation is not needed, and the simulation of macroscopic components with dimensions of, say, centimeters becomes computationally tractable.

1.4 Thesis structure

The specific structure of this thesis is as follows. In Part I, we discuss in detail the modeling of high-temperature metal oxidation. Specifically, in Chapter 3, we present our chemo-thermo-mechanically coupled theory for high-temperature oxidation of metals. In Chapter 4, we apply our coupled theory to the oxidation of a model bond-coat material, the iron-based heat-resistant alloy Fe-22Cr-4.8Al-0.3Y (also known simply as *FeCrAlY*). We implement the theory numerically in the commercial finite-element program ABAQUS/Standard [93] as a *user-element subroutine*, and *estimate* the numerous material parameters in our theory based on existing information in the literature and our own numerical simulations. We then show that using our numerical simulation capability and the material parameters for FeCrAlY, we are able to reproduce, with reasonable accuracy, (i) the oxide thickness, (ii) residual stresses, and (iii) deformations of oxidizing FeCrAlY specimens.

In Part II, the goal is to simulate the behavior of macroscopic thermal-barrier-coated components. Chapter 5 gives an introduction to this topic. In order to circumvent use of the fine mesh needed for the chemo-thermo-mechanically coupled simulations, we make use of an existing constitutive model for the elastic-plastic behavior of interfaces [28, 98]; this model is discussed in Chapter 6. We then implement this model numerically in ABAQUS/Explicit [94] as a *user-material subroutine*, and apply to the top-coat/TGO interface in a specific kind of TBC system in Chapter 7. Specifically, we calibrate the material parameters using our numerical simulation capability, and then show that the model is capable of predicting with reasonable accuracy the load at which crack initiation occurs in a notched four-point bend test experimentally studied in the literature, as well as the overall qualitative load-displacement behavior in this test.

Finally, in Chapter 8 we present some concluding remarks, and future research directions are outlined in Chapter 9.

1.5 Publications related to this thesis

The two publications in peer-reviewed journals listed below comprise content that is closely related to this thesis; in fact, a substantial amount of the text in this thesis is drawn from them.

1. K. Loeffel and L. Anand. A chemo-thermo-mechanically coupled theory for elastic-viscoplastic deformation, diffusion, and volumetric swelling due to a chemical reaction. *International Journal of Plasticity*, 27:1409–1431, 2011.

2. K. Loeffel, L. Anand, and Z. Gasem. On modeling the oxidation of high-temperature alloys. *Acta materialia*, 2012 (accepted for publication).

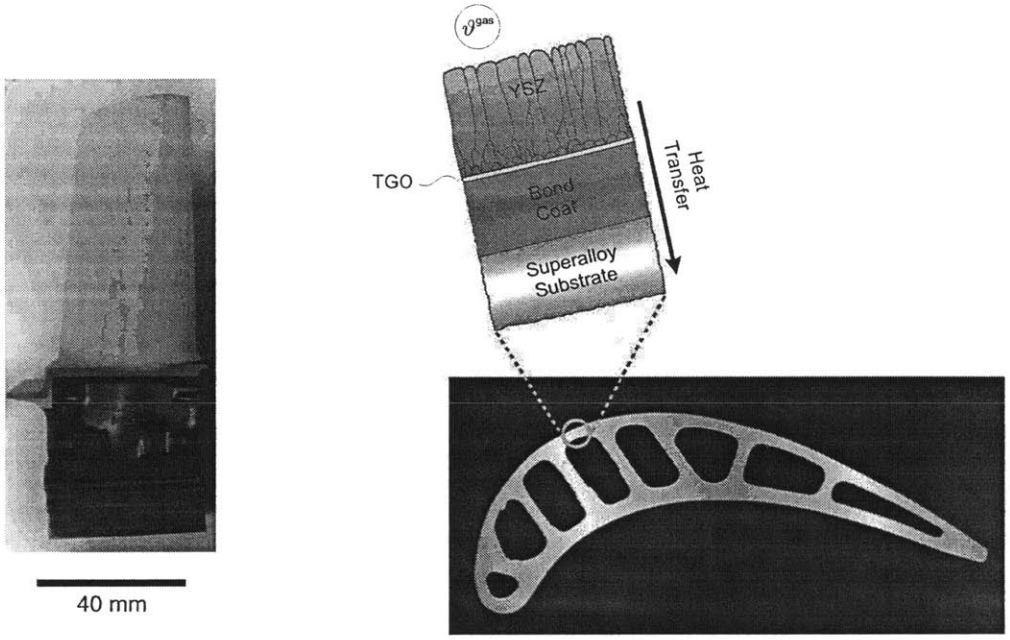

Figure 1-1: (a) Coated turbine blade [adapted from 11]; (b) Schematic of turbine blade cross section with a magnification of the surface region [adapted from 40].

Part I

Modeling of high-temperature metal oxidation

Chapter 2

Introduction

The protective oxide which is formed on an oxidizing high-temperature alloy thickens as well as grows laterally with time. Constrained by the underlying material being oxidized, the lateral growth strain produces a compressive stress in the growing oxide. The development of compressive stresses accompanying the growth of the surface oxide in thin sheets (or rods) of the alloy is balanced by corresponding tensile stresses in the unoxidized base alloy, and at elevated temperatures these tensile stresses typically exceed the flow strength of the alloy and cause a permanent elongation of the sheet (or rod), which provides a relaxation mechanism for the magnitude of the compressive stresses in the oxide; cf. Clarke [26], Clarke and Levi [27], and the schematic in Fig. 2-1.

The fact that growth stresses arise during oxidation, and are caused by the constraint of a lateral growth strain, has been known for a long time.[1] Further, it is widely-agreed that the two major mechanisms which give rise to the lateral growth strains are the molar volume increase associated with oxide formation [81], and the formation of layers of new oxide at grain boundaries which lie perpendicular to the oxide-metal interface [88]. While the macroscopic physical manifestations of oxidation and the probable underlying causes for these macroscopic manifestations are qualitatively well understood, detailed and definitive experimental studies including measurements of oxide thickness, growth stresses, and dimensional changes as functions of oxidation time are relatively recent, and due to Tolpygo et al. [103] and Tolpygo and Clarke [102].[2]

Specifically, Clarke and his co-workers conducted oxidation experiments in which rectangular sheet specimens ($12 \times 15\,\text{mm}$) of an Fe-22Cr-4.8Al-0.3Y (FeCrAlY) heat-resistant alloy of various thicknesses (ranging from 0.16 mm to 4.04 mm) were oxidized at different high temperatures (1000, 1100, 1200, and 1300°C) in air, and subsequently cooled to room temperature. After oxidation and cool-down they measured (i) the thickness of the surface layer of α-Al_2O_3 oxide; (ii) the compressive (biaxial) residual stresses in the oxide after cool-

[1] Oxide growth in the direction normal to the specimen surface is unconstrained and accordingly does not produce any stress.

[2] See Huntz [57] for a review of earlier studies of stresses in oxide scales.

down;[3] and (iii) the lateral elongation of the specimens after cool-down. Fig. 2-2 shows some representative results from their experiments:

(i) Fig. 2-2a shows the variation of the oxide thickness h_0 (in microns), on a plate of 0.9 mm thickness, as a function of time (in hours) on a log-log plot at the four different oxidation temperatures.

- The straight lines on this plot indicate power-law oxidation kinetics.

(ii) Fig. 2-2b shows the in-plane residual stress in the oxide (after cool-down) as a function of oxidation time at 1200°C for plates of the six different initial thicknesses. Note that

- The stresses are compressive, and they exhibit a very fast increase at low oxidation times followed by a gradual decline, with a maximum value of ≈ -5.5 GPa being reached in about 1 hour at 1200°C.
- For any given oxidation time the stress in the oxide is greater for the thicker specimen.

(iii) Fig. 2-2c shows the total lateral strain (in percent) of the plates of six different initial thicknesses as a function of oxidation time at 1200°C.

- The total elongational strain increases with decreasing specimen thickness. After 250 hours of oxidation the strain varies from a fraction of a percent for the thickest plate, to about 2.5% as the plate thickness decreases.
- These strain levels far exceed the elastic strains of the metals that might be expected to arise due to the difference between the thermal expansion coefficients of the metal and the oxide, and this provides direct evidence that the oxidation-induced stresses produce plastic deformation of the base metal being oxidized.
- The continued increase of the lateral dimensions with time indicates a continuous generation of the growth stress in the oxide and accompanying stress relaxation by creep of the base alloy.
- Even for the thickest specimens studied at 1200°C, the residual stress in the oxide gradually decreases after a few hours of oxidation. By this time little or no detectable specimen elongation had occurred, which indicates that stress relaxation also takes place by high-temperature *creep or plasticity of the oxide* during its growth.

Thus, the experimental results of Clarke and co-workers show that the compressive stress in the oxide after cool-down from a fixed high-temperature varies non-monotonously with time, which implies that the stress is not only due to thermal mismatch stress, but also includes stress generated during the growth of the oxide. The actual value of the growth stress attained is a result of a competition between that generated by the lateral growth strain and any stress relaxation processes. Barring a change in shape (i.e., wrinkling), two

[3]The residual stress in the oxide was measured using a novel method involving the piezospectroscopic shift in photostimulated Cr^{3+} luminescence from the trace chromium incorporated in the α-Al_2O_3 scale during oxidation [cf., e.g., 70].

simultaneous relaxation processes for the growth stresses can occur during oxidation: plastic deformation in the underlying alloy and plastic deformation in the oxide. The relative contribution of these two relaxation processes depends on the oxide-to-metal thickness ratio. In their paper Tolpygo et al. [103] carry out a one-dimensional analysis to estimate the in-plane lateral growth strain, the concurrent creep strain in the oxide during oxidation, as well as the growth stress in aluminum oxide. They find that the growth stress can be as large as $\approx -1.5\,\mathrm{GPa}$ in FeCrAlY.

As is clear, oxidation of high-temperature alloys represents a number of complex, strongly-coupled, non-linear phenomena; in an attempt to integrate them, in Chapter 3 we introduce a new theory that aims to describe these processes and their couplings. Specifically, our theory accounts for

(a) diffusion of oxygen,

(b) oxidation accompanied by anisotropic swelling,

(c) large elastic-viscoplastic deformations, and

(d) transient heat conduction.

Regarding the mechanism of oxidation in Al-containing high-temperature alloys, an important issue is the question which species – oxygen, aluminum, or both – are diffusing during the oxidation process. It has been experimentally observed that the presence of a reactive element such as yttrium even in a trace amount (a few hundredths or tenths of a percent), can significantly increase the oxidation resistance of the alloy by improving scale adherence and reducing scale growth by suppressing the outward diffusion of aluminum [cf., e.g., 56, 117]. Specifically, in FeCrAlY the presence of the reactive element yttrium favors the inward transport of oxygen along the grain boundaries of the thermally-grown oxide – leading to an inward-growing, columnar oxide scale [cf., e.g., 49]. Based on this experimental observation, we limit our considerations in this work to the inward diffusion of oxygen, and neglect the outward diffusion of aluminum. Further, we consider the diffusion to occur exclusively by free oxygen interstitials, which thus constitute the "diffusing species" in our theory.

In Chapter 4, we discuss the application of the constitutive framework introduced in Chapter 3 to the oxidation of FeCrAlY. To this end, we have numerically implemented our theory in ABAQUS/Standard [93] by writing a *user-element subroutine*. Using this numerical capability we have conducted simulations of the flat-plate oxidation experiments of Tolpygo et al. [102, 103] on FeCrAlY. Based on existing information in the literature as well as our own numerical simulations we have *estimated* the numerous material parameters in our theory. These are only briefly discussed in in Chapter 4, and for clarity of presentation a detailed discussion of our estimation procedure for the material parameters is relegated to an Appendix. We show that using our numerical simulation capability and the material parameters for FeCrAlY, we are able to reproduce — with reasonable accuracy — the experimental results of Tolpygo et al. on (i) the thickness of the surface layers of α-Al_2O_3; (ii) the compressive residual stresses in the oxide; and (iii) the lateral elongation of the specimens.

In addition, as an application of our numerical simulation capability we consider the oxidation of an FeCrAlY sheet with an initial groove-like undulation on the surface of a

sheet — a geometry which has been experimentally studied by Davis and Evans [30]. Our numerical simulations reasonably approximate the *rumpling* or shape-distortion of the groove upon oxidation, measured by these authors. This example has obvious ramifications for delamination failure of a ceramic top coat on a TGO layer in a TBC system. While rumpling relieves the TGO of some of its compressive strain energy, the associated vertical movement can induce tensile stresses in the adjacent ceramic top coat which may lead to crack nucleation and propagation at the TGO/top-coat interface.

With a view of a possible application of our theory and numerical simulation capability to model the response of TBC systems, henceforth and whenever convenient, we refer to the high-temperature alloy as the *bond coat*, and the oxide that forms on the surface of the bond-coat as the *thermally-grown oxide* (TGO).

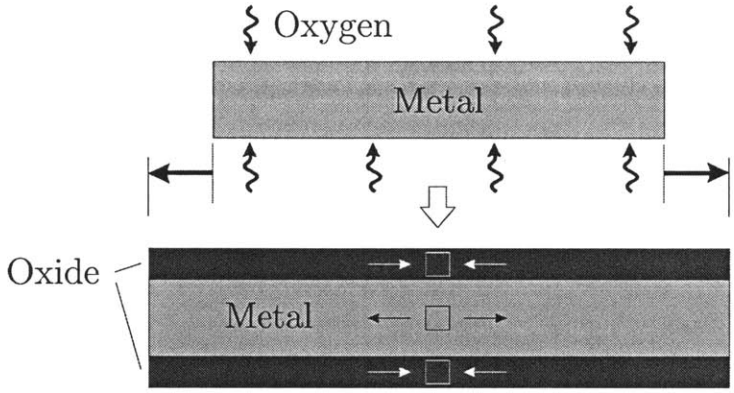

Figure 2-1: Schematic of oxidation of a plate. The oxide thickens as well as grows laterally with time. The lateral growth strain produces a compressive stress in the growing oxide which is balanced by a corresponding tensile stress in the unoxidized base alloy; the latter causes a permanent elongation of the sheet.

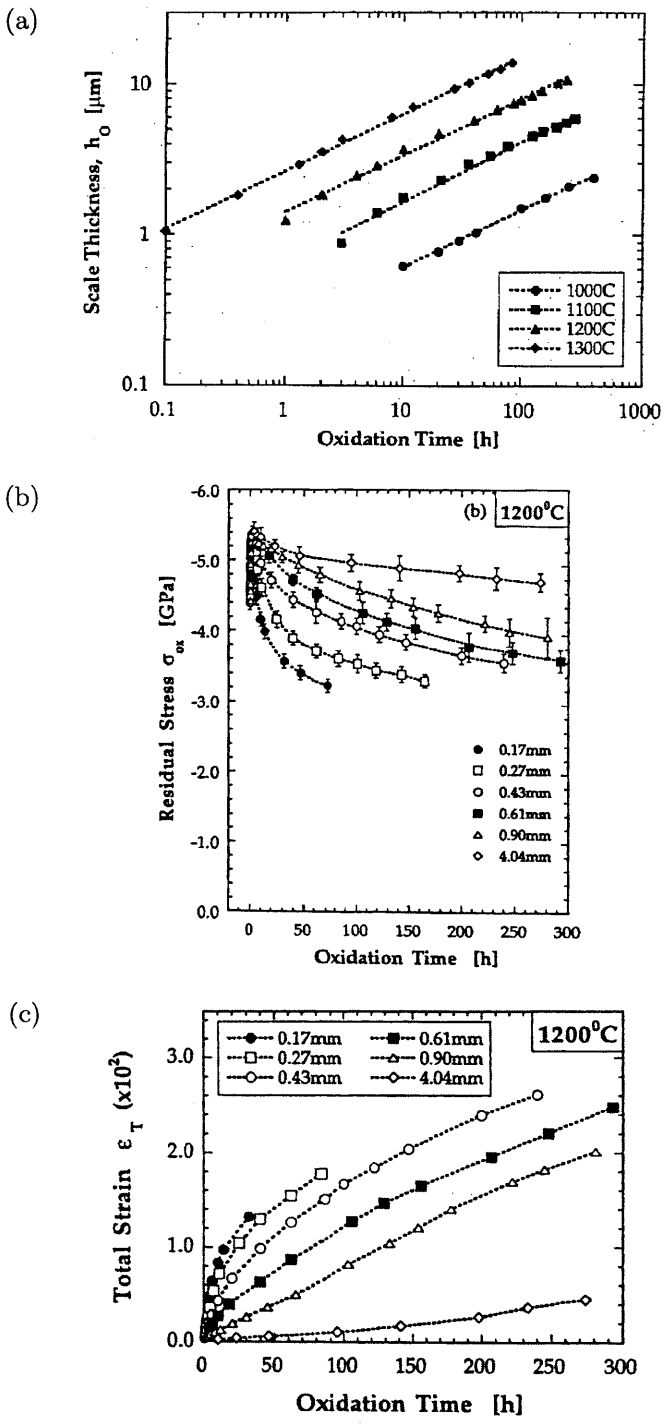

Figure 2-2: Results from Tolpygo et al. [102, 103]: (a) oxide thickness for plate thickness 0.90 mm; (b) in-plane stress in oxide at room temperature for various thicknesses; (c) total strain at room temperature for various thicknesses.

Chapter 3

Chemo-thermo-mechanically coupled theory for elastic-viscoplastic deformation, diffusion, and volumetric swelling due to a chemical reaction

3.1 Kinematics

3.1.1 Multiplicative decomposition of the deformation gradient

Consider a macroscopically-homogeneous body B with the region of space it occupies in a fixed reference configuration, and denote by $\mathbf{X}$ an arbitrary material point of B. A motion of B is then a smooth one-to-one mapping $\mathbf{x} = \boldsymbol{\chi}(\mathbf{X}, t)$ with deformation gradient, velocity, and velocity gradient given by[1]

$$\mathbf{F} = \nabla\boldsymbol{\chi}, \qquad \mathbf{v} = \dot{\boldsymbol{\chi}}, \qquad \mathbf{L} = \operatorname{grad}\mathbf{v} = \dot{\mathbf{F}}\mathbf{F}^{-1}. \tag{3.1}$$

Following modern developments of large-deformation plasticity theory [cf., e.g., 48], we base our theory on the Kröner [68] decomposition of the deformation gradient,

$$\mathbf{F} = \mathbf{F}^e\mathbf{F}^i. \tag{3.2}$$

As is standard, we assume that

$$J \overset{\text{def}}{=} \det\mathbf{F} > 0, \tag{3.3}$$

[1]Notation: We use standard notation of modern continuum mechanics [48]. Specifically: ∇ and Div denote the gradient and divergence with respect to the material point $\mathbf{X}$ in the reference configuration; grad and div denote these operators with respect to the point $\mathbf{x} = \boldsymbol{\chi}(\mathbf{X}, t)$ in the deformed body; a superposed dot denotes the material time-derivative. Throughout, we write $\mathbf{F}^{e-1} = (\mathbf{F}^e)^{-1}$, $\mathbf{F}^{e-\mathsf{T}} = (\mathbf{F}^e)^{-\mathsf{T}}$, etc. We write $\operatorname{tr}\mathbf{A}$, $\operatorname{sym}\mathbf{A}$, $\operatorname{skw}\mathbf{A}$, $\mathbf{A}_0$, and $\operatorname{sym}_0\mathbf{A}$ respectively, for the trace, symmetric, skew, deviatoric, and symmetric-deviatoric parts of a tensor $\mathbf{A}$. Also, the inner product of tensors $\mathbf{A}$ and $\mathbf{B}$ is denoted by $\mathbf{A}:\mathbf{B}$, and the magnitude of $\mathbf{A}$ by $|\mathbf{A}| = \sqrt{\mathbf{A}:\mathbf{A}}$.

and hence, using (3.2),

$$J = J^e J^i, \qquad \text{where} \qquad J^e \stackrel{\text{def}}{=} \det \mathbf{F}^e > 0 \qquad \text{and} \qquad J^i \stackrel{\text{def}}{=} \det \mathbf{F}^i > 0, \tag{3.4}$$

so that $\mathbf{F}^e$ and $\mathbf{F}^i$ are invertible. Here, suppressing the argument t:

(i) $\mathbf{F}^e(\mathbf{X})$ represents the local deformation of material in an infinitesimal neighborhood of $\mathbf{X}$ due to stretch and rotation of the microscopic structure;

(ii) $\mathbf{F}^i(\mathbf{X})$ represents the local deformation in an infinitesimal neighborhood of material at $\mathbf{X}$ due to the two major micromechanisms for inelastic deformation under consideration: (a) isochoric viscoplastic deformation due to motion of dislocations, and (b) permanent volumetric swelling due to a chemical reaction.

We refer to $\mathbf{F}^e$ and $\mathbf{F}^i$ as the elastic and inelastic distortions.

The deformation gradient $\mathbf{F}(\mathbf{X})$ maps material vectors to spatial vectors; thus consistent with (3.2), the domain of $\mathbf{F}^i(\mathbf{X})$ is the reference space, the space of material vectors, and the range of $\mathbf{F}^e(\mathbf{X})$ is the observed space, the space of spatial vectors. By (3.2) the output of $\mathbf{F}^i(\mathbf{X})$ must equal the input of $\mathbf{F}^e(\mathbf{X})$; that is

$$\text{the range of } \mathbf{F}^i(\mathbf{X}) = \text{the domain of } \mathbf{F}^e(\mathbf{X}) \stackrel{\text{def}}{=} \mathcal{I}(\mathbf{X}). \tag{3.5}$$

We refer to $\mathcal{I}(\mathbf{X})$ as the *intermediate space* for $\mathbf{X}$. Thus, for any material point $\mathbf{X}$, $\mathbf{F}^i(\mathbf{X})$ maps material vectors to vectors in $\mathcal{I}(\mathbf{X})$, and $\mathbf{F}^e(\mathbf{X})$ maps vectors in $\mathcal{I}(\mathbf{X})$ to spatial vectors.

The right polar decomposition of $\mathbf{F}^e$ is given by

$$\mathbf{F}^e = \mathbf{R}^e \mathbf{U}^e, \tag{3.6}$$

where $\mathbf{R}^e$ is a rotation, while $\mathbf{U}^e$ is a symmetric, positive-definite tensor with

$$\mathbf{U}^e = \sqrt{\mathbf{F}^{e\mathsf{T}} \mathbf{F}^e}. \tag{3.7}$$

As is standard, we define

$$\mathbf{C}^e = \mathbf{U}^{e2} = \mathbf{F}^{e\mathsf{T}} \mathbf{F}^e. \tag{3.8}$$

By $(3.1)_3$ and (3.2),

$$\mathbf{L} = \mathbf{L}^e + \mathbf{F}^e \mathbf{L}^i \mathbf{F}^{e-1}, \tag{3.9}$$

with

$$\mathbf{L}^e = \dot{\mathbf{F}}^e \mathbf{F}^{e-1}, \qquad \mathbf{L}^i = \dot{\mathbf{F}}^i \mathbf{F}^{i-1}. \tag{3.10}$$

As is standard, we define the elastic and inelastic stretching and spin tensors through

$$\left.\begin{aligned} \mathbf{D}^e &= \operatorname{sym} \mathbf{L}^e, \qquad \mathbf{W}^e = \operatorname{skw} \mathbf{L}^e, \\ \mathbf{D}^i &= \operatorname{sym} \mathbf{L}^i, \qquad \mathbf{W}^i = \operatorname{skw} \mathbf{L}^i, \end{aligned}\right\} \tag{3.11}$$

so that $\mathbf{L}^e = \mathbf{D}^e + \mathbf{W}^e$ and $\mathbf{L}^i = \mathbf{D}^i + \mathbf{W}^i$.

We make the following additional kinematical assumptions concerning inelastic flow:

(i) First, from the outset we constrain the theory by limiting our discussion to circumstances under which the material may be idealized as isotropic in every respect except that of swelling due to oxidation. For isotropic elastic-viscoplastic theories utilizing the Kröner decomposition, it is widely assumed that the plastic flow is irrotational, in the sense that[2]

$$\mathbf{W}^i = \mathbf{0}. \tag{3.12}$$

Then, trivially, $\mathbf{L}^i \equiv \mathbf{D}^i$ and

$$\dot{\mathbf{F}}^i = \mathbf{D}^i\mathbf{F}^i. \tag{3.13}$$

(ii) Next, we assume that the inelastic stretching $\mathbf{D}^i$ is additively decomposable as

$$\mathbf{D}^i = \mathbf{D}^s + \mathbf{D}^p, \qquad \text{with} \qquad \operatorname{tr}\mathbf{D}^p = 0, \tag{3.14}$$

where $\mathbf{D}^s$ represents the inelastic stretching resulting from swelling due to the oxidation reaction, and $\mathbf{D}^p$ is the inelastic stretching due to incompressible viscoplastic flow of the bond coat and the oxide.

(a) First consider the swell-stretching $\mathbf{D}^s$. Oxidation studies in the literature [cf., e.g., 26, 58, 103] indicate that $\mathbf{D}^s$ is not spherical in form, and that the underlying microstructure of the material causes swelling to occur in a preferential direction in the material. In particular, if the material point $\mathbf{X}$ lies on the surface of the bond coat then the preferred oxidation direction is in the direction of the outward unit normal to the surface.

Thus, let $\Pi_{\mathrm{R}}(\mathbf{X})$ denote a plane through an infinitesimal neighborhood of $\mathbf{X}$ in the reference body oriented by a unit normal vector $\mathbf{m}_{\mathrm{R}}(\mathbf{X})$. Then

$$\mathbf{m} \stackrel{\text{def}}{=} \frac{\mathbf{F}^{i-\mathsf{T}}\mathbf{m}_{\mathrm{R}}(\mathbf{X})}{|\mathbf{F}^{i-\mathsf{T}}\mathbf{m}_{\mathrm{R}}(\mathbf{X})|} \tag{3.15}$$

is the unit normal to the image Π of $\Pi_{\mathrm{R}}(\mathbf{X})$ in the intermediate space.[3]

Next, with $\xi(\mathbf{X}, t)$ $(0 \leq \xi \leq 1)$ denoting the local *volume fraction of oxide* at $\mathbf{X}$ at time t, we take $\mathbf{D}^s$ to be given by

$$\mathbf{D}^s = \dot{\xi}\,\mathbb{S}, \qquad \dot{\xi} \geq 0, \tag{3.16}$$

with

$$\mathbb{S} = \beta_p \mathbf{m} \otimes \mathbf{m} + \beta_l(\mathbf{1} - \mathbf{m} \otimes \mathbf{m}), \tag{3.17}$$

where β_p and β_l are, respectively, the swelling strains in the preferred direction $\mathbf{m}$ and in the plane Π perpendicular to $\mathbf{m}$ in the intermediate space $\mathcal{I}(\mathbf{X})$.

(b) Next, we assume that the viscoplastic stretching $\mathbf{D}^p$ may be decomposed as

$$\mathbf{D}^p = (1 - \omega)\mathbf{D}^p_{\text{bc}} + \omega\mathbf{D}^p_{\text{ox}}, \tag{3.18}$$

[2]This assumption is adopted here solely on pragmatic grounds: when discussing finite deformations the theory without plastic spin is far simpler than one with plastic spin.

[3]Cf., discussion of deformation of a normal in Section 8 of Gurtin et al. [48].

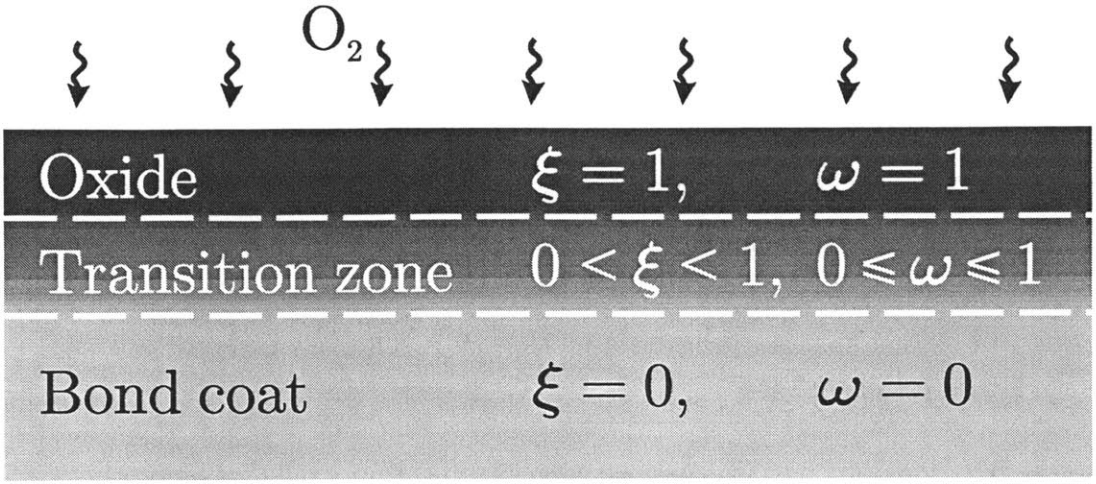

Figure 3-1: Schematic of the oxidation process.

where

$$\mathbf{D}^p_{\text{bc}} \qquad \text{with} \qquad \operatorname{tr}\mathbf{D}^p_{\text{bc}} = 0, \tag{3.19}$$

represents an incompressible plastic stretching due to viscoplastic flow of the unoxidized bond coat, while

$$\mathbf{D}^p_{\text{ox}} \qquad \text{with} \qquad \operatorname{tr}\mathbf{D}^p_{\text{ox}} = 0, \tag{3.20}$$

represents an incompressible plastic stretching due to viscoplastic flow of the oxide. Further,

$$\omega = \omega(\xi) \qquad \text{with} \qquad \omega \in [0, 1], \tag{3.21}$$

represents a "proportioning function" that characterizes the relative extents of plastic flow of the bond coat material and the oxide in the "oxidizing transition zone." A schematic of the oxidized and unoxidized bond-coat, along with the transition zone, is shown in Fig. 3-1.

For later use we define a scalar plastic flow rate and the direction of plastic flow of the unoxidized bond-coat by

$$d^p_{\text{bc}} \stackrel{\text{def}}{=} |\mathbf{D}^p_{\text{bc}}| \geq 0, \qquad \mathbf{N}^p_{\text{bc}} \stackrel{\text{def}}{=} \frac{\mathbf{D}^p_{\text{bc}}}{d^p_{\text{bc}}} \ \text{(when } d^p_{\text{bc}} > 0), \qquad \text{so that} \qquad \mathbf{D}^p_{\text{bc}} = d^p_{\text{bc}}\mathbf{N}^p_{\text{bc}}. \tag{3.22}$$

Similarly, we define a scalar plastic flow rate and the direction of plastic flow of the oxide by

$$d^p_{\text{ox}} \stackrel{\text{def}}{=} |\mathbf{D}^p_{\text{ox}}| \geq 0, \qquad \mathbf{N}^p_{\text{ox}} \stackrel{\text{def}}{=} \frac{\mathbf{D}^p_{\text{ox}}}{d^p_{\text{ox}}} \ \text{(when } d^p_{\text{ox}} > 0), \qquad \text{so that} \qquad \mathbf{D}^p_{\text{ox}} = d^p_{\text{ox}}\mathbf{N}^p_{\text{ox}}. \tag{3.23}$$

3.1.2 Mean swelling strain. Pilling-Bedworth ratio. Relation between J^i and ξ

We define a *mean swelling strain* by

$$\beta = \tfrac{1}{3}\mathrm{tr}\mathbb{S} = \tfrac{1}{3}(\beta_p + 2\beta_l). \tag{3.24}$$

The mean swelling strain β may be related to the classical *Pilling-Bedworth ratio* in the oxidation literature [81] as follows. Consider a simple chemical reaction

$$a\mathrm{M} + b\mathrm{O} \to \mathrm{M}_a\mathrm{O}_b, \tag{3.25}$$

in which M denotes a pure metal which is being oxidized, O denotes the diffusing species which reacts with M to form the oxide, and a and b are stoichiometric coefficients. The *Pilling-Bedworth ratio* for the oxide $\mathrm{M}_a\mathrm{O}_b$ is defined as

$$J_{\mathrm{PB}} \stackrel{\mathrm{def}}{=} \frac{V_{\mathrm{M}_a\mathrm{O}_b}}{aV_{\mathrm{M}}} = \frac{\mathcal{M}_{\mathrm{M}_a\mathrm{O}_b}/\rho_{\mathrm{M}_a\mathrm{O}_b}}{a\,\mathcal{M}_{\mathrm{M}}/\,\rho_{\mathrm{M}}}, \tag{3.26}$$

where $V_{\mathrm{M}_a\mathrm{O}_b}$ is the molar volume of the oxide, and V_{M} is the molar volume of the element M. Also, $\mathcal{M}_{\mathrm{M}_a\mathrm{O}_b}$ is the molar mass of $\mathrm{M}_a\mathrm{O}_b$, $\mathcal{M}_{\mathrm{M}}$ is the molar mass of M, and $\rho_{\mathrm{M}_a\mathrm{O}_b}$ and ρ_{M} are the mass densities of the oxide $\mathrm{M}_a\mathrm{O}_b$ and the element M, respectively. The mean swelling strain β is related to the Pilling-Bedworth ratio by

$$\beta = \tfrac{1}{3}\ln\left(J_{\mathrm{PB}}\right). \tag{3.27}$$

As a specific example, consider the oxidation of aluminum to aluminum oxide,

$$2\mathrm{Al} + \tfrac{3}{2}\mathrm{O}_2 \to \mathrm{Al}_2\mathrm{O}_3. \tag{3.28}$$

This reaction indicates that two Al atoms combine with three O atoms to form alumina. The Pilling-Bedworth ratio for $\mathrm{Al}_2\mathrm{O}_3$ is

$$J_{\mathrm{PB}} = \frac{V_{\mathrm{Al}_2\mathrm{O}_3}}{2V_{\mathrm{Al}}} = 1.28, \tag{3.29}$$

a value which is well in excess of unity. In this case the mean swelling strain is

$$\beta = 0.0823.$$

Next, a standard result from continuum mechanics is that

$$\dot{J}^i = J^i \mathrm{tr}\mathbf{D}^i. \tag{3.30}$$

Eqs. (3.16), (3.17), and (3.24) yield

$$\mathrm{tr}\mathbf{D}^i = 3\beta\dot{\xi}, \tag{3.31}$$

substitution of which in (3.30) gives

$$\overline{\ln J^i} = 3\beta\dot{\xi}. \tag{3.32}$$

Integration of (3.32) subject to the initial condition

$$J^i = 1 \quad \text{when} \quad \xi = 0 \tag{3.33}$$

gives

$$J^i = \exp(3\beta\xi). \tag{3.34}$$

Using (3.27), this relation between J^i and ξ may be be rewritten as

$$J^i = (J_{\text{PB}})^{\xi} \qquad \Longrightarrow \qquad \xi = \frac{\ln J^i}{\ln J_{\text{PB}}}. \tag{3.35}$$

For later use, we also note that

$$\frac{\partial J^i}{\partial \xi} = (\ln J_{\text{PB}})(J_{\text{PB}})^{\xi} = 3\beta J^i. \tag{3.36}$$

3.2 Frame-indifference

A *change in frame*, at each *fixed time* t, is a transformation — defined by a rotation $\mathbf{Q}(t)$ and a spatial point $\mathbf{y}(t)$ — which transforms *spatial points* $\mathbf{x}$ to spatial points

$$\mathbf{x}^* = \mathcal{F}(\mathbf{x}), \tag{3.37}$$

$$= \mathbf{y}(t) + \mathbf{Q}(t)(\mathbf{x} - \mathbf{o}), \tag{3.38}$$

with $\mathbf{o}$ a fixed spatial origin, and the function $\mathcal{F}$ represents a rigid mapping of the observed space into itself. By (3.38) the transformation law for the motion $\mathbf{x} = \boldsymbol{\chi}(\mathbf{X}, t)$ has the form

$$\boldsymbol{\chi}^*(\mathbf{X}, t) = \mathbf{y}(t) + \mathbf{Q}(t)(\boldsymbol{\chi}(\mathbf{X}, t) - \mathbf{o}). \tag{3.39}$$

Hence the deformation gradient $\mathbf{F}$ transforms according to

$$\mathbf{F}^* = \mathbf{Q}\mathbf{F}. \tag{3.40}$$

The reference configuration and the intermediate structural space are independent of the choice of such changes in frame; thus

$$\mathbf{F}^i \quad \text{is invariant under a change in frame.} \tag{3.41}$$

This observation, (3.2), and (3.40) yield the transformation law

$$\mathbf{F}^{e\,*} = \mathbf{Q}\mathbf{F}^e. \tag{3.42}$$

Also, by $(3.10)_2$

$$\mathrm{L}^i \text{ is invariant,} \tag{3.43}$$

and, by $(3.10)_1$, $\mathbf{L}^{e*} = \mathbf{Q}\mathbf{L}^e\mathbf{Q}^\top + \dot{\mathbf{Q}}\mathbf{Q}^\top$, and hence

$$\mathbf{D}^{e*} = \mathbf{Q}\mathbf{D}^e\mathbf{Q}^\top, \qquad \mathbf{W}^{e*} = \mathbf{Q}\mathbf{W}^e\mathbf{Q}^\top + \dot{\mathbf{Q}}\mathbf{Q}^\top. \tag{3.44}$$

Further, by (3.6),

$$\mathbf{F}^{e*} = \mathbf{Q}\mathbf{R}^e\mathbf{U}^e,$$

and we may conclude from the uniqueness of the polar decomposition that

$$\mathbf{R}^{e*} = \mathbf{Q}\mathbf{R}^e, \quad \text{and} \quad \mathbf{U}^e \text{ is invariant,} \tag{3.45}$$

and hence also that

$$\mathrm{C}^e \text{ is invariant.} \tag{3.46}$$

3.3 Balance of forces and moments

Throughout, we denote by P an arbitrary *part* of the reference body B with $\mathbf{n}_\mathrm{R}$ the outward unit normal on the boundary $\partial\mathrm{P}$ of P.

Since time scales associated with species diffusion are usually considerably longer than those associated with wave propagation, we neglect all inertial effects. Then standard considerations of balance of forces and moments, when expressed referentially, give:

(a) There exists a stress tensor $\mathbf{T}_\mathrm{R}$, called the Piola stress, such that the surface traction on an element of the surface $\partial\mathrm{P}$ of P, is given by

$$\mathbf{t}_\mathrm{R}(\mathbf{n}_\mathrm{R}) = \mathbf{T}_\mathrm{R}\mathbf{n}_\mathrm{R}. \tag{3.47}$$

(b) $\mathbf{T}_\mathrm{R}$ satisfies the macroscopic force balance

$$\mathrm{Div}\,\mathbf{T}_\mathrm{R} + \mathbf{b}_\mathrm{R} = \mathbf{0}, \tag{3.48}$$

where $\mathbf{b}_\mathrm{R}$ is an external body force per unit reference volume, which, consistent with neglect of inertial effects, is taken to be time-independent.

(c) $\mathbf{T}_\mathrm{R}$ obeys the symmetry condition

$$\mathbf{T}_\mathrm{R}\mathbf{F}^\top = \mathbf{F}\mathbf{T}_\mathrm{R}^\top, \tag{3.49}$$

which represents a balance of moments.

Finally, as is standard, the Piola stress $\mathbf{T}_\mathrm{R}$ is related to the standard symmetric Cauchy stress $\mathbf{T}$ in the deformed body by

$$\mathbf{T}_\mathrm{R} = J\,\mathbf{T}\,\mathbf{F}^{-\top}, \tag{3.50}$$

so that

$$\mathbf{T} = J^{-1}\mathbf{T}_{\mathrm{R}}\mathbf{F}^{\mathsf{T}}; \tag{3.51}$$

and, as is also standard, under a change in frame $\mathbf{T}$ transforms as

$$\mathbf{T}^{*} = \mathbf{Q}\mathbf{T}\mathbf{Q}^{\mathsf{T}}. \tag{3.52}$$

3.4 Balance law for the diffusing species

Let

$$c_{\mathrm{R}}(\mathbf{X}, t) \tag{3.53}$$

denote the number of moles of diffusing species per unit reference volume which can cause a chemical reaction. Changes in c_{R} in P are brought about by the diffusion across the boundary ∂P, and the consumption of c_{R} by the chemical reaction. The diffusion is characterized by a flux $\mathbf{j}_{\mathrm{R}}(\mathbf{X}, t)$, the number of moles of diffusing species measured per unit area per unit time, so that

$$-\int_{\partial \mathrm{P}} \mathbf{j}_{\mathrm{R}} \cdot \mathbf{n}_{\mathrm{R}}\, da_{\mathrm{R}}$$

represents the number of moles of diffusing species entering P across ∂P per unit time. Further, the consumption of the diffusing species due to the chemical reaction is characterized by

$$-\int_{\mathrm{P}} r_{\mathrm{R}}\, dv_{\mathrm{R}},$$

where r_{R} is the rate of consumption measured in number of moles per unit reference volume per unit time— a sink term. The balance law for the diffusing species therefore takes the form

$$\dot{\int_{\mathrm{P}} c_{\mathrm{R}}\, dv_{\mathrm{R}}} = -\int_{\partial \mathrm{P}} \mathbf{j}_{\mathrm{R}} \cdot \mathbf{n}_{\mathrm{R}}\, da_{\mathrm{R}} - \int_{\mathrm{P}} r_{\mathrm{R}}\, dv_{\mathrm{R}}, \tag{3.54}$$

for every part P. Bringing the time derivative in (3.54) inside the integral and using the divergence theorem on the integral over ∂P, we find that

$$\int_{\mathrm{P}} (\dot{c}_{\mathrm{R}} + \mathrm{Div}\mathbf{j}_{\mathrm{R}} + r_{\mathrm{R}})\, dv_{\mathrm{R}} = 0. \tag{3.55}$$

Since P is arbitrary, this leads to the following local balance:

$$\dot{c}_{\mathrm{R}} = -\mathrm{Div}\mathbf{j}_{\mathrm{R}} - r_{\mathrm{R}}. \tag{3.56}$$

The consumption rate r_{R} may be related to the rate of change of ξ by

$$r_{\mathrm{R}} = \mathcal{R}\dot{\xi}, \tag{3.57}$$

where $\mathcal{R}$, a positive constant, is the amount of diffusing species consumed per unit reference volume in the complete chemical reaction. Using (3.57) in (3.56) we arrive at the following

local balance law for c_{R},

$$\dot{c}_{\mathrm{R}} = -\mathrm{Div}\,\mathbf{j}_{\mathrm{R}} - \mathcal{R}\,\dot{\xi}. \tag{3.58}$$

3.5 Balance of energy. Entropy imbalance

Our discussion of thermodynamics follows Gurtin et al. [48, §64] and involves the following fields:

ε_{R}	the internal energy density per unit reference volume,
η_{R}	the entropy density per unit reference volume,
$\mathbf{q}_{\mathrm{R}}$	the heat flux per unit reference area,
q_{R}	the external heat supply per unit reference volume,
ϑ	the absolute temperature ($\vartheta > 0$),
μ	the chemical potential.

Consider a material region P. Then, consistent with our omission of inertial effects, we neglect kinetic energy, and take the balance law for energy as

$$\dot{\int_{\mathrm{P}} \varepsilon_{\mathrm{R}}\, dv_{\mathrm{R}}} = \int_{\partial \mathrm{P}} (\mathbf{T}_{\mathrm{R}}\mathbf{n}_{\mathrm{R}})\cdot\dot{\boldsymbol{\chi}}\, da_{\mathrm{R}} + \int_{\mathrm{P}} \mathbf{b}_{\mathrm{R}}\cdot\dot{\boldsymbol{\chi}}\, dv_{\mathrm{R}} - \int_{\partial \mathrm{P}} \mathbf{q}_{\mathrm{R}}\mathbf{n}_{\mathrm{R}}\, da_{\mathrm{R}} + \int_{\mathrm{P}} q_{\mathrm{R}}\, dv_{\mathrm{R}} - \int_{\partial \mathrm{P}} \mu\,\mathbf{j}_{\mathrm{R}}\cdot\mathbf{n}_{\mathrm{R}} da_{\mathrm{R}}, \tag{3.59}$$

where the last term in (3.59) represents the energy contribution to P by the diffusing species.

Applying the divergence theorem to the terms in (3.59) involving integrals over the boundary ∂P of P, we obtain

$$\int_{\mathrm{P}} \Big(\dot{\varepsilon}_{\mathrm{R}} - (\mathrm{Div}\,\mathbf{T}_{\mathrm{R}} + \mathbf{b}_{\mathrm{R}})\cdot\dot{\boldsymbol{\chi}} - \mathbf{T}_{\mathrm{R}} : \dot{\mathbf{F}} + \mathrm{Div}\,\mathbf{q}_{\mathrm{R}} - q_{\mathrm{R}} + \mu \mathrm{Div}\,\mathbf{j}_{\mathrm{R}} + \mathbf{j}_{\mathrm{R}}\cdot\nabla\mu \Big)\, dv_{\mathrm{R}} = 0, \tag{3.60}$$

which upon use of the balance laws (3.48) and (3.58), and using the fact that (3.60) must hold for all parts P, gives the local form of the energy balance as

$$\dot{\varepsilon}_{\mathrm{R}} = \mathbf{T}_{\mathrm{R}} : \dot{\mathbf{F}} + \mu(\dot{c}_{\mathrm{R}} + \mathcal{R}\dot{\xi}) - \mathrm{Div}\,\mathbf{q}_{\mathrm{R}} + q_{\mathrm{R}} - \mathbf{j}_{\mathrm{R}}\cdot\nabla\mu\,. \tag{3.61}$$

Also, the second law takes the form of an entropy imbalance

$$\dot{\int_{\mathrm{P}} \eta_{\mathrm{R}}\, dv_{\mathrm{R}}} \geq -\int_{\partial \mathrm{P}} \frac{\mathbf{q}_{\mathrm{R}}\cdot\mathbf{n}_{\mathrm{R}}}{\vartheta}\, da_{\mathrm{R}} + \int_{\mathrm{P}} \frac{q_{\mathrm{R}}}{\vartheta}\, dv_{\mathrm{R}}, \tag{3.62}$$

in which case the local entropy imbalance has the form

$$\dot{\eta}_{\mathrm{R}} \geq -\mathrm{Div}\left(\frac{\mathbf{q}_{\mathrm{R}}}{\vartheta}\right) + \frac{q_{\mathrm{R}}}{\vartheta}. \tag{3.63}$$

Then, in view of the local energy balance (3.61),

$$-\mathrm{Div}\Big(\frac{\mathbf{q}_{\mathrm{R}}}{\vartheta}\Big)+\frac{q_{\mathrm{R}}}{\vartheta}=\frac{1}{\vartheta}(-\mathrm{Div}\,\mathbf{q}_{\mathrm{R}}+q_{\mathrm{R}})+\frac{1}{\vartheta^2}\,\mathbf{q}_{\mathrm{R}}\cdot\nabla\vartheta,$$
$$=\frac{1}{\vartheta}\Big(\dot{\varepsilon}_{\mathrm{R}}-\mathbf{T}_{\mathrm{R}}:\dot{\mathbf{F}}-\mu(\dot{c}_{\mathrm{R}}+\mathcal{R}\dot{\xi})+\frac{1}{\vartheta}\,\mathbf{q}_{\mathrm{R}}\cdot\nabla\vartheta+\mathbf{j}_{\mathrm{R}}\cdot\nabla\mu\Big),$$

and this with the local entropy imbalance (3.63) implies that

$$(\dot{\varepsilon}_{\mathrm{R}}-\vartheta\dot{\eta}_{\mathrm{R}})-\mathbf{T}_{\mathrm{R}}:\dot{\mathbf{F}}-\mu(\dot{c}_{\mathrm{R}}+\mathcal{R}\dot{\xi})+\frac{1}{\vartheta}\,\mathbf{q}_{\mathrm{R}}\cdot\nabla\vartheta+\mathbf{j}_{\mathrm{R}}\cdot\nabla\mu\leq 0\,. \tag{3.64}$$

Introducing the Helmholtz free energy

$$\psi_{\mathrm{R}}=\varepsilon_{\mathrm{R}}-\vartheta\eta_{\mathrm{R}}, \tag{3.65}$$

(3.64) yields the following local free-energy imbalance

$$\dot{\psi}_{\mathrm{R}}+\eta_{\mathrm{R}}\dot{\vartheta}-\mathbf{T}_{\mathrm{R}}:\dot{\mathbf{F}}-\mu(\dot{c}_{\mathrm{R}}+\mathcal{R}\dot{\xi})+\frac{1}{\vartheta}\,\mathbf{q}_{\mathrm{R}}\cdot\nabla\vartheta+\mathbf{j}_{\mathrm{R}}\cdot\nabla\mu\leq 0\,. \tag{3.66}$$

3.5.1 Stress-power

The term $\mathbf{T}_{\mathrm{R}}:\dot{\mathbf{F}}$ represents the stress-power per unit reference volume. Using (3.2), (3.50), and $(3.10)_2$ the stress-power may be written as

$$\begin{aligned}\mathbf{T}_{\mathrm{R}}:\dot{\mathbf{F}}&=\mathbf{T}_{\mathrm{R}}:(\dot{\mathbf{F}}^{e}\mathbf{F}^{i}+\mathbf{F}^{e}\dot{\mathbf{F}}^{i}),\\&=(\mathbf{T}_{\mathrm{R}}\mathbf{F}^{i\mathsf{T}}):\dot{\mathbf{F}}^{e}+(\mathbf{F}^{e\mathsf{T}}\mathbf{T}_{\mathrm{R}}):\dot{\mathbf{F}}^{i},\\&=(J\mathbf{F}^{e-1}\mathbf{T}\mathbf{F}^{e-\mathsf{T}}):(\mathbf{F}^{e\mathsf{T}}\dot{\mathbf{F}}^{e})+(\mathbf{C}^{e}J\mathbf{F}^{e-1}\mathbf{T}\mathbf{F}^{e-\mathsf{T}}):\mathbf{L}^{i}.\end{aligned} \tag{3.67}$$

In view of (3.67), we introduce two new stress measures:

- The elastic second Piola stress,

$$\mathbf{T}^{e}\stackrel{\mathrm{def}}{=}J\mathbf{F}^{e-1}\mathbf{T}\mathbf{F}^{e-\mathsf{T}}, \tag{3.68}$$

  which is *symmetric* on account of the symmetry of the Cauchy stress $\mathbf{T}$.

- The Mandel stress,

$$\mathbf{M}^{e}\stackrel{\mathrm{def}}{=}\mathbf{C}^{e}\mathbf{T}^{e}, \tag{3.69}$$

  which in general is *not symmetric.*[4]

[4]Substituting (3.68) into (3.69), we obtain that the Mandel stress is given by $\mathbf{M}^{e}=J\mathbf{F}^{e\mathsf{T}}\mathbf{T}\mathbf{F}^{e-\mathsf{T}}$. Note that for materials which are elastically isotropic and plastically incompressible, the Mandel stress is traditionally defined as $\mathbf{M}^{e}\stackrel{\mathrm{def}}{=}J^{e}\mathbf{F}^{e\mathsf{T}}\mathbf{T}\mathbf{F}^{e-\mathsf{T}}$. Here, since we are dealing with a situation in which the oxidizing material is inelastically dilatant, that is $J^{i}>1$, we define the Mandel stress as $\mathbf{M}^{e}\stackrel{\mathrm{def}}{=}J\mathbf{F}^{e\mathsf{T}}\mathbf{T}\mathbf{F}^{e-\mathsf{T}}$, which uses $J=J^{e}J^{i}$, and not just J^{e}.

Note that on account of the transformation rule (3.42) for $\mathbf{F}^e$, and the transformation rule (3.52), the elastic second Piola stress and the Mandel stress are invariant under a change in frame,

$$\mathbf{T}^{e*} = \mathbf{T}^e \qquad \text{and} \qquad \mathbf{M}^{e*} = \mathbf{M}^e. \tag{3.70}$$

Further, from (3.8)

$$\dot{\mathbf{C}}^e = \dot{\mathbf{F}}^{e\mathsf{T}}\mathbf{F}^e + \mathbf{F}^{e\mathsf{T}}\dot{\mathbf{F}}^e\,. \tag{3.71}$$

Thus, using the definitions (3.68), (3.69) and the relation (3.71), the stress-power (3.67) may be written as

$$\mathbf{T}_{\mathrm{R}} : \dot{\mathbf{F}} = \underbrace{\tfrac{1}{2}\mathbf{T}^e : \dot{\mathbf{C}}^e}_{\text{elastic power}} + \underbrace{\mathbf{M}^e : \mathbf{L}^i}_{\text{inelastic power}}\,. \tag{3.72}$$

Further, use of the assumptions (3.14), (3.16), (3.19), (3.20), and (3.12) concerning plastic flow gives

$$\mathbf{T}_{\mathrm{R}} : \dot{\mathbf{F}} = \tfrac{1}{2}\mathbf{T}^e : \dot{\mathbf{C}}^e + (1-\omega)\,\mathbf{M}_0^e : \mathbf{D}_{\mathrm{bc}}^p + \omega\,\mathbf{M}_0^e : \mathbf{D}_{\mathrm{ox}}^p + \dot{\xi}\mathbf{M}^e : \mathbb{S}. \tag{3.73}$$

Using (3.73) in (3.66) allows us to write the free energy imbalance as

$$\dot{\psi}_{\mathrm{R}} + \eta_{\mathrm{R}}\dot{\vartheta} - \tfrac{1}{2}\mathbf{T}^e : \dot{\mathbf{C}}^e - (1-\omega)\,\mathbf{M}_0^e : \mathbf{D}_{\mathrm{bc}}^p - \omega\,\mathbf{M}_0^e : \mathbf{D}_{\mathrm{ox}}^p - (\mathbf{M}^e : \mathbb{S} + \mu\mathcal{R})\dot{\xi} - \mu\dot{c}_{\mathrm{R}} + \frac{1}{\vartheta}\,\mathbf{q}_{\mathrm{R}}\cdot\nabla\vartheta + \mathbf{j}_{\mathrm{R}}\cdot\nabla\mu \le 0\,. \tag{3.74}$$

Finally, note that ψ_{R}, η_{R}, ϑ, ξ, and c_{R} are invariant under a change in frame since they are scalar fields, and on account of the transformation rules discussed in §3.2, and the transformation rules (3.70), the fields

$$\mathbf{C}^e, \quad \mathbf{D}_{\mathrm{bc}}^p, \quad \mathbf{D}_{\mathrm{ox}}^p, \quad \mathbb{S}, \quad \mathbf{T}^e, \quad \text{and} \quad \mathbf{M}^e, \tag{3.75}$$

are also invariant, as are the fields

$$\mathbf{q}_{\mathrm{R}}, \quad \nabla\vartheta, \quad \mathbf{j}_{\mathrm{R}}, \qquad \text{and} \quad \nabla\mu, \tag{3.76}$$

since they are referential vector fields.

3.6 Constitutive theory

3.6.1 Basic constitutive equations

Next, guided by the free-energy imbalance (3.74), we first consider the following set of constitutive equations for the free energy ψ_{R}, the stress $\mathbf{T}^e$, the entropy η_{R}, and the chemical

potential μ:

$$\left.\begin{aligned} \psi_{\mathrm{R}} &= \bar{\psi}_{\mathrm{R}}(\mathbf{\Lambda}), \\ \mathbf{T}^e &= \bar{\mathbf{T}}^e(\mathbf{\Lambda}), \\ \eta_{\mathrm{R}} &= \bar{\eta}_{\mathrm{R}}(\mathbf{\Lambda}), \\ \mu &= \bar{\mu}(\mathbf{\Lambda}), \end{aligned}\right\} \tag{3.77}$$

where $\mathbf{\Lambda}$ denotes the list

$$\mathbf{\Lambda} = (\mathbf{C}^e, \vartheta, c_{\mathrm{R}}, \xi). \tag{3.78}$$

Substituting the constitutive equations (3.77) into the dissipation inequality, we find that the free-energy imbalance (3.74) may then be written as

$$\begin{aligned} &\Big(\frac{\partial\bar{\psi}_{\mathrm{R}}}{\partial\mathbf{C}^e} - \tfrac{1}{2}\bar{\mathbf{T}}^e\Big) : \dot{\mathbf{C}}^e + \Big(\frac{\partial\bar{\psi}_{\mathrm{R}}}{\partial\vartheta} + \bar{\eta}_{\mathrm{R}}\Big)\dot{\vartheta} + \Big(\frac{\partial\bar{\psi}_{\mathrm{R}}}{\partial c_{\mathrm{R}}} - \bar{\mu}\Big)\dot{c}_{\mathrm{R}} \\ &\quad - (1-\omega)\mathbf{M}_0^e : \mathbf{D}_{\mathrm{bc}}^p - \omega\mathbf{M}_0^e : \mathbf{D}_{\mathrm{ox}}^p - \Big(\mathbf{M}^e : \mathbb{S} + \bar{\mu}\mathcal{R} - \frac{\partial\bar{\psi}_{\mathrm{R}}}{\partial\xi}\Big)\dot{\xi} + \frac{1}{\vartheta}\,\mathbf{q}_{\mathrm{R}}\cdot\nabla\vartheta + \mathbf{j}_{\mathrm{R}}\cdot\nabla\bar{\mu} \le 0\,. \end{aligned} \tag{3.79}$$

As is classical, we now assume that the stress $\mathbf{T}^e$, the entropy η_{R}, and the chemical potential μ are given by the state relations

$$\left.\begin{aligned} \mathbf{T}^e &= 2\frac{\partial\bar{\psi}_{\mathrm{R}}(\mathbf{\Lambda})}{\partial\mathbf{C}^e}, \\ \eta_{\mathrm{R}} &= -\frac{\partial\bar{\psi}_{\mathrm{R}}(\mathbf{\Lambda})}{\partial\vartheta}, \\ \mu &= \frac{\partial\bar{\psi}_{\mathrm{R}}(\mathbf{\Lambda})}{\partial c_{\mathrm{R}}}. \end{aligned}\right\} \tag{3.80}$$

We are then left with the following reduced dissipation inequality

$$(1-\omega)\mathbf{M}_0^e : \mathbf{D}_{\mathrm{bc}}^p + \omega\mathbf{M}_0^e : \mathbf{D}_{\mathrm{ox}}^p + \mathcal{F}\,\dot{\xi} - \frac{1}{\vartheta}\,\mathbf{q}_{\mathrm{R}}\cdot\nabla\vartheta - \mathbf{j}_{\mathrm{R}}\cdot\nabla\mu \ge 0\,, \tag{3.81}$$

where

$$\mathcal{F} \stackrel{\text{def}}{=} \mathcal{A} + \mathbf{M}^e : \mathbb{S} + \mu\mathcal{R} \tag{3.82}$$

represents a *dissipative* thermodynamic force conjugate to the oxide volume fraction ξ, with

$$\mathcal{A}(\mathbf{\Lambda}) \stackrel{\text{def}}{=} -\frac{\partial\bar{\psi}_{\mathrm{R}}(\mathbf{\Lambda})}{\partial\xi}, \tag{3.83}$$

an energetic constitutive response function, which we call the *affinity* of the chemical reaction; as we shall see, the dissipative force $\mathcal{F}$ plays a fundamental role in the theory.

Henceforth, for brevity and whenever convenient, we write

$$\mathbf{D}_\alpha^p, \qquad \alpha = 1, 2, \tag{3.84}$$

with the understanding that

$$\mathbf{D}_1^p \equiv \mathbf{D}_{\rm bc}^p, \qquad \text{and} \qquad \mathbf{D}_2^p \equiv \mathbf{D}_{\rm ox}^p. \tag{3.85}$$

We also introduce a pair of scalar *internal variables*

$$S_\alpha, \qquad \alpha = 1, 2 \tag{3.86}$$

to represent the microstructural resistance to plastic flow. Since S_α are scalar fields, they are invariant under a change in frame. Then, guided by (3.81), and experience with plasticity theories we assume that

$$\left.\begin{aligned} \mathbf{D}_\alpha^p &= \bar{\mathbf{D}}_\alpha^p(\mathbf{M}_0^e, \vartheta, S_\alpha), \\ \dot{S}_\alpha &= h_\alpha(d_\alpha^p, \vartheta, S_\alpha), \\ \dot{\xi} &= \bar{\dot{\xi}}(\mathcal{F}, \vartheta, \xi). \end{aligned}\right\} \tag{3.87}$$

To the constitutive equations (3.77) and (3.87), we append a Fourier-type relation for the heat flux, and a Fick-type relation for the flux of the diffusing species,

$$\left.\begin{aligned} \mathbf{q}_{\rm R} &= -\mathbf{K}(\mathbf{\Lambda})\,\nabla\vartheta, \\ \mathbf{j}_{\rm R} &= -\mathbf{M}(\mathbf{\Lambda})\,\nabla\mu, \end{aligned}\right\} \tag{3.88}$$

where $\mathbf{K}$ is a *thermal conductivity tensor*, and $\mathbf{M}$ is a *mobility tensor*.[5]

Using (3.87), (3.88), (3.22) and (3.23), the dissipation inequality (3.81) may be written as

$$(1-\omega)(\mathbf{M}_0^e : \bar{\mathbf{N}}_{\rm bc}^p)\bar{d}_{\rm bc}^p + \omega(\mathbf{M}_0^e : \bar{\mathbf{N}}_{\rm ox}^p)\bar{d}_{\rm ox}^p + \mathcal{F}\,\bar{\dot{\xi}} + \frac{1}{\vartheta}\,\nabla\vartheta \cdot \mathbf{K}\nabla\vartheta + \nabla\mu \cdot \mathbf{M}\nabla\mu \geq 0. \tag{3.89}$$

Henceforth, we write

$$\bar{\sigma}_\alpha \stackrel{\rm def}{=} \mathbf{M}_0^e : \bar{\mathbf{N}}_\alpha^p \tag{3.90}$$

for the Mandel stress resolved in the plastic flow direction. We also assume that the material is *strongly dissipative* in the sense that

$$\bar{\sigma}_\alpha\, d_\alpha^p > 0 \quad \text{for} \quad d_\alpha^p > 0, \tag{3.91}$$

$$\mathcal{F}\,\dot{\xi} > 0 \quad \text{for} \quad \dot{\xi} > 0, \tag{3.92}$$

$$\nabla\vartheta \cdot \mathbf{K}(\mathbf{\Lambda})\nabla\vartheta > 0 \quad \text{for} \quad \nabla\vartheta \neq \mathbf{0}, \tag{3.93}$$

$$\nabla\mu \cdot \mathbf{M}(\mathbf{\Lambda})\nabla\mu > 0 \quad \text{for} \quad \nabla\mu \neq \mathbf{0}. \tag{3.94}$$

Thus note that the thermal conductivity tensor $\mathbf{K}$ and the mobility tensor $\mathbf{M}$ are positive-definite.

Note that on account of the transformation rules listed in the paragraph containing (3.75) and (3.76), *the constitutive equations* (3.77), (3.87), *and* (3.88) *are frame-indifferent.*

[5] We neglect Soret-type coupling effects in which $\mathbf{j}_{\rm R}$ is affected by $\nabla\vartheta$, and $\mathbf{q}_{\rm R}$ by $\nabla\mu$.

3.6.2 Further consequences of thermodynamics

In view of (3.77), (3.80) and (3.83), we have the *first Gibbs relation*,

$$\dot{\psi}_{\mathrm{R}} = \tfrac{1}{2}\mathbf{T}^e : \dot{\mathbf{C}}^e - \eta_{\mathrm{R}}\dot{\vartheta} + \mu\dot{c}_{\mathrm{R}} - \mathcal{A}\dot{\xi}, \tag{3.95}$$

which, with (3.65), yields the *second Gibbs relation*

$$\dot{\varepsilon}_{\mathrm{R}} = \vartheta\dot{\eta}_{\mathrm{R}} + \tfrac{1}{2}\mathbf{T}^e : \dot{\mathbf{C}}^e + \mu\dot{c}_{\mathrm{R}} - \mathcal{A}\dot{\xi}. \tag{3.96}$$

Using balance of energy (3.61), the stress-power relation (3.73), the second Gibbs relation (3.96), the constitutive equations $(3.77)_{2,3}$ and (3.87), and equations (3.91) through (3.94) we arrive at the *entropy balance*

$$\vartheta\dot{\eta}_{\mathrm{R}} = -\mathrm{Div}\,\mathbf{q}_{\mathrm{R}} + q_{\mathrm{R}} + (1-\omega)\,\bar{\sigma}_{\mathrm{bc}}\,d^p_{\mathrm{bc}} + \omega\,\bar{\sigma}_{\mathrm{ox}}\,d^p_{\mathrm{ox}} + \mathcal{F}\,\dot{\xi} + \nabla\mu\cdot\mathbf{M}\nabla\mu. \tag{3.97}$$

Granted the thermodynamically restricted constitutive relations (3.80), this balance is equivalent to the balance of energy.

Next, the internal energy density is given by

$$\varepsilon_{\mathrm{R}} = \bar{\varepsilon}_{\mathrm{R}}(\mathbf{\Lambda}) \stackrel{\mathrm{def}}{=} \bar{\psi}_{\mathrm{R}}(\mathbf{\Lambda}) + \vartheta\,\bar{\eta}_{\mathrm{R}}(\mathbf{\Lambda}), \tag{3.98}$$

and, as is standard, the *specific heat* is defined by

$$c \stackrel{\mathrm{def}}{=} \frac{\partial\bar{\varepsilon}(\mathbf{\Lambda})}{\partial\vartheta}. \tag{3.99}$$

Hence, from (3.98)

$$c = \Big(\frac{\partial\bar{\psi}(\mathbf{\Lambda})}{\partial\vartheta} + \bar{\eta}(\mathbf{\Lambda}) + \vartheta\,\frac{\partial\bar{\eta}(\mathbf{\Lambda})}{\partial\vartheta}\Big), \tag{3.100}$$

and use of (3.80) gives

$$c = -\vartheta\,\frac{\partial^2\bar{\psi}(\mathbf{\Lambda})}{\partial\vartheta^2}. \tag{3.101}$$

Next, from (3.80), (3.83), and (3.101),

$$\begin{aligned}\vartheta\,\dot{\eta}_{\mathrm{R}} &= -\vartheta\,\frac{\partial^2\bar{\psi}(\mathbf{\Lambda})}{\partial\vartheta\,\partial\mathbf{C}^e} : \dot{\mathbf{C}}^e + c\,\dot{\vartheta} - \vartheta\,\frac{\partial^2\bar{\psi}(\mathbf{\Lambda})}{\partial\vartheta\,\partial c_{\mathrm{R}}}\,\dot{c}_{\mathrm{R}} - \vartheta\,\frac{\partial^2\bar{\psi}(\mathbf{\Lambda})}{\partial\vartheta\,\partial\xi}\,\dot{\xi}\\ &= -\tfrac{1}{2}\,\vartheta\,\frac{\partial\mathbf{T}^e}{\partial\vartheta} : \dot{\mathbf{C}}^e + c\,\dot{\vartheta} - \vartheta\,\frac{\partial\mu}{\partial\vartheta}\,\dot{c}_{\mathrm{R}} + \vartheta\,\frac{\partial\mathcal{A}}{\partial\vartheta}\dot{\xi},\end{aligned} \tag{3.102}$$

Then, using (3.101) and (3.102) in (3.97) gives the following partial differential equation for the temperature

$$c\dot{\vartheta} = -\mathrm{Div}\,\mathbf{q}_{\mathrm{R}} + q_{\mathrm{R}} + (1-\omega)\,\bar{\sigma}_{\mathrm{bc}}\,d^p_{\mathrm{bc}} + \omega\,\bar{\sigma}_{\mathrm{ox}}\,d^p_{\mathrm{ox}} + \mathcal{F}\,\dot{\xi} + \nabla\mu\cdot\mathbf{M}\nabla\mu + \tfrac{1}{2}\vartheta\,\frac{\partial\mathbf{T}^e}{\partial\vartheta} : \dot{\mathbf{C}}^e + \vartheta\,\frac{\partial\mu}{\partial\vartheta}\,\dot{c}_{\mathrm{R}} - \vartheta\,\frac{\partial\mathcal{A}}{\partial\vartheta}\dot{\xi}. \tag{3.103}$$

3.6.3 Isotropy

We now restrict all material response, except the swelling due to oxidation, to be isotropic. In this case,

(†) the thermal conductivity and the mobility tensors have the representations

$$\mathbf{K}(\mathbf{\Lambda}) = \kappa(\mathbf{\Lambda})\mathbf{1}, \qquad \text{with} \qquad \kappa(\mathbf{\Lambda}) > 0 \tag{3.104}$$

a scalar thermal conductivity, and

$$\mathbf{M}(\mathbf{\Lambda}) = m(\mathbf{\Lambda})\mathbf{1}, \qquad \text{with} \qquad m(\mathbf{\Lambda}) > 0 \tag{3.105}$$

a scalar mobility, and

(‡) the response functions $\bar{\psi}_{\mathrm{R}}$, $\bar{\mathbf{T}}^e$, $\bar{\eta}_{\mathrm{R}}$, $\bar{\mu}$, $\bar{\mathbf{D}}^p_\alpha$, h_α, κ, and m must also each be *isotropic.*

Isotropic free energy

An immediate consequence of the isotropy of the free energy is that the free energy function has the representation

$$\bar{\psi}_{\mathrm{R}}(\mathbf{C}^e, \vartheta, c_{\mathrm{R}}, \xi)) = \tilde{\psi}_{\mathrm{R}}(\mathcal{I}_{\mathbf{C}^e}, \vartheta, c_{\mathrm{R}}, \xi), \tag{3.106}$$

where

$$\mathcal{I}_{\mathbf{C}^e} = \Big(I_1(\mathbf{C}^e), I_2(\mathbf{C}^e), I_3(\mathbf{C}^e)\Big)$$

is the list of principal invariants of $\mathbf{C}^e$. Thus, from $(3.80)_1$, it follows that

$$\mathbf{T}^e = \bar{\mathbf{T}}^e(\mathcal{I}_{\mathbf{C}^e}, \vartheta, c_{\mathrm{R}}, \xi) = 2\frac{\partial\tilde{\psi}(\mathcal{I}_{\mathbf{C}^e}, \vartheta, c_{\mathrm{R}}, \xi)}{\partial \mathbf{C}^e}, \tag{3.107}$$

and that $\bar{\mathbf{T}}^e$ is an *isotropic function of* $\mathbf{C}^e$. Then since the Mandel stress is defined by (cf. (3.69))

$$\mathbf{M}^e = \mathbf{C}^e\mathbf{T}^e,$$

we find that $\mathbf{T}^e$ and $\mathbf{C}^e$ commute,

$$\mathbf{C}^e\mathbf{T}^e = \mathbf{T}^e\mathbf{C}^e, \tag{3.108}$$

and hence that *the Mandel stress* $\mathbf{M}^e$ *is symmetric.*

Next, the spectral representation of $\mathbf{C}^e$ is

$$\mathbf{C}^e = \sum_{i=1}^{3} \omega_i^e \mathbf{r}_i^e \otimes \mathbf{r}_i^e, \qquad \text{with} \qquad \omega_i^e = \lambda_i^{e\,2}, \tag{3.109}$$

where $(\mathbf{r}_1^e, \mathbf{r}_2^e, \mathbf{r}_2^e)$ are the orthonormal eigenvectors of $\mathbf{C}^e$ and $\mathbf{U}^e$, and $(\lambda_1^e, \lambda_2^e, \lambda_3^e)$ are the positive eigenvalues of $\mathbf{U}^e$. Instead of using the invariants $\mathcal{I}_{\mathbf{C}^e}$, the free energy $\bar{\psi}_{\mathrm{R}}$ may then

be alternatively expressed in terms of the principal stretches as

$$\psi_{\mathrm{R}} = \breve{\psi}_{\mathrm{R}}(\lambda_1^e, \lambda_2^e, \lambda_3^e, \vartheta, c_{\mathrm{R}}, \xi). \tag{3.110}$$

Let

$$\mathbf{E}^e \stackrel{\text{def}}{=} \ln \mathbf{U}^e = \sum_{i=1}^{3} E_i^e \, \mathbf{r}_i^e \otimes \mathbf{r}_i^e, \tag{3.111}$$

denote the logarithmic elastic strain with principal values

$$E_i^e \stackrel{\text{def}}{=} \ln \lambda_i^e, \tag{3.112}$$

and consider an elastic free energy function of the form

$$\breve{\psi}_{\mathrm{R}}(\lambda_1^e, \lambda_2^e, \lambda_3^e, \vartheta, c_{\mathrm{R}}, \xi) = \breve{\psi}_{\mathrm{R}}(E_1^e, E_2^e, E_3^e, \vartheta, c_{\mathrm{R}}, \xi). \tag{3.113}$$

Then, straightforward calculations [cf., e.g., 5] show that the Mandel stress is given by

$$\mathbf{M}^e = \sum_{i=1}^{3} \frac{\partial \breve{\psi}(E_1^e, E_2^e, E_3^e, \vartheta, c_{\mathrm{R}}, \xi)}{\partial E_i^e} \mathbf{r}_i^e \otimes \mathbf{r}_i^e. \tag{3.114}$$

With the logarithmic elastic strain defined by (3.111), and bearing (3.113) and (3.114), for isotropic elastic materials we henceforth consider a free energy of the form

$$\psi_{\mathrm{R}} = \hat{\psi}_{\mathrm{R}}(\mathcal{I}_{\mathbf{E}^e}, \vartheta, c_{\mathrm{R}}, \xi) \tag{3.115}$$

with $\mathcal{I}_{\mathbf{E}^e}$ a list of principal invariants of $\mathbf{E}^e$, or equivalently a list of principal values of $\mathbf{E}^e$. The Mandel stress is then given by

$$\mathbf{M}^e = \frac{\partial \hat{\psi}_{\mathrm{R}}(\mathcal{I}_{\mathbf{E}^e}, \vartheta, c_{\mathrm{R}}, \xi)}{\partial \mathbf{E}^e}, \tag{3.116}$$

and the corresponding Cauchy stress is

$$\mathbf{T} = J^{-1} \mathbf{R}^e \mathbf{M}^e \mathbf{R}^{e\mathsf{T}}. \tag{3.117}$$

3.6.4 Plastic flow rule

Recall the constitutive equation $(3.87)_1$ for the plastic stretchings $\mathbf{D}_\alpha^p$,

$$\mathbf{D}_\alpha^p = \bar{\mathbf{D}}_\alpha^p(\mathbf{M}_0^e, \vartheta, S_\alpha) = \bar{d}_\alpha^p(\mathbf{M}_0^e, \vartheta, S_\alpha) \, \bar{\mathbf{N}}_\alpha^p(\mathbf{M}^e, \vartheta, S_\alpha). \tag{3.118}$$

Guided by (3.89), we adopt the classical *co-directionality hypothesis* and assume henceforth that each direction of plastic flow $\bar{\mathbf{N}}_\alpha^p$ is parallel to and points in the same direction as $\mathbf{M}_0^e$, so that

$$\bar{\mathbf{N}}_\alpha^p = \frac{\mathbf{M}_0^e}{|\mathbf{M}_0^e|}. \tag{3.119}$$

Further, note that on account of the isotropy of $\bar{\mathbf{D}}^p_\alpha$, the scalar flow rate function $\bar{d}^p_\alpha(\mathbf{M}^e, \vartheta, S_\alpha)$ is also isotropic, and has the representation

$$d^p_\alpha = \bar{d}^p_\alpha(\mathcal{I}_{\mathbf{M}^e_0}, \vartheta, S_\alpha) \geq 0, \tag{3.120}$$

where $\mathcal{I}_{\mathbf{M}^e_0}$ is the list of principal invariants of $\mathbf{M}^e_0$.

Note that in our *homogenized model*, on account of (3.119) the plastic flow directions for the bond-coat and the oxide are *identical*

$$\bar{\mathbf{N}}^p_{\text{bc}} = \bar{\mathbf{N}}^p_{\text{ox}} = \frac{\mathbf{M}^e_0}{|\mathbf{M}^e_0|} \equiv \mathbf{N}^p, \tag{3.121}$$

and henceforth denoted by $\mathbf{N}^p$. A further consequence of (3.119) and (3.121) is that from the definition (3.90) for the resolved Mandel stress, we have that the resolved stresses in the bond coat and the oxide are also the same,

$$\bar{\sigma}_{\text{bc}} = \bar{\sigma}_{\text{ox}} = \mathbf{N}^p : \mathbf{M}^e_0 = |\mathbf{M}^e_0| \equiv \bar{\sigma}. \tag{3.122}$$

Next, to make connection with the widely used terminology in the plasticity literature, we replace $\bar{\sigma} = |\mathbf{M}^e_0|$ by

$$\bar{\sigma} \stackrel{\text{def}}{=} \sqrt{3/2}\,|\mathbf{M}^e_0|, \tag{3.123}$$

and call this newly defined quantity an *equivalent tensile stress*. Correspondingly, we define *equivalent plastic tensile rates* for the bond coat and oxide by

$$\dot{\bar{\epsilon}}^p_\alpha \stackrel{\text{def}}{=} \sqrt{2/3}\,d^p_\alpha. \tag{3.124}$$

Then, using (3.123), (3.124), and (3.119), the plastic stretchings $\mathbf{D}^p_\alpha$ in (3.118) may be written as

$$\mathbf{D}^p_\alpha = \dot{\bar{\epsilon}}^p_\alpha \left(\frac{3\mathbf{M}^e_0}{2\bar{\sigma}}\right), \tag{3.125}$$

with

$$\dot{\bar{\epsilon}}^p_\alpha = \tilde{\dot{\bar{\epsilon}}}^p_\alpha(\mathcal{I}_{\mathbf{M}^e_0}, \vartheta, S_\alpha) \geq 0. \tag{3.126}$$

In accordance with prior experience, we henceforth neglect any dependence of viscoplastic flow on $\det \mathbf{M}^e_0$, and assume that the equivalent plastic tensile strain rates are given by

$$\dot{\bar{\epsilon}}^p_\alpha = \tilde{\dot{\bar{\epsilon}}}^p_\alpha(\bar{\sigma}, \vartheta, S_\alpha) \geq 0. \tag{3.127}$$

Further, in view of (3.124), the evolution equations of the resistances S_α are taken to be given by

$$\dot{S}_\alpha = h_\alpha(\dot{\bar{\epsilon}}^p_\alpha, \vartheta, S_\alpha). \tag{3.128}$$

Finally, since the directions of plastic flow are identical, it is useful to introduce an overall equivalent plastic tensile strain rate

$$\dot{\bar{\epsilon}}^p = \omega\dot{\bar{\epsilon}}^p_{\text{ox}} + (1-\omega)\dot{\bar{\epsilon}}^p_{\text{bc}}, \tag{3.129}$$

so that

$$\mathbf{D}^p = \dot{\bar{\epsilon}}^p \left(\frac{3\mathbf{M}_0^e}{2\bar{\sigma}} \right). \tag{3.130}$$

3.7 Summary

In this section we summarize our constitutive theory. The theory relates the following basic fields:

$\mathbf{x} = \boldsymbol{\chi}(\mathbf{X}, t)$,	motion;
$\mathbf{F} = \nabla\boldsymbol{\chi}, \quad J = \det \mathbf{F} > 0$,	deformation gradient;
$\mathbf{F} = \mathbf{F}^e\mathbf{F}^i$,	multiplicative decomposition of $\mathbf{F}$;
$\mathbf{F}^e, \quad J^e = \det \mathbf{F}^e > 0$,	elastic distortion;
$\mathbf{F}^i, \quad J^i = \det \mathbf{F}^i > 0$,	inelastic distortion;
$\mathbf{F}^e = \mathbf{R}^e\mathbf{U}^e$,	polar decomposition of $\mathbf{F}^e$;
$\mathbf{C}^e = \mathbf{F}^{e\mathsf{T}}\mathbf{F}^e = \mathbf{U}^{e\,2}$,	elastic right Cauchy-Green tensor;
$\mathbf{U}^e = \sum_{\alpha=1}^{3} \lambda_\alpha^e \mathbf{r}_\alpha^e \otimes \mathbf{r}_\alpha^e$,	spectral decomposition of $\mathbf{U}^e$;
$\mathbf{E}^e = \sum_{\alpha=1}^{3} (\ln \lambda_\alpha^e)\mathbf{r}_\alpha^e \otimes \mathbf{r}_\alpha^e$,	logarithmic elastic strain;
$\mathbf{T} = \mathbf{T}^\mathsf{T}$,	Cauchy stress;
$\mathbf{T}^e = J\mathbf{F}^{e-1}\mathbf{T}\mathbf{F}^{e-\mathsf{T}}$,	Elastic second Piola stress;
$\mathbf{M}^e = J\mathbf{R}^{e\mathsf{T}}\mathbf{T}\mathbf{R}^e$,	Mandel stress;
$\mathbf{T}_{\mathrm{R}} = J\mathbf{T}\mathbf{F}^{-\mathsf{T}}$,	Piola stress;
ψ_{R},	free energy density per unit reference volume;
η_{R},	entropy density per unit reference volume;
$\vartheta > 0$,	absolute temperature;
$\nabla\vartheta$,	referential temperature gradient;
$\mathbf{q}_{\mathrm{R}}$,	referential heat flux vector;
c_{R},	concentration of diffusing oxygen in moles per unit reference volume;
μ,	chemical potential of diffusing oxygen;
$\nabla\mu$,	referential gradient of chemical potential;
$\mathbf{j}_{\mathrm{R}}$,	referential oxygen flux vector;
$\xi \in [0, 1]$,	local volume fraction of oxide;
$S_{\mathrm{bc}}, S_{\mathrm{ox}}$,	scalar internal variables representing the flow resistances of the bond coat and oxide.

3.7.1 Constitutive equations

1. **Free energy**

$$\psi_{\mathrm{R}} = \hat{\psi}_{\mathrm{R}}(\mathcal{I}_{\mathbf{E}^e}, \vartheta, c_{\mathrm{R}}, \xi), \tag{3.131}$$

where $\mathcal{I}_{\mathbf{E}^e}$ represents a list of the principal invariants of the logarithmic elastic strain $\mathbf{E}^e$.

2. **Mandel stress. Cauchy stress**

The Mandel stress is given by

$$\mathbf{M}^e = \frac{\partial \hat{\psi}_{\mathrm{R}}(\mathcal{I}_{\mathbf{E}^e}, \vartheta, c_{\mathrm{R}}, \xi)}{\partial \mathbf{E}^e}, \tag{3.132}$$

which, on account of the isotropy of $\hat{\psi}_{\mathrm{R}}$ is symmetric. We call the quantity

$$\bar{\sigma} \stackrel{\text{def}}{=} \sqrt{3/2}\,|\mathbf{M}_0^e|, \tag{3.133}$$

the equivalent tensile stress. The Cauchy stress in the deformed body is related to the Mandel stress by

$$\mathbf{T} = J^{-1}\,(\mathbf{R}^e \mathbf{M}^e \mathbf{R}^{e\mathrm{T}}). \tag{3.134}$$

3. **Entropy. Chemical potential. Affinity**

The partial derivatives of the free energy

$$\left.\begin{aligned} \eta_{\mathrm{R}} &= -\frac{\partial \hat{\psi}_{\mathrm{R}}(\mathcal{I}_{\mathbf{E}^e}, \vartheta, c_{\mathrm{R}}, \xi)}{\partial \vartheta}, \\ \mu &= \frac{\partial \hat{\psi}_{\mathrm{R}}(\mathcal{I}_{\mathbf{E}^e}, \vartheta, c_{\mathrm{R}}, \xi)}{\partial c_{\mathrm{R}}}, \\ \mathcal{A} &= -\frac{\partial \hat{\psi}_{\mathrm{R}}(\mathcal{I}_{\mathbf{E}^e}, \vartheta, c_{\mathrm{R}}, \xi)}{\partial \xi}, \end{aligned}\right\} \tag{3.135}$$

respectively, represent the entropy, chemical potential, and a thermodynamic force related to the oxide volume fraction ξ. We call $\mathcal{A}$ the affinity of the oxidation reaction.

4. **Flow rule**

The evolution equation for the inelastic distortion $\mathbf{F}^i$ is

$$\dot{\mathbf{F}}^i = \left(\mathbf{D}^s + \mathbf{D}^p\right) \mathbf{F}^i, \tag{3.136}$$

where $\mathbf{D}^s$ represents the inelastic stretching resulting from swelling due to the oxidation reaction, and $\mathbf{D}^p$ is the inelastic stretching due to incompressible viscoplastic flow of the bond-coat and the oxide.

(i) The swell stretching $\mathbf{D}^s$ is given by

$$\mathbf{D}^s = \dot{\xi}\,\mathbb{S}, \qquad \dot{\xi} \geq 0, \tag{3.137}$$

where

$$\mathbb{S} = \beta_p \mathbf{m} \otimes \mathbf{m} + \beta_l (\mathbf{1} - \mathbf{m} \otimes \mathbf{m}), \tag{3.138}$$

gives the direction and magnitude of the swelling strain accompanying the chemical reaction. The constants β_p and β_l are the swelling strains in a preferred direction $\mathbf{m}$, and in the plane perpendicular to $\mathbf{m}$ in the intermediate space. The

unit vector $\mathbf{m}$ itself is given by the *normalized contravariant transformation* of a (material) unit normal vector $\mathbf{m}_{\mathrm{R}}(\mathbf{X})$ to a plane $\Pi_{\mathrm{R}}(\mathbf{X})$ in an infinitesimal neighborhood of $\mathbf{X}$ in the reference body:

$$\mathbf{m} \stackrel{\text{def}}{=} \frac{\mathbf{F}^{i-\mathsf{T}}\mathbf{m}_{\mathrm{R}}(\mathbf{X})}{|\mathbf{F}^{i-\mathsf{T}}\mathbf{m}_{\mathrm{R}}(\mathbf{X})|}. \tag{3.139}$$

Further, with

$$\mathcal{F} \stackrel{\text{def}}{=} \mathcal{A} + \mathbf{M}^e : \mathbb{S} + \mu\mathcal{R} \tag{3.140}$$

the thermodynamic force conjugate to $\dot{\xi}$, the volume fraction of oxide ξ is assumed to evolve according to a constitutive relation

$$\dot{\xi} = \hat{\dot{\xi}}(\mathcal{F}, \vartheta, \xi) \geq 0, \tag{3.141}$$

with $\mathcal{F}\dot{\xi} > 0$ whenever $\dot{\xi} > 0$.

(ii) We take the viscoplastic stretching $\mathbf{D}^p$ to be given by

$$\mathbf{D}^p = \dot{\bar{\epsilon}}^p \left(\frac{3\mathbf{M}_0^e}{2\bar{\sigma}}\right), \tag{3.142}$$

with the equivalent tensile plastic strain rate $\dot{\bar{\epsilon}}^p \geq 0$ decomposed as

$$\dot{\bar{\epsilon}}^p = \omega\dot{\bar{\epsilon}}^p_{\mathrm{ox}} + (1-\omega)\dot{\bar{\epsilon}}^p_{\mathrm{bc}}. \tag{3.143}$$

Here, $\dot{\bar{\epsilon}}^p_{\mathrm{bc}}$ represents a contribution to $\dot{\bar{\epsilon}}^p$ due to viscoplastic flow of the unoxidized bond-coat, while $\dot{\bar{\epsilon}}^p_{\mathrm{ox}}$ represents a contribution due to viscoplastic flow of the oxide. Also, $\omega(\xi)$ represents a *proportioning function*, which satisfies $\omega(0) = 0$ and $\omega(1) = 1$, and characterizes the relative amount of plastic flow between the bond-coat and the oxide during the oxidation reaction.

We take the two contributions $\dot{\bar{\epsilon}}^p_{\mathrm{bc}}$ and $\dot{\bar{\epsilon}}^p_{\mathrm{ox}}$ to the total equivalent tensile plastic strain rate $\dot{\bar{\epsilon}}^p$, to be given by the flow functions

$$\dot{\bar{\epsilon}}^p_{\mathrm{bc}} = \hat{\dot{\bar{\epsilon}}}^p_{\mathrm{bc}}(\bar{\sigma}, \vartheta, S_{\mathrm{bc}}) \geq 0, \quad \text{and} \quad \dot{\bar{\epsilon}}^p_{\mathrm{ox}} = \hat{\dot{\bar{\epsilon}}}^p_{\mathrm{ox}}(\bar{\sigma}, \vartheta, S_{\mathrm{ox}}) \geq 0, \tag{3.144}$$

with $\bar{\sigma}$ the equivalent tensile stress defined in (3.133), and ϑ the absolute temperature. Also, S_{bc} is a stress-dimensioned internal variable representing the flow resistance of the bondcoat, and S_{ox} a stress-dimensioned internal variable representing the flow resistance of the oxide.

5. **Evolution equations for internal variables S_{bc} and S_{ox}**

The evolution equations are taken to be given by

$$\dot{S}_{\mathrm{bc}} = h_{\mathrm{bc}}(\dot{\bar{\epsilon}}^p_{\mathrm{bc}}, \vartheta, S_{\mathrm{bc}}), \quad \text{and} \quad \dot{S}_{\mathrm{ox}} = h_{\mathrm{bc}}(\dot{\bar{\epsilon}}^p_{\mathrm{ox}}, \vartheta, S_{\mathrm{ox}}). \tag{3.145}$$

The evolution equations for $\mathbf{F}^i$, ξ, S_{bc}, and S_{ox} need to be accompanied by initial conditions. Typical initial conditions presume that the body is initially (at time $t = 0$,

say) in a virgin state in the sense that

$$\mathbf{F}(\mathbf{X},0)=\mathbf{F}^i(\mathbf{X},0)=\mathbf{1},\quad \xi(\mathbf{X},0)=0,\quad S_{\text{bc}}(\mathbf{X},0)=S_{\text{bc},0}\,(=\text{const.}),\quad S_{\text{ox}}(\mathbf{X},0)=S_{\text{ox},0}\,(=\text{const.}) \tag{3.146}$$

so that by $\mathbf{F}=\mathbf{F}^e\mathbf{F}^i$ we also have $\mathbf{F}^e(\mathbf{X},0)=\mathbf{1}$.

6. **Fourier's Law**

   The heat flux $\mathbf{q}_{\text{R}}$ is presumed to obey Fourier's law,

$$\mathbf{q}_{\text{R}}=-\kappa\,\nabla\vartheta, \tag{3.147}$$

   with $\kappa(\mathcal{I}_{\mathbf{E}^e},\vartheta,c_{\text{R}},\xi)>0$ the thermal conductivity.

7. **Fick's Law**

   The species flux $\mathbf{j}_{\text{R}}$ is presumed to obey Fick's law

$$\mathbf{j}_{\text{R}}=-m\,\nabla\mu, \tag{3.148}$$

   with $m(\mathcal{I}_{\mathbf{E}^e},\vartheta,c_{\text{R}},\xi)>0$ the species mobility.

3.8 Governing partial differential equations

The governing partial differential equations consist of:

1. The local force balance, viz.

$$\text{Div}\,\mathbf{T}_{\text{R}}+\mathbf{b}_{\text{R}}=\mathbf{0}, \tag{3.149}$$

   where $\mathbf{T}_{\text{R}}=J\mathbf{T}\mathbf{F}^{-\text{T}}$ is the Piola stress, with $\mathbf{T}$ given by (3.132) and (3.134), and $\mathbf{b}_{\text{R}}$ is the non-inertial body force.

2. The local balance equation for the concentration of diffusing oxygen

$$\dot{c}_{\text{R}}=-\text{Div}\,\mathbf{j}_{\text{R}}-\mathcal{R}\,\dot{\xi}, \tag{3.150}$$

   with the flux $\mathbf{j}_{\text{R}}$ given by (3.148) and $\dot{\xi}$ given by (3.141), and where $\mathcal{R}$ is a material constant.[6] This diffusion-reaction equation connects the oxide volume fraction ξ to the concentration c_{R} of the free oxygen.

3. The local balance of energy, which, together with (3.147) and (3.148), gives the following partial differential equation for the temperature

$$c\dot{\vartheta}=\text{Div}\,(\kappa\nabla\vartheta)+q_{\text{R}}+(1-\omega)\,\bar{\sigma}\,\dot{\bar{\varepsilon}}^p_{\text{bc}}+\omega\,\bar{\sigma}\,\dot{\bar{\varepsilon}}^p_{\text{ox}}+\mathcal{F}\,\dot{\xi}+m|\nabla\mu|^2+\tfrac{1}{2}\vartheta\,\frac{\partial\mathbf{T}^e}{\partial\vartheta}:\dot{\mathbf{C}}^e+\vartheta\,\frac{\partial\mu}{\partial\vartheta}\,\dot{c}_{\text{R}}-\vartheta\,\frac{\partial\mathcal{A}}{\partial\vartheta}\dot{\xi}, \tag{3.151}$$

[6] Cf. Section B.2 for a discussion on how to estimate the constant $\mathcal{R}$ for a material system.

in which

$$c = -\vartheta \frac{\partial^2 \hat{\psi}(\mathcal{I}_{\mathbf{E}^e}, \vartheta, c_{\mathrm{R}}, \xi)}{\partial \vartheta^2} \tag{3.152}$$

is the specific heat.

3.9 Specialization of the constitutive equations

The theory presented thus far is quite general. Since the precise nature of the various coupling effects have not been completely elucidated in the existing literature, we now introduce special constitutive equations which should provide a suitable beginning for analysis and future refinement.

3.9.1 Free energy

We consider a separable free energy of the form

$$\hat{\psi}_{\mathrm{R}}(\mathcal{I}_{\mathbf{E}^e}, \vartheta, c_{\mathrm{R}}, \xi) = \psi^e_{\mathrm{R}}(\mathcal{I}_{\mathbf{E}^e}, \vartheta, \xi) + \psi^{\mathrm{mix}}_{\mathrm{R}}(\vartheta, c_{\mathrm{R}}) + \psi^{\mathrm{chem}}_{\mathrm{R}}(\vartheta, \xi). \tag{3.153}$$

Here:

(i) ψ^e is a thermo-elastic energy given by

$$\psi^e_{\mathrm{R}}(\mathcal{I}_{\mathbf{E}^e}, \vartheta, \xi) = J^i \underbrace{\left(G|\mathbf{E}^e|^2 + \tfrac{1}{2}(K - \tfrac{2}{3}G)(\mathrm{tr}\,\mathbf{E}^e)^2 - (\vartheta - \vartheta_0)(3\,K\,\alpha)(\mathrm{tr}\,\mathbf{E}^e)\right)}_{\psi^0} + c\,(\vartheta - \vartheta_0) - c\,\vartheta\,\ln\left(\frac{\vartheta}{\vartheta_0}\right), \tag{3.154}$$

which is a simple generalization of the classical strain energy function of infinitesimal isotropic thermo-elasticity. Note that the energy ψ^0 is measured per unit volume of the intermediate space; multiplication by J^i converts it to a quantity measured per unit volume of the reference space. The parameters

$$\begin{aligned} G(\vartheta, \xi) &= (1 - \xi)\, G_{\mathrm{bc}}(\vartheta) + \xi\, G_{\mathrm{ox}}(\vartheta) > 0, \\ K(\vartheta, \xi) &= (1 - \xi)\, K_{\mathrm{bc}}(\vartheta) + \xi\, K_{\mathrm{ox}}(\vartheta) > 0, \\ \alpha(\vartheta, \xi) &= (1 - \xi)\, \alpha_{\mathrm{bc}}(\vartheta) + \xi\, \alpha_{\mathrm{ox}}(\vartheta) > 0, \end{aligned} \tag{3.155}$$

are the shear modulus, bulk modulus, and coefficient of thermal expansion, respectively, and $c > 0$ is a constant specific heat. Also, ϑ_0 is a *reference temperature*, which is to be taken as a nominal elevated temperature of interest.

(ii) $\psi^{\mathrm{mix}}_{\mathrm{R}}$ is a chemical energy related to species diffusion, taken to be given by

$$\psi^{\mathrm{mix}}_{\mathrm{R}} = \mu^0\, c_{\mathrm{R}} + R\,\vartheta\, c_{\mathrm{R}}\,(\ln \tilde{c}_{\mathrm{R}} - 1), \tag{3.156}$$

where μ^0 is a reference chemical potential for the interstitial oxygen, R is the universal gas constant, and $\tilde{c}_{\mathrm{R}}$ is a normalized species concentration given by

$$\tilde{c}_{\mathrm{R}} \stackrel{\mathrm{def}}{=} \frac{c_{\mathrm{R}}}{c_{\max}}, \qquad 0 \leq \tilde{c}_{\mathrm{R}} \leq 1, \tag{3.157}$$

with $c_{\max}$ the concentration of interstitial sites available to the diffusing species, in moles per unit reference volume.

(iii) $\psi_{\mathrm{R}}^{\mathrm{chem}}$ is a chemical energy related to the oxidation reaction, taken to be given by

$$\psi_{\mathrm{R}}^{\mathrm{chem}} = \tfrac{1}{2}H(1-\xi)^2, \tag{3.158}$$

where the parameter $H(\vartheta) > 0$ is a *chemistry modulus.* This term in the free energy favors the local state $\xi = 1$.[7]

Thus, the free energy may be written as

$$\psi_{\mathrm{R}} = J^i\psi^0 + c\,(\vartheta - \vartheta_0) - c\vartheta\,\ln\left(\frac{\vartheta}{\vartheta_0}\right) + \mu^0\,c_{\mathrm{R}} + R\vartheta\,c_{\mathrm{R}}(\ln\tilde{c}_{\mathrm{R}} - 1) + \tfrac{1}{2}H(1-\xi)^2, \tag{3.159}$$

with

$$\psi^0 = G|\mathbf{E}^e|^2 + \tfrac{1}{2}(K - \tfrac{2}{3}G)(\mathrm{tr}\,\mathbf{E}^e)^2 - (\vartheta - \vartheta_0)(3\,K\,\alpha)(\mathrm{tr}\,\mathbf{E}^e). \tag{3.160}$$

Then, using (3.132), (3.135), and (3.36), the Mandel stress, the entropy, the chemical potential, and the affinity are given by

$$\begin{aligned}
\mathbf{M}^e &= J^i\Big(2G\mathbf{E}^e_0 + K(\mathrm{tr}\,\mathbf{E}^e)\mathbf{1} - 3K\alpha(\vartheta - \vartheta_0)\mathbf{1}\Big),\\
\eta_{\mathrm{R}} &= c\ln\left(\frac{\vartheta}{\vartheta_0}\right) + 3J^iK\alpha(\mathrm{tr}\,\mathbf{E}^e) - R\,c_{\mathrm{R}}(\ln\tilde{c}_{\mathrm{R}} - 1) - \frac{1}{2}\frac{\partial H}{\partial\vartheta}(1-\xi)^2 - A,\\
\mu &= \mu^0 + R\vartheta\ln\tilde{c}_{\mathrm{R}},\\
\mathcal{A} &= H(1-\xi) - B - 3\beta J^i\psi^0,
\end{aligned} \tag{3.161}$$

where

$$A = J^i\left(\frac{\partial G}{\partial\vartheta}|\mathbf{E}^e|^2 + \frac{1}{2}\left(\frac{\partial K}{\partial\vartheta} - \frac{2}{3}\frac{\partial G}{\partial\vartheta}\right)(\mathrm{tr}\,\mathbf{E}^e)^2 - 3(\vartheta - \vartheta_0)\left(\frac{\partial K}{\partial\vartheta}\alpha + K\frac{\partial\alpha}{\partial\vartheta}\right)(\mathrm{tr}\,\mathbf{E}^e)\right), \tag{3.162}$$

and

$$\begin{aligned}
B = J^i\Big((G_{\mathrm{ox}} - G_{\mathrm{bc}})|\mathbf{E}^e|^2 + \frac{1}{2}\Big((K_{\mathrm{ox}} - K_{\mathrm{bc}}) - \frac{2}{3}(G_{\mathrm{ox}} - G_{\mathrm{bc}})\Big)(\mathrm{tr}\,\mathbf{E}^e)^2\\
- 3(\vartheta - \vartheta_0)\left((K_{\mathrm{ox}} - K_{\mathrm{bc}})\alpha + K(\alpha_{\mathrm{ox}} - \alpha_{\mathrm{bc}})\right)\mathrm{tr}\,\mathbf{E}^e\Big)
\end{aligned} \tag{3.163}$$

[7] This special form for ψ^{chem} is motivated by a paper of Ulm et al. [106] on chemo-mechanics of alkali-silica reactions and their effects on deterioration of concrete structures.

account for the variation of the thermoelastic moduli with temperature ϑ and the volume fraction of oxide ξ, respectively.

3.9.2 Inelastic deformation of the bond-coat and the oxide

For the flow function $(3.144)_1$, which specifies the equivalent plastic tensile strain rate in the bond coat, we choose a thermally activated relation with power-law stress dependence,

$$\dot{\bar{\epsilon}}^p_{\rm bc} = \begin{cases} 0 & \text{if} \quad \bar{\sigma} = 0, \\ A_{\rm bc} \exp\left(\dfrac{-Q_{\rm bc}}{R\vartheta}\right) \left(\dfrac{\bar{\sigma}}{S_{\rm bc}}\right)^{1/m_{\rm bc}} & \text{if} \quad \bar{\sigma} > 0. \end{cases} \tag{3.164}$$

Here $A_{\rm bc}$ is pre-exponential factor, $Q_{\rm bc}$ is an activation energy, and $m_{\rm bc} > 0$ is a strain-rate sensitivity parameter. The stress-dimensioned variable $S_{\rm bc}$ represents a *tensile creep strength* of the bond-coat, which for simplicity is here taken to be constant.

Remark: As is well-known in the high-temperature metals literature, this simple relation for $\dot{\bar{\epsilon}}^p_{\rm bc}$ is expected to be applicable only in the high-homologous temperature regime at temperatures ϑ greater than $\approx 0.5\vartheta_{m,\rm bc}$ where $\vartheta_{m,\rm bc}$ is the melting temperature of the bond-coat. Because of the exponential dependence of temperature in (3.164), at temperatures lower than $\approx 0.5\vartheta_{m,\rm bc}$ the stress required to cause a significant plastic strain rate would be enormously large, indicating that at these lower temperatures the viscoplastic flow of the bond-coat would essentially be shut down.

Next, since the strain-rate sensitivity of the oxide is expected to be significantly smaller than that of the bond-coat, for the flow function $(3.144)_2$ for the oxide we assume that

$$\dot{\bar{\epsilon}}^p_{\rm ox} = \begin{cases} 0 & \text{if} \quad \bar{\sigma} = 0, \\ \dot{\bar{\epsilon}}^0_{\rm ox} \left(\dfrac{\bar{\sigma}}{S_{\rm ox}}\right)^{1/m_{\rm ox}} & \text{if} \quad \bar{\sigma} > 0, \end{cases} \tag{3.165}$$

with $\dot{\bar{\epsilon}}^0_{\rm ox}$ a reference plastic strain rate and $m_{\rm ox}$ a small strain-rate sensitivity parameter, both assumed to be constant in the temperature range of interest.

- The strain-rate sensitivity parameter $m_{\rm ox}$ will be taken to have a small value in order to model the plasticity of the oxide as essentially *rate-independent.*

Further, any temperature dependence of the plasticity of the oxide is assumed to come solely from the temperature dependence of the flow resistance $S_{\rm ox}$. For simplicity, we assume this temperature dependence to be linear,

$$S_{\rm ox} = S^0_{\rm ox} + M_{\rm ox}(\vartheta - \vartheta_{\rm ref}), \tag{3.166}$$

where $S^0_{\rm ox}$ and $M_{\rm ox}$ are material parameters, and $\vartheta_{\rm ref}$ is another reference temperature.[8]

[8]The reference temperature ϑ_0 that was introduced in (3.154) is the temperature at which there are *no thermal stresses and/or strains in the material.* Since it may be convenient in applications to change ϑ_0 from one case to another, an additional reference temperature $\vartheta_{\rm ref}$ is introduced here.

We also need to specify the proportioning function $\omega(\xi)$ between plastic flow of the bond-coat and the oxide in the oxidizing region (cf. (3.143)). The simplest assumption would be to set $\omega = \xi$. However, since the metallic bond-coat material has a much higher propensity to creep than the oxide, the contribution from the viscoplastic strain rate of the bond coat, $\dot{\bar{\epsilon}}^p_{\rm bc}$, will dominate the overall viscoplastic strain rate, $\dot{\bar{\epsilon}}^p$ of the oxide/bond-coat mixture. As a result, the inelastic swelling deformation due to oxidation may easily be "compensated" for by the corresponding viscoplastic deformation of the bond-coat/oxide mixture, and this would not lead to the development of significant stresses due to the oxidation reaction — which is in disagreement with the well-documented development of large growth stresses which are produced due to the volumetric expansion from oxidation. The precise nature of viscoplastic deformation at a material point that is in the process of being oxidized is not well-known. However, it is clear that when the material point has fully oxidized it will have the plasticity properties of the oxide. For this reason, and for simplicity, we assume that as soon as a material point starts to oxidize, its creep rate is determined by that of the oxide. Accordingly, we assume that

$$\omega = \begin{cases} 0 & \text{if} \quad \xi = 0, \\ 1 & \text{otherwise.} \end{cases} \tag{3.167}$$

Finally, note that in our specialized constitutive equations, in accordance with previous studies on high-temperature oxidation, we have neglected any evolution of $S_{\rm bc}$ and $S_{\rm ox}$ with plastic flow. Thus, the evolution equations (3.145) are redundant.

3.9.3 Evolution equation for ξ

As a simple special form for (3.141) we assume a thermally-activated relation for $\dot{\xi}$, with linear dependence on its conjugate driving force $\mathcal{F}$:

$$\dot{\xi} = \begin{cases} C_\xi \exp\left(\dfrac{-Q_s}{R\vartheta}\right)\mathcal{F} & \text{if} \quad \mathcal{F} > 0 \quad \text{and} \quad \xi < 1, \\ 0 & \text{otherwise,} \end{cases} \tag{3.168}$$

where, from (3.140) and $(3.161)_4$, the driving force $\mathcal{F}$ is given by

$$\mathcal{F} = H(1-\xi) - B - 3\beta J^i \psi^0 + \mathbf{M}^e : \mathbb{S} + \mathcal{R}\left(\mu^0 + R\vartheta \ln(\tilde{c}_{\rm R})\right). \tag{3.169}$$

In (3.168) the the pre-exponential factor C_ξ has units of 1/(s MPa), and Q_s is an activation energy with units of kJ/mol. Note that the fourth term in (3.169), $\mathbf{M}^e : \mathbb{S}$, characterizes the influence of the stress state on the driving force of the oxidation reaction. With $\mathbb{S}$ given in (3.138),

$$\mathbf{M}^e : \mathbb{S} = \beta_l \mathrm{tr}\mathbf{M}^e + (\beta_p - \beta_l)(\mathbf{m} \cdot \mathbf{M}^e \mathbf{m}), \tag{3.170}$$

which shows that hydrostatic tension ($\mathrm{tr}\mathbf{M}^e > 0$) increases $\mathcal{F}$ (and thus $\dot{\xi}$), while hydrostatic pressure decreases it. The second term in (3.170) accounts for the anisotropy in swelling ($\beta_l \neq \beta_p$), and is proportional to the normal stress $\mathbf{m} \cdot \mathbf{M}^e \mathbf{m}$ in the direction of $\mathbf{m}$. If this normal stress is tensile, $\mathcal{F}$ is further increased, while for a compressive stress in the $\mathbf{m}$-direction, it is decreased.

3.9.4 Heat flux. Species flux

From (3.147), we have that the heat flux is given by

$$\mathbf{q}_{\mathrm{R}} = -\kappa \nabla \vartheta, \tag{3.171}$$

with $\kappa(\mathcal{I}_{\mathbf{E}^e}, \vartheta, c_{\mathrm{R}}, \xi) > 0$ the thermal conductivity. At this point in time the dependence of the thermal conductivity on the elastic deformation and species concentration is not well understood. Accordingly, here we ignore any such dependence and assume that

$$\kappa = (1-\xi)\kappa_{\mathrm{bc}} + \xi \kappa_{\mathrm{ox}}, \tag{3.172}$$

where $\kappa_{\mathrm{bc}}(\vartheta) > 0$ and $\kappa_{\mathrm{ox}}(\vartheta) > 0$ are the temperature-dependent thermal conductivities of the bond-coat and the oxide, respectively, which presumably are experimentally measurable.

Further, from (3.148) we have that the species flux is given by

$$\mathbf{j}_{\mathrm{R}} = -m \nabla \mu, \tag{3.173}$$

with $m(\mathcal{I}_{\mathbf{E}^e}, \vartheta, c_{\mathrm{R}}, \xi) > 0$ the species mobility. From $(3.161)_3$

$$\nabla \mu = \frac{R\vartheta}{c_{\mathrm{R}}} \nabla c_{\mathrm{R}} + R \ln \tilde{c}_{\mathrm{R}} \, \nabla \vartheta \, . \tag{3.174}$$

The second term in (3.174) represents an unexpected Soret-type coupling effect, in that if we use this term in (3.173) for the species flux, then we would obtain that the species flux $\mathbf{j}_{\mathrm{R}}$ depends on the temperature gradient $\nabla \vartheta$. Here, we *choose to neglect the term involving* $\nabla \vartheta$ *in* (3.174), and take

$$\nabla \mu \doteq \frac{R\vartheta}{c_{\mathrm{R}}} \nabla c_{\mathrm{R}}. \tag{3.175}$$

Next, defining a *diffusivity* by

$$D(\mathcal{I}_{\mathbf{E}^e}, \vartheta, c_{\mathrm{R}}, \xi) \stackrel{\mathrm{def}}{=} m(\mathcal{I}_{\mathbf{E}^e}, \vartheta, c_{\mathrm{R}}, \xi) \times \frac{R\vartheta}{c_{\mathrm{R}}}, \tag{3.176}$$

and using (3.175), we may write (3.173) as

$$\mathbf{j}_{\mathrm{R}} = -D \nabla c_{\mathrm{R}}. \tag{3.177}$$

As for the thermal conductivity, the dependence of the species diffusivity on the elastic deformation and species concentration is not well understood; accordingly, we ignore any such dependence and assume that

$$D = (1-\xi) D_{\mathrm{bc}} + \xi D_{\mathrm{ox}}, \tag{3.178}$$

where $D_{\mathrm{bc}}(\vartheta) > 0$ and $D_{\mathrm{ox}}(\vartheta) > 0$ are the diffusivities of the interstitial oxygen in the bond-coat and the oxide, respectively. These diffusivities typically exhibit an exponential

dependence on temperature

$$D_{\mathrm{bc}}(\vartheta) = D_{0,\mathrm{bc}} \exp\left(-\frac{Q_{d,\mathrm{bc}}}{R\vartheta}\right), \quad D_{\mathrm{ox}}(\vartheta) = D_{0,\mathrm{ox}} \exp\left(-\frac{Q_{d,\mathrm{ox}}}{R\vartheta}\right), \tag{3.179}$$

where $D_{0,\mathrm{bc}}$ and $D_{0,\mathrm{ox}}$ are reference values, and $Q_{d,\mathrm{bc}}$ and $Q_{d,\mathrm{ox}}$ represent the *activation energies* for diffusion of free oxygen in the bond-coat and the oxide, respectively.

3.9.5 Governing partial differential equations for the specialized constitutive equations. Boundary conditions

The governing partial differential equations consist of:

1. The local force balance (3.149), viz.

$$\mathrm{Div}\,\mathbf{T}_{\mathrm{R}} + \mathbf{b}_{\mathrm{R}} = \mathbf{0}, \tag{3.180}$$

   where $\mathbf{T}_{\mathrm{R}} = J\mathbf{T}\mathbf{F}^{-\mathrm{T}}$ is the Piola stress, with $\mathbf{T}$ given by (3.134) and $(3.161)_1$, and $\mathbf{b}_{\mathrm{R}}$ is the non-inertial body force.

2. The local balance equation for the concentration of diffusing species (3.150), which, using (3.175) and (3.176), may alternatively be written as

$$\dot{c}_{\mathrm{R}} = \mathrm{Div}\,(D\nabla c_{\mathrm{R}}) - \mathcal{R}\dot{\xi}, \tag{3.181}$$

   with the diffusivity D given by (3.178) and (3.179).

3. The local balance of energy (3.151), which, together with $(3.161)_3$ and (3.177), gives the following partial differential equation for the temperature

$$c\dot{\vartheta} = \mathrm{Div}\,(\kappa\nabla\vartheta) + q_{\mathrm{R}} + (1-\omega)\,\bar{\sigma}\,\dot{\bar{\epsilon}}_{\mathrm{bc}} + \omega\,\bar{\sigma}\,\dot{\bar{\epsilon}}_{\mathrm{ox}} + \mathcal{F}\dot{\xi} + D\,\frac{c_{\mathrm{R}}}{R\vartheta}\,|\nabla\mu|^2 + \vartheta\,\tfrac{1}{2}\frac{\partial \mathbf{T}^e}{\partial\vartheta} : \dot{\mathbf{C}}^e + (\mu-\mu_0)\dot{c}_{\mathrm{R}} - \vartheta\,\frac{\partial\mathcal{A}}{\partial\vartheta}\dot{\xi}, \tag{3.182}$$

   with ω given by (3.167).

We also need initial and boundary conditions to complete the theory. Let $\mathcal{S}_{\boldsymbol{\chi}}$ and $\mathcal{S}_{\mathbf{t}_{\mathrm{R}}}$ be complementary subsurfaces of the boundary $\partial\mathrm{B}$ of the body B. Similarly, let $\mathcal{S}_{c_{\mathrm{R}}}$ and $\mathcal{S}_{\mathbf{j}_{\mathrm{R}}}$ be a pair of complementary subsurfaces, and $\mathcal{S}_{\vartheta}$ and $\mathcal{S}_{\mathbf{q}_{\mathrm{R}}}$ another pair of complementary subsurfaces of the boundary. Then for a time interval $t \in [0,T]$ we consider a pair of boundary conditions in which the motion is specified on $\mathcal{S}_{\boldsymbol{\chi}}$ and the surface traction on $\mathcal{S}_{\mathbf{t}_{\mathrm{R}}}$:

$$\left.\begin{aligned} \boldsymbol{\chi} &= \breve{\boldsymbol{\chi}} \quad \text{on } \mathcal{S}_{\boldsymbol{\chi}} \times [0,T], \\ \mathbf{T}_{\mathrm{R}}\mathbf{n}_{\mathrm{R}} &= \breve{\mathbf{t}}_{\mathrm{R}} \quad \text{on } \mathcal{S}_{\mathbf{t}_{\mathrm{R}}} \times [0,T], \end{aligned}\right\} \tag{3.183}$$

another pair of boundary conditions in which the concentration is specified on $\mathcal{S}_{c_R}$ and the species flux on $\mathcal{S}_{j_R}$

$$\left.\begin{aligned} c_R &= \breve{c}_R \quad \text{on } \mathcal{S}_{c_R} \times [0,T], \\ -D(\nabla c_R)\cdot \mathbf{n}_R &= \breve{j}_R \quad \text{on } \mathcal{S}_{j_R} \times [0,T], \end{aligned}\right\} \tag{3.184}$$

and a final pair of boundary conditions in which the temperature is specified on $\mathcal{S}_\vartheta$ and the heat flux on $\mathcal{S}_{q_R}$

$$\left.\begin{aligned} \vartheta &= \breve{\vartheta} \quad \text{on } \mathcal{S}_\vartheta \times [0,T], \\ -\kappa(\nabla\vartheta)\cdot \mathbf{n}_R &= \breve{q}_R \quad \text{on } \mathcal{S}_{q_R} \times [0,T], \end{aligned}\right\} \tag{3.185}$$

with $\breve{\chi}$, $\breve{\mathbf{t}}_R$, $\breve{\vartheta}$, $\breve{q}_R$, $\breve{c}_R$, and $\breve{j}_R$ *prescribed* functions of $\mathbf{X}$ and t, and the initial data

$$\chi(\mathbf{X},0) = \chi_0(\mathbf{X}), \qquad c_R(\mathbf{X},0) = c_{R,0}(\mathbf{X}) \qquad \text{and} \qquad \vartheta(\mathbf{X},0) = \vartheta_0(\mathbf{X}) \qquad \text{in} \qquad \mathrm{B}. \tag{3.186}$$

The coupled set of equations (3.180), (3.182), and (3.181), together with (3.183), (3.184), (3.185), and (3.186), yield an initial boundary-value problem for the motion $\chi(\mathbf{X},t)$, the temperature $\vartheta(\mathbf{X},t)$, and the oxygen concentration $c_R(\mathbf{X},t)$.

More on the boundary condition $(3.184)_1$

In the boundary condition $(3.184)_1$ $\breve{c}_R$ represents the the concentration of oxygen interstitials in the solid. Let

$$\breve{\breve{c}}_R \stackrel{\text{def}}{=} \frac{\breve{c}_R}{c_{\max}} \tag{3.187}$$

denote the normalized value of $\breve{c}_R$. This normalized value of the boundary concentration of interstitial oxygen atoms is determined as follows.

Let X_{O_2} denote the mole fraction of the oxygen molecules in the surrounding gas which is at a pressure p. Then the partial pressure of the oxygen molecules in the gas is given by

$$p_{O_2} = X_{O_2} \times p\,, \tag{3.188}$$

and with the gas taken to be *ideal*, the corresponding chemical potential of the oxygen molecules in the gas is

$$\mu_{O_2} = \mu^0_{O_2} + R\vartheta \ln\left(\frac{p_{O_2}}{p^0}\right), \tag{3.189}$$

with p^0 a reference pressure.[9]

We assume that equilibrium conditions prevail between between the diatomic oxygen molecule O_2 in the gas and the interstitial oxygen atom O_i in the material:

$$\frac{1}{2}O_2 \leftrightarrow O_i. \tag{3.190}$$

[9]In this paper we limit our considerations to the temperature range between roughly 300 K and 2000 K, and a partial pressure below 1 bar. Under these circumstances one may assume that gas behaves in an ideal manner. However, at high pressures when the gas can no longer be assumed to be *ideal*, the partial pressure in (3.189) would then need to be replaced by the *fugacity* of the oxygen molecules in the gas mixture.

At equilibrium, the chemical potential of the gas must equal the chemical potential of the oxygen interstitials in the solid,

$$\tfrac{1}{2}\,\mu_{O_2} = \mu_{O_i}. \tag{3.191}$$

Thus, using (3.189) and $(3.161)_3$

$$\tfrac{1}{2}\left(\mu^0_{O_2} + R\vartheta \ln\left(\frac{p_{O_2}}{p^0}\right)\right) = \mu^0_{O_i} + R\vartheta \ln \breve{c}_R\,, \tag{3.192}$$

where we note that what was simply written as μ^0 in $(3.161)_3$, is the reference value of the chemical potential for the interstitial oxygen atoms, $\mu^0_{O_i}$,

$$\mu^0 \equiv \mu^0_{O_i}. \tag{3.193}$$

Eqs (3.187) and (3.192) give

$$\breve{c}_R = c_{max}\, k \left(\frac{p_{O_2}}{p^0}\right)^{\frac{1}{2}} \qquad \text{with} \qquad k = \exp\Big(-\frac{\Delta\mu^0}{R\vartheta}\Big), \tag{3.194}$$

where

$$\Delta\mu^0 \stackrel{\text{def}}{=} \mu^0_{O_i} - \tfrac{1}{2}\,\mu^0_{O_2}\,. \tag{3.195}$$

Eq. (3.194) provides the relation between the site fraction at the surface of the oxidizing material, $\breve{c}_R$, and the partial pressure of oxygen p_{O_2} in the surrounding oxygen gas.

Further, a gas of O_2 molecules represents the *reference state* of the element oxygen. But the chemical potential of an element in its reference state is zero [7, pp. 119, 159]:

$$\mu_{O_2}(p^0 = p_{O_2} = 1 \text{ bar}) = 0. \tag{3.196}$$

Thus from (3.196) and (3.189) we have that

$$\mu^0_{O_2} = 0. \tag{3.197}$$

Hence (3.195) reduces to

$$\Delta\mu^0 = \mu^0_{O_i}\,. \tag{3.198}$$

Chapter 4

Application of the theory to modeling of dimensional changes and residual stresses in oxidizing FeCrAlY specimens

4.1 Numerical implementation

We numerically implemented our theory in ABAQUS/Standard [93] by writing a user-element subroutine (UEL) for two-dimensional (plane-strain and axisymmetric), four-noded, reduced-integration elements with the displacement, oxygen concentration, and temperature as the nodal degrees of freedom. This numerical implementation is discussed in detail in Appendix A.

4.2 Material parameters for FeCrAlY

Our theory is highly-coupled, and the numerous material parameters for the diffusivities, reaction rate, and mechanical properties of the bond-coat and the oxide in the entire temperature range of interest are individually not known for any given high-temperature alloy. We have attempted to estimate the material parameters in our specialized theory for an Fe-22.0%Cr-4.8%Al-0.3%Y (weight percent) heat-resistant alloy experimentally studied by Tolpygo et al. [103]. The material parameters were estimated by

(i) conducting a literature search for available experimental data; and

(ii) by conducting a calibration procedure in which we adjust certain material parameters so that the predictions from our theory match the experimentally-measured results on oxide-thickness growth, plate elongation, and residual-stress development reported by Tolpygo et al. [103].

For clarity of presentation, a detailed discussion of our estimation procedure for the material parameters is relegated to Appendix B. Values of the estimated material parameters are listed in Tables 4.1 and 4.2 on page 65.

4.3 Oxidation of flat plates

In this section we discuss the numerical simulation of oxidation of flat plates, and compare the results for (a) oxide thickness evolution, (b) elongational strain, and (c) residual stress levels in the oxide — after oxidation at high temperature and cool-down to room temperature — against corresponding experimental results of Tolpygo et al. [102, 103]. To a large extent, the comparisons to be discussed below show that our theory, together with the material parameters which we have estimated for the FeCrAlY studied by these authors, is capable of reproducing — not perfectly, but with reasonable accuracy — the experimentally-measured features of high-temperature oxidation in this alloy.

We consider two-sided oxidation of a circular plate of thickness $2h$. A schematic of the cross-section of the plate is shown in Fig. 4-1a. We numerically simulate only the axi-symmetric cylindrical domain ABCD indicated in this figure; the corresponding mesh is displayed in Fig. 4-1b. Edge AB is the central axis of symmetry, while edge BC represents the mid-plane of the plate and is thus also a plane of symmetry. Regarding the mechanical boundary conditions, the displacement component u_r is prescribed to have a value $u_r = 0$ on edge AB, and correspondingly $u_z = 0$ is prescribed on edge BC. Edge CD is constrained to remain straight and vertical, but it may move in the $\mathbf{e}_r$-direction. Finally, edge DA is taken to be traction-free. As initial conditions, we choose $\vartheta_0 = \vartheta_{\text{hot}}$, and $c_{\text{R},0} = 0$.[1]

For the temperature boundary conditions we ramp the temperature on edge DA linearly from 298 K to ϑ_{hot} over 120 seconds, while zero heat flux is prescribed on all other edges. During the dwell time t_{hot} at ϑ_{hot}, we prescribe the temperature at all nodes to be equal to ϑ_{hot}. Then, during the cool-down, we again ramp the temperature on edge DA linearly from ϑ_{hot} to 298 K over 120 seconds, while again zero heat flux is prescribed on all other edges.

For the diffusion of oxygen, no species flux is allowed on edges AB, BC, and CD at any time. On edge DA we prescribe the boundary condition for the oxygen concentration, $\check{c}_{\text{R}}$; this is determined by the partial pressure of the surrounding oxygen gas p_{O_2} through (3.194). Since the experiments of Tolpygo et al. [102, 103] were conducted in air at atmospheric pressure, we take the p_{O_2} to be given by $p_{O_2} = 0.21$ bar $= 0.021$ MPa.

As outputs from our simulations, we report the following three quantities as a function of temperature and time: the oxide thickness, the room-temperature in-plane elongation, and the room-temperature in-plane compressive stresses in the oxide. In reporting our simulation results, we have adopted the following conventions:

(a) First, for the numerical estimation of oxide thickness, a material point is considered to have completely oxidized if the oxide volume fraction ξ has reached a value of $\xi \geq 0.8$.

(b) Second, for the in-plane stresses at room temperature, we note that the simulated stress in the oxide layer (that is, where $\xi \geq 0.8$) will *vary* across the layer, while the experimental measurements of Tolpygo et al. [102, 103] represent an *average* stress value in the oxide layer. Thus the reported simulated stress values represent the *average* of

[1] The initial temperature ϑ_0 needs to be the temperature at which most of the oxidation will take place, i.e. ϑ_{hot}; otherwise, there would be thermal stresses in the oxide even at ϑ_{hot}, which is unphysical. Therefore the simulation is started at ϑ_{hot} with an "artificial" cool-down step down to 298 K, at which point the simulation of the experiment, described above, begins.

the stress distribution through the thickness of the oxide layer. The variation of stresses across the oxide layer will be discussed shortly.

In Fig. 4-2, the simulation results for the oxide thickness as a function of time, at three different oxidation temperatures $\vartheta_{\text{hot}} = 1373\,\text{K}$, $1473\,\text{K}$, and $1573\,\text{K}$, for a plate of thickness $2h = 0.9\,\text{mm}$, are compared against the corresponding experimental measurements by Tolpygo et al. [102, 103]. The hollow symbols represent the experimental measurements, while the filled symbols represent the numerically simulated results. The numerical simulations clearly pick up the trend that the oxide depth at a given oxidation time increases with increasing temperature. Also the simulated oxidation depths are in the right experimentally-measured ranges of $\lessapprox 5\mu\text{m}$ for 1373K, and $\lessapprox 15\mu\text{m}$ for 1573K.

In Fig. 4-3 the simulation results for the in-plane elongations and in-plane compressive stresses in the oxide for three oxidation temperatures, $\vartheta_{\text{hot}} = 1373\,\text{K}$, $1473\,\text{K}$, and $1573\,\text{K}$, are compared against the corresponding experimental measurements by Tolpygo et al. [102, 103]; the relevant plate-thicknesses are also indicated in the figure. The numerical simulations clearly pick up experimentally measured trends:

- The elongational strain increases with decreasing specimen thickness and increasing temperature. It varies from a fraction of a percent for the thickest plate at the lowest temperature, to about 2.5% as the plate thickness decreases and the temperature increases.

- The compressive stresses in the oxide exhibit a very fast increase at the beginning of oxidation to attain a value of $\approx -5.5\,\text{GPa}$, which is followed by a gradual decline. Also, for any given oxidation time at a given temperature, the stress in the oxide is greater for a thicker specimen.

We examine next, in slightly greater detail, the in-plane stress state ($T_{11} \equiv T_{rr}$) near the surface of a plate where the oxidation is occurring. For a plate of thickness $2h = 0.43\,\text{mm}$ which is oxidized at $\vartheta_{\text{hot}} = 1473\,\text{K}$ for 250 hours and subsequently cooled down to room temperaure, Fig. 4-4a shows contour plots of the volume fraction of oxide ξ, Fig. 4-4b shows the in-plane stress before cool-down, while Fig. 4-4c shows the in-plane stress after cool-down. The stress distribution in the oxide layer shown in Fig. 4-4b is not uniformly compressive, but ranges from a compressive stress of $\approx -2\,\text{GPa}$ in the bottom of the layer which has just begun to be oxidized, to a tensile stress of $\approx 1.8\,\text{GPa}$ near the surface which was the first portion of the layer to have oxidized. This non-uniform stress state at $1473\,\text{K}$ arises for the following reason. Consider a material point below the sample surface, initially at $\xi = 0$. As this material starts to oxidize and ξ increases, compressive stresses are generated at that point since the substrate below impedes the lateral expansion which occurs due to the oxidation. The simulations indicate that at the high temperature, the compressive stress level reaches a value of $\approx -2\,\text{GPa}$, which is limited by the onset of plastic flow in the oxide. However, as time progresses the substrate below the oxidizing layer also expands laterally, thus relieving some of the initial constraint on the previously oxidized region, and this reduces the magnitude of the compressive stress level. If for thin specimens the substrate expansion is large enough, then the initial large compressive stresses can turn into an eventual tensile stress state near the free surface which was the first to oxidize. Fig. 4-4c shows the stress

distribution *after cool-down* — this stress distribution simply reflects the stress distribution caused by the large temperature change and the thermal expansion mismatch, superposed on the stress-distribution shown in Fig. 4-4b. Note that after cool-down the maximum compressive stress level is $\approx -5.5\,\mathrm{GPa}$.

Remark: For comparison we give below the analytical result from linear thermo-elasticity, denoted by T^a_{11}, which corresponds to purely thermal compressive stress (i.e., no growth stress) for the *complete reaction* (i.e. $\xi = 1$) for the case of a thin oxide layer on a very thick bond coat. This value may be estimated using a classical Stoney formula [13] as

$$T^a_{11} \approx \frac{E_{\mathrm{ox}}(\alpha_{\mathrm{bc}} - \alpha_{\mathrm{ox}})(\vartheta_{\mathrm{room}} - \vartheta_{\mathrm{hot}})}{(1 - \nu_{\mathrm{ox}})} = -3750\ \mathrm{MPa}, \tag{4.1}$$

where E_{ox} and ν_{ox} are the Young's modulus and Poisson's ratio of the oxide, respectively, $\vartheta_{\mathrm{hot}} = 1473\,\mathrm{K}$, and $\vartheta_{\mathrm{room}} = 298\,\mathrm{K}$.

Regarding the distribution of the oxide volume fraction ξ shown in Fig. 4-4a, it can be seen that there is a very clear contrast between the oxidized and unoxidized regions, that is, where ξ is close to unity and close to zero, respectively. Note that in the oxidized zone the maximum value reached by ξ is around 0.93, which is smaller than the value of unity that one might expect. The difference between this maximum value and unity stems from the fact that the driving force $\mathcal{F}$ (cf. (3.169)) contains a contribution by the chemical potential μ, which remains negative even at high oxygen concentrations. These negative values of μ cause $\mathcal{F}$ to become negative for sufficiently large ξ, and this terminates the oxidation reaction (cf. (3.168)).

Remark: The theory formulated here is highly non-linear and involves strong coupling between many mechanisms. One of the major benefits of our numerical implementation of the coupled phenomena under consideration here, is that one can identify the relative contribution of a particular mechanism to the overall response by just switching it on or off, or by varying the numerical parameters representing the particular mechanism in the simulations. We present the results of such a parametric study in Appendix C.

4.4 Surface rumpling of a plate with an initial groove-like undulation

In this section, to check the predictive capabilities of our theory and its numerical implementation, we consider the oxidation of an FeCrAlY sheet with an initial groove-like surface undulation, a geometry which has been experimentally studied by Davis and Evans [30].

Fig. 4-5a shows an optical profilometer trace of a representative groove introduced on the polished surface of a 5 mm thick FeCrAlY plate. Fig. 4-5b shows the distortion of the surface after the sheet specimen was oxidized for 24 thermal cycles. Each thermal cycle consisted of a 2 min heat-up to 1423 K, a 60 min hold, 2 min cool-down, and 10 min hold at 298 K; cf. Fig. 4-6. Davis and Evans [30] conducted their experiments with various groove geometries ranging between 2 to 8 μm in depth, and 15 to 40 μm width; the grooves were spaced 200 μm apart on the sheet surface. Fig. 4-7 shows a scanning electron micrograph of the distortion

of a groove in a FeCrAlY specimen upon cyclic oxidation; this figure is taken from an earlier paper by Evans and co-workers [86].

Here, we simulate one of the groove geometries studied by Davis and Evans [30], in which the grooves were $5\,\mu$m in depth and $15\,\mu$m in width, spaced $200\,\mu$m apart on the surface of a FeCrAlY plate. We assume *generalized plane strain*[2] conditions prevail along the length of the groove, and due to symmetry we consider only one half of the groove geometry. The finite element mesh used in our simulations is shown in Fig. 4-8. As initial conditions we choose $c_{\mathrm{R},0} = 0$ and $\vartheta_0 = 1423\,\mathrm{K}$.[3]

As diffusion boundary conditions, with respect to Fig. 4-8, no oxygen flux is allowed on edges AB, BC, and DA. On edge CD we prescribe the normalized oxygen concentration, $\check{c}_{\mathrm{R}}$, via the partial pressure of oxygen $p_{\mathrm{O}_2} = 0.021$ MPa (cf. (3.194)) of the surrounding oxygen gas at atmospheric pressure. For the mechanical problem boundary conditions we set $u_1 = 0$ on edge DA, $u_2 = 0$ on edge AB. We constrain edge BC to remain plane and vertical, but it is allowed to move in the horizontal $\mathbf{e}_1$-direction. Finally, for the temperature, we prescribe the thermal history according to Fig. 4-6 at *every node* in the finite-element mesh. Under the generalized plane-strain conditions under consideration here, the dimensional change in the out-of-plane $\mathbf{e}_3$-direction due to temperature cycling is accounted for by setting

$$E_{33} \equiv \alpha_{\mathrm{bc}}(\vartheta - \vartheta_0), \tag{4.2}$$

where α_{bc} is the coefficient of thermal expansion of the geometrically-dominant bond coat material. Thus, in order to accommodate the out-of-plane dimensional changes due to thermal contraction upon cool-down, we have adopted an assumption of generalized plane-strain, and simplified our analysis by neglecting transient heat transfer in our simulations.

Another ingredient needed in our anlaysis is to specify the preferred swelling direction $\mathbf{m}_{\mathrm{R}}$; cf. the discussion on page 48, in the section containing (3.139). As discussed there, if an oxidizing material point lies on the *surface* of the bond coat, the preferred direction $\mathbf{m}_{\mathrm{R}}$ is simply the local surface normal. With respect to Fig. 4-8, let the X_2-coordinate of a material point lying on the edge CD be parameterized as $s(X_1)$.[4] Then, if $\mathbf{X}$ lies on edge DC, this unit normal can be expressed as

$$\mathbf{m}_{\mathrm{R}}(\mathbf{X}) = \frac{1}{\sqrt{(\partial s/\partial X_1)^2 + 1}}\Big(- (\partial s/\partial X_1)\,\mathbf{e}_1 + \mathbf{e}_2\Big). \tag{4.3}$$

Next, we need to specify $\mathbf{m}_{\mathrm{R}}$ for material points that are not located on edge DC. In this regard, note that the oxidation reaction under consideration here is essentially confined to a *thin* region near the surface of the body. It is therefore reasonable to assume that (4.3) holds not only if $\mathbf{X}$ lies exactly on DC, but also at any other oxidizing material point — which necessarily lies close to edge DC. We make this assumption here. A quiver-plot of the assumed vector field for $\mathbf{m}_{\mathrm{R}}$ in the vicinity of the groove is shown in Fig. 4-9.

[2]We allow for a *uniform* strain in the out-of-plane $\mathbf{e}_3$-direction.

[3]Again an "artificial" initial cool-down step from $\vartheta_0 = 1423\,\mathrm{K}$ to 298 K was used; cf. Footnote 1.

[4]The specific form for s is given by joining two circular arcs to represent the half-groove, and a straight line to the right of the groove. For brevity we do not write out this functional form here.

Fig. 4-10a shows contour plots of the oxide volume fraction on the deformed geometry in the vicinity of the groove at the end of the 24 thermal cycles. For visual reference concerning the degree of oxidation and distortion of the groove, a 10μm marker is also shown in Fig. 4-10. The contours of oxide volume fraction ξ indicate that oxidation has progressed to about two microns into the material, and that the initial groove geometry has been significantly distorted with a "pile-up" of oxidized material in the vicinity of the initial intersection of the groove with the free surface. Such a pile-up is observed experimentally, and shown in Fig. 4-5b from Davis and Evans [30]. Fig. 4-10a is also remarkably similar in appearance to that from the work of Rebollo et al. [86] shown in Fig. 4-7. Fig. 4-10b shows the corresponding contours of the in-plane Cauchy stress T_{11}. The maximum compressive stress level in the oxide is ≈ -5.3 GPa, which is of similar magnitude to the stress values observed in the flat-plate experiments by Tolpygo et al. [103], discussed earlier. Finally, Fig. 4-10c shows contours of the equivalent tensile plastic strain $\bar{\epsilon}^p$; note that in order to accommodate the material pile-up around the groove edges, the underlying bond coat material has undergone a plastic strain of up to almost 50 percent. This high local value of $\bar{\epsilon}^p$ emphasizes the need for a finite-deformation framework to study the oxidation-type problems considered here.

Finally, Fig. 4-11 shows a comparison of the numerically-predicted and experimentally-measured traces of the initial and final groove geometries. The numerically-predicted final groove profiles are again, not perfect but in reasonable agreement with those measured by Davis and Evans [30] .

Table 4.1: Elastic and thermal material parameters for Fe-22Cr-4.8Al-0.3Y; $\vartheta_{\text{ref}} = 1473\,\text{K}$.

	Parameter	Value	Source
Thermoelasticity of bond coat	G_{bc}^0 [GPa]	39	[16]
"	M_1 [GPa/K]	-0.033	[16]
"	K_{bc}^0 [GPa]	88	[16]
"	M_2 [GPa/K]	-0.066	[16]
"	α_{bc} [1/K]	14.3×10^{-6}	[43]
Thermoelasticity of oxide	G_{ox}^0 [GPa]	132	[43]
"	M_3 [GPa/K]	-0.029	[43]
"	K_{ox}^0 [GPa]	172	[43]
"	M_4 [GPa/K]	-0.069	[43]
"	α_{ox} [1/K]	8.3×10^{-6}	[43]
Thermal conductivity of bond coat	κ_{bc}^0 [W/(m×K)]	31	[84]
"	M_5 [W/(m×K^2)]	0.018	[84]
Thermal conductivity of oxide	κ_{ox}^0 [W/(m×K)]	5.5	[109]
"	M_6 [W/(m×K^2)]	-0.020	[109]
Specific heat for both materials	c [MJ/(m^3×K)]	5.00	[84]

Table 4.2: Viscoplasticity, diffusion, and oxidation material parameters for Fe-22Cr-4.8Al-0.3Y.

	Parameter	Value	Source
Viscoplasticity of bond coat	A_{bc} [1/s]	48×10^3	calibrated
"	S_{bc} [MPa]	20	calibrated
"	m_{bc} [-]	0.25	calibrated
"	Q_{bc} [kJ/mol]	282	calibrated
Plasticity of oxide	$\dot{\bar{\epsilon}}_{\text{ox}}^0$ [1/s]	1×10^{-3}	calibrated
"	S_{ox}^0 [MPa]	2405	calibrated
"	M_{ox} [MPa/K]	-3.63	calibrated
"	m_{ox} [-]	0.005	calibrated
Diffusion in bond coat	$D_{0,\text{bc}}$ [m^2/s]	7.5×10^{-9}	calibrated
"	$Q_{d,\text{bc}}$ [kJ/mol]	100	calibrated
Diffusion in oxide	$D_{0,\text{ox}}$ [m^2/s]	7.5×10^{-9}	calibrated
"	$Q_{d,\text{ox}}$ [kJ/mol]	100	calibrated
"	$c_{\max}$ [mol/m^3]	0.08×10^6	[84]
Reference value for chemical potential of oxygen	$\mu^0(=\mu_{\text{O}_i}^0)$ [kJ/mol]	112	[82]
Oxidation from bond coat to oxide	β_l [-]	0.03	calibrated
"	C_ξ [1/(MPa×s)]	1.8×10^{-6}	calibrated
"	Q_s [kJ/mol]	100	calibrated
"	H [GJ/m^3]	387	[22]
"	J_{PB} [-]	1.28	[81]
"	$\mathcal{R}$ [mol/m^3]	0.24×10^6	[84]

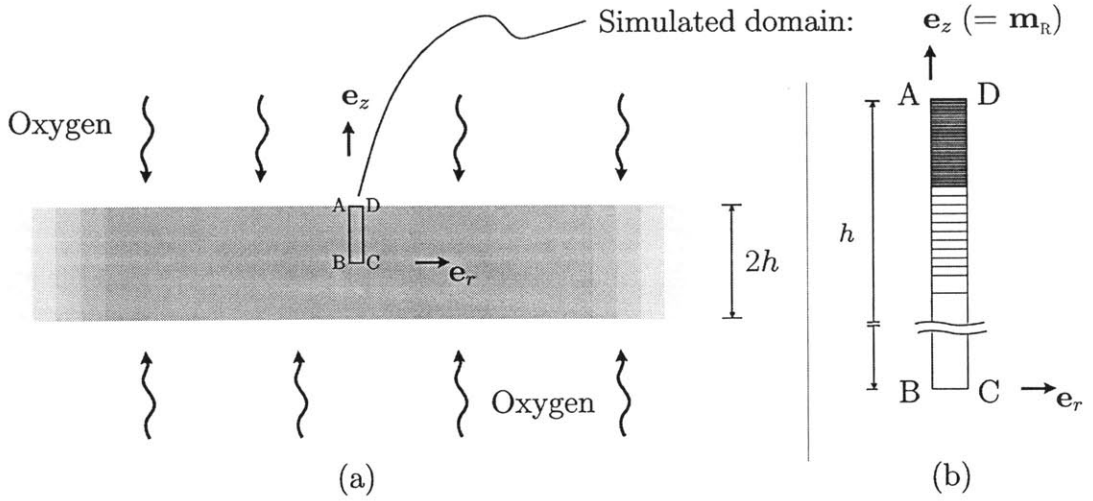

Figure 4-1: (a) Schematic of oxidizing plate. (b) Mesh of simulated domain.

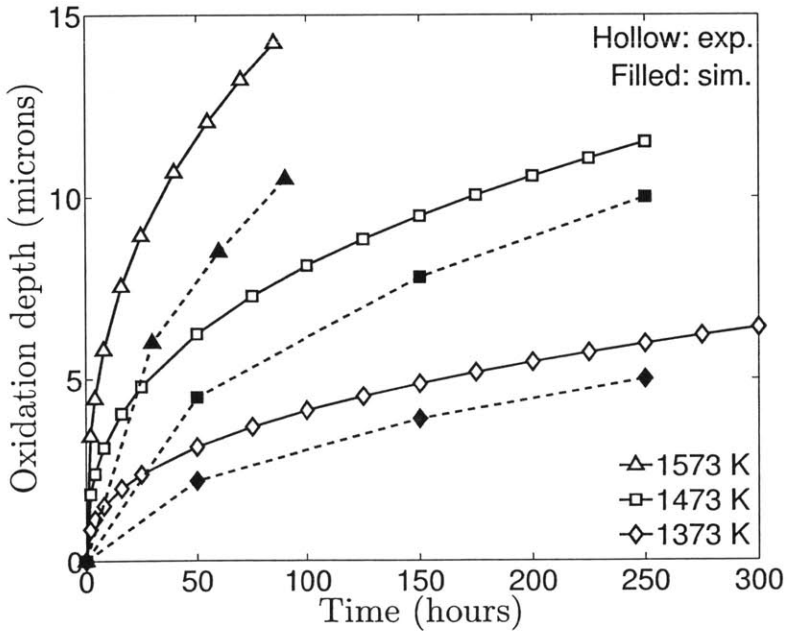

Figure 4-2: Comparison of numerically-predicted and experimentally-measured oxide depth as a function of oxidation time for different values of oxidation temperatures $\vartheta_{\text{hot}} = 1373, 1473, 1573\,\text{K}$; plate thickness of $2h = 0.90\,\text{mm}$. Hollow symbols represent experimental measurements [103], while the filled symbols represent simulation results.

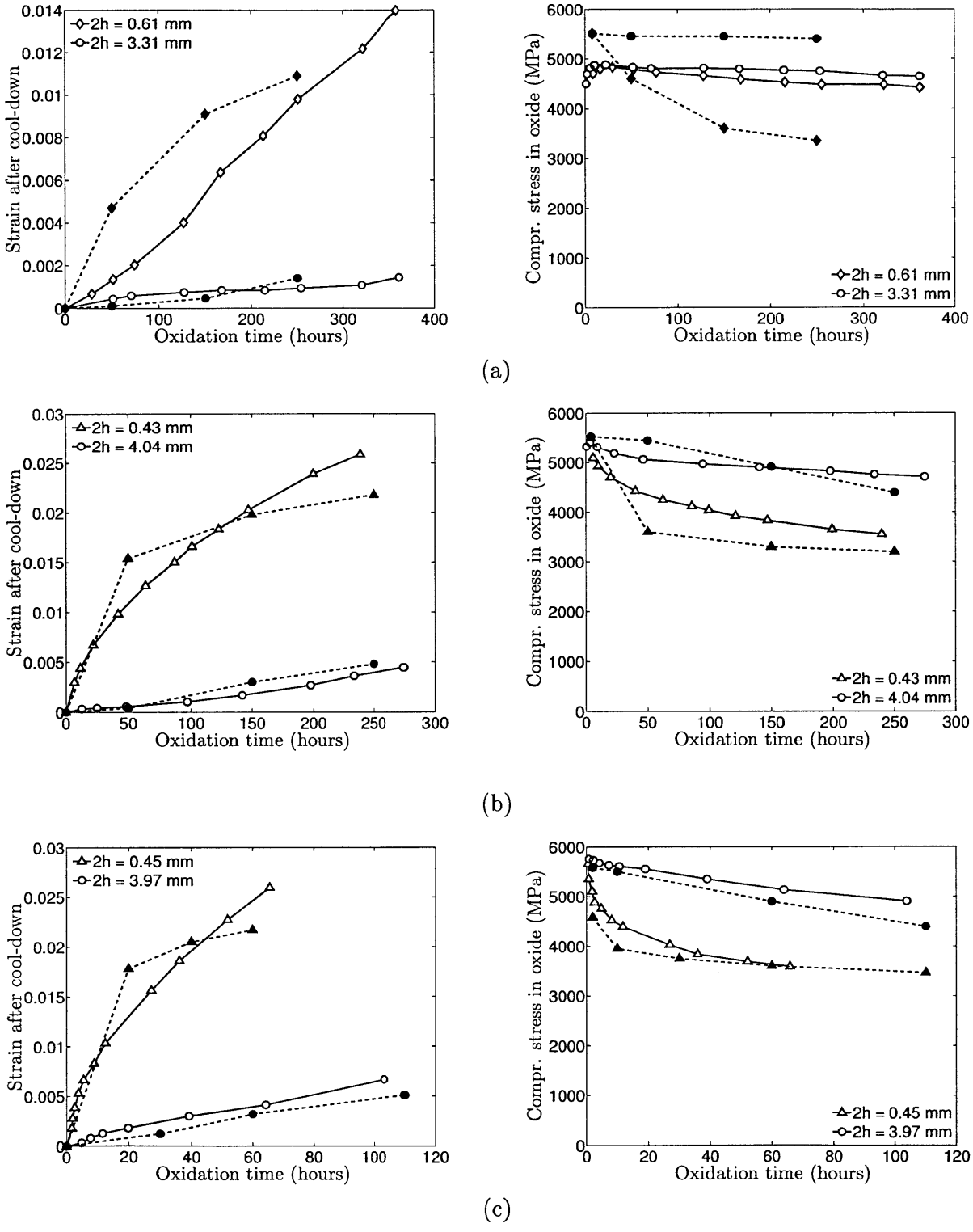

Figure 4-3: Comparison of of numerical simulations (filled symbols) of plate elongational strain and magnitude of the compressive residual stress in the oxide against corresponding experimental measurements (hollow symbols) from Tolpygo et al. [103] for (a) $\vartheta_{\text{hot}} = 1373\,\text{K}$; (b) $\vartheta_{\text{hot}} = 1473\,\text{K}$; and (c) $\vartheta_{\text{hot}} = 1573\,\text{K}$ for plate thicknesses $2h$ indicated in the figure.

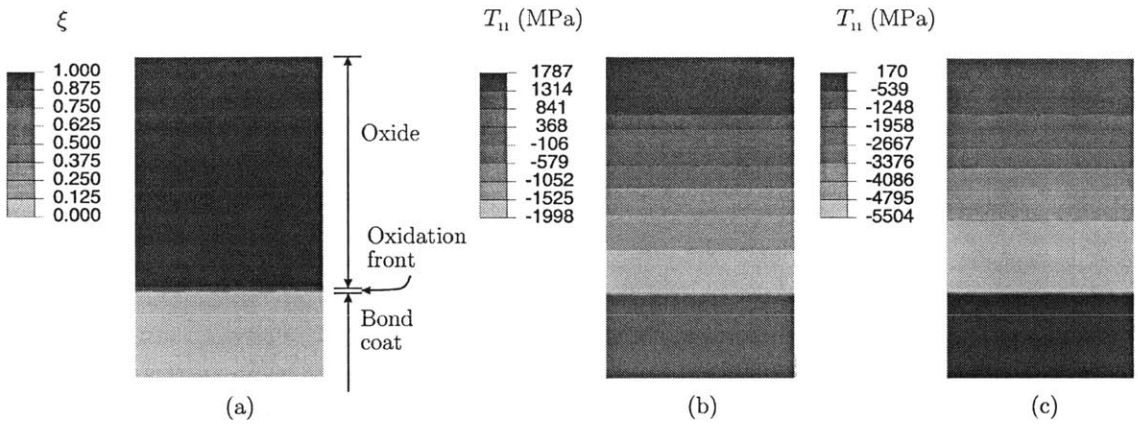

Figure 4-4: Stress state near the surface of a plate where the oxidation is occurring. Plate of thickness $2h = 0.43\,\text{mm}$ which is oxidized at $\vartheta_{\text{hot}} = 1473\,\text{K}$ for 250 hours and subsequently cooled down to room temperature. Contour plots of: (a) volume fraction of oxide; (b) in-plane stress before cool-down; and (c) in-plane stress after cool-down. The simulated mesh (cf. Fig. 4-1b) has been patterned side-by-side numerous times for ease of visualization.

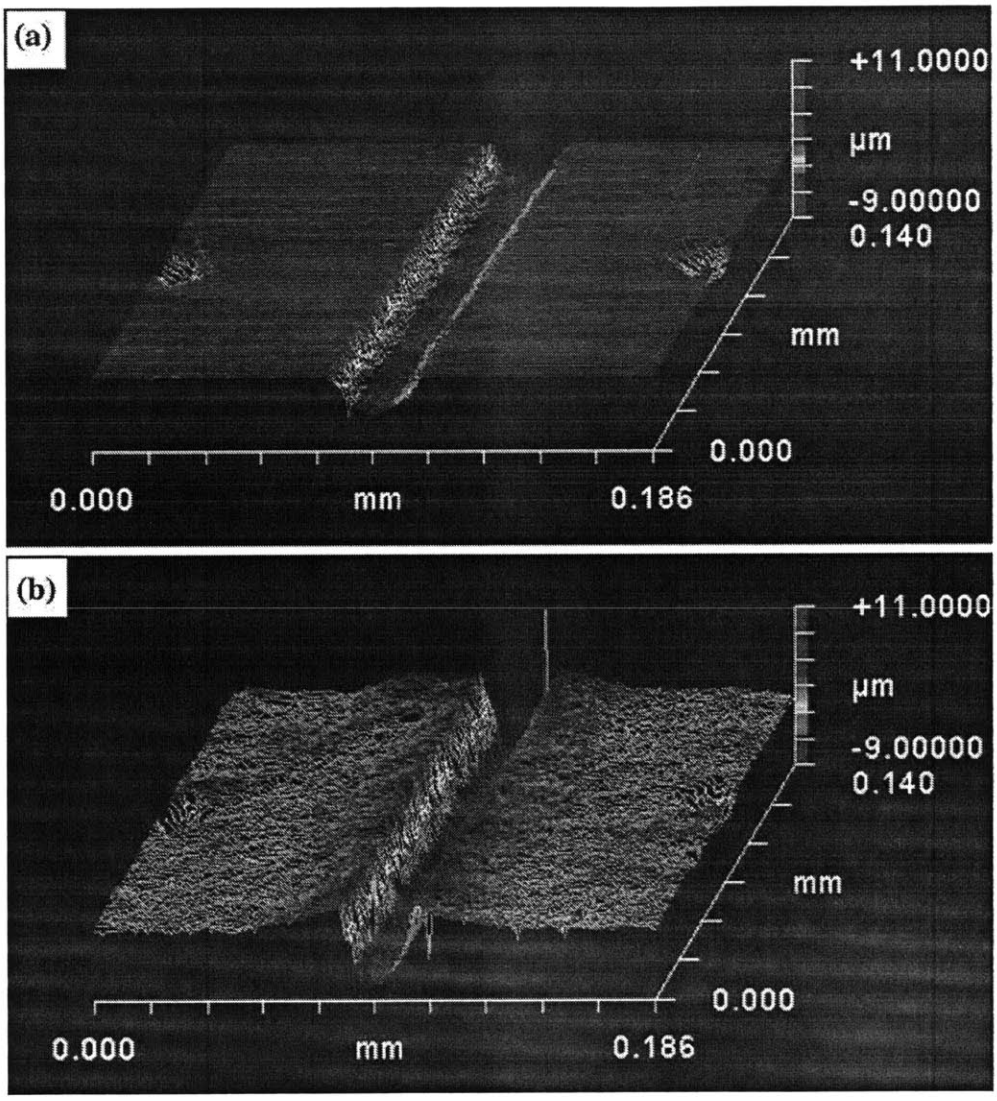

Figure 4-5: Profiles for (a) groove introduced into the surface of FeCrAlY sheet; (b) Surface rumpling after 24 thermal cycles shown in Fig. 4-6. From Davis and Evans [30].

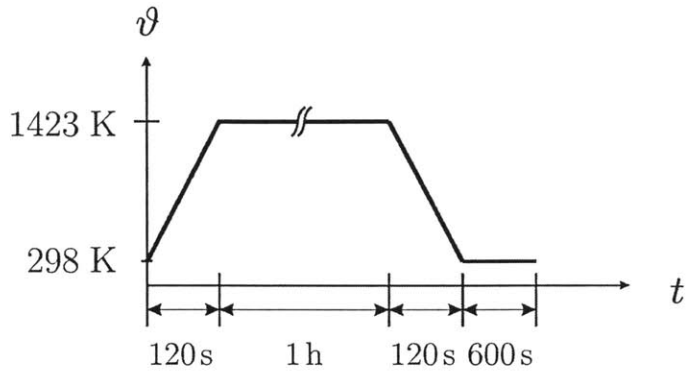

Figure 4-6: Thermal cycle used by Davis and Evans [30] in their groove-rumpling experiments.

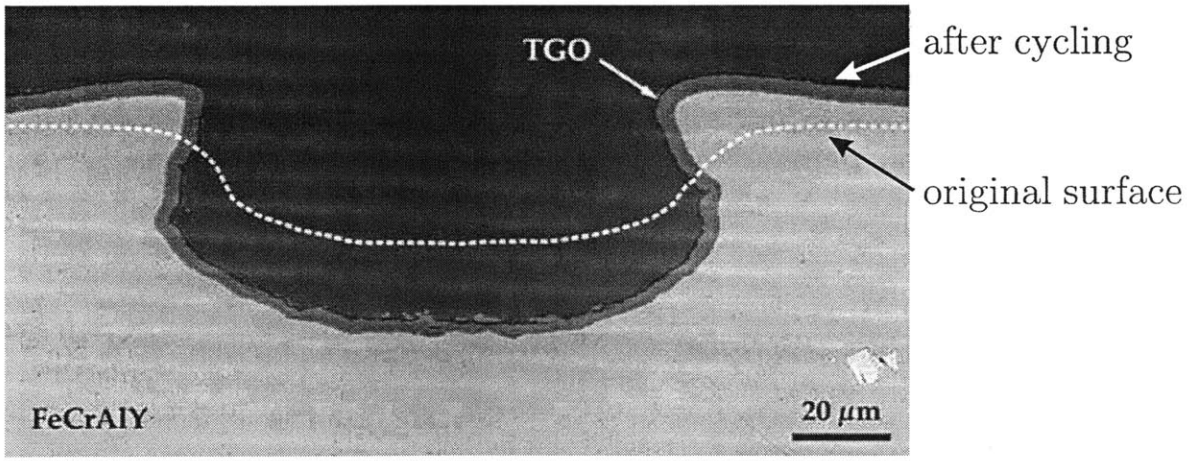

Figure 4-7: Distortion of a groove in a FeCrAlY specimen upon cyclic oxidation. Adapted from Davis and Evans [30]; also see Rebollo et al. [86].

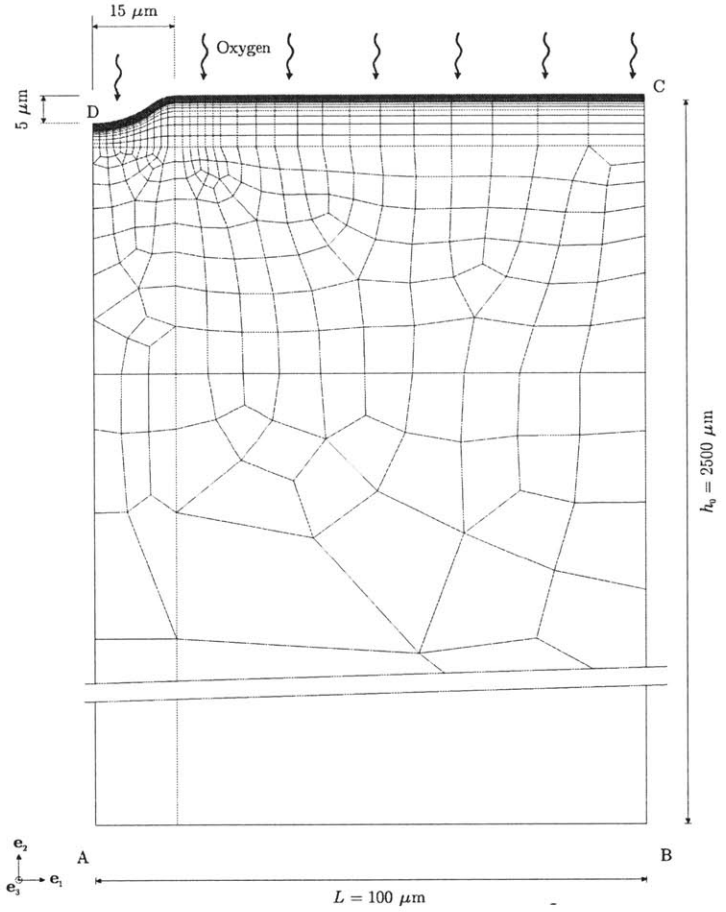

Figure 4-8: Geometry and mesh for the groove rumpling simulation.

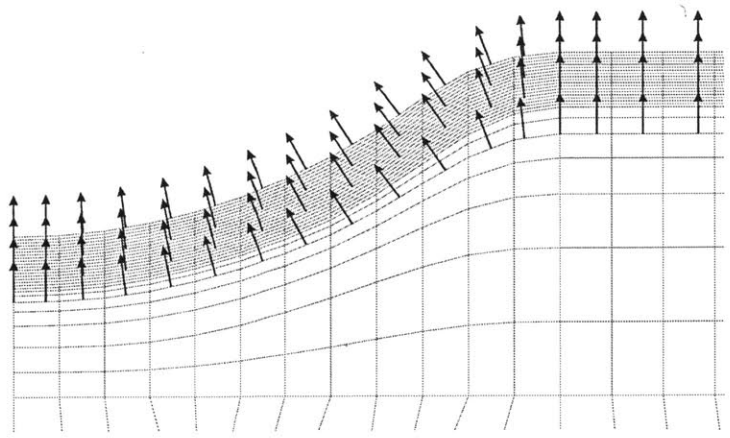

Figure 4-9: Quiver-map of the preferred oxidizing direction $\mathbf{m}_R$ in the vicinity of the groove in Fig. 4-8.

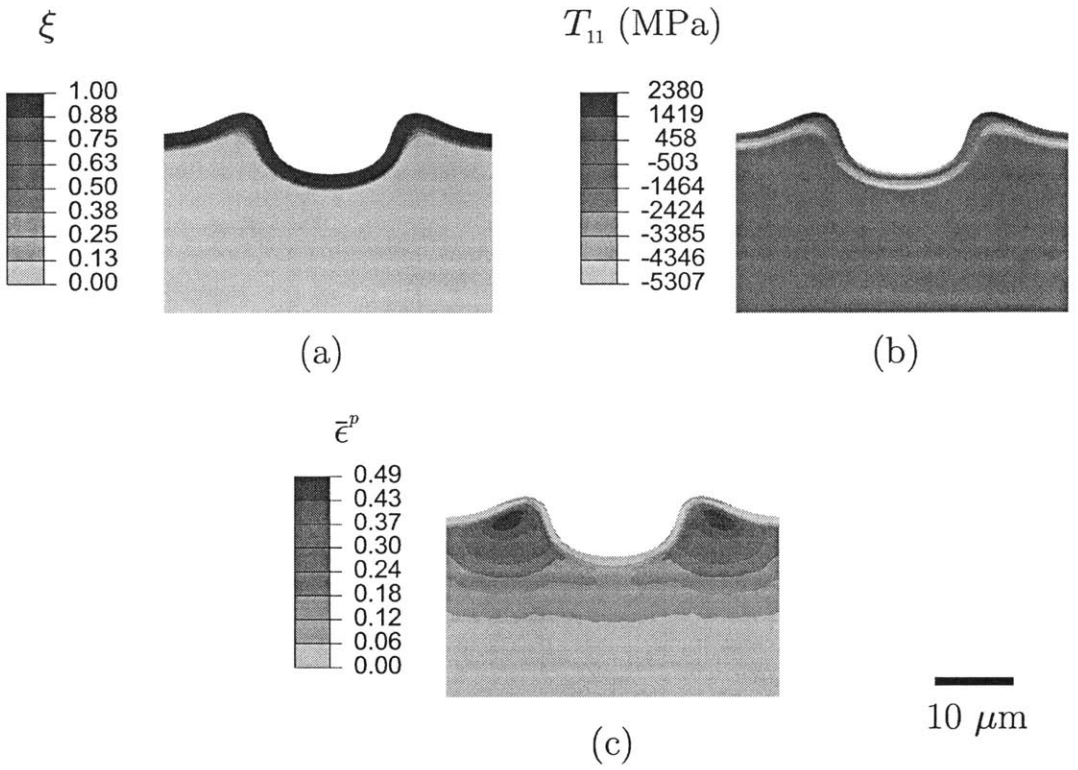

Figure 4-10: Contour plots for the groove oxidation and rumpling at end of simulation: (a) the oxide volume fraction; (b) the in-plane stress T_{11}; and (c) the equivalent tensile plastic strain $\bar{\epsilon}^p$. For reference a 10μm marker is also shown in the figure.

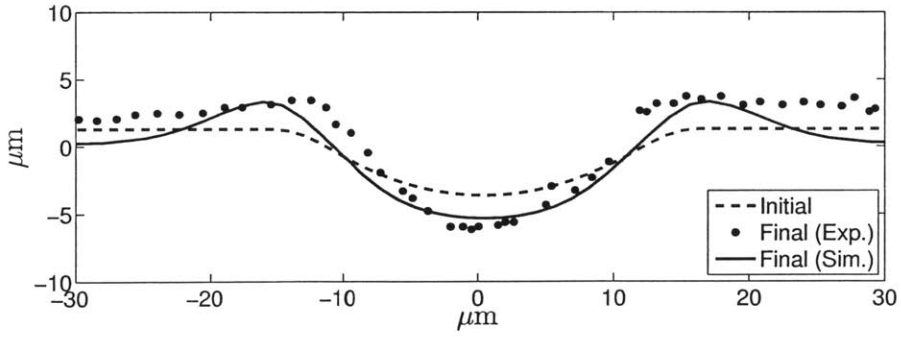

Figure 4-11: Comparison of numerically-predicted and experimentally-measured [30] traces of the final groove geometries.

Part II

Modeling of failure in macroscopic thermal-barrier-coated components

Chapter 5

Introduction

In Part I, we simulated the coupled oxidation of a high-temperature alloy with the motivation that, as discussed in Chapter 1, it is the oxidation of the high-temperature *bond-coat alloy* in a TBC system which is ultimately responsible for its degradation and failure. The material we considered in Part I was FeCrAlY, which is a *model bond-coat alloy* for TBC systems; if we now add the YSZ *top coat* to this concept, then the model comprises the full TBC system. In this second part, we shall examine how the overall TBC system behaves, especially with regard to its eventual failure.

Since we are now considering the entire TBC system *including the top coat* made of YSZ, it is suitable to briefly consider how the top coat is manufactured. There are two manufacturing processes that are commonly used:

(a) electron-beam physical vapor deposition (EBPVD), and

(b) deposition by plasma spray (PS).

The two processes lead to two profoundly different microstructures as shown in Figs. 5-3 and 5-4. In EBPVD coatings, the columnar microstructure provides the strain compliance needed to accommodate the thermal mismatch with the underlying metallic material (i.e. the bond coat and substrate). In PS coatings, this strain tolerance comes from porosity between the individual splats ("pancakes") of material [cf., e.g., 74]. Due to the lower cost associated with PS deposition, this process is widely used [39]. *In this work, we therefore limit ourselves to the consideration of plasma-sprayed TBC systems.*

The computational modeling of the complete TBC system has been a popular topic of research over the past decade [cf.,e.g., 15–18, 26, 31, 38–40, 51, 61, 75, 77, 80, 110, and the references to the substantial literature therein]. Particularly, authors have investigated a *unit-cell geometry* of an imperfection at the top-coat/bond-coat interface, and how stresses and strains develop as oxidation takes place in this setting.[1] The process by which the degradation and failure of a TBC system (deposited by PS or EBPVD) occurs is that the *volumetric expansion associated with oxidation* generates large local stresses and strains, since the growing oxide wants to increase its volume by a factor of 1.3 as compared to the

[1]To the best of our knowledge, as discussed in Part I, the oxidation models used in these publications do not incorporate all the oxidation-related phenomena incorporated by our own oxidation model.

virgin alloy, but this expansion occurs in the highly constrained setting of the bond-coat/top-coat interface. Because of the deformation of the growing oxide, the top coat adjacent to it necessarily undergoes similar deformations. However, the interface region between the thermally-grown oxide (TGO) and the top coat has widely been observed experimentally to be a "weak link" in the PS TBC system [cf., e.g., 59, 104, 112, 116, 121], and therefore microcracks tend to develop in this region when oxide growth takes place.

While this generation of microcracks has been known for a while, only more recently researchers have begun to explicitly consider a failure-prone interface in the TBC system in their simulations; cf., e.g., Caliez et al. [19], Bialas [12], and Hille et al. [54, 55]. (Note that these papers focus on EBPVD coatings; the methodology discussed therein equally applies for plasma-sprayed coatings, though.) In these works, the authors make use of *cohesive elements*: these are special-purpose finite elements that are used to join the top coat and oxidizing bond coat together, and which model the behavior of this interface. Cohesive elements represent a powerful tool, the basic concept for which can be traced back to the work of Barenblatt [10] and Dugdale [35] on cohesive interface modeling. They are especially popular in the study of *composite materials* [cf., e.g., 20, 42], which by definition abound with interfaces.

The constitutive behavior of cohesive elements is described by a *traction-separation law* relating the traction on the interface to the displacement jump between the two joined bulk materials. In composites, the interface will exhibit elastic behavior, and once its damage initiates, it will rather abruptly reach failure. This behavior is embodied in a *triangular* traction-separation law with an elastic branch, and a *linear softening branch*; see Fig. 5-5. (Abrupt or *brittle* failure is characterized by a steep softening branch.) A detailed discussion for this type of traction-separation law is given in Camanho and Davila [20]. This triangular law has been widely employed also for a failure-prone interface in TBC systems.

To illustrate the approach found in literature of examining an top-coat/bond-coat imperfection on the microscale as it deforms and ultimately forms a microcrack, we add to our "groove geometry" from Chapter 4 a top coat, forming the entire TBC system, and simulate the behavior of this material system. The top coat and oxidizing bond coat are connected by *cohesive elements*; the resulting finite-element mesh is shown in Fig. 5-1.[2] As oxidation begins, the imperfection wants to *rumple* much like it does in the simulation without top coat, cf. Fig. 4-10; however, the top coat now strongly inhibits this motion. To achieve this constraint, stresses have to be transmitted at the top-coat/oxidizing bond-coat interface; it is the cohesive elements that play this role. Once these stresses reach a damage initiation criterion, they cease to further increase and instead start to soften; when they are reduced to a value of zero, *the interface has locally failed.* This process is illustrated in detail in Fig. 5-2 (where failed cohesive elements are removed from the plot): oxidation starts in the virgin setting, starting to cause stress and deformation. Finally, two symmetric cracks initiate and then coalesce to form a larger one. *It is this process that is at the origin of the ultimate failure of TBC systems.*

[2]We consider an *isothermal scenario* at $\vartheta = 1423$ K and for simplicity consider the top coat to be elastic with $E = 22$ GPa and $\nu = 0.20$ [16]. We use cohesive elements built into Abaqus/STANDARD [20, 93]; damage initiates at a stress of 50 MPa (tension and shear), and the fracture energy in both tension and shear is taken as 10 J/m^2. A triangular traction-separation law as discussed above is employed. For the oxidizing bond coat, our numerical implementation from Part I and associated material parameters are used.

Such a microscale investigation is powerful in that it allows us to *trace in detail the initiation and propagation of TBC system degradation.* However, there is a limitiation to this approach: in the groove simulation, the smallest finite elements had a thickness of about 0.08 microns. As discussed in Chapter 1, this fine discretization yields the simulation of a *macroscopic component* quickly very challenging. For this reason, we now *shift our attention away from the microscale considerations* from Part I and the simulation including the top coat discussed above, and instead attempt to formulate a framework that facilitates the simulation of degradation and failure of a *macroscopic* thermal-barrier-coated component.

To this end, we note that the *macroscopic* manifestation of the oxidation process is simply that it causes a change in the resistance of the TBC system to spallation failure as a function of dwell time. Here, we therefore adopt a description of the TBC system in which *we do not explicitly model oxidation; rather, we assume that oxidation is manifested only indirectly by changing the resistance of the TBC system to spallation.* With such an approach, the very fine mesh required by explicitly modeling oxidation is not needed, and the simulation of macroscopic objects with dimensions of, say, centimeters becomes computationally tractable.[3]

On the macroscopic scale, it has been popular to use the analytical tool of *linear-elastic fracture mechanics* (LEFM) to analyze and interpret experimental data. While such an approach provides some important information, using LEFM one is limited to considering an *already-existing crack* and cannot predict the initiation of this crack, which warrants instead a *numerical investigation.* However, the numerical simulation of *macroscopic components* with applied TBC systems has, to our best knowledge, only garnered limited attention in the literature, for example by Cao et al. [21], Zhao et al. [119], and Xu et al. [111]. In their publication, Cao et al. [21] consider *perfectly-bonded* interfaces in the TBC system; while this yields an initial stress distribution, they can therefore not make a prediction beyond the onset of degradation. Zhao et al. [119] follow the approach of introducing a pre-existing crack into the finite-element mesh from the beginning, not employing a criterion for this crack to propagate further. In their case, they are therefore limited to considering a specimen statically at a set crack length, and then have to run a new simulation with a new mesh to examine the propagated crack.

Xu et al. [111], however, go further by making use of *cohesive elements* as discussed above. We believe this choice of using cohesive elements *also at the macroscale* is as promising as discussed before for the microscale. We shall therefore follow this avenue here and *attempt to model the failure of macroscopic thermal-barrier-coated parts using cohesive elements.*

The next question then regards the specific constitutive behavior of the failure-prone interface in the TBC system, i.e. the behavior of the cohesive elements. The triangular traction-separation law as previously discussed is especially suitable in situations where *inelastic deformations of the interface are small*; considering Fig. 5-5, once the strength of the interface is reached, it goes *directly* into softening. However, in preliminary experiments performed in our own group, there is evidence that in PS TBC systems, once the failure-prone top-coat/TGO interface reaches its strength, it is then able to *undergo some continuing*

[3]If one is interested in the detailed deformation and degradation process at the *microlevel* as for the "groove with top coat" simulation discussed above, this assumption can obviously not be made, and the coupled theory and associated numerical implementation are needed.

deformation at this strength level, i.e. it exhibits a *plastic plateau*. This behavior cannot be captured by the triangular traction-separation law; in this thesis, we therefore use a different, *trapezoidal* law which exhibits this plastic plateau.

Using a traction-separation law, the cases in which the interface is loaded either purely in shear or purely in tension are straightforward to consider. However, once there is a *certain combination* of these two modes, i.e. there is some *mode mixity*, one has to prescribe whether/how the behavior under this mixed-mode loading differs from the pure-mode cases. While the importance of mode mixity has been widely investigated for *delamination of composites* [cf., e.g., 87, 105], the TBC community is only starting to consider it [59]. Therefore, to the best of our knowledge there is not enough richness in available experimental data to definitely answer the fundamental question of whether mode mixity is important in TBC system failure. For generality, in our traction-separation law, *we thus choose several material parameters to depend on mode mixity.*

In the next Chapter, we discuss in detail our trapezoidal traction-separation law, which was introduced by Cookson [28], and is based on the work by Su et al. [98]. The traction-separation law has been implemented as a *user-material subroutine* in Abaqus/EXPLICIT [94], and we have made use of this implementation to apply the traction-separation law to the top-coat/TGO interface in PS TBC systems; this is discussed in Chapter 7. Specifically, the model has been calibrated by simulating (i) a mode-II delamination test performed in our group by Dr. Haowen Liu, and (ii) a four-point notched bend test by Zhao et al. [121]. Also, we have checked the predictive capability of our model by simulating a notched four-point bend test performed by Zhao et al. [121].

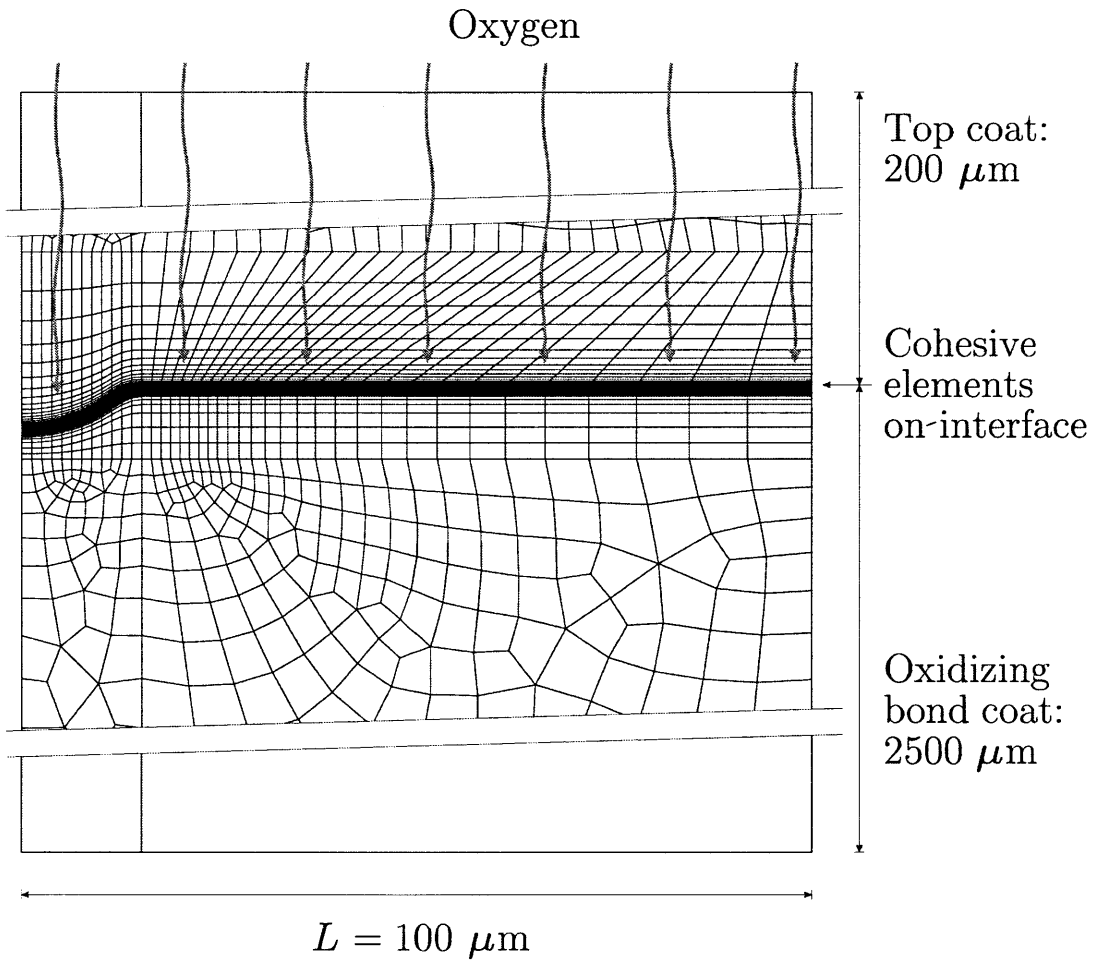

Figure 5-1: Finite element mesh for simulation of an imperfection in a top-coat/bond-coat interface.

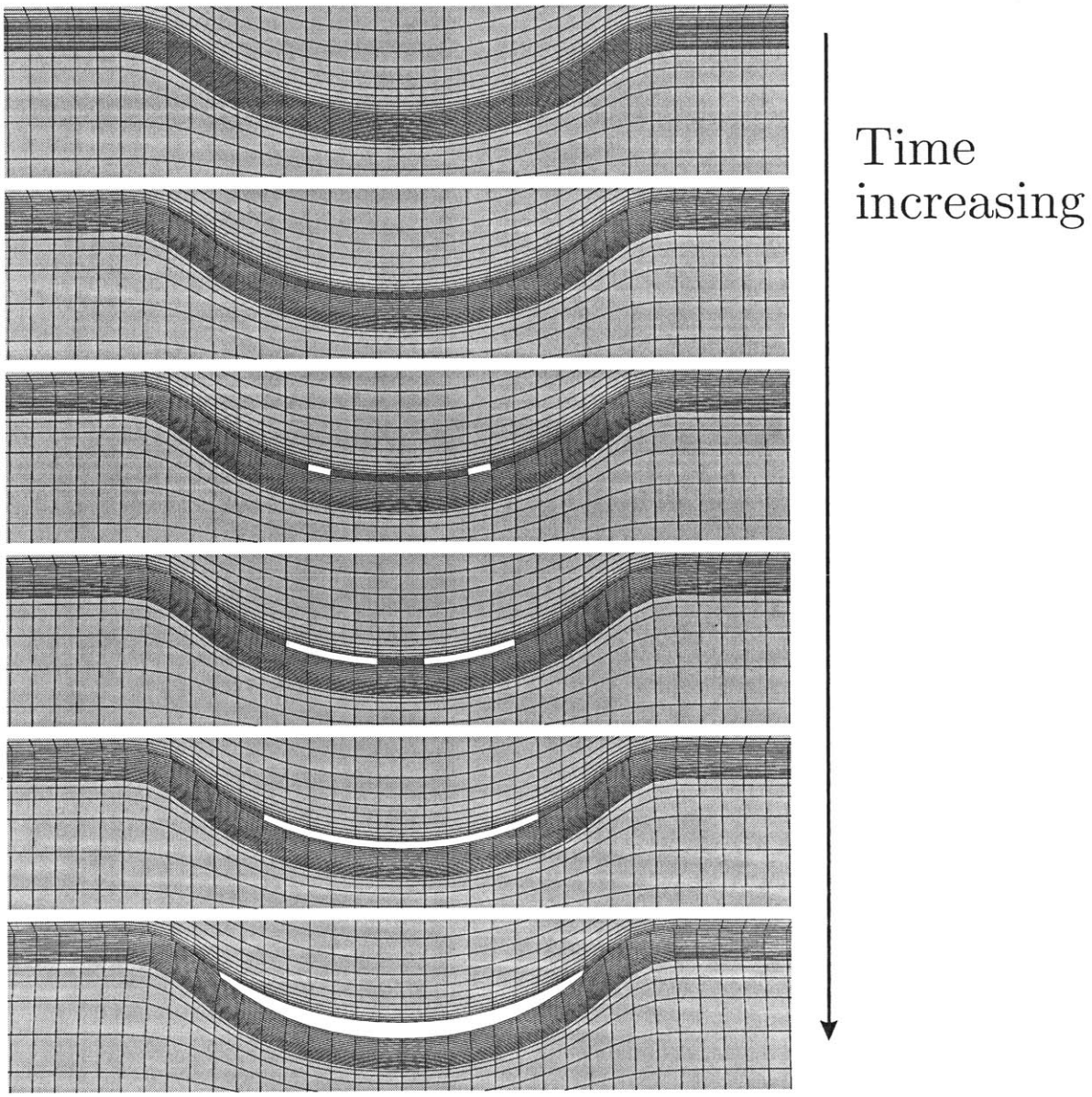

Figure 5-2: Development of interfacial crack at imperfection.

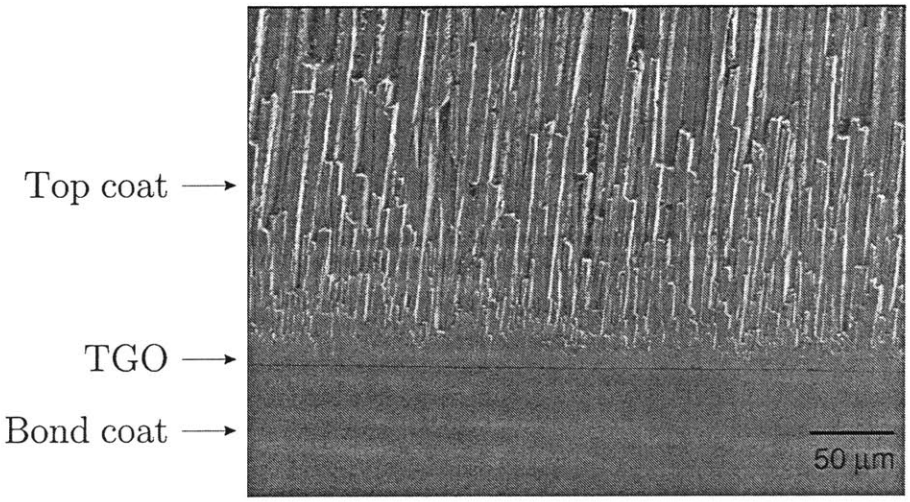

Figure 5-3: Micrograph of a top coat deposited by EBPVD. Adapted from Kim et al. [64].

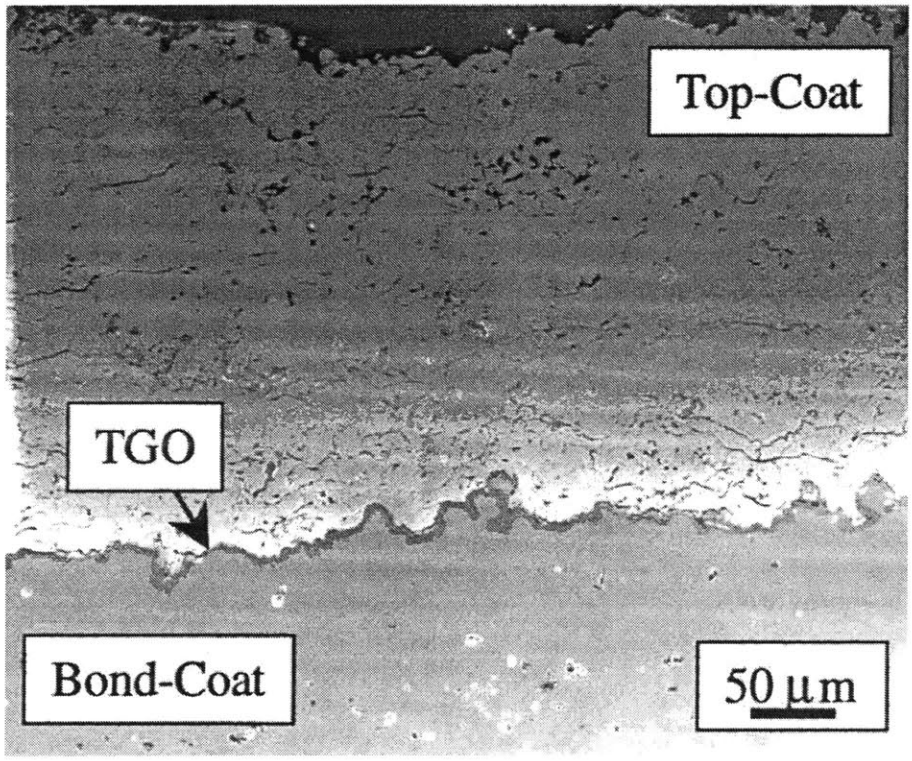

Figure 5-4: Micrograph of a plasma-sprayed top coat from Schlichting et al. [91].

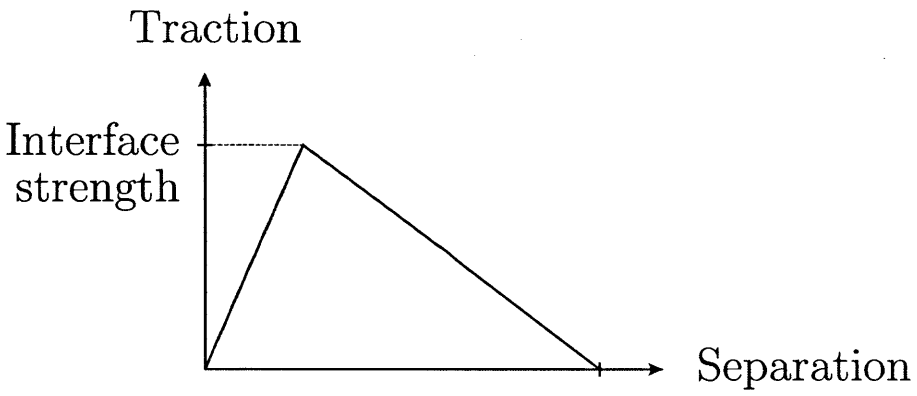

Figure 5-5: Schematic of a triangular traction-separation law.

Chapter 6

Interface constitutive model

In the next Section we summarize the framework by Su et al. [98]. In the work of Su et al. [98], this general framework was then specialized with the aim of modeling the response of a polymeric adhesive. Here, we choose a different and simpler specialization – the one to a trapezoidal traction-separation behavior – which is aimed at modeling the top-coat/TGO interface in plasma-sprayed TBC systems. Our specialization is discussed in Section 6.2.

6.1 Summary of the general framework by Su et al. [98]

We consider two bodies $\mathcal{B}^+$ and $\mathcal{B}^-$separated by an interface $\mathcal{I}_\mathbf{B}$ (Fig. 6-1). Let $\{\hat{\mathbf{e}}_1, \hat{\mathbf{e}}_2, \hat{\mathbf{e}}_3\}$ be an orthonormal triad, with $\hat{\mathbf{e}}_1$ aligned with the normal $\mathbf{n}$ to the interface, and $\{\hat{\mathbf{e}}_2, \hat{\mathbf{e}}_3\}$ in the tangent plane at the point of the interface under consideration.

Let $\boldsymbol{\delta}$ denote the displacement jump across the cohesive surface, and $\mathbf{t}$ the power-conjugate traction, such that $\mathbf{t} \cdot \dot{\boldsymbol{\delta}}$ gives the power per unit area of the interface in the reference configuration.

We assume that the displacement jump may be additively decomposed as

$$\boldsymbol{\delta} = \boldsymbol{\delta}^e + \boldsymbol{\delta}^p, \tag{6.1}$$

where $\boldsymbol{\delta}^e$ and $\boldsymbol{\delta}^p$, respectively, denote the elastic and plastic parts of $\boldsymbol{\delta}$. Additionally, for later use we also introduce a second decomposition of $\boldsymbol{\delta}$ into normal and tangential parts,

$$\boldsymbol{\delta} = \boldsymbol{\delta}_N + \boldsymbol{\delta}_T, \qquad \boldsymbol{\delta}_N = (\mathbf{n} \otimes \mathbf{n})\boldsymbol{\delta} = (\boldsymbol{\delta} \cdot \mathbf{n})\mathbf{n} = \delta_N \mathbf{n}, \qquad \boldsymbol{\delta}_T = (\mathbf{1} - \mathbf{n} \otimes \mathbf{n})\boldsymbol{\delta} = \boldsymbol{\delta} - \boldsymbol{\delta}_N, \tag{6.2}$$

where the scalar δ_N represents the displacement jump in the normal direction. The magnitude of the displacement jump in the tangential direction is denoted by

$$\delta_T = |\boldsymbol{\delta}_T|. \tag{6.3}$$

The *displacement jump angle* β is then defined as

$$\beta = \arctan\left(\frac{\delta_N}{|\boldsymbol{\delta}_T|}\right). \tag{6.4}$$

We are concerned with interfaces in which the elastic displacement jumps are small, but but the plastic displacement jumps may be arbitrarily large. For small elastic displacement jumps we assume a simple quadratic free-energy φ

$$\varphi = \frac{1}{2}\boldsymbol{\delta}^e \cdot \mathbf{K}\boldsymbol{\delta}^e, \tag{6.5}$$

with $\mathbf{K}$, the interface elastic stiffness tensor, positive definite. In this case standard arguments give that [98]

$$\mathbf{t} = \frac{\partial\hat{\varphi}(\boldsymbol{\delta}^e)}{\partial\boldsymbol{\delta}^e} = \mathbf{K}\boldsymbol{\delta}^e = \mathbf{K}(\boldsymbol{\delta} - \boldsymbol{\delta}^p). \tag{6.6}$$

We consider an interface model which is *isotropic* in its tangential response, and take $\mathbf{K}$ to be given by

$$\mathbf{K} = K_N\mathbf{n}\otimes\mathbf{n} + K_T(\mathbf{1} - \mathbf{n}\otimes\mathbf{n}), \tag{6.7}$$

with $K_N > 0$ and $K_T > 0$ normal and tangential elastic stiffness moduli.

The interface traction $\mathbf{t}$ may be decomposed into normal and tangential parts, $\mathbf{t}_N$ and $\mathbf{t}_T$, respectively, as

$$\mathbf{t} = \mathbf{t}_N + \mathbf{t}_T, \quad \mathbf{t}_N \equiv (\mathbf{n}\otimes\mathbf{n})\,\mathbf{t} = (\mathbf{t}\cdot\mathbf{n})\,\mathbf{n} \equiv t_N\,\mathbf{n} \quad \mathbf{t}_T \equiv (\mathbf{1} - \mathbf{n}\otimes\mathbf{n})\,\mathbf{t} = \mathbf{t} - t_N\,\mathbf{n}. \tag{6.8}$$

The quantity t_N represents the *normal stress* at the interface. We denote the magnitude of the tangential traction vector $\mathbf{t}_T$ by

$$\bar{\tau} \equiv \sqrt{\mathbf{t}_T\cdot\mathbf{t}_T}\,, \tag{6.9}$$

and call it the *effective tangential traction*, or simply the *shear stress*.

We take the elastic domain in our elastic-plastic model to be defined by the interior of the intersection of two convex yield surfaces.[1] The yield functions corresponding to each surface are taken as

$$\Phi^{(i)}(\mathbf{t}, s^{(i)}) \leq 0, \qquad i = 1, 2, \tag{6.10}$$

and henceforth we indentify the index $i = 1$ with a "normal" mechanism, and the index $i = 2$ with a "shear" mechanism. The scalar internal variable $s^{(1)}$ represents the deformation resistance for the normal mechanism, and $s^{(2)}$ represents the deformation resistance for the shear mechanism. In particular, we consider the following simple specific functional form for the yield functions:

$$\Phi^{(1)} = t_N - s^{(1)} \leq 0, \qquad \Phi^{(2)} = \bar{\tau} + \mu t_N - s^{(2)} \leq 0, \tag{6.11}$$

[1] It may be possible to develop a theory with only a single yield surface with a rounded corner to model the yield response of the interface, but we have not followed this avenue.

where μ represents a *friction coefficient.* The surface $\Phi^{(i)} = 0$ denotes the ith yield surface in traction space, and

$$\mathbf{n}^{(1)} = \frac{\partial \Phi^{(1)}}{\partial \mathbf{t}} = \mathbf{n}, \qquad \mathbf{n}^{(2)} = \frac{\partial \Phi^{(2)}}{\partial \mathbf{t}} = \frac{1}{\sqrt{1+\mu^2}}\left(\frac{\mathbf{t}_T}{\bar{\tau}} + \mu \mathbf{n}\right) \tag{6.12}$$

denote the outward unit normals to the yield surface at the current point in traction space; see Fig. 6-2.

The equation for $\dot{\boldsymbol{\delta}}^p$, the *flow rule*, is taken to be representable as a sum of the contribution from each mechanism

$$\dot{\boldsymbol{\delta}}^p = \sum_{i=1}^{2} \nu^{(i)} \mathbf{m}^{(i)}, \qquad \nu^{(i)} \geq 0, \qquad \nu^{(i)} \Phi^{(i)} = 0, \quad \text{with} \tag{6.13}$$

$$\mathbf{m}^{(1)} = \mathbf{n}, \qquad \mathbf{m}^{(2)} = \frac{\mathbf{t}_T}{\bar{\tau}}. \tag{6.14}$$

Note that since $\mathbf{m}^{(2)} \neq \mathbf{n}^{(2)}$, we have a *non-normal* flow rule for the shear response.[2]

The evolution equations for the internal variables $s^{(i)}$ are taken as a pair of ordinary differential equations

$$\dot{s}^{(i)} = \sum_{j=1}^{2} h^{(ij)} \nu^{(j)}, \tag{6.15}$$

where the coefficients $h^{(ij)}$ denote hardening/softening moduli.

Finally, during inelastic deformation, an active mechanism must satisfy the *consistency condition*

$$\nu^{(i)} \dot{\Phi}^{(i)} = 0 \qquad \text{when} \qquad \Phi^{(i)} = 0. \tag{6.16}$$

The consistency condition serves to determine the inelastic deformation rates $\nu^{(i)}$ when inelastic deformation occurs. Straightforward calculations using (6.6) – (6.15) give

$$\dot{\Phi}^{(i)} = \mathbf{n}^{(i)} \cdot \mathbf{K} \dot{\boldsymbol{\delta}} - \sum_{j} \left[\mathbf{n}^{(i)} \cdot \mathbf{K} \mathbf{m}^{(j)} + h^{(ij)} \right] \nu^{(j)}.$$

For $\nu^{(i)} > 0$, when $\Phi^i = 0$ the consistency condition requires that $\dot{\Phi}^{(i)} = 0$. This gives the following system of linear equations for $\nu^{(i)} > 0$:

$$\sum_{j=1}^{2} A^{(ij)} \nu^{(j)} = b^{(i)}, \qquad A^{(ij)} = \mathbf{n}^{(i)} \cdot \mathbf{K} \mathbf{m}^{(j)} + h^{(ij)}, \qquad b^{(i)} = \mathbf{n}^{(i)} \cdot \mathbf{K} \dot{\boldsymbol{\delta}}. \tag{6.17}$$

We assume that *the matrix A is invertible*, so that the $\nu^{(j)}$ are uniquely determined.

[2]Such a non-normal flow rule for the shear response is common in interface models for friction, where there is strong effect of the compressive normal traction on the resistance to plastic flow, but the plastic flow in shear is essentially non-dilational.

6.2 Specific form for the evolution equations: trapezoidal traction-separation law with dependence on mode mixity

6.2.1 General

Let

$$\gamma^{(1)} = \int_0^t \nu^{(i)}(\zeta)d\zeta, \qquad \gamma^{(2)} = \int_0^t \nu^{(2)}(\zeta)d\zeta, \tag{6.18}$$

denote the *relative plastic displacements* in the normal and shear directions, respectively. The traction-separation behavior we assume here is shown in Fig. 6-3. In both the normal and the shear directions, the flow resistances $s^{(i)}$ are taken to be constant before the corresponding plastic displacements $\gamma^{(i)}$ reach critical values $\gamma_c^{(i)}$. However, the initial values for $s^{(i)}$, denoted $s_0^{(i)}$, are taken to be a function of the initial loading angle (cf. (6.4)) at time $t = 0$,

$$\beta_0 = \beta(t = 0), \tag{6.19}$$

which can be written as

$$s_0^{(i)} = \hat{s}_0^{(i)}(\beta_0). \tag{6.20}$$

Thereby we introduce a simple dependence of the flow resistance on the loading angle, i.e. a *dependence on mode mixity.* We assume that the parameter $\gamma_c^{(i)}$ also depends on β_0:

$$\gamma_c^{(i)} = \hat{\gamma}_c^{(i)}(\beta_0). \tag{6.21}$$

After the interface reaches $\gamma_c^{(i)}$, the flow resistance $s^{(i)}$ linearly decreases until it reaches a value of zero when the plastic displacement reaches its failure value $\gamma_f^{(i)}$.The quantity $\gamma_f^{(i)}$ is again assumed to be a function of β_0:

$$\gamma_f^{(i)} = \hat{\gamma}_f^{(i)}(\beta_0). \tag{6.22}$$

Note that since β_0 is the loading angle at *zero time*, at a given material point, the values for $\hat{s}_0^{(i)}(\beta_0)$, $\hat{\gamma}_c^{(i)}(\beta_0)$, and $\hat{\gamma}_f^{(i)}(\beta_0)$ are therefore set *for all times* at $t = 0$. We point out the possibility that this specific form of mode-mixity dependence may have to be modified in the future if one needs to account for a *(significant) change in loading angle during the deformation history.*

Referring back to Fig. 6-3, we have

$$s^{(i)}(\gamma^{(i)}, \beta_0) = s_0^{(i)}(\beta_0) \qquad \text{for} \quad \gamma^{(i)} \leq \gamma_c^{(i)}(\beta_0), \qquad i = 1, 2, \tag{6.23}$$

and consequently

$$\dot{s}^{(i)}(\nu^{(i)}, \gamma^{(i)}, \beta_0) = 0 \qquad \text{for} \quad \gamma^{(i)} \leq \gamma_c^{(i)}(\beta_0), \qquad i = 1, 2. \tag{6.24}$$

since β_0 is constant. Considering (6.15), (6.24) gives that

$$h^{(11)}(\beta_0) = 0, \quad h^{(12)}(\beta_0) = 0 \qquad \text{for} \quad \gamma^{(1)} \leq \gamma_c^{(1)}(\beta_0), \tag{6.25}$$

$$h^{(21)}(\beta_0) = 0, \quad h^{(22)}(\beta_0) = 0 \qquad \text{for} \quad \gamma^{(2)} \leq \gamma_c^{(2)}(\beta_0). \tag{6.26}$$

Next, the desired linear softening shown in Fig. 6-3 is described by

$$s^{(i)}(\gamma^{(i)}, \beta_0) = s_0^{(i)}(\beta_0) \left(\frac{\gamma_f^{(i)}(\beta_0) - \gamma^{(i)}}{\gamma_f^{(i)}(\beta_0) - \gamma_c^{(i)}(\beta_0)} \right) \qquad \text{for} \quad \gamma_c^{(i)}(\beta_0) < \gamma^{(i)} \leq \gamma_f^{(i)}(\beta_0), \qquad i = 1, 2, \tag{6.27}$$

which means that

$$\dot{s}^{(i)}(\nu^{(i)}, \gamma^{(i)}, \beta_0) = -\frac{s_0^{(i)}(\beta_0)}{\gamma_f^{(i)}(\beta_0) - \gamma_c^{(i)}(\beta_0)} \nu^{(i)} \qquad \text{for} \quad \gamma_c(\beta_0)^{(i)} < \gamma^{(i)} \leq \gamma_f^{(i)}(\beta_0), \qquad i = 1, 2, \tag{6.28}$$

since from (6.18)

$$\dot{\gamma}^{(1)} = \nu^{(1)}, \qquad \dot{\gamma}^{(2)} = \nu^{(2)}. \tag{6.29}$$

Then, from (6.15) and (6.28),

$$h^{(11)}(\beta_0) = -\frac{s_0^{(1)}(\beta_0)}{\gamma_f^{(1)}(\beta_0) - \gamma_c^{(1)}(\beta_0)} \quad \text{and} \quad h^{(12)}(\beta_0) = 0 \qquad \text{for} \quad \gamma_c^{(1)}(\beta_0) < \gamma^{(1)} \leq \gamma_f^{(1)}(\beta_0), \tag{6.30}$$

$$h^{(22)}(\beta_0) = -\frac{s_0^{(2)}(\beta_0)}{\gamma_f^{(2)}(\beta_0) - \gamma_c^{(2)}(\beta_0)} \quad \text{and} \quad h^{(21)}(\beta_0) = 0 \qquad \text{for} \quad \gamma_c^{(2)}(\beta_0) < \gamma^{(2)} \leq \gamma_f^{(2)}(\beta_0). \tag{6.31}$$

A simple time-integration procedure for an interface constitutive model of this type is given in Su et al. [98] and also summarized in the Appendix. Using this procedure, we implemented our model in ABAQUS/Explicit [93] as a *user-material subroutine for cohesive elements.*[3]

6.2.2 Fracture energy

A quantity of central importance in the delamination process is the *interfacial fracture energy*, which is the energy that is dissipated during delamination; this fracture energy is denoted G_c and can be calculated as

$$G_c = G_{Ic} + G_{IIc}, \tag{6.32}$$

[3]In Su et al. [98], the interface model is numerically implemented in ABAQUS/Explicit as a user *interface* as opposed to a user *material*. A user interface in ABAQUS always requires a numerical *contact definition* for the two bodies which together form the interface, and this contact may cause numerical difficulty. If the two bodies are joined by cohesive elements, though, no contact definition has to be made. For this reason cohesive elements were chosen for the numerical implementation in this work.

where G_{Ic} and G_{IIc} are the contributions from modes I and II, respectively. These *mode-I and mode-II interfacial fracture energies* are simply equal to the area under the corresponding curve in Fig. 6-3; accordingly, they can be calculated as

$$G_{\mathrm{Ic}} = \frac{\left(s_0^{(1)}\right)^2}{2K_N} + s_0^{(1)}\gamma_c^{(1)} + \frac{s_0^{(1)}}{2}\left(\gamma_f^{(1)} - \gamma_c^{(1)} - \frac{s_0^{(1)}}{K_N}\right), \tag{6.33}$$

$$G_{\mathrm{IIc}} = \frac{\left(s_0^{(2)} - \mu t_N\right)^2}{2K_T} + \left(s^{(2)} - \mu t_N\right)_0 \gamma_c^{(2)} + \frac{s_0^{(2)} - \mu t_N}{2}\left(\gamma_f^{(2)} - \gamma_c^{(2)} - \frac{s_0^{(1)} - \mu t_N}{K_T}\right), \tag{6.34}$$

where the expression for G_{IIc} is written for *constant* t_N. (6.33) and (6.34) can be simplified to read

$$G_{\mathrm{Ic}} = \tfrac{1}{2} s_0^{(1)}\left(\gamma_c^{(1)} + \gamma_f^{(1)}\right), \tag{6.35}$$

$$G_{\mathrm{IIc}} = \tfrac{1}{2}\left(s_0^{(2)} - \mu t_N\right)\left(\gamma_c^{(2)} + \gamma_f^{(2)}\right), \tag{6.36}$$

with (6.36) again for constant t_N.

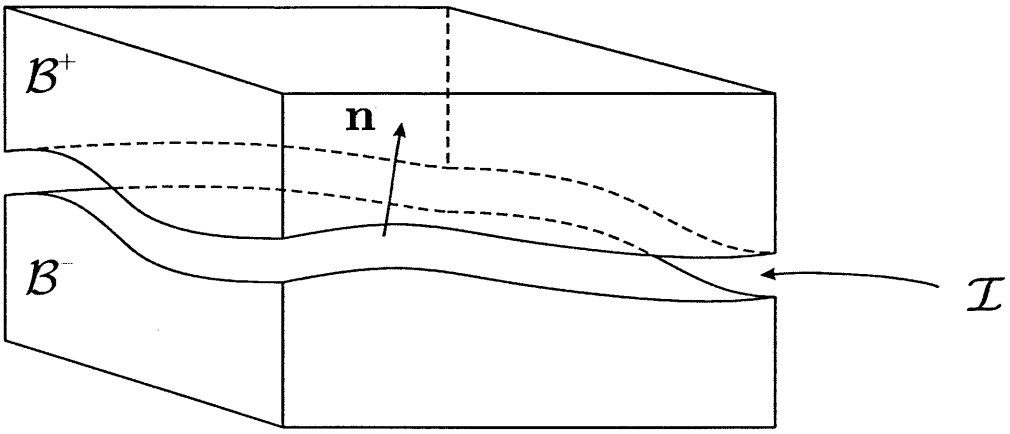

Figure 6-1: Schematic of interface between two bodies $\mathcal{B}^+$ and $\mathcal{B}^-$.

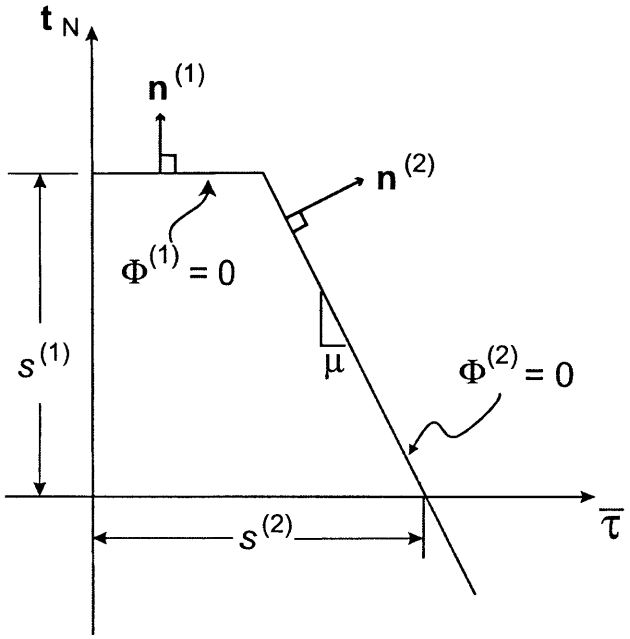

Figure 6-2: Schematic of yield surfaces for the normal and shear mechanisms. From Su et al. [98].

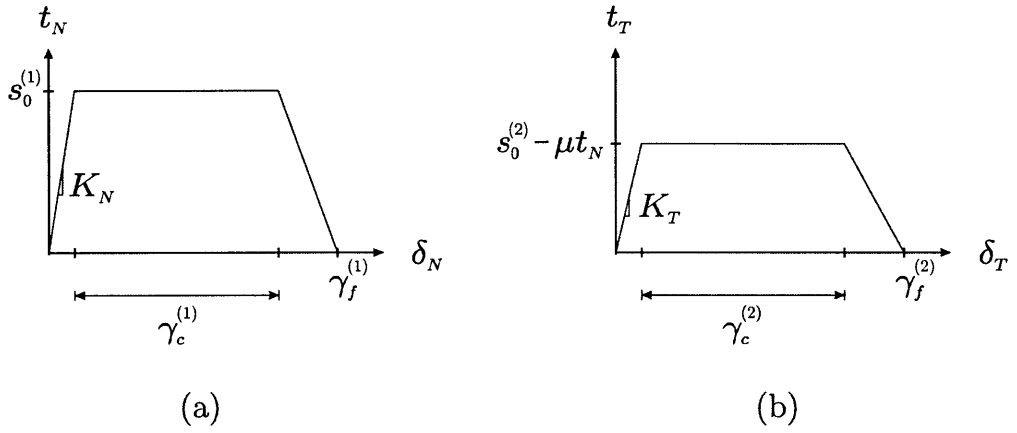

Figure 6-3: Traction-separation behavior in the (a) normal and (b) shear directions. Note that in (b), the normal traction t_N is taken to be constant.

Chapter 7

Application of the interface model to the top-coat/TGO interface in a plasma-sprayed TBC system

7.1 Material parameter calibration

In this Chapter, we discuss the application of the interface constitutive model summarized in Chapter 6 to the top-coat/TGO interface in TBC systems. As discussed before, the properties of this interface are generally expected to be a function of high-temperature exposure time. Here, as a first step, *we only consider the as-sprayed condition*, in which specimens have not yet been thermally exposed, and accordingly *do not consider such a variation of the material parameters with time.*

As was pointed out, the *investigation of the dependence of interface strengths on mode mixity* has recently become an important focus in the experimental investigation of TBC system failure [cf., e.g., 59]; for this reason several material parameters were chosen to depend on mode mixity in Section 6.2. However, to the knowledge of the authors there are no conclusive experimental results in the literature on the exact nature of this dependence. For now, we therefore assume in this work that there is *no mode-mixity dependence of any of the material parameters.* (This assumption may need to be modified in the future as more experimental evidence becomes available.) Thus, we have that

$$\hat{s}_0^{(i)}(\beta_0) = s_0^{(i)} = \text{ const.}; \qquad \hat{\gamma}_c^{(i)}(\beta_0) = \gamma_c^{(i)} = \text{ const.}; \qquad \hat{\gamma}_f^{(i)}(\beta_0) = \gamma_f^{(i)} = \text{ const.} \tag{7.1}$$

For the interface, we therefore need numerical values for the following parameters: the stiffnesses K_N and K_T; the (constant) resistances $s_0^{(i)}$; the (constant) critical and failure plastic displacements $\gamma_c^{(i)}$ and $\gamma_f^{(i)}$; and the friction coefficient μ. *In this work, for simplicity we set* $\mu = 0$. The remaining properties were determined by simulating two *calibration experiments*: one is the mode-II delamination test performed as part of this work, and the other one is the *asymmetric bend test* by Zhao et al. [119]. These experiments were simulated, and the material parameters were *adjusted until reasonable agreement is obtained.* Note that with our assumption that there is no mode mixity dependence of the material parameters, we

need at least two calibration experiments to determine the constitutive behavior in shear and in tension; as its name implies, the mode-II delamination test is dominated by the response in shear, and for this simulation, even a considerable change in the tension properties would not affect the simulation result very strongly. Therefore, we also simulate the asymmetric bend test, in which the interface is *loaded in a mixed mode*, i.e. both in shear and in tension. Due to the additional significant presence of tension in this latter experiment, we are able in this way to determine the tension-related material properties. The two calibration experiments and simulations are discussed in detail in the upcoming two Sections.

Apart from the interface constitutive behavior, we also need to describe the constitutive behavior of the bulk material. In this regard, we note that as pointed out by Rabiei and Evans [85], there is a thin TGO layer (< 0.5 μm) even in the as-sprayed condition. However, since this TGO thickness is small compared with all other dimensions, in this work we *choose to neglect the TGO layer.*[1] (The interface we are considering in the particular case here thus effectively becomes the "top-coat/bond-coat interface", with no TGO in between.)

Finally, in the two bend experiments, use is made of metallic *stiffeners* glued onto the top coat to produce the desired stress distribution and delamination. The constitutive behavior of these stiffeners, as well as the adhesive used to bond the stiffeners to the top coat, needs to be specified as well.

Consequently, the bulk material consists of (i) top coat, (ii) bond coat, (iii) substrate, and (for the bend tests) (iv) stiffeners and (v) adhesive. In the three experiments considered in this work, the top coat consisted of plasma-sprayed yttria-stabilized zirconia; the bond coat was deposited by plasma spray, and of either NiCoCrAlY or NiCrAlY composition; and the substrate was the Ni-based superalloy Inconel 718 (mode-II delamination and notched bend test) or a Q235 steel (asymmetric bend test). The stiffeners were either also made of Inconel 718 (notched bend test) or stainless steel (asymmetric bend test); and for both bend tests, an epoxy adhesive was used.

First, the bond coat, substrate, and stiffeners are taken to be linearly elastic since in all cases considered here, the metal parts are always below their yield strength. Secondly, for the top coat, while it is known that there is some nonlinearity in its behavior even at room temperature [cf., e.g., 6], for simplicity here *we choose to neglect any nonlinearity in the top coat*, and also take it to be linearly elastic. For the same reason, the adhesive, too, is modeled as linear-elastic. The parameters for the bulk materials were taken from Busso et al. [16], Special Metals Corporation [95], and Zhao et al. [119], and are given in Table 7.3.

In the upcoming Sections, we discuss the two calibration experiments and corresponding simulations.

[1] For a detailed description of the deformation and degradation process at the *microlevel*, this simplification cannot be made. Also, as pointed out in Footnote 3, in that case the growth of the TGO, i.e. the oxidation, needs to be taken into account explicitly and not only through a possible change in interface properties.

7.1.1 Mode-II delamination test

In our group, a mode-II delamination experiment on a plasma-sprayed TBC system was conducted by Dr. Haowen Liu.[2] We removed the top coat around a small top coat "island" so that one can move in a tool to shear off this island. A schematic of the test is shown in Fig. 7-1, and an optical micrograph of the test set-up is given in Fig. 7-2; the dark object on the left is the steel tool block, which is blurry because its side edge is not in the focal plane of the microscope. Note that this micrograph is for illustration only as the dimensions of the top-coat island in Fig. 7-2 are not the same as the ones used in the experiment for which the data is given in this work. This is due to the difficulty associated with controlling the diamond saw used for top-coat removal for sub-millimeter dimensions.

The specimen for the test was coated by *air plasma spray* (APS) by Longevity Coatings (Allentown, PA); it consisted of a 2.45 mm thick Inconel 718 alloy substrate, a 0.35 mm thick NiCrAlY bond coat, and a 0.35 mm thick plasma-sprayed yttria-stabilized zirconia (YSZ) top coat. It was cut by waterjet to a width of 3 mm and a length of 20 mm. Next, the top coat was carefully removed around an island which spanned the width of the specimen and had a length of 0.26 mm. For the actual experiment we used a micromechanical testing machine designed by Gearing [45] which had a horizontal force capacity of 20 N; the entire apparatus is shown in Fig. 7-3. The actuator of the machine was an inchworm. The tool block was moved at a velocity of 5 μm/s, and displacement of the top-coat island relative to the metal was monitored using digital image correlation with Vic2D software from Correlated Solutions, Inc. The specimen was tested until failure.

The experimentally-obtained force-displacement curve is shown in Fig. 7-4. (The displacement in Fig. 7-4 is that of the midpoint of the top-coat island relative to a point located about 175 μm below the top-coat/bond-coat interface.) Due to the very small displacements there is some noise, but an initial nominally elastic stage and a subsequent nonlinear part can clearly be seen. The load eventually forms a plateau, after which failure occurs and all load-carrying capacity is lost.

For the simulation, the finite-element mesh of the domain is shown in Fig. 7-5 along with a detail of the top-coat island. Edges DA and BC are fixed horizontally, and the bottom, i.e. edge AB, is fixed vertically. On the top edge of the tool, the horizontal velocity is prescribed as 5 μm/s, and no vertical motion is allowed.[3] All other edges are traction-free. Between the tool block and the specimen, we allow for contact, which is taken to be frictionless.

The numerical force-displacement curve, along with the experimental one, is shown in Fig. 7-6. Comparing the two, we see that the initial slope in the simulation seems to be slightly stiffer than the experiment, and that in the experiment, rather shortly after the beginning of loading, the curve becomes nonlinear, while the simulation continues to predict linear behavior. Both curves eventually reach a peak load, which is of similar magnitude in simulation and experiment. Due to the longer linear behavior of the simulation, its plateau is somewhat longer than that of the experiment since it needs to "catch up" with

[2]Our experiment is inspired by Xu et al. [111], who conducted a similar test on a TBC system with *flame-sprayed* top coat. (The flame-spray deposition process is different from plasma-spraying in that the particle velocities in flame-spraying are much lower than in plasma-spraying [99].)

[3]The steel tool is modeled as linearly elastic with $E = 200$ GPa and $\nu = 0.3$.

the experimental displacement. Finally, in the experiment failure occurs fairly abruptly, while the simulation undergoes linear softening before the load reaches zero.

For illustration of the deformation process, the left end of the top-coat/bond-coat interface, labeled as "E" in Fig. 7-5b, is shown at four different stages of the simulation in Fig. 7-7. The four stages are also labeled correspondingly in Fig. 7-6. Before loading (stage (i)) the cohesive elements are not visible as they have zero thickness and are completely undeformed. As the loading is applied (stages (ii) and (iii)), the pictured cohesive elements deform in shear and also in tension. (The tension stems from the fact that the tool, while shearing the island, also applies a moment to it, which has to be balanced by tension and compression at the left and right ends, respectively, of the interface.) Finally, after failure of the interface in shear (stage (iv)), the top coat is permanently displaced horizontally from the bond coat, and the normal displacement has vanished.

7.1.2 Asymmetric four-point bend test

As a second calibration experiment, in our group an *asymmetric bend test* was conducted by Dr. Haowen Liu and Claudio Di Leo.[4] A schematic of the specimen is shown in Fig. 7-8, and the experimental set-up is depicted in Fig. 7-9. The coating on the specimen was also deposited by APS by Longevity Coatings. The substrate was a 2.96 mm thick Inconel 718 alloy; furthermore, a 0.35 mm thick NiCrAlY bond coat, a 0.35 mm thick plasma-sprayed YSZ top coat, and a 0.91 mm thick Aluminum stiffener were used. The stiffener was glued onto the top coat with an epoxy-based adhesive whose thickness was estimated to be less than ten microns.

For the experiment we used a micromechanical testing machine designed by Gudlavalleti et al. [47] which had a vertical force capacity of 86 N. The experiment was conducted in load control at a loading rate of 0.043 N/s, and the relative roller displacement was again measured by digital image correlation.

The experimental curve of load versus roller displacement is shown in Fig. 7-10. Examining this data, we see that there is first a linear region before initial cracking occurs between 20 and 25 N, which is manifested by a pronounced kink in the load-displacement curve.[5] After crack initiation, the crack continues to propagate, and the specimen continues to deform while the load increases due to the remaining stiffness of the partially cracked sample.

For the simulation, the finite-element mesh is shown in Fig. 7-11. Due to the small thickness of the adhesive layer, it was not explicitly included in the simulation. The numerical and experimental load-displacement curves are given in Fig. 7-12; comparing the two, we note that the simulation is able to capture the experimental behavior reasonably well. Also, in Fig. 7-13, the cracked geometry at the end of the test is shown both in the experiment as well as in the simulation, and reasonable agreement can be observed.

[4]Our experiment is inspired by Zhao et al. [119], who conducted a similar test.

[5]The stiffness at the very beginning of loading, i.e. at a load of less than 2 N, is believed to be reduced due to initial settling of the specimen between the top and bottom rollers.

7.1.3 Calibrated parameters. Interface fracture energy

The calibrated material parameters are shown in Tables 7.1 and 7.2; as mentioned before, they were obtained by running the two calibration simulations *several times with different parameters* until reasonable agreement *in both experiments* was obtained.

From the calibrated parameters, it is possible to calculate the *interface fracture energies* in tension and shear. From (6.35) and (6.36) (with $\mu = 0$), they amount to

$$G_{\mathrm{Ic}} = 41 \text{ J/m}^2, \qquad G_{\mathrm{IIc}} = 49 \text{ J/m}^2, \tag{7.2}$$

and from (6.32), the total fracture energy is then given by

$$G_{\mathrm{c}} = G_{\mathrm{Ic}} + G_{\mathrm{IIc}} = 90 \text{ J/m}^2. \tag{7.3}$$

In the literature, interface fracture energies were mostly determined through an analysis using *linear-elastic fracture mechanics*, and published values range from as low as $G_{\mathrm{c}} = G_{\mathrm{Ic}} + G_{\mathrm{IIc}} = 40$ J/m^2 [121] to as high as $G_{\mathrm{IIc}} = 260$ J/m^2 [111] and thus implying $G_{\mathrm{c}} > G_{\mathrm{IIc}} = 260$ J/m^2. Thus, our calibrated total fracture energy of $G_{\mathrm{c}} = 90$ J/m^2 lies within these previously reported measurements.

It should be noted that the TBC system on both our calibration specimens was deposited by Longevity Coatings, and that the calibrated material parameters therefore apply *to this specific TBC system.* Our preliminary experiments on specimens that were coated by another source, the State University of New York at Stony Brook, indicate strength values that are considerably higher than the ones for the specimens coated by Longevity Coatings.

With all the material parameters determined, in the next Section we examine how the model is able to *predict* the material behavior in the case of a (symmetric) notched bend test.

7.2 Notched four-point bend test

To examine the predictive capability of our model, we simulated a notched four-point bend test; the corresponding experiment was performed by Zhao et al. [121]. Their specimen consisted of an Inconel 718 alloy substrate, a NiCoCrAlY bond coat, a plasma-sprayed YSZ top coat, and a stiffener (also made of Inconel 718) glued onto the top coat. The thicknesses of bond coat, top coat, and adhesive were 150 microns, 200 microns, and 100 microns, respectively. After gluing, the notch was introduced through the entire stiffener and top coat, up to the top-coat/bond-coat interface.

The experimental curve of load vs. roller displacement is shown in Fig. 7-14. The load first increases almost linearly up to a load of about 150 N, at which point the curve becomes nonlinear and then goes through a peak at about 170 N. During this peak the interface crack at the top-coat/bond-coat interface is believed to initiate. After the peak the load again falls below 150 N, where it stabilizes and then slightly increases again.[6]

[6]Zhao et al. [121] briefly mention the introduction of a "pre-crack" in their paper, but they do not specify further details such as how far any such pre-crack propagated. To the authors the experimental load-displacement behavior as shown in Fig. 7-16 with the prominent local peak seems only plausible if there

For the simulation, the finite-element mesh and dimensions of the simulated geometry are shown in Fig. 7-15. Due to symmetry only one-half of the specimen was simulated. Consequently, symmetry boundary conditions were applied on edge DE, and all other edges were traction-free. The rollers were modeled as analytical surfaces, and contact between rollers and specimen was again taken to be frictionless.

The numerically-simulated and experimentally-observed curves are shown in Fig. 7-16. The numerically-simulated curve starts out with a linear increase in load. At just above 170 N, the load also goes through a peak, which corresponds to interface failure at the top-coat/bond-coat interface right by the notch. A decrease in load of about 10 N follows. The interface crack starts to stably propagate, first at an approximately constant load and then with the load again starting to slightly increase due to the bending stiffness of the partially cracked specimen. For illustration of the deformation, a deformed beam is shown in Fig. 7-17; cohesive elements that have failed were removed from the plot.[7]

Comparing simulation and experiment, we note that they both show a similar qualitative response with an initial nominally elastic stage, followed by a load peak at crack initiation, a load plateau when the crack first propagates, and an eventual slight increase in the load due to the the remaining stiffness of the partially cracked specimen. Quantitatively, the initial slope of the simulation is, as observed for the other experiments, again larger than the simulated one by a small amount. For the *load at crack initiation* (the local load peak), there is fairly good agreement; however, the simulated load drop occurs more suddenly and is less in value than in the experiment, and the load plateau in the simulation is also shorter than experimentally measured.

In conclusion, given that the experimental notched bend specimen was manufactured by another entity than the mode-II delamination and asymmetric bend specimens (and material properties related to the top coat and top-coat/bond-coat interface generally exhibit a large amount of scatter [cf., e.g., 111]), we believe that the reasonable qualitative agreement in overall behavior between simulation and experiment, and the close quantitative agreement in load at crack initiation, is encouraging and shows that our model and simulation capability represent a first step in the right direction for modeling the failure of macroscopic thermal-barrier-coated components.

---

is no significant pre-crack in the sample. For this reason, we assume here that if there was any pre-crack which was introduced in the experiment, its length is small, and we therefore *neglect any such small pre-crack that might have been present.*

[7] At crack initiation, the simulated displacement is less than 50 μm as can be seen from Fig. 7-16. When the crack initiates, the specimen is only very slightly bent; for this reason we show the deformed beam at the larger displacement of 400 μm.

Table 7.1: Elastic interface material properties.

K_N (GPa/μm)	K_T (GPa/μm)
10	10

Table 7.2: Inelastic interface material properties.

$s_0^{(1)}$ (MPa)	$s_0^{(2)}$ (MPa)	$\gamma_c^{(1)}$ (μm)	$\gamma_c^{(2)}$ (μm)	$\gamma_f^{(1)}$ (μm)	$\gamma_f^{(2)}$ (μm)	μ
15	10	2.5	3.5	3.0	6.3	0

Table 7.3: Bulk material properties.

	Young's modulus, E (GPa)	Poisson's ratio, ν
Top coat	37	0.18
Bond coat	200	0.30
Inconel 718	200	0.30
Q235 steel	200	0.30
Stainless steel	200	0.30
Epoxy adhesive	2.5	0.30

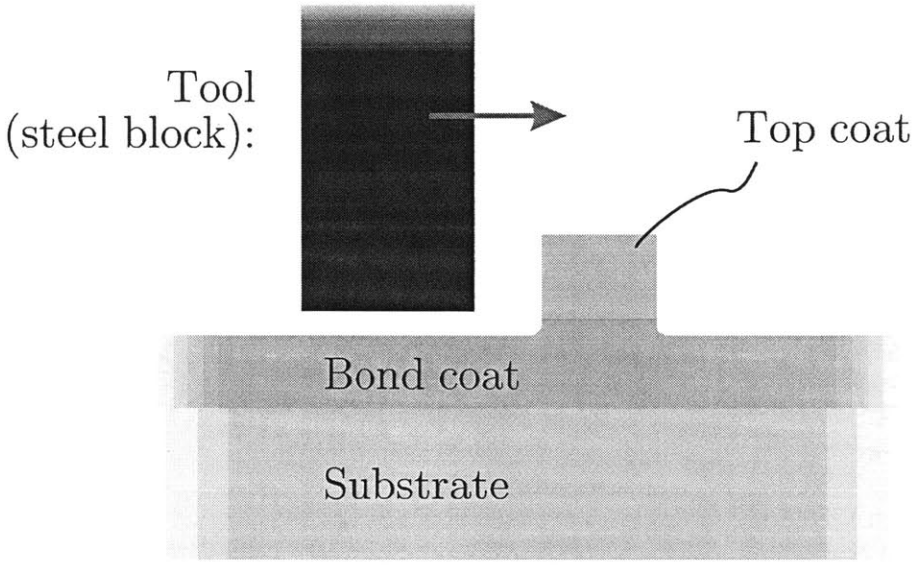

Figure 7-1: Schematic of the shear-delamination test.

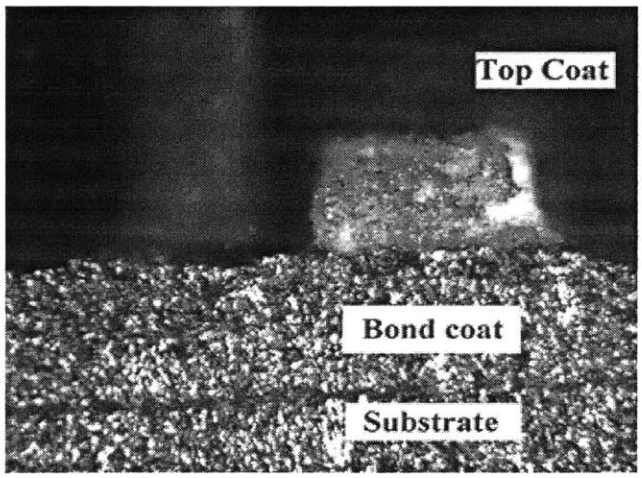

Figure 7-2: Optical micrograph of the top-coat island for the mode-II delamination experiment. Note that this micrograph is for illustration only as the dimensions of the top-coat island are not the same as the ones used in the experiment for which the data is given here (see text).

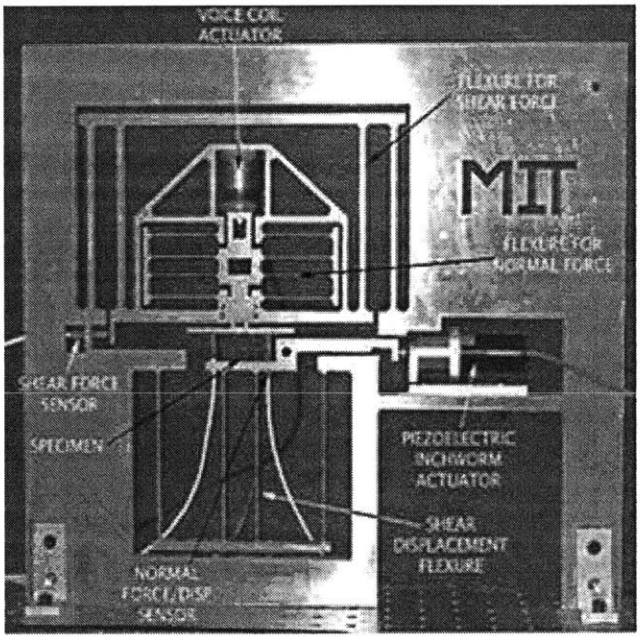

Figure 7-3: Micromechanical testing apparatus used for the mode-II delamination experiment; from Gearing [45].

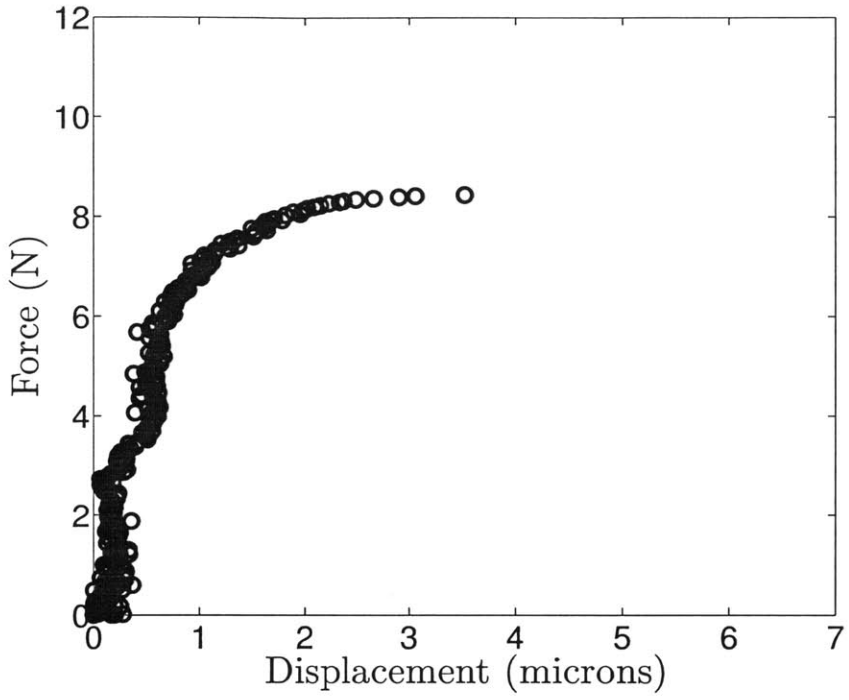

Figure 7-4: Experimental force-displacement curve for the mode-II delamination test.

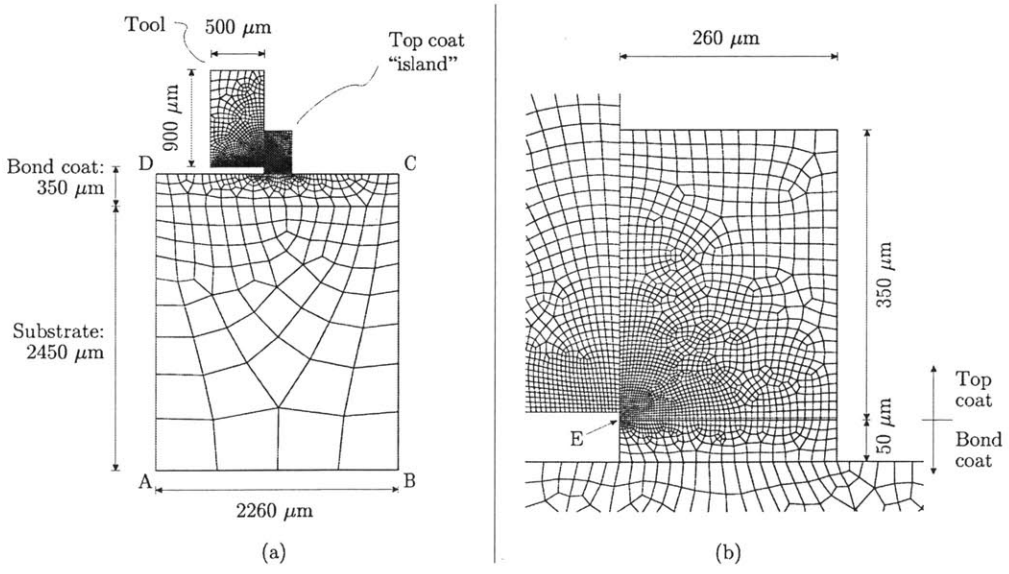

Figure 7-5: Finite-element mesh and dimensions for the mode-II delamination simulation: (a) overview and (b) detailed view of the top-coat island.

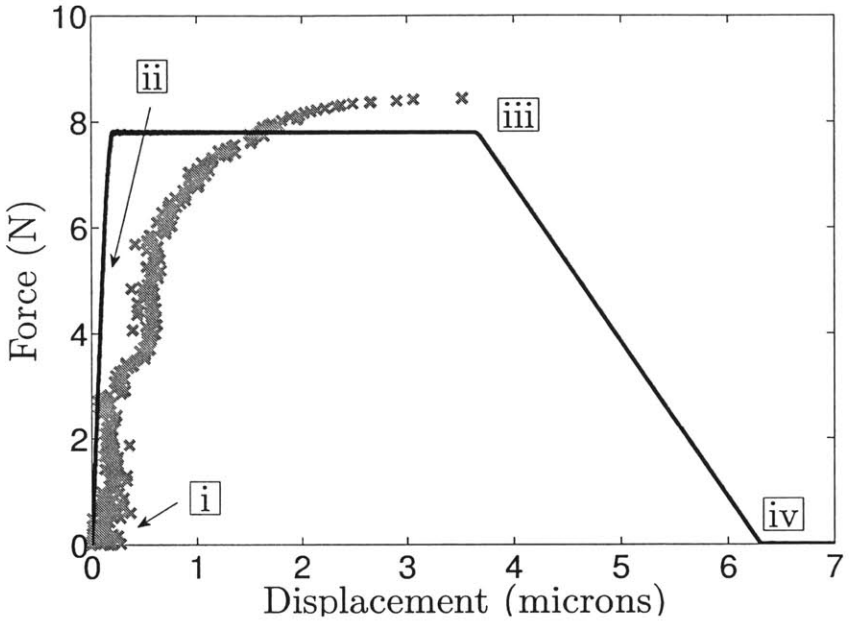

Figure 7-6: Force-displacement curves for the mode-II delamination experiment. Line: simulation; crosses: experiment. The numerals correspond to the labels in Fig. 7-7.

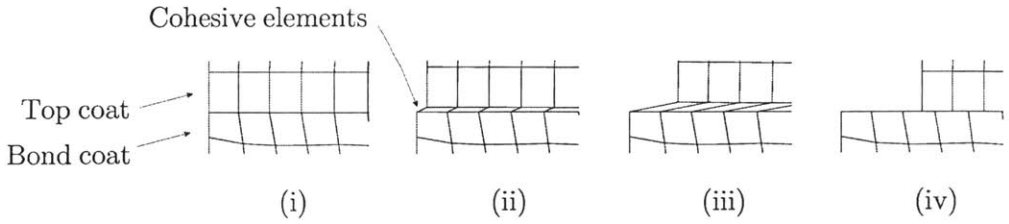

Figure 7-7: Left end of the top-coat/bond-coat interface (labeled "E" in Fig. 7-5b) at various stages during the simulation.

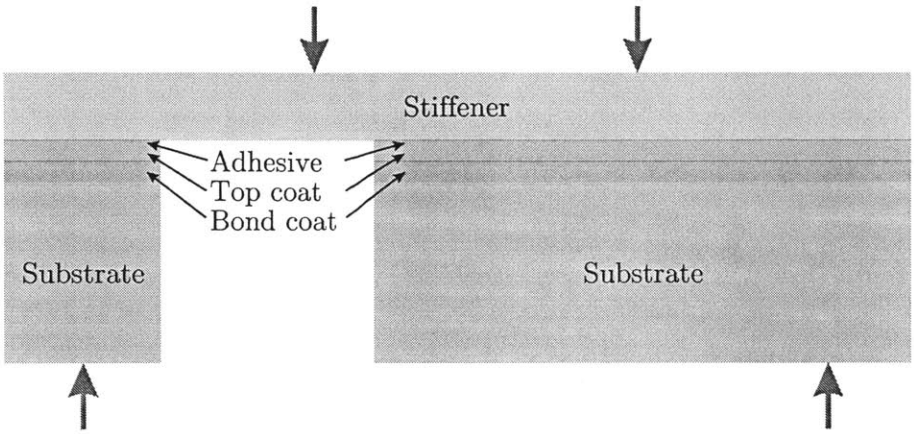

Figure 7-8: Schematic of the asymmetric bend test.

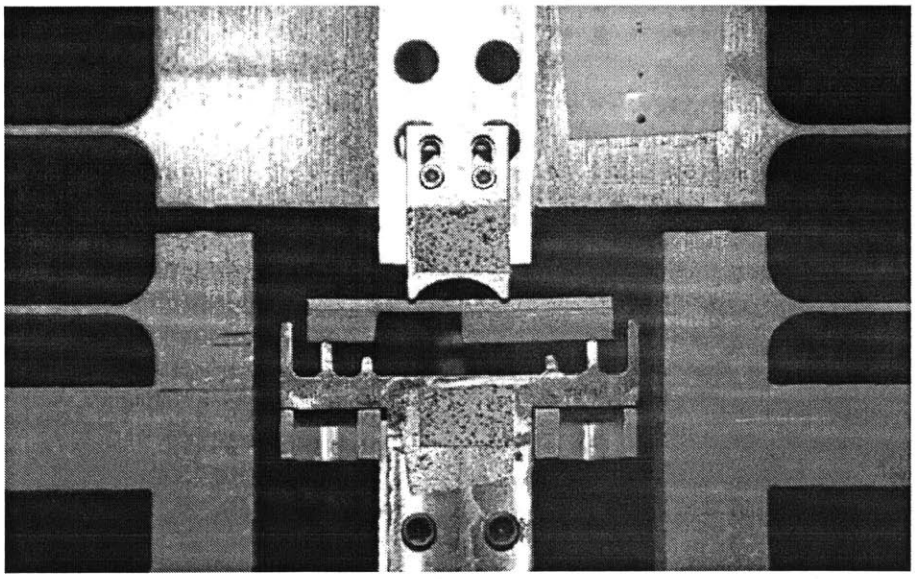

Figure 7-9: Experimental set-up for the asymmetric bend test.

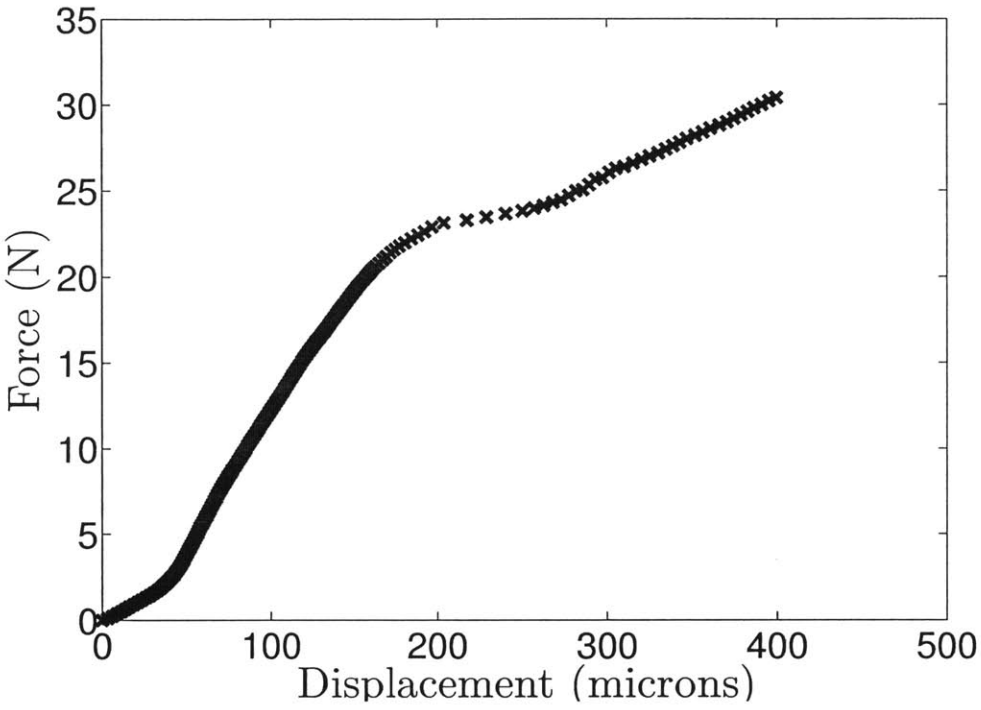

Figure 7-10: Experimental curve of load vs. roller displacement in the asymmetric bend test.

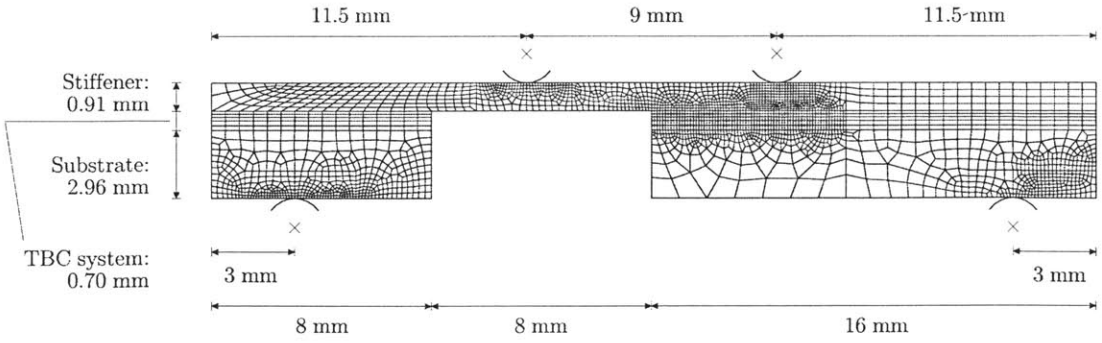

Figure 7-11: Finite-element mesh for the asymmetric beam simulation.

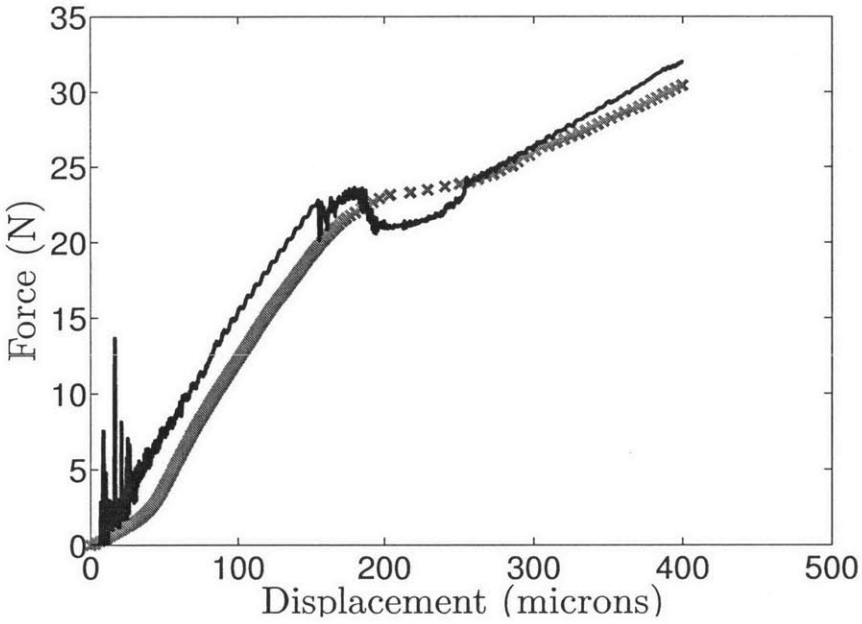

Figure 7-12: Load vs. roller displacement for the asymmetric beam test. Line: simulation; crosses: experiment.

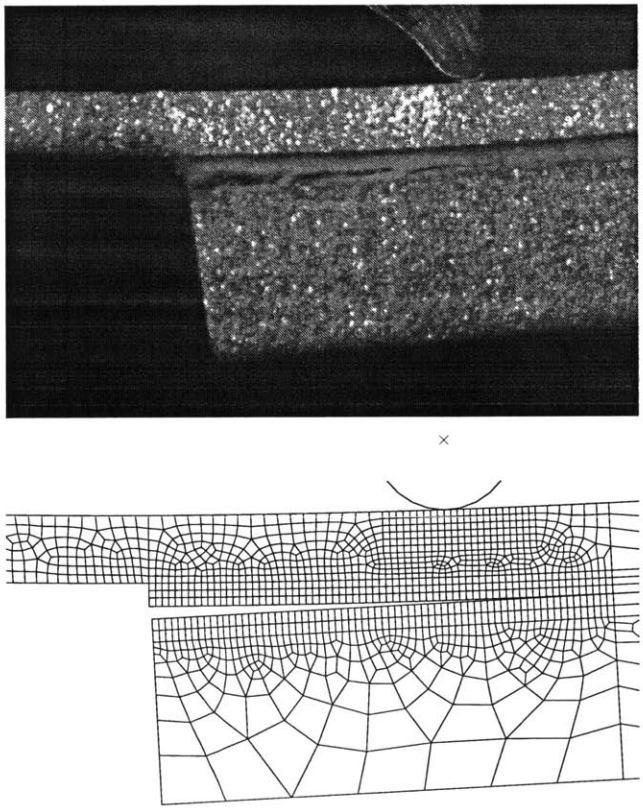

Figure 7-13: Zoom-in image on cracked geometry at the end of the experiment (top) and in the simulation (bottom).

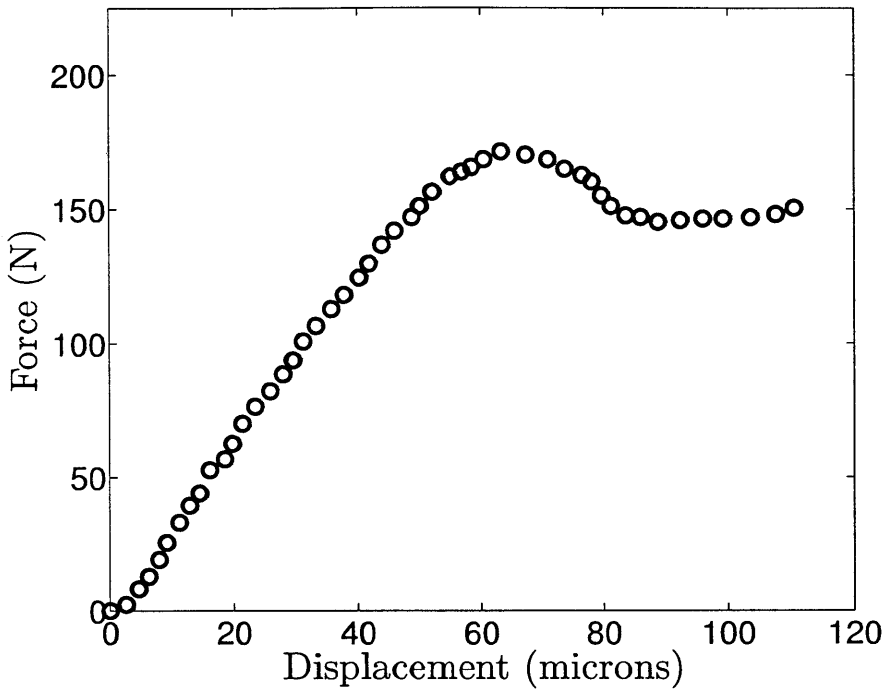

Figure 7-14: Experimental curve of force vs. roller displacement for the notched four-point bend test by Zhao et al. [121].

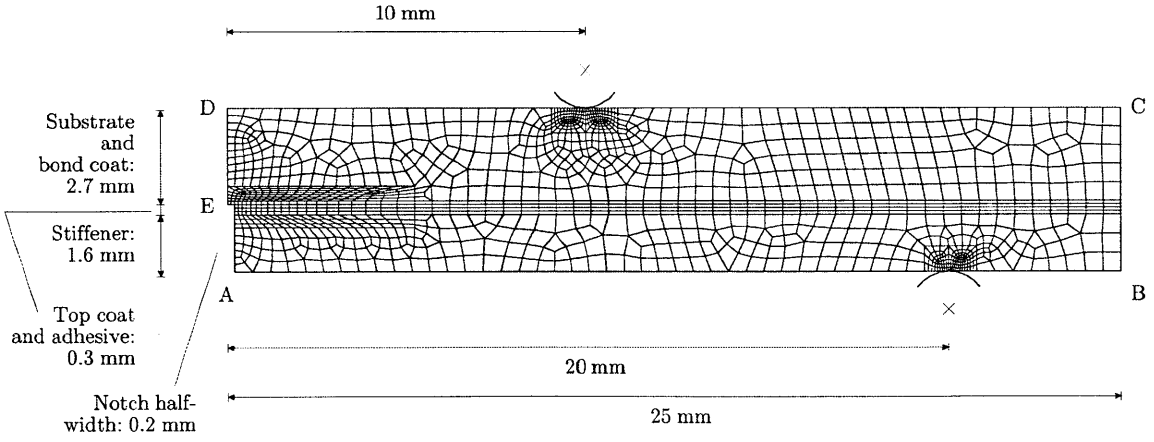

Figure 7-15: Finite-element mesh and dimensions for the notched four-point bend simulations.

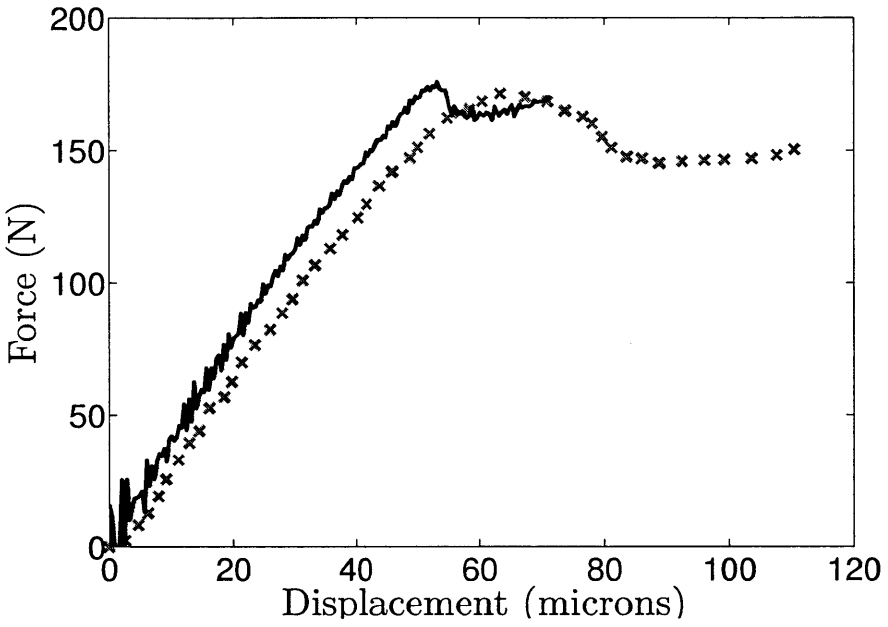

Figure 7-16: Force-displacement curves for the notched four-point bend simulations. Line: simulation; crosses: experiment.

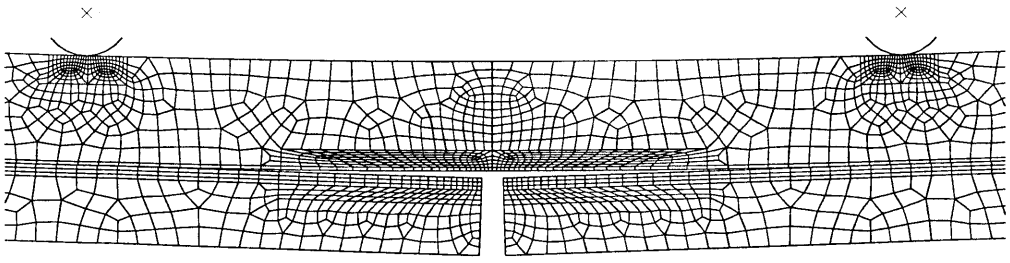

Figure 7-17: Deformed finite-element mesh of the beam at a displacement of 400 μm. Failed cohesive elements were removed from the plot.

Part III

Concluding remarks, future work, and bibliography

Chapter 8

Concluding remarks

Thermal barrier coating (TBC) systems are applied to superalloy turbine blades to provide thermal insulation and oxidation protection. A TBC system consists of (a) an outer oxide layer (top coat) that imparts thermal insulation, and (b) a metallic layer (bond coat) that affords oxidation protection for the substrate through the formation of a second, protective oxide layer. This bond-coat oxidation is the *intrinsic mechanism which controls the mechanical integrity of the TBC system* since the oxidation is accompanied by a large, anisotropic volumetric change on the order of 30 percent. In order to gain an understanding of this microscale degradation process induced by oxidation, an essential requisite is a *constitutive model for high-temperature metal oxidation* that describes the coupled phenomena of (a) diffusion of oxygen, (b) oxidation with accompanying anisotropic volume change, (c) thermo-elasto-viscoplastic deformations that may be locally large, and (d) transient heat conduction. In this thesis we have formulated a continuum-level, chemo-thermo-mechanically coupled, thermodynamically-consistent theory which integrates these various nonlinear phenomena. We have numerically implemented our coupled theory in a finite-element program, and we have also calibrated the material parameters in our theory for an Fe-22Cr-4.8Al-0.3Y heat-resistant alloy experimentally studied by Tolpygo et al. [102, 103]. Using our theory we have simulated the high-temperature oxidation of thin sheets of FeCrAlY, and have shown that our theory is capable of reproducing the oxide thickness evolution with time at different temperatures, the permanent extensional changes in dimensions of the base material being oxidized, as well as the development of large compressive residual stresses in the protective surface oxide which forms.

As an application of this numerical simulation capability, we have also considered the oxidation of an FeCrAlY sheet with an initial groove-like surface undulation of a depth of about 5 microns, a geometry which has been experimentally studied by Davis and Evans [30]. We have shown our numerical simulations to reproduce (with reasonable accuracy) the shape-distortion of the groove upon oxidation, measured by these authors.

For the consideration of *macroscopic* thermal-barrier-coated components, a limitation of this type of model is that numerical simulations quickly become very challenging due to the sub-micron resolution of the required mesh. In a second part of this thesis, we have therefore presented a framework that facilitates simulations of macroscopic components by noting that the macroscopic effect of oxidation is simply to degrade some mechanical properties in the TBC system. In this framework oxidation is thus *not modeled explicitly*, but only indirectly

manifested by *changing the resistance of the TBC system to spallation.* We have implemented this model in an explicit finite-element program, applied it to a failure-prone interface in a plasma-sprayed TBC system, and calibrated the material parameters appearing in our theory. We finally showed that the model is capable of predicting with reasonable accuracy the load at which crack initiation occurs in a notched four-point bend test experimentally studied in the literature, as well as the overall qualitative load-displacement behavior in this test.

Chapter 9

Future work

In our discussion of future work, we follow the same avenue as previously in this thesis: we first examine next steps in research on the *microscale process of high-temperature oxidation* and its ramifications for failure of TBC systems, and then consider the next steps that need to be taken in research on degradation and failure of *macroscopic* thermal-barrier-coated components.

9.1 Modeling of high-temperature oxidation and its role in failure of TBC systems

- In this thesis, we have shed light on how stresses and deformations arise in high-temperature oxidation, which is known to be the cause for the ultimate failure of TBC systems. In our microscale investigation, we have focussed on the *oxidizing bond coat*. An important next step is to consider in detail the material behavior of the *top coat*, and how it affects the overall performance of the TBC system. Specifically, plasma-sprayed top coats display some non-linear mechanical behavior even at room temperature [cf., e.g., 6], and there is considerably more **top-coat creep** at elevated temperatures. In addition, the ceramic top coat is known to *sinter* considerably in the earlier stages of high-temperature exposure, and this **top-coat sintering** strongly affects material behavior [cf., e.g., 16]; in a top-coat constitutive model, it should be accounted for as well.

- In conjunction with a suitable model for the top coat, our chemo-thermo-mechanically coupled model can be used to simulate degradation and failure of TBC systems at the microscale, as was done in the imperfection simulation discussed in Chapter 5. (There, as a simple demonstration, the top coat was considered purely elastic.) One then also needs to prescribe the constitutive behavior of the failure-prone top-coat/TGO interface; since the chemo-thermo-mechanically coupled theory is implemented in the *implicit* program Abaqus/Standard as a user element (UEL), it may be necessary to numerically implement a traction-separation law as a **user material for cohesive elements in Abaqus/Standard (UMAT)** as opposed to the one in Abaqus/Explicit (VUMAT) used in this thesis.

- As discussed in Chapter 5, a considerable effort in the literature has been made to consider a *unit-cell geometry* of an undulated interface in a TBC system. An important next step is to simulate **geometries that contain more than just a single unit cell**. While it is not the goal of such a step to be able to simulate macroscopic components as discussed in Part II of this thesis (as it would be too computationally expensive), the simulation of *larger and more complex microscale geometries* will further illuminate how degradation and failure occur *locally*.

- Furthermore, it is not only the *interface(s)* in the TBC system which can fail; another failure mechanism is the development of cracks in the top coat that are *perpendicular* to the layer structure – "mud cracks" [cf., e.g., 23]. Such degradation behavior might be suitably modeled with a **continuum damage model for the top coat**. The behavior of the entire TBC system can then be simulated using our chemo-thermo-mechanically coupled model for oxidation, along with the damage model for the top coat.

- Another failure mechanism for TBC systems is the degradation due to **chemical reactions of the top coat with impurities in the turbine fuel** (such as, for example, vanadium); this phenomenon is broadly known as *hot corrosion* [cf., e.g., 76]. Our chemo-thermo-mechanically coupled model can readily be applied to model such chemical reactions, the associated volume changes, and the consequences on the stress and strain states of the TBC system.

- Yet a different kind of failure of TBC systems is induced by the **YSZ phase transformation** of the desirable tetragonal-prime phase to the monoclinic phase [107], which causes a volumetric change of 3 to 5 percent. While a phase transformation differs from a chemical reaction in that it is only the crystal structure that changes and not the overall chemical composition, we believe that our chemo-thermo-mechanically coupled theory can be adapted to model this phase transformation of the top coat.

- On a broader perspective, another situation in which the volume change associated with a chemical reaction is of central interest is the **oxidation of metallic "interconnects" in solid-oxide fuel cells** [89]. Our chemo-thermo-mechanically coupled theory and numerical simulation capability can readily be applied to this different setting.

9.2 Degradation and failure of macroscopic thermal-barrier-coated components

As documented in Appendix D, there has been a considerable effort in the Mechanics and Materials community to *experimentally characterize* the macroscopic degradation and failure of plasma-sprayed TBC systems. However, what exists to date is a collection of "isolated" experiments that determine *one* specific property such as a tensile or shear fracture energy, and which were performed on specimens that were manufactured using a wide range of

specific manufacturing conditions (such as spraying parameters). Therefore, the following items are needed:

- A **coherent suite of experiments**, meaning that these experiments together are able to determine *all of the failure-related material properties* of a plasma-sprayed TBC system that was manufactured in a certain way. The following specific types of experiments are deemed most suitable (cf. also Appendix D):
  - **Bend test**: In bending, one can sample different mode mixities by simply changing the position of the load(s). For this reason, bend tests have become increasingly popular in characterizing failure of TBC systems, and they should be used in one or more configurations for model calibration.
  - **Shear-delamination test**: This test is comparatively simple to be performed and tests the TBC system mainly in shear as implied by the name.
  - **Tension test**: In the sense of the discussion in Section D.3.3, we mean a tensile test of the TBC system by gluing a connector on top of the top coat and then pulling on the connector.

  These experiments should be performed on as-sprayed samples as well as ones that have been **thermally exposed** for various times. The mechanical testing can then take place *at room temperature*, since as pointed out by Hutchinson and Hutchinson [59], failure usually occurs during the cool-down process when thermal mismatch stresses are superposed onto the growth stresses, and consequently it is the room-temperature failure-related mechanical properties of the TBC system which are the ones of interest.

- Once the material properties are determined in this fashion, they can serve as an *input* into the *interface constitutive model discussed in Part II of this thesis.* The ultimate goal is then to **use the numerical implementation of the calibrated model to predict the failure behavior** of macroscopic thermal-barrier-coated components in a corresponding validation experiment. For this validation, an **indentation test** on a cross section of the TBC system at the failure-prone top-coat/TGO interface [73, 113] is suitable as the associated deformation is clearly non-homogeneous.

Bibliography

[1] L. Anand. Hencky's approximate strain-energy function for moderate deformations. *Journal of Applied Mechanics*, 46:78–82, 1979.

[2] L. Anand. Constitutive equations for the rate-dependent deformation of metals at elevated temperatures. *Journal of Engineering Materials and Technology*, 1982.

[3] L. Anand. Moderate deformations in extension torsion of incompressible elastic materials. *Journal of the Mechanics and Physics of Solids*, 34:293–304, 1986.

[4] L. Anand and M.E. Gurtin. A theory of amorphous solids undergoing large deformations, with applications to polymeric glasses. *International Journal of Solids and Structures*, 40:1465–1487, 2003.

[5] L. Anand and C. Su. A theory for amorphous viscoplastic materials undergoing finite deformations, with application to metallic glasses. *Journal of the Mechanics and Physics of Solids*, 53:13621396, 2005.

[6] S. Asghari, M. Salimi, and M. Salehi. Modeling nonlinear elastic behavior of plasma sprayed ceramics and its evolution with sintering. *Materials Science and Engineering A*, 527:4241–4249, 2010.

[7] P. Atkins and J. De Paula. *Physical Chemistry, Ninth Edition.* Freeman and Company, 2010.

[8] D.S. Balint and J.W. Hutchinson. An analytical model of rumpling in thermal barrier coatings. *Journal of the Mechanics and Physics of Solids*, 53:949–973, 2005.

[9] D.S. Balint, T.Xu, J.W. Hutchinson, and A.G. Evans. Influence of bond coat thickness on the cyclic rumpling of thermally grown oxides. *Acta materialia*, 54:1815–1820, 2006.

[10] G.I. Barenblatt. The formation of equilibrium cracks during brittle fracture: general ideas and hypotheses; axially symmetric cracks. *Applied Mathematics and Mechanics*, 1959.

[11] T. Besmann. Interface science of thermal barrier coatings. *Journal of Materials Science*, 44:1661–1663, 2009.

[12] M. Bialas. Finite element analysis of stress distribution in thermal barrier coatings. *Surface & Coatings Technology*, 202:6002–6010, 2008.

[13] N. Birks, G.H. Meier, and F.S. Pettit. *High-temperature oxidation of metals, second edition.* Cambridge University Press, 2006.

[14] S.B. Brown, K.H. Kim, and L. Anand. An internal variable constitutive model for hot working of metals. *International Journal of Plasticity*, 1989.

[15] E.P. Busso and Z.Q. Qian. A mechanistic study of microcracking in transversely isotropic ceramic-metal systems. *Acta materialia*, 54:1529–1536, 2006.

[16] E.P. Busso, J. Lin, and S. Sakurai. A mechanistic study of oxidation-induced degradation in a plasma-sprayed thermal barrier coating system. Part I: Life prediction model. *Acta materialia*, 49:1529–1536, 2001.

[17] E.P. Busso, Z.Q. Qian, M.P. Taylor, and H.E. Evans. The influence of bondcoat and topcoat mechanical properties on stress development in thermal barrier coating systems. *Acta materialia*, 57:2349–2361, 2009.

[18] E.P. Busso, H.E. Evans, Z.Q. Qian, and M.P. Taylor. Effects of breakaway oxidation on local stresses in thermal barrier coatings. *Acta materialia*, 58:1242–1251, 2010.

[19] M. Caliez, J.-L. Chaboche, F. Feyel, and S. Kruch. Numerical simulation of ebpvd thermal barrier coatings spallation. *Acta Materialia*, 51:1133–1141, 2003.

[20] P. Camanho and C. Davila. Mixed-mode decohesion finite elements for the simulation of delamination in composite materials. *NASA/TM-2002-211737*, 2002.

[21] N.Y. Cao, Y. Kagawa, and Y.F. Liu. Stress analysis of a barb test for thermal barrier coatings. *Surface and Coatings Technology*, 2008.

[22] M.W. Chase Jr., C.A. Davies, J.R. Downey Jr., D.J. Frurip, R.A. McDonald, and A.N. Syverud. *JANAF Thermochemical Tables.* Dow Chemical USA, 1985.

[23] Z.B. Chen, Z.G. Wang, and S.J. Zhu. Tensile fracture behavior of thermal barrier coatings on superalloy. *Surface and coatings technology*, 2011.

[24] S.A. Chester. *Mechanics of amorphous polymers and polymer gels.* PhD thesis, Massachusetts Institute of Technology, 2011.

[25] R.J. Christensen, D.M. Lipkin, D.R. Clarke, and K. Murphy. Nondestructive evaluation of the oxidation stresses through thermal barrier coatings using Cr^{3+} piezospectroscopy. *Applied Physics Letters*, 69:78–82, 1996.

[26] D.R. Clarke. The lateral growth strain accompanying the formation of a thermally grown oxide. *Acta materialia*, 51:1393–1407, 2003.

[27] D.R. Clarke and C.G. Levi. Materials design for the next generation thermal barrier coatings. *Annual Reviews of Materials Research*, 33:383–417, 2003.

[28] M.C. Cookson. An elastic-plastic interface constitutive model for combined normal and shear loading: application to adhesively bonded joints. Master's thesis, Massachusetts Institute of Technology, 2010.

[29] Instron Corporation. *Microelectronics Testing Solutions: Ultra High Precision Testing Systems - Instron 5848.* 2008.

[30] A. Davis and A.G. Evans. Some effects of imperfection geometry on the cyclic distortion of thermally grown oxides. *"Oxidation of Metals"*, 65:1–14, 2006.

[31] A.W. Davis and A.G. Evans. Effects of bond-coat misfit strains on the rumpling of thermally-grown oxides. *Metallurgical and Materials Transactions*, 37A:2085–2095, 2006.

[32] A.W. Davis and A.G. Evans. Effects of bond-coat misfit strains on the rumpling of thermally-grown oxides. *Metallurgical and Materials Transactions*, 37A:2085–2095, 2006.

[33] E.A. de Souza Neto, D. Peric, M. Dutko, and D.R.J. Owen. Design of simple low order finite elements for large strain analysis of nearly incompressible solids. *International Journal of Solids and Structures*, 1996.

[34] J.T. DeMasi-Marcin, K.D. Sheffler, and S. Bose. Mechanisms of degradation and failure in a plasma-deposited thermal barrier coating. *Journal of Engineering for Gas Turbines and Power*, 112:521–526, 1990.

[35] D.S. Dugdale. Yielding of steel sheets containing slits. *Journal of the Mechanics and Physics of Solids*, 1960.

[36] E. Echsler, D. Renusch, and M. Schutze. Mechanical behaviour of as sprayed and sintered air plasma sprayed partially stabilised zirconia. *Materials Science and Technology*, 2004.

[37] R. Eriksson, H. Brodin, S. Johansson, L. Ostergren, and X.H. Li. Fractographic and microstructural study of isothermally and cyclically heat treater thermal barrier coatings. *Surface and coatings technology*, 2012.

[38] A.G. Evans and J.W. Hutchinson. The mechanics of coating delamination in thermal gradients. *Surface & Coatings Technology*, 201:7905–7916, 2007.

[39] A.G. Evans, D.R. Mumm, J.W. Hutchinson, G.H. Meier, and F.S. Pettit. Mechanisms controlling the durability of thermal barrier coatings. *Progress in Materials Science*, 46:505–553, 2001.

[40] A.G. Evans, D.R. Clarke, and C.G. Levi. The influence of oxides on the performance of advanced gas turbines. *Journal of the European Ceramic Society*, 28:1405–1419, 2008.

[41] A. Feuerstein, J. Knapp, T. Taylor, A. Ashary, A. Bolcavage, and N. Hitchman. Technical and economical aspects of current thermal barrier coating systems for gas turbine engines by thermal spray and ebpvd: A review. *Journal of Thermal Spray Technology*, 17:199–213, 2008.

[42] J.W. Foulk, D.H. Allen, and K.L.E. Helms. Formulation of a three-dimensional cohesive zone model for application to a finite element algorithm. *Computer methods in applied mechanics and engineering*, 2000.

[43] J. Frachon. *Multiscale approach to predict the lifetime of EB-PVD thermal barrier coatings.* PhD thesis, Mines ParisTECH, 2009.

[44] H.J. Frost and M.F. Ashby. *Deformation-mechanism maps.* Pergamon Press, 1982.

[45] B.P. Gearing. *Constitutive equations and failure criteria for amorphous polymeric solids.* PhD thesis, Massachusetts Institute of Technology, 2002.

[46] S. Gudlavalleti. Mechanical testing of solid materials at the micro-scale. Master's thesis, Massachusetts Institute of Technology, 2002.

[47] S. Gudlavalleti, B.P. Gearing, and L. Anand. Flexure-based micromechanical testing machines. *Experimental Mechanics*, 2005.

[48] M.E. Gurtin, E. Fried, and L. Anand. *The Mechanics and Thermodynamics of Continua.* Cambridge University Press, 2010.

[49] J.A. Haynes, M.K. Ferber, W.D. Porter, and E.D. Rigney. Characterization of alumina scales formed during isothermal and cyclic oxidation of plasma-sprayed TBC systems at 1150°C. *Oxidation of Metals*, 52:31–76, 1999.

[50] M.Y. He, A.G. Evans, and J.W. Hutchinson. The ratcheting of compressed thermally grown thin films on ductile substrates. *Acta Materialia*, 48:2593–2601, 2000.

[51] M.Y. He, J.W. Hutchinson, and A.G. Evans. Simulation of stresses and delamination in a plasma-sprayed thermal barrier system upon thermal cycling. *Materials Science and Engineering A*, 345:172–178, 2003.

[52] S. Heckmann, R. Herzog, R.W. Steinbrech, F. Schubert, and L. Singheiser. Viscoplastic properties of separated thermal barrier coatings under compression loading. *Materials for advanced power engineering 2002: Proceedings of the 7th Liege Conference*, 2002.

[53] A.H. Heuer. Oxygen and aluminum diffusion in α-Al_2O_3: How much do we really understand? *Journal of the European Ceramic Society*, 28:1495–1507, 2008.

[54] T.S. Hille, T.J. Nijdam, A.S.J. Suiker, S. Turteltaub, and W.G. Sloof. Damage growth triggered by interface irregularities in thermal barrier coatings. *Acta Materialia*, 57: 2624–2630, 2009.

[55] T.S. Hille, S. Turteltaub, and A.S.J. Suiker. Oxide growth and damage evolution in thermal barrier coatings. *Engineering Fracture Mechanics*, 78:2139–2152, 2011.

[56] P.Y. Hou and J. Stringer. The effect of reactive element additions on the selective oxidation, growth and adhesion of chromia scales. *Materials Science and Engineering A*, 202:1–10, 1995.

[57] A.M. Huntz. Stresses in NiO, Cr_2O_3 and Al_2O_3 oxide scales. *Materials Science and Engineering A*, 201:211–228, 1995.

[58] A.M. Huntz, G.C. Amiri, H.E. Evans, and G. Cailletaud. Comparison of oxidation-growth stresses in nio film measured by deflection and calculated using creep analysis or finite element modeling. *Oxidation of Metals*, 57:499–521, 2002.

[59] R.G. Hutchinson and J.W. Hutchinson. Lifetime assessment for thermal barrier coatings: Tests for measuring mixed mode delamination toughness. *Journal of the American Ceramic Society*, 94:S85–S95, 2011.

[60] A.M. Karlsson and A.G. Evans. A numerical model for the cyclic instability of thermally grown oxides in thermal barrier systems. *Acta materialia*, 49:1793–1804, 2001.

[61] A.M. Karlsson, T. Xu, and A.G. Evans. The effect of the thermal barrier coating on the displacement instability in thermal barrier systems. *Acta materialia*, 50:1211–1220, 2002.

[62] A.M. Karlsson, J.W. Hutchinson, and A.G. Evans. The displacement of the thermally grown oxide in thermal barrier systems upon temperature cycling. *Materials Science and Engineering A*, 351:244–257, 2003.

[63] D.J. Kim, I.H. Shin, J.M. Koo, C.S. Seok, and T.W. Lee. Failure mechanisms of coin-type plasma-sprayed thermal barrier coatings with thermal fatigue. *Surface and coatings technology*, 2010.

[64] S.S. Kim, Y.F. Liu, and Y. Kagawa. Evaluation of interfacial mechanical properties under shear loading in eb-pvd tbcs by the pushout method. *Acta Materialia*, 55: 3771–3781, 2007.

[65] R. Kitazawa, M. Tanaka, Y. Kagawa, and Y.F. Liu. Damage evolution of tbc system under in-phase thermo-mechanical tests. *Materials Science and Engineering B*, 2010.

[66] A. Krell and O.V. Bakun. High-temperature hardness of Al_2O_3-base ceramics. *Acta metallurgica*, 34:1315–1319, 1986.

[67] F.A. Kroger. Defect related properties of doped alumina. *Solid State Ionics*, 12:189–199, 1984.

[68] E. Kröner. Allgemeine kontinuumstheorie der versetzungen und eigenspannungen. *Archive for Rational Mechanics and Analysis*, 4:273–334, 1960.

[69] K.P.D. Lagerlof and R.W. Grimes. The defect chemistry of sapphire (α-Al_2O_3). *Acta materialia*, 46:5689–5700, 1998.

[70] D.M. Lipkin and D.R. Clarke. Measurement of the stress in oxide scales formed by oxidation of alumina-forming alloys. *Oxidation of Metals*, 45:267–280, 1996.

[71] K. Loeffel and L. Anand. A chemo-thermo-mechanically coupled theory for elastic-viscoplastic deformation, diffusion, and volumetric swelling due to a chemical reaction. *International Journal of Plasticity*, 27:1409–1431, 2011.

[72] K. Loeffel, L. Anand, and Z. Gasem (submitted). On modeling the oxidation of high-temperature alloys. *Acta Materialia*, 2012.

[73] W.G. Mao, J. Wan, C.Y. Dai, J. Ding, Y. Zhang, Y.C. Zhou, and C. Lu. Evaluation of microhardness, fracture toughness and residual stress in a thermal barrier coating system: A modified vickers indentation technique. *Surface and coatings technology*, 2012.

[74] R. McPherson. A review of microstructure and properties of plasma sprayed ceramic coatings. *Surface & Coatings Technology*, 39/40:173–181, 1989.

[75] C. Mercer, D. Hovis, A.H. Heuer, T. Tomimatsu, Y. Kagawa, and A.G. Evans. Influence of thermal cycle on surface evolution and oxide formation in a superalloy system with a NiCoCrAlY bond-coat. *Surface & Coatings Technology*, 202:4915–4921, 2008.

[76] P. Mohan, B. Yuan, T. Patterson, V.H. Desai, and Y.H. Sohn. Degradation of yttria-stabilized zirconia thermal barrier coatings by vanadium pentoxide, phosphorous pentoxide, and sodium sulfate. *Journal of the American Ceramic Society*, 2007.

[77] D.R. Mumm and A.G. Evans. On the role of imperfections in the failure of a thermal barrier coating made by electron beam deposition. *Acta materialia*, 48:1815–1827, 2000.

[78] G.C. Oates. *Aerothermodynamics of Aircraft Engine Components.* AIAA, 1985.

[79] Y. Oishi and W.D. Kingery. Self-diffusion of oxygen in single crystal and polycrystalline aluminum oxide. *Journal of Chemical Physics*, 33:480–486, 1960.

[80] N.P. Padture and M. Gell. Thermal barrier coatings for gas turbine engine applications. *Science*, 296:280–284, 2002.

[81] N.B. Pilling and R.E. Bedworth. The oxidation of metals at high temperatures. *Journal of the Institute of Metals*, 29:529–591, 1923.

[82] D. Prot and C. Monty. Self-diffusion in α-Al_2O_3. ii. oxygen diffusion in 'undoped' single crystals. *Philosophical Magazine A*, 73:899–917, 1996.

[83] G. Qian, T. Nakamura, C.C. Berndt, and S.H. Leigh. Tensile toughness test and high temperature fracture analysis of thermal barrier coatings. *Acta materialia*, 1997.

[84] P.N. Quested, R.F. Brooks, L. Chapman, R. Morrell, Y. Youssef, and K.C. Mills. Measurement and estimation of thermophysical properties of Nickel based superalloys. *Materials Science and Technology*, 25:154–162, 2009.

[85] A. Rabiei and A.G. Evans. Failure mechanisms associated with the thermally grown oxide in plasma-sprayed thermal barrier coatings. *Acta Materialia*, 48:3963–3976, 2000.

[86] N.R. Rebollo, M.Y. He, C.G. Levi, and A.G. Evans. Mechanisms governing the distortion of alumina-forming alloys upon cyclic oxidation. *Zeitschrift fur Metallkunde*, 94:171–179, 2003.

[87] J.R. Reeder and J.H. Crews Jr. Mixed-mode bending method for delamination testing. *AIAA Journal*, 1990.

[88] F.N. Rhines and J.S. Wolf. The role of microstructure and growth stresses in the high-temperature scaling of nickel. *Metallurgical Transactions*, 1:1701–1710, 1970.

[89] A. Saillard, M. Cherkaoui, and H. El Kadiri. Stress-induced roughness development during oxide scale growth on a metallic alloy for sofc interconnects. *Modelling and Simulation in Materials Science and Engineering*, 2011.

[90] C. San Marchi, B.P. Somerday, and S.L. Robinson. Permeability, solubility and diffusivity of hydrogen isotopes in stainless steels at high gas pressures. *International Journal of Hydrogen Energy*, 32:100–116, 2007.

[91] K.W. Schlichting, N.P. Padture, E.H. Jordan, and M. Gell. Failure modes in plasma-sprayed thermal barrier coatings. *Materials Science and Engineering A*, 342:120–130, 2003.

[92] S.K. Sharma, G.D. Ko, and K.J. Kang. High temperature creep and tensile properties of alumina formed on Fecralloy foils doped with Yttrium. *Journal of the European Ceramic Society*, 29:355–362, 2009.

[93] SIMULIA. *Abaqus/Standard, Version 6.10.* 2010.

[94] SIMULIA. *Abaqus/EXPLICIT, Version 6.10.* 2010.

[95] Special Metals Corporation. *INCONEL alloy 718 data sheet.* 2007.

[96] S. Sridharan, L. Xie, E.H. Jordan, and K.S. Murphy. Stress variation with thermal cycling in the thermally grown oxide of an eb-pvd thermal barrier coating. *Surface and Coatings Technology*, 179:286–296, 2004.

[97] S. Sridharan, L. Xie, M. Gell, E.H. Jordan, and K.S. Murphy. Damage evolution in an electron beam physical vapor deposited thermal barrier coating as a function of cycle temperature and time. *Materials Science & Engineering A*, 393:51–62, 2005.

[98] C. Su, Y.J. Wei, and L. Anand. An elasticplastic interface constitutive model: application to adhesive joints. *International Journal of Plasticity*, 20:2063–2081, 2004.

[99] Progressive Surface. *What is thermal spraying?* Retrieved at http://www.progressivesurface.com/thermalspraying.php on 1/8/2012.

[100] M. Tanaka, Y.F. Liu, S.S. Kim, and Y. Kagawa. Delamination toughness of electron beam physical vapor deposition (eb-pvd) ysz thermal barrier coatings by the pushout method: effect of thermal cycling temperature. *Journal of Materials Research*, 2008.

[101] P.Y. Thery, M. Poulain, M. Dupeux, and M. Braccini. Spallation of two thermal barrier coating systems: experimental study of adhesion and energetic approach to lifetime during cyclic oxidation. *Journal of Materials Science*, 2009.

[102] V.K. Tolpygo and D.R. Clarke. Stress generation and relaxation during oxidation of a Fe-Cr-Al-Y alloy. *Oxidation of Metals*, 49:187–212, 1998.

[103] V.K. Tolpygo, J.R. Dryden, and D.R. Clarke. Determination of the growth stress and strain in α-Al_2O_3scales during the oxidation of Fe-22Cr-4.8Al-0.3Y alloy. *Acta materialia*, 46:927–937, 1998.

[104] O. Trunova, T. Beck, R. Herzog, R.W. Steinbrech, and L. Singheiser. Damage mechanisms and lifetime behavior of plasma sprayed thermal barrier coating systems for gas turbines – part i: Experiments. *Surface & Coatings Technology*, 202:5027–5032, 2008.

[105] A. Turon, P.P. Camanho, J. Costa, and J. Renart. Accurate simulation of delamination growth under mixed-mode loading using cohesive elements: Definition of interlaminar strengths and elastic stiffness. *Composite Structures*, 2010.

[106] F.J. Ulm, O. Coussy, L. Kefei, and C. Larive. Thermo-chemo-mechanics of ASR expansion in concrete structures. *ASCE Journal of Engineering Mechanics*, 12:233–242, 2000.

[107] J.R. VanValzah and H.E. Eaton. Cooling rate effects on the tetragonal to monoclinic phase transformation in aged plasma-sprayed yttria partially stabilized zirconia. *Surface and Coatings Technology*, 1991.

[108] G. Weber and L. Anand. Finite deformation constitutive equations and a time integration procedure for isotropic, hyperelastic-viscoplastic solids. *Computer methods in applied mechanics and engineering*, 1990.

[109] K. Wefers and G.M. Bell. *Alcoa Technical Paper No. 19: Oxides and hydroxides of aluminum.* Alcoa Research Laboratories, 1972.

[110] T. Xu, M.Y. He, and A.G. Evans. A numerical assessment of the durability of thermal barrier systems that fail by ratcheting of the thermally-grown oxide. *Acta materialia*, 51:807–820, 2003.

[111] Z. Xu, Y. Yang, P. Huang, and X. Li. Determination of interfacial properties of thermal barrier coatings by shear test and inverse finite element method. *Acta Materialia*, 58: 5972–5979, 2010.

[112] Y. Yamazaki, A. Schmidt, and A. Scholz. The determination of the delamination resistance in thermal barrier coating system by four-point bending tests. *Surface & Coatings Technology*, 201:744–754, 2006.

[113] Y. Yamazaki, S.Kuga, and M. Jayaprakash. Interfacial strength evaluation technique for thermal barrier coated components by using indentation method. *Engineering Procedia*, 2011.

[114] J. Yan, T. Leist, M. Bartsch, and A.M. Karlsson. On cracks and delaminations of thermal barrier coatings due to indentation testing: experimental investigations. *Acta materialia*, 2008.

[115] J. Yan, A.M. Karlsson, M. Bartsch, and X. Chen. On stresses induced in a thermal barrier coating due to indentation testing. *Computational Materials Science*, 2009.

[116] N.M. Yanar, M. Helminiak, G.H. Meier, and F.S. Pettit. Comparison of the failures during cyclic oxidation of yttria-stabilized (7 to 8 weight percent) zirconia thermal barrier coatings fabricated via electron beam physical vapor deposition and air plasma spray. *Metallurgical and Materials Transactions A*, 42A:905–921, 2011.

[117] Z. Yang. Recent advances in metallic interconnects for solid oxide fuel cells. *International Materials Reviews*, 53:39–54, 2008.

[118] D.J. Young. *High temperature oxidation and corrosion of metals.* Elsevier, 2008.

[119] P.F. Zhao, C.A. Sun, X.Y. Zhu, F.L. Shang, and C.J. Li. Fracture toughness measurements of plasma-sprayed thermal barrier coatings using a modified four-point bending method. *Surface and coatings technology*, 2010.

[120] P.F. Zhao, X.D. Li, F.L. Shang, and C.J. Li. Interlamellar cracking of thermal barrier coatings with tgos by non-standard four-point bending tests. *Materials Science and Engineering A*, 2011.

[121] Y. Zhao, A. Shinmi, X. Zhao, P.J. Withers, S. Van Boxel, N. Markocsan, P. Nylen, and P. Xiao. Investigation of interfacial properties of atmospheric plasma sprayed thermal barrier coatings with four-point bending and computed tomography technique. *Surface & Coatings Technology*, doi:10.1016/j.surfcoat.2012.05.099, 2012.

[122] H. Zhou, J. Qu, and M. Cherkaoui. Stress-oxidation interaction in selective oxidation of cr-fe alloys. *"Mechanics of Materials"*, 42:63–71, 2010.

Part IV

Appendices related to Part I

Appendix A

Finite-element implementation for coupled theory

In this Appendix we discuss the finite-element implementation of the coupled theory discussed in Chapter 3. Specifically, the theory was implemented as a *user-element subroutine* in the commercial implicit finite-element program ABAQUS/Standard [93].

We point out that our numerical implementation employs some simple utility subroutines, e.g. for the calculation of the shape functions, that were originally written by Chester [24].

A.1 PDE for displacement, (3.180)

A.1.1 General formulation

The governing referential field equation for the stress in a body B is given by

$$\text{Div}\,\mathbf{T}_{\text{R}} + \mathbf{b}_{\text{R}} = \mathbf{0}, \tag{A.1}$$

which corresponds to the expression

$$\text{div}\,\mathbf{T} + \mathbf{b} = \mathbf{0} \tag{A.2}$$

in the deformed configuration, where

$$\mathbf{b} = J^{-1}\,\mathbf{b}_{\text{R}} \tag{A.3}$$

stands for the body force per unit volume in the deformed body. In index form, (A.2) may be written as

$$\frac{\partial T_{ij}}{\partial x_j} + b_i = 0. \tag{A.4}$$

Thus the strong form of the deformation problem is given by

$$\begin{cases} T_{ij,j} + b_i = 0 & \text{in } \mathrm{B}_t, \\ u_i = \breve{u}_i & \text{on } \partial\mathrm{B}_{t1}, \\ t_i = \breve{t}_i & \text{on } \partial\mathrm{B}_{t2}, \end{cases} \tag{A.5}$$

where the comma always indicates a spatial derivative, and

$$\mathbf{u} = \mathbf{x} - \mathbf{X} \tag{A.6}$$

is the displacement; also, the current configuration of B is denoted by B_t, and we prescribe displacements and tractions on the surfaces $\partial\mathrm{B}_{t1}$ and $\partial\mathrm{B}_{t2}$, respectively; B_{t1} and B_{t2} are *complementary subsurfaces* of the boundary $\partial\mathrm{B}_t$ of B_t. (It is pointed out that the implemented user subroutine does not support surface traction boundary conditions other than traction-free conditions. However, they are included here for generality.) Upon multiplying by a test function $\mathbf{w}$ (which vanishes on $\partial\mathrm{B}_{t1}$), the weak form of (A.5) can be stated as

$$\int_{\mathrm{B}_t} w_i \left(T_{ij,j} + b_i\right) dV = 0, \tag{A.7}$$

which, upon integration by parts, may be rewritten as

$$\int_{\mathrm{B}_t} \left(- w_{i,j} T_{ij} + w_i b_i \right) dV + \int_{\partial\mathrm{B}_t} w_i T_{ij} n_j \, dA = 0. \tag{A.8}$$

The traction condition in index notation is simply given by $t_i = T_{ij} n_j$, with $t_i = \breve{t}_i$ on $\partial\mathrm{B}_{t2}$; thus

$$\int_{\mathrm{B}_t} \left(- w_{i,j} T_{ij} + w_i b_i \right) dV + \int_{\partial\mathrm{B}_{t2}} w_i \breve{t}_i \, dA = 0. \tag{A.9}$$

We now introduce the shape function N_A corresponding to node A of the element, and approximate the functions w_i inside each element by

$$w_i = N_A w_{Ai}, \tag{A.10}$$

where w_{Ai} is the value of w_i at A, and summation is also always implied over repeated nodal subscripts unless otherwise stated. On the element level we thus have

$$\int_{\mathrm{B}_t^e} \left(- w_{Ai} N_{A,j} T_{ij} + N_A w_{Ai} b_i \right) dV + \int_{\partial\mathrm{B}_{t2}^e} N_A w_{Ai} \breve{t}_i \, dA = 0, \tag{A.11}$$

with B_t^e denoting an element in the current configuration and $\partial\mathrm{B}_{t2}^e$ the part of its boundary where tractions are prescribed (if any). Next, (A.11) has to hold for any w_{Ai}, and thus allows us to define the displacement residual

$$r_{Ai}^u = \int_{\mathrm{B}_t^e} \left(- N_{A,j} T_{ij} + N_A b_i \right) dV + \int_{\partial\mathrm{B}_{t2}^e} N_A \breve{t}_i \, dA. \tag{A.12}$$

The stiffness needed is defined as

$$K^u_{AiBk} = -\frac{\partial r^u_{Ai}}{\partial u_{Bk}}, \tag{A.13}$$

where u_{Bk} denotes the displacement in the k-direction at node B. From (A.12) we then obtain

$$K^u_{AiBk} = \int_{\mathrm{B}^e_t} \left(N_{A,j}\frac{\partial T_{ij}}{\partial u_{Bk}}\right) dV. \tag{A.14}$$

Note that the deformation gradient $\mathbf{F}$ in component form is given by

$$F_{mn} = \delta_{mn} + \frac{\partial N_A}{\partial X_n} u_{Am}, \tag{A.15}$$

yielding

$$\frac{\partial F_{mn}}{\partial u_{Bk}} = \frac{\partial N_B}{\partial X_n}\delta_{mk}. \tag{A.16}$$

Also, we have that

$$\frac{\partial T_{ij}}{\partial u_{Bk}} = \frac{\partial T_{ij}}{\partial F_{mn}}\frac{\partial F_{mn}}{\partial u_{Bk}}, \tag{A.17}$$

which, with (A.16), gives

$$\frac{\partial T_{ij}}{\partial u_{Bk}} = \frac{\partial N_B}{\partial X_n}\frac{\partial T_{ij}}{\partial F_{kn}}. \tag{A.18}$$

Combining (A.14) and (A.18) then finally gives that

$$K^u_{AiBk} = \int_{\mathrm{B}^e_t} \left(N_{A,j}\frac{\partial N_B}{\partial X_n}\frac{\partial T_{ij}}{\partial F_{kn}}\right) dV. \tag{A.19}$$

An estimate for the tensor $\partial\mathbf{T}/\partial\mathbf{F}$ is given in section A.6, after discussion of the integration procedure for $\mathbf{F}^i$.

Also, it has been found that the *off-diagonal* stiffness component of displacement with respect to temperature is important; with (A.12), it is given by

$$K^{u\vartheta}_{AiB} = -\frac{\partial r^u_{Ai}}{\partial(\vartheta)^B} = \int_{\mathrm{B}^e_t} \left(N_{A,j}\frac{\partial T_{ij}}{\partial(\vartheta)^B}\right) dV. \tag{A.20}$$

The temperature at any point within the element is found using the interpolation

$$\vartheta = N_C(\vartheta)^C, \tag{A.21}$$

and this directly yields that

$$\frac{\partial}{\partial(\vartheta)^B} = \frac{\partial}{\partial\vartheta}\frac{\partial\vartheta}{\partial(\vartheta)^B} = N_B\frac{\partial}{\partial\vartheta}. \tag{A.22}$$

Using (A.22) in (A.20) then lets us calculate $K^{u\vartheta}_{AiB}$ as

$$K^{u\vartheta}_{AiB} = \int_{\mathrm{B}^e_i} \left(N_{A,j} N_B \frac{\partial T_{ij}}{\partial \vartheta}\right) dV. \tag{A.23}$$

An estimate for $\partial \mathbf{T}/\partial\vartheta$ is also given in section A.6.

Remark: Some types of finite elements can exhibit *locking behavior* in incompressible deformation. A method to mitigate this locking behavior is documented in detail in de Souza Neto et al. [33] – the "F-bar method." The discussion in de Souza Neto et al. [33] is written for the *balance of momentum in the deformed configuration.* Even though in this work, we limit ourselves to *reduced-order* elements (see Section A.7 for details), for compatibility with de Souza Neto et al. [33] and to facilitate a possible future fully-integrated implementation, we also formulate our balance of momentum in the *deformed configuration* in this thesis.

A.2 PDE for temperature, (3.182)

A.2.1 Residual and stiffness

We rewrite (3.182) as

$$c\dot{\vartheta} = \mathrm{Div}\,(\kappa \nabla\vartheta) + g, \tag{A.24}$$

where g is defined by

$$g = q_{\mathrm{R}} + (1-\xi)\,\bar{\tau}\,\nu^p{}_{\mathrm{bc}} + \xi\,\bar{\tau}\,\nu^p{}_{\mathrm{ox}} + \mathcal{F}\dot{\xi} + D\,\frac{c_{\mathrm{R}}}{R\vartheta}\,|\nabla\mu|^2 + \vartheta\,\tfrac{1}{2}\frac{\partial \mathbf{T}^e}{\partial\vartheta} : \dot{\mathbf{C}}^e + (\mu-\mu_0)\dot{c}_{\mathrm{R}} - \vartheta\,\frac{\partial \mathcal{A}}{\partial\vartheta}\dot{\xi}. \tag{A.25}$$

Fully stated, the problem is thus described by

$$\begin{cases} c\dot{\vartheta} = \dfrac{\partial}{\partial X_i}\left(\kappa \dfrac{\partial\vartheta}{\partial X_i}\right) + g & \text{in B}, \\ \vartheta = \breve{\vartheta} & \text{on } \partial\mathrm{B}_\vartheta, \\ -\kappa \dfrac{\partial\vartheta}{\partial X_i} n_i = \breve{q}_{\mathrm{R}} & \text{on } \partial\mathrm{B}_{\mathbf{q}_{\mathrm{R}}}, \end{cases} \tag{A.26}$$

with temperature prescribed on $\partial\mathrm{B}_\vartheta$ and heat flux prescribed on $\partial\mathrm{B}_{\mathbf{q}_{\mathrm{R}}}$. B_ϑ and $\mathrm{B}_{\mathbf{q}_{\mathrm{R}}}$ are *complementary subsurfaces* of the boundary $\partial\mathrm{B}$ of B.(Again, flux boundary conditions other than the no-flux condition are not supported by the implemented version of the user element subroutine, but are mentioned in this discussion for generality.) The weak form of (A.26) can then be stated as

$$\int_{\mathrm{B}} w \left(c\dot{\vartheta} - \frac{\partial}{\partial X_i}\left(\kappa \frac{\partial\vartheta}{\partial X_i}\right) - g\right) dV_{\mathrm{R}} = 0, \tag{A.27}$$

with w a test function that vanishes on $\partial\mathrm{B}_\vartheta$. Using the divergence theorem and the identity

$$\mathrm{Div}\,(\gamma \mathbf{f}) = \gamma\,\mathrm{Div}\,\mathbf{f} + \nabla\gamma \cdot \mathbf{f}, \tag{A.28}$$

(A.27) may be written as

$$\int_{\mathrm{B}} w\big(c\dot{\vartheta} - g + \kappa\frac{\partial w}{\partial X_i}\frac{\partial \vartheta}{\partial X_i}\big)\, dV_{\mathrm{R}} - \int_{\partial \mathrm{B}_{\mathbf{q}_{\mathrm{R}}}} w\kappa\frac{\partial \vartheta}{\partial X_i} n_i\, dA_{\mathrm{R}} = 0. \tag{A.29}$$

From $(A.26)_3$, we can reformulate the last term in (A.29), and with (A.21) and the element-level interpolation

$$w = N_A w_A, \tag{A.30}$$

we obtain

$$\int_{\mathrm{B}^e} \big(N_A w_A(c\dot{\vartheta} - g) + w_A\kappa\frac{\partial N_A}{\partial X_i}\frac{\partial \vartheta}{\partial X_i}\big)\, dV_{\mathrm{R}} + \int_{\partial \mathrm{B}^e_{\mathbf{q}_{\mathrm{R}}}} N_A w_A \breve{q}_{\mathrm{R}}\, dA_{\mathrm{R}} = 0 \tag{A.31}$$

with

$$\frac{\partial \vartheta}{\partial X_i} = \frac{\partial N_B}{\partial X_i}(\vartheta)^B, \tag{A.32}$$

for an element B^e in the reference configuration, and $\partial \mathrm{B}^e_{\mathbf{q}_{\mathrm{R}}}$ its boundary on which heat flux is prescribed (if any). (A.31) again has to hold for all w. We can thus write the residual for the heat problem as

$$r^{\vartheta}_A = \int_{\mathrm{B}^e} \big(N_A(c\dot{\vartheta} - g) + \kappa\frac{\partial N_A}{\partial X_i}\frac{\partial \vartheta}{\partial X_i}\big)\, dV_{\mathrm{R}} + \int_{\partial \mathrm{B}^e_{\mathbf{q}_{\mathrm{R}}}} N_A \breve{q}_{\mathrm{R}}\, dA_{\mathrm{R}}. \tag{A.33}$$

The stiffness needed is given by

$$K^{\vartheta}_{AC} = -\frac{\partial r^{\vartheta}_A}{\partial(\vartheta)^C} \tag{A.34}$$

and can be calculated as

$$K^{\vartheta}_{AC} = -\int_{\mathrm{B}^e} \Big(c\frac{N_A N_C}{\Delta t} - N_A N_C\frac{\partial g}{\partial \vartheta} + \kappa\frac{\partial N_A}{\partial X_i}\frac{\partial N_C}{\partial X_i} + \frac{\partial \kappa}{\partial \vartheta}N^C\frac{\partial N_A}{\partial X_i}\frac{\partial \vartheta}{\partial X_i}\Big)\, dV_{\mathrm{R}}. \tag{A.35}$$

(Specific heat c is taken to be constant in temperature, as pointed out before. We also assume that the flux boundary condition does not depend on temperature.) Note that we made use of a backward-Euler formulation between t_m and $t_{m+1} = t_m + \Delta t$ for $\dot{\vartheta}$,

$$\dot{\vartheta} = \frac{\vartheta_{m+1} - \vartheta_m}{\Delta t}, \tag{A.36}$$

which, with (A.21), gives

$$\frac{\partial \dot{\vartheta}}{\partial(\vartheta)^C} = \frac{N_C}{\Delta t}, \tag{A.37}$$

and we calculated $\partial g/\partial(\vartheta)^C$ with (A.21) as

$$\frac{\partial g}{\partial(\vartheta)^C} = \frac{\partial g}{\partial \vartheta}N_C. \tag{A.38}$$

A.2.2 Estimate for $\partial g/\partial\vartheta$

The source term g in the heat equation, given in (A.25), can easily be rewritten as

$$g = q_{\mathrm{R}} + (1-\xi)\,\bar{\tau}\,\nu^{p}{}_{\mathrm{bc}} + \xi\,\bar{\tau}\,\nu^{p}{}_{\mathrm{ox}} + \mathcal{F}\dot{\xi} + D\,\frac{R\vartheta}{c_{\mathrm{R}}}\,|\nabla c_{\mathrm{R}}|^2 + \frac{\vartheta}{2}\left[\left(\mathbf{C}^{e-1}\frac{\partial \mathbf{M}^e}{\partial\vartheta}\right):\dot{\mathbf{C}}^e\right] + R\vartheta\dot{c}_{\mathrm{R}}\log\left(\tilde{c}_{\mathrm{R}}\right) - \vartheta\,\frac{\partial\mathcal{A}}{\partial\vartheta}\dot{\xi} \tag{A.39}$$

upon noting that

$$\mathbf{M}^e = \mathbf{C}^e\mathbf{T}^e$$

and using

$$\mu = \mu^0 + R\vartheta\log\left(\tilde{c}_{\mathrm{R}}\right).$$

For calculation of the stiffness given in (A.35), we need the derivative $\partial g/\partial\vartheta$, or an estimate for its value. (Note that any approximation in the stiffnesses *does not influence the accuracy of the solution*, but only affects the rate of convergence.) Here, we assume that this derivative may be approximated as

$$\frac{\partial g}{\partial\vartheta} \doteq D\frac{R}{c_{\mathrm{R}}}|\nabla c_{\mathrm{R}}|^2 + \frac{1}{2}\left[\left(\mathbf{C}^{e-1}\frac{\partial \mathbf{M}^e}{\partial\vartheta}\right):\dot{\mathbf{C}}^e\right] + R\dot{c}_{\mathrm{R}}\log\left(\tilde{c}_{\mathrm{R}}\right). \tag{A.40}$$

A.3 PDE for oxygen concentration, (3.181)

The governing field equation for the concentration in a part P of the body is given by

$$\dot{c}_{\mathrm{R}} = \mathrm{Div}\left(D\nabla c_{\mathrm{R}}\right) - r_{\mathrm{R}} \tag{A.41}$$

with

$$r_{\mathrm{R}} = \mathcal{R}\dot{\xi}. \tag{A.42}$$

The strong form of (A.19) can thus be written as

$$\begin{cases} \dot{c}_{\mathrm{R}} = \dfrac{\partial}{\partial X_i}\left(D\dfrac{\partial c_{\mathrm{R}}}{\partial X_i}\right) - r_{\mathrm{R}} & \text{in } \mathrm{B}, \\ c_{\mathrm{R}} = \breve{c}_{\mathrm{R}} & \text{on } \partial\mathrm{B}_{c_{\mathrm{R}}}, \\ -D\dfrac{\partial c_{\mathrm{R}}}{\partial X_i}n_i = \breve{j}_{\mathrm{R}} & \text{on } \partial\mathrm{B}_{\mathrm{j}_{\mathrm{R}}}, \end{cases} \tag{A.43}$$

with concentration prescribed on $\partial\mathrm{B}_{c_{\mathrm{R}}}$ and oxygen flux prescribed on $\partial\mathrm{B}_{\mathrm{j}_{\mathrm{R}}}$; $\partial\mathrm{B}_{c_{\mathrm{R}}}$ and $\partial\mathrm{B}_{\mathrm{j}_{\mathrm{R}}}$ are complementary subsurfaces of $\partial\mathrm{B}$. (Again, flux boundary conditions other than the no-flux condition are not supported by the implemented version of the user element subroutine, but are mentioned in this discussion for generality.) The weak form of (A.43) can then be stated as

$$\int_{\mathrm{B}} w\left(\dot{c}_{\mathrm{R}} - \frac{\partial}{\partial X_i}\left(D\frac{\partial c_{\mathrm{R}}}{\partial X_i}\right) + r_{\mathrm{R}}\right)\,dV_{\mathrm{R}} = 0, \tag{A.44}$$

with w a test function that vanishes on $\partial \mathrm{P}_{\mathrm{j_R}}$. Using the divergence theorem and the identity

$$\mathrm{Div}\,(\gamma \mathbf{f}) = \gamma\,\mathrm{Div}\,\mathbf{f} + \nabla\gamma \cdot \mathbf{f}, \tag{A.45}$$

(A.44) may be written as

$$\int_{\mathrm{B}} w\big(\dot{c}_{\mathrm{R}} + r_{\mathrm{R}} + D\frac{\partial w}{\partial X_i}\frac{\partial c_{\mathrm{R}}}{\partial X_i}\big)\,dV_{\mathrm{R}} - \int_{\partial \mathrm{B}_{\mathrm{j_R}}} wD\frac{\partial c_{\mathrm{R}}}{\partial X_i} n_i\,dA_{\mathrm{R}} = 0. \tag{A.46}$$

From $(\mathrm{A}.43)_3$, we can reformulate the last term in (A.46), and introducing the element-level interpolations

$$w = N_A w_A, \quad c_{\mathrm{R}} = N_A (c_{\mathrm{R}})^A, \tag{A.47}$$

where $(c_{\mathrm{R}})^A$ denotes c_{R} at node A, we obtain

$$\int_{\mathrm{B}^e} \big(N_A w_A(\dot{c}_{\mathrm{R}} + r_{\mathrm{R}}) + w_A D\frac{\partial N_A}{\partial X_i}\frac{\partial c_{\mathrm{R}}}{\partial X_i}\big)\,dV_{\mathrm{R}} + \int_{\partial \mathrm{B}^e_{\mathrm{j_R}}} N_A w_A \breve{j}_{\mathrm{R}}\,dA_{\mathrm{R}} = 0 \tag{A.48}$$

with

$$\frac{\partial c_{\mathrm{R}}}{\partial X_i} = \frac{\partial N_B}{\partial X_i}(c_{\mathrm{R}})^B, \tag{A.49}$$

with $\partial \mathrm{B}^e_{\mathrm{j_R}}$ the boundary of B^e on which oxygen flux is prescribed (if any). (A.48) again has to hold for all w. We can thus write the residual for the oxygen diffusion problem as

$$r_A^{c_{\mathrm{R}}} = \int_{\mathrm{B}^e} \big(N_A(\dot{c}_{\mathrm{R}} + r_{\mathrm{R}}) + D\frac{\partial N_A}{\partial X_i}\frac{\partial c_{\mathrm{R}}}{\partial X_i}\big)\,dV_{\mathrm{R}} + \int_{\partial \mathrm{B}^e_{\mathrm{j_R}}} N_A \breve{j}_{\mathrm{R}}\,dA_{\mathrm{R}}. \tag{A.50}$$

The stiffness related to changes in c_{R} is given by

$$K_{AC}^{c_{\mathrm{R}}} = -\frac{\partial r_A^{c_{\mathrm{R}}}}{\partial (c_{\mathrm{R}})^C} \tag{A.51}$$

and can be calculated as

$$K_{AC}^{c_{\mathrm{R}}} = -\int_{\mathrm{B}^e} \Big(\frac{N_A N_C}{\Delta t} + N_A N_C \frac{\partial r_{\mathrm{R}}}{\partial c_{\mathrm{R}}} + D\frac{\partial N_A}{\partial X_i}\frac{\partial N_C}{\partial X_i} + \frac{\partial D}{\partial c_{\mathrm{R}}} N_C \frac{\partial N_A}{\partial X_i}\frac{\partial c_{\mathrm{R}}}{\partial X_i}\Big)\,dV_{\mathrm{R}}. \tag{A.52}$$

(We assume that the flux boundary condition does not depend on concentration.) Note that we made use of a backward-Euler formulation between t_m and $t_{m+1} = t_m + \Delta t$ for $\dot{c}_{\mathrm{R}}$,

$$\dot{c}_{\mathrm{R}} = \frac{(c_{\mathrm{R}})_{m+1} - (c_{\mathrm{R}})_m}{\Delta t}, \tag{A.53}$$

which, with $(\mathrm{A}.47)_2$, gives

$$\frac{\partial \dot{c}_{\mathrm{R}}}{\partial (c_{\mathrm{R}})^C} = \frac{N_C}{\Delta t}, \tag{A.54}$$

and we calculated $\partial r_{\mathrm{R}}/\partial(c_{\mathrm{R}})^C$ with $(\mathrm{A}.47)_2$ as

$$\frac{\partial r_{\mathrm{R}}}{\partial(c_{\mathrm{R}})^C} = \frac{\partial r_{\mathrm{R}}}{\partial c_{\mathrm{R}}} N_C. \tag{A.55}$$

For the concentration residual, it has been found that the *off-diagonal* stiffness component with respect to temperature may also be relevant. It is given by

$$K_{AC}^{c_{\mathrm{R}}\vartheta} = -\frac{\partial r_A^{c_{\mathrm{R}}}}{\partial(\vartheta)^C}. \tag{A.56}$$

With (A.50), it may be written as

$$K_{AC}^{c_{\mathrm{R}}\vartheta} = -\int_{\mathrm{B}^e} \left(N_A N_C \frac{\partial r_{\mathrm{R}}}{\partial \vartheta} + \frac{\partial D}{\partial \vartheta} N_C \frac{\partial N_A}{\partial X_i} \frac{\partial c_{\mathrm{R}}}{\partial X_i} \right) dV_{\mathrm{R}}, \tag{A.57}$$

where we assumed that the flux boundary condition does not depend on temperature.

A.4 Integration procedure for ξ

For the user-element subroutine UEL, we need an integration procedure for the constitutive equations. In this Section, we consider the integration of ξ; the integration of $\mathbf{F}^i$ will be discussed in Section A.5.

A.4.1 General formulation

We examine a time step Δt going from t_m to t_{m+1}. The time derivative of ξ is approximated by a fully-implicit Euler-backward formulation:

$$\dot{\xi}_{m+1} \doteq \frac{\xi_{m+1} - \xi_m}{\Delta t}, \tag{A.58}$$

which allows us to compute ξ_{m+1} according to

$$\xi_{m+1} = \xi_m + \Delta t \dot{\xi}_{m+1}. \tag{A.59}$$

We can calculate the driving force $\mathcal{F}$ at t_{m+1} readily as

$$\mathcal{F}_{m+1} = H(1 - \xi_{m+1}) + \bar{\mathcal{F}}_{m+1}, \tag{A.60}$$

where

$$\bar{\mathcal{F}}_{m+1} = -B_{m+1} - 3\beta J^i_{m+1} \psi^0_{m+1} + \mathbb{S}_{m+1} : \mathbf{M}^e_{m+1} + \mathcal{R}\left(\mu^0 + R\vartheta_{m+1} \ln\left((\tilde{c}_{\mathrm{R}})_{m+1}\right)\right), \tag{A.61}$$

with $B_{m+1} = B(\vartheta_{m+1}, \mathbf{E}^e_{m+1})$ given by (3.163). From (3.168) we have that the reaction rate $\dot{\xi}$ is given by

$$\dot{\xi}_{m+1} = \begin{cases} \hat{C}_\xi \mathcal{F}_{m+1} & \text{if} \quad \mathcal{F}_{m+1} > 0 \quad \text{and} \quad \xi_{m+1} < 1, \\ 0 & \text{else,} \end{cases} \tag{A.62}$$

where we have introduced

$$\hat{C}_\xi = C_\xi \exp\left(\tfrac{-Q_s}{R\vartheta_{m+1}}\right). \tag{A.63}$$

We now consider (A.62) in detail. When there is no diffusing oxygen available for the reaction to consume, clearly the rate $\dot{\xi}$ must vanish: this is ensured by term involving the logarithm of $\tilde{c}_\mathrm{R}$ in the driving force, which causes the driving force to tend to negative infinity as c_R tends to zero. Next, the conversion term r_R in (A.43) at t_{m+1} is simply given by

$$(r_\mathrm{R})_{m+1} = \mathcal{R}\dot{\xi}_{m+1}, \tag{A.64}$$

or, combined with (A.62),

$$(r_\mathrm{R})_{m+1} = \begin{cases} \mathcal{R}\hat{C}_\xi \mathcal{F}_{m+1} & \text{if} \quad \mathcal{F}_{m+1} > 0 \quad \text{and} \quad \xi_{m+1} < 1, \\ 0 & \text{else.} \end{cases} \tag{A.65}$$

$(r_\mathrm{R})_{m+1}$ thus depends on the logarithm of $(\tilde{c}_\mathrm{R})_{m+1}$ due to this logarithm in $\mathcal{F}_{m+1}$. Let us for now consider $(r_\mathrm{R})_{m+1}$ only as a function of (non-normalized) $(c_\mathrm{R})_{m+1}$, which is illustrated in Fig. A-1. In a region in which oxidation is currently ongoing, it is expected that the concentration of diffusing oxygen will always be low since much of it will be consumed by the reaction at any given time. Therefore, the value of c_R will be right around where $\mathcal{F} = 0$: when $\mathcal{F}$ is slightly negative, there will be no reaction, and c_R is allowed to increase, eventually making $\mathcal{F}$ positive. At this time the reaction will resume, c_R will decrease, and eventually again $\mathcal{F}$ will again be negative.

Now consider the region around $\mathcal{F} = 0$ in Fig A-1. The slope of r_R is very steep as soon as $\mathcal{F}$ becomes positive. This immediately causes the residual of the concentration, (A.50) (in which r_R of course appears), to be very stiff with respect to c_R. Indeed, it is found that if (A.62) (and thus (A.65)) is implemented as it is stated above, the simulation does not converge for the range of parameters considered in this work. This can be overcome by adopting a slightly modified expression for $\dot{\xi}$ in this region of high stiffness, which we assume is located in the region where $\mathcal{F} > 0$, but the concentration is below a certain threshold value $c_\mathrm{R}^\mathrm{thr}$.

Specifically, we choose the following relation for $\dot{\xi}$ in the numerical implementation:

$$\dot{\xi}_{m+1} = \begin{cases} \hat{C}_\xi \mathcal{F}_{m+1} & \text{if} \quad \mathcal{F}_{m+1} > 0, \quad \xi_{m+1} < 1, \quad \text{and} \quad (c_\mathrm{R})_{m+1} > c_\mathrm{R}^\mathrm{thr}, \\ \frac{(c_\mathrm{R})_{m+1}}{c_\mathrm{R}^\mathrm{thr}} \hat{C}_\xi \mathcal{F}^\mathrm{thr}_{m+1} & \text{if} \quad \mathcal{F}_{m+1} > 0, \quad \xi_{m+1} < 1, \quad \text{and} \quad (c_\mathrm{R})_{m+1} \leq c_\mathrm{R}^\mathrm{thr}, \\ 0, & \text{else,} \end{cases} \tag{A.66}$$

where $\mathcal{F}^{\text{thr}}_{m+1}$ is given by

$$\mathcal{F}^{\text{thr}}_{m+1} = H(1-\xi_{m+1}) \underbrace{-B_{m+1} - 3\beta J^i_{m+1}\psi^0_{m+1} + \mathbb{S}_{m+1} : \mathbf{M}^e_{m+1} + \mathcal{R}\left(\mu^0 + R\vartheta_{m+1}\ln\left(\frac{c^{\text{thr}}_{\text{R}}}{c_{\max}}\right)\right)}_{\bar{\mathcal{F}}^{\text{thr}}_{m+1}}. \tag{A.67}$$

The conversion term $(r_{\text{R}})_{m+1}$, considered only as a function of $(c_{\text{R}})_{m+1}$ and calculated with (A.64) and (A.66), is shown in Fig. A-2.

Calculating $\dot{\xi}_{m+1}$ with (A.66) requires knowledge of $\mathcal{F}_{m+1}$ from (A.60) and (A.61). In the user element subroutine, the values of c_{R} and ϑ are known at t_{m+1}; however, we want to perform the integration of ξ before the integration of $\mathbf{F}^i$ at every integration point, and thus do not have the values of $\mathbf{E}^e_{m+1}$ available, which in turn determines $\mathbb{S}_{m+1} : \mathbf{M}^e_{m+1}$, B_{m+1}, and ψ^0_{m+1}. We therefore make our first approximation:

(A1) We assume that the time step Δt is small, so that we may approximate $\bar{\mathcal{F}}_{m+1}$ and $\bar{\mathcal{F}}^{\text{thr}}_{m+1}$ by the following expressions:

$$\bar{\mathcal{F}}_{m+1} \doteq -B_m - 3\beta J^i_m \psi^0_m + \mathbb{S}_m : \mathbf{M}^e_m + \mathcal{R}\left(\mu^0 + R\vartheta_{m+1}\ln\left(\frac{(c_{\text{R}})_{m+1}}{c_{\max}}\right)\right), \tag{A.68}$$

$$\bar{\mathcal{F}}^{\text{thr}}_{m+1} \doteq -B_m - 3\beta J^i_m \psi^0_m + \mathbb{S}_m : \mathbf{M}^e_m + \mathcal{R}\left(\mu^0 + R\vartheta_{m+1}\ln\left(\frac{c^{\text{thr}}_{\text{R}}}{c_{\max}}\right)\right). \tag{A.69}$$

Remark: Approximation (A1) is further legitimized by the fact that the term $H(1-\xi_{m+1})$ in (A.60) and (A.67) is much larger than $\bar{\mathcal{F}}_{m+1}$ or $\bar{\mathcal{F}}^{\text{thr}}_{m+1}$ for typical material parameters and whenever $\mathcal{F}_{m+1} > 0$. $\bar{\mathcal{F}}_{m+1}$ and $\bar{\mathcal{F}}^{\text{thr}}_{m+1}$ thus don't have much influence on the value of the driving force $\mathcal{F}_{m+1}$.

Remark: Note that due to approximation (A1), the integration procedure we use in this work is thus *semi-implicit*.

For the computation of ξ_{m+1}, we now first assume that $\mathcal{F}_{m+1} > 0$ and $\xi_{m+1} < 1$, which will have to be verified after we obtain ξ_{m+1}. For this case, we can combine (A.59), (A.66), (A.61), and (A.67), and after some algebra we obtain the following expression for ξ_{m+1}:

$$\xi_{m+1} = \begin{cases} (\xi_m + \Delta t\hat{C}_\xi(H + \bar{\mathcal{F}}_{m+1}))(1 + \Delta t\hat{C}_\xi H)^{-1} & \text{if} \quad (c_{\text{R}})_{m+1} > c^{\text{thr}}_{\text{R}}, \\ \left(\xi_m + \Delta t\frac{(c_{\text{R}})_{m+1}}{c^{\text{thr}}_{\text{R}}}\hat{C}_\xi(H + \bar{\mathcal{F}}^{\text{thr}}_{m+1})\right)(1 + \Delta t\frac{(c_{\text{R}})_{m+1}}{c^{\text{thr}}_{\text{R}}}\hat{C}_\xi H)^{-1} & \text{if} \quad (c_{\text{R}})_{m+1} \leq c^{\text{thr}}_{\text{R}}, \end{cases} \tag{A.70}$$

where we then choose to approximate $\bar{\mathcal{F}}_{m+1}$ and $\bar{\mathcal{F}}^{\text{thr}}_{m+1}$ by (A.69) and (A.67), respectively. After calculation of ξ_{m+1} from (A.70), we first check if indeed

$$\mathcal{F}_{m+1} > 0; \tag{A.71}$$

if this is not the case, we must instead set

$$\xi_{m+1} = \xi_m. \tag{A.72}$$

If (A.71) does hold, we still need to check if $\xi_{m+1} < 1$; if this is not the case, we set $\xi_{m+1} = 1$.

A.4.2 Calculation of $\partial r_{\mathrm{R}}/\partial c_{\mathrm{R}}$ and $\partial r_{\mathrm{R}}/\partial \vartheta$

For the calculation of the stiffness related to the concentration residual, we need the derivatives $\partial r_{\mathrm{R}}/\partial c_{\mathrm{R}}$ and $\partial r_{\mathrm{R}}/\partial \vartheta$ at t_{m+1}, as can be seen from (A.52) and (A.57), respectively. The former, $\partial r_{\mathrm{R}}/\partial c_{\mathrm{R}}$, can be calculated noting that with (A.64), we have

$$\frac{\partial (r_{\mathrm{R}})_{m+1}}{\partial (c_{\mathrm{R}})_{m+1}} = \frac{\partial (r_{\mathrm{R}})_{m+1}}{\partial \dot{\xi}_{m+1}} \frac{\partial \dot{\xi}_{m+1}}{\partial \xi_{m+1}} \frac{\partial \xi_{m+1}}{\partial (c_{\mathrm{R}})_{m+1}} = \frac{\mathcal{R}}{\Delta t} \frac{\partial \xi_{m+1}}{\partial (c_{\mathrm{R}})_{m+1}}, \tag{A.73}$$

where we have used (A.58) to obtain

$$\frac{\partial \dot{\xi}_{m+1}}{\partial \xi_{m+1}} = \frac{1}{\Delta t}. \tag{A.74}$$

Taking the needed derivative of ξ_{m+1} with respect to $(c_{\mathrm{R}})_{m+1}$ from (A.70), we finally obtain

$$\frac{\partial (r_{\mathrm{R}})_{m+1}}{\partial (c_{\mathrm{R}})_{m+1}} = \begin{cases} \hat{C}_\xi \mathcal{R}^2 R \times \frac{\vartheta_{m+1}}{(c_{\mathrm{R}})_{m+1} P} & \text{if} \quad \mathcal{F}_{m+1} > 0, \quad \xi_{m+1} < 1, \quad \text{and} \quad (c_{\mathrm{R}})_{m+1} > c_{\mathrm{R}}^{\mathrm{thr}}, \\ \hat{C}_\xi \mathcal{R} \times \frac{H(1-\xi_m) + \bar{\mathcal{F}}_{m+1}^{\mathrm{thr}}}{c_{\mathrm{R}}^{\mathrm{thr}} \left(\tilde{P}_{m+1}^{\mathrm{thr}}\right)^2} & \text{if} \quad \mathcal{F}_{m+1} > 0, \quad \xi_{m+1} < 1, \quad \text{and} \quad (c_{\mathrm{R}})_{m+1} \leq c_{\mathrm{R}}^{\mathrm{thr}}, \\ 0, & \text{else}, \end{cases} \tag{A.75}$$

with

$$P = 1 + \Delta t \hat{C}_\xi H, \qquad \tilde{P}_{m+1}^{\mathrm{thr}} = 1 + \Delta t \frac{(c_{\mathrm{R}})_{m+1}}{c_{\mathrm{R}}^{\mathrm{thr}}} \hat{C}_\xi H. \tag{A.76}$$

For $\partial r_{\mathrm{R}}/\partial \vartheta$, we again use (A.58) and (A.74) to obtain

$$\frac{\partial (r_{\mathrm{R}})_{m+1}}{\partial (\vartheta)_{m+1}} = -\frac{\mathcal{R}}{\Delta t} \frac{\partial \xi_{m+1}}{\partial (\vartheta)_{m+1}}. \tag{A.77}$$

Taking the needed derivative of ξ_{m+1} with respect to $(\vartheta)_{m+1}$ from (A.70), after some algebra we obtain

$$\frac{\partial (r_{\mathrm{R}})_{m+1}}{\partial (\vartheta)_{m+1}} = \begin{cases} \frac{\mathcal{R}\hat{C}_\xi}{P^2} \left[\frac{\partial H}{\partial (\vartheta)_{m+1}} (1 - \xi_m) + PR\mathcal{R} \ln\left(\frac{(c_{\mathrm{R}})_{m+1}}{c_{\max}}\right) - \Delta t \hat{C}_\xi \frac{\partial H}{\partial (\vartheta)_{m+1}} \bar{\mathcal{F}}_{m+1}^{\mathrm{thr}} \right], \\ \frac{\mathcal{R}\hat{C}_\xi}{(\tilde{P}_{m+1}^{\mathrm{thr}})^2} \left[\frac{\partial H}{\partial (\vartheta)_{m+1}} (1 - \xi_m) + \tilde{P}_{m+1}^{\mathrm{thr}} R\mathcal{R} \ln\left(\frac{c_{\mathrm{R}}^{\mathrm{thr}}}{c_{\max}}\right) - \Delta t \frac{(c_{\mathrm{R}})_{m+1}}{c_{\mathrm{R}}^{\mathrm{thr}}} \hat{C}_\xi \frac{\partial H}{\partial (\vartheta)_{m+1}} \bar{\mathcal{F}}_{m+1}^{\mathrm{thr}} \right], \\ 0, \end{cases} \tag{A.78}$$

where the different equations in (A.78) refer to the same cases (in the same order) as in (A.75). (The designations have been omitted for ease of display.)

A.5 Integration procedure for $\mathbf{F}^i$

The computational problem for the integration of the inelastic deformation gradient $\mathbf{F}^i$ is to find

$$\mathbf{T}_{m+1} \quad \text{and} \quad \mathbf{F}^i_{m+1}, \tag{A.79}$$

where the subscripts indicate the time at which the respective quantities are evaluated, when we are given

$$\mathbf{T}_m, \quad \mathbf{F}^i_m, \quad \mathbf{F}_m, \quad \text{as well as} \quad \mathbf{F}_{m+1}, \quad \dot{\xi}_{m+1}. \tag{A.80}$$

(Note that ξ thus needs to be integrated before the integration of $\mathbf{F}^i$ takes place, so that $\dot{\xi}_{m+1}$ is known.) The procedure documented here follows closely the work of Weber and Anand [108] and is modified only to allow for (i) swelling deformation with preferred direction and (ii) viscoplasticity both in the bond coat as well as in the oxide.

The total inelastic stretching $\mathbf{D}^i$ is given by

$$\mathbf{D}^i = \mathbf{D}^s + (1-\omega)\mathbf{D}^p_{\text{bc}} + \omega\mathbf{D}^p_{\text{ox}}, \tag{A.81}$$

which, with (3.164) and (3.165) may be written as

$$\mathbf{D}^i = \mathbf{D}^s + \sqrt{\tfrac{3}{2}}\dot{\bar{\epsilon}}^p\mathbf{N}^p, \tag{A.82}$$

where

$$\dot{\bar{\epsilon}}^p = (1-\omega)\dot{\bar{\epsilon}}^p_{\text{bc}} + \omega\dot{\bar{\epsilon}}^p_{\text{ox}} \tag{A.83}$$

is an overall equivalent tensile plastic strain rate, and

$$\mathbf{N}^p = \sqrt{\tfrac{3}{2}}\frac{\mathbf{M}^e_0}{\bar{\sigma}} \tag{A.84}$$

is the direction of plastic flow.

The evolution equation for $\mathbf{F}^i$ given by (3.136) and repeated here for convenience,

$$\dot{\mathbf{F}}^i = \mathbf{D}^i\mathbf{F}^i,$$

is then integrated through the (implicit) exponential map

$$\mathbf{F}^i_{m+1} = \exp\left(\Delta t\mathbf{D}^i_{m+1}\right)\mathbf{F}^i_m, \quad \mathbf{D}^i_{m+1} = \hat{\mathbf{D}}^i_{m+1}(\mathbf{M}^e_{m+1}, \vartheta). \tag{A.85}$$

We can thus calculate $\mathbf{F}^e$ at the end of the step as

$$\mathbf{F}^e_{m+1} = \mathbf{F}^{e\ \text{trial}}_{m+1}\exp\left(-\Delta t\mathbf{D}^i_{m+1}\right), \tag{A.86}$$

where

$$\mathbf{F}^{e\ \text{trial}}_{m+1} = \mathbf{F}_{m+1}\mathbf{F}^{i-1}_m \tag{A.87}$$

is the trial value of the elastic deformation gradient. The elastic right Cauchy-Green tensor and its trial value at the end of the step are

$$\mathbf{C}^e_{m+1} = \mathbf{F}^{e\mathsf{T}}_{m+1}\mathbf{F}^e_{m+1}, \quad \mathbf{C}^{e\,\text{trial}}_{m+1} = (\mathbf{F}^{e\,\text{trial}}_{m+1})^{\mathsf{T}}\mathbf{F}^{e\,\text{trial}}_{m+1}, \tag{A.88}$$

respectively. For later use, we also note the polar decompositions of $\mathbf{F}^e_{m+1}$ and $\mathbf{F}^{e\,\text{trial}}_{m+1}$ given by

$$\mathbf{F}^e_{m+1} = \mathbf{R}^e_{m+1}\mathbf{U}^e_{m+1}, \quad \text{and} \quad \mathbf{F}^{e\,\text{trial}}_{m+1} = \mathbf{R}^{e\,\text{trial}}_{m+1}\mathbf{U}^{e\,\text{trial}}_{m+1}, \tag{A.89}$$

respectively, where we have elastic strains

$$\mathbf{E}^e_{m+1} = \ln \mathbf{U}^e_{m+1} \quad \text{and} \quad \mathbf{E}^{e\,\text{trial}}_{m+1} = \ln \mathbf{U}^{e\,\text{trial}}_{m+1} \tag{A.90}$$

at the end of the increment and as a trial value, respectively. Also,

$$\mathbf{C}^e_{m+1} = \left(\mathbf{U}^e_{m+1}\right)^2, \quad \mathbf{C}^{e\,\text{trial}}_{m+1} = \left(\mathbf{U}^{e\,\text{trial}}_{m+1}\right)^2. \tag{A.91}$$

From (A.86) we now have that

$$\mathbf{C}^e_{m+1} = \exp\Big(-\Delta t\mathbf{D}^i_{m+1}\Big)\mathbf{C}^{e\,\text{trial}}_{m+1}\exp\Big(-\Delta t\mathbf{D}^i_{m+1}\Big). \tag{A.92}$$

Under the assumption of small time steps (A1) from Section A.4, we may also write to first order that

$$\exp\Big(-\Delta t\mathbf{D}^i_{m+1}\Big) \doteq \mathbf{1} - \Delta t\mathbf{D}^i_{m+1}. \tag{A.93}$$

In that case,

$$\mathbf{C}^e_{m+1} \doteq (\mathbf{1} - \Delta t\mathbf{D}^i_{m+1})\mathbf{C}^{e\,\text{trial}}_{m+1}(\mathbf{1} - \Delta t\mathbf{D}^i_{m+1}), \tag{A.94}$$

and again under the assumption of small time steps, we then have that

$$\mathbf{C}^e_{m+1} \doteq \mathbf{C}^{e\,\text{trial}}_{m+1} - \Delta t\mathbf{C}^{e\,\text{trial}}_{m+1}\mathbf{D}^i_{m+1} - \Delta t\mathbf{D}^i_{m+1}\mathbf{C}^{e\,\text{trial}}_{m+1} \tag{A.95}$$

$$\doteq \mathbf{C}^{e\,\text{trial}}_{m+1}\left(\mathbf{1} - \Delta t(\mathbf{C}^{e\,\text{trial}}_{m+1})^{-1}\mathbf{D}^i_{m+1}\mathbf{C}^{e\,\text{trial}}_{m+1} - \Delta t\mathbf{D}^i_{m+1}\right). \tag{A.96}$$

We now introduce a Green strain $\mathbf{E}^{eG}_{\text{trial}} = \frac{1}{2}(\mathbf{C}^{e\,\text{trial}}_{m+1} - \mathbf{1})$ corresponding to $\mathbf{C}^{e\,\text{trial}}_{m+1}$; then,

$$\mathbf{C}^{e\,\text{trial}}_{m+1} = \mathbf{1} + 2\mathbf{E}^{eG}_{\text{trial}}. \tag{A.97}$$

We proceed to make the next approximation:

(A2) we assume that $|\mathbf{E}^{eG}_{\text{trial}}| \ll 1$.

Examining the term $(\mathbf{C}^{e\,\text{trial}}_{m+1})^{-1}\mathbf{D}^i_{m+1}\mathbf{C}^{e\,\text{trial}}_{m+1}$ in (A.96),we find with (A2) that

$$(\mathbf{C}^{e\,\text{trial}}_{m+1})^{-1}\mathbf{D}^i_{m+1}\mathbf{C}^{e\,\text{trial}}_{m+1} \doteq (\mathbf{1} - 2\mathbf{E}^{eG}_{\text{trial}})\mathbf{D}^i_{m+1}(\mathbf{1} + 2\mathbf{E}^{eG}_{\text{trial}}) \tag{A.98}$$

$$\doteq \mathbf{D}^i_{m+1} + 2\mathbf{D}^i_{m+1}\mathbf{E}^{eG}_{\text{trial}} - 2\mathbf{E}^{eG}_{\text{trial}}\mathbf{D}^i_{m+1} - 4\mathbf{E}^{eG}_{\text{trial}}\mathbf{D}^i_{m+1}\mathbf{E}^{eG}_{\text{trial}}, \tag{A.99}$$

which gives

$$(\mathbf{C}^{e\,\text{trial}}_{m+1})^{-1}\mathbf{D}^i_{m+1}\mathbf{C}^{e\,\text{trial}}_{m+1} \doteq \mathbf{D}^i_{m+1}. \tag{A.100}$$

With this result, (A.96) reduces to

$$\mathbf{C}^e_{m+1} \doteq \mathbf{C}^{e\,\text{trial}}_{m+1}(\mathbf{1} - 2\Delta t\mathbf{D}^i_{m+1}). \tag{A.101}$$

Further, using the symmetry of $\mathbf{C}^e_{m+1}$, we note that the symmetric tensors $\mathbf{C}^{e\,\text{trial}}_{m+1}$ and $(\mathbf{1} - 2\Delta t\mathbf{D}^i_{m+1})$ *commute*, and hence share the same principal directions. We can thus take the logarithm of (A.101) and obtain

$$\mathbf{E}^e_{m+1} \doteq \mathbf{E}^{e\,\text{trial}}_{m+1} + \tfrac{1}{2}\ln(\mathbf{1} - 2\Delta t\mathbf{D}^i_{m+1}), \tag{A.102}$$

where, from (A.90) and (A.91),

$$\mathbf{E}^e_{m+1} = \tfrac{1}{2}\ln\mathbf{C}^e_{m+1}, \quad \mathbf{E}^{e\,\text{trial}}_{m+1} = \tfrac{1}{2}\ln\mathbf{C}^{e\,\text{trial}}_{m+1}. \tag{A.103}$$

With the approximation of small time steps Δt, (A1), we now also assume that

$$\ln(\mathbf{1} - 2\Delta t\mathbf{D}^i_{m+1}) \doteq -2\Delta t\mathbf{D}^i_{m+1}. \tag{A.104}$$

Using (A.104) in (A.102) then gives the important relation

$$\mathbf{E}^e_{m+1} \doteq \mathbf{E}^{e\,\text{trial}}_{m+1} - \Delta t\mathbf{D}^i_{m+1}, \tag{A.105}$$

and the exponential of expression (A.105), with (A.90), leads us to

$$\mathbf{U}^e_{m+1} \doteq \mathbf{U}^{e\,\text{trial}}_{m+1}\exp\left(-\Delta t\mathbf{D}^i_{m+1}\right). \tag{A.106}$$

In this context, we now also combine (A.86) and (A.89), with which we can write

$$\mathbf{R}^e_{m+1}\mathbf{U}^e_{m+1} = \mathbf{R}^{e\,\text{trial}}_{m+1}\mathbf{U}^{e\,\text{trial}}_{m+1}\exp\left(-\Delta t\mathbf{D}^i_{m+1}\right). \tag{A.107}$$

Then, the uniqueness of the polar decomposition, along with (A.106), immediately give

$$\mathbf{R}^e_{m+1} = \mathbf{R}^{e\,\text{trial}}_{m+1}, \tag{A.108}$$

another result we will later make use of. Through the thermoelastic relation (cf. 3.161_1)

$$\mathbf{M}^e = J^i\Big(\mathbb{C}[\mathbf{E}^e] - 3K\alpha(\vartheta - \vartheta_0)\mathbf{1}\Big), \qquad \mathbb{C} = 2G(\mathbb{I} - \tfrac{1}{3}\mathbf{1}\otimes\mathbf{1}) + K(\mathbf{1}\otimes\mathbf{1}), \tag{A.109}$$

with fourth-order elasticity tensor $\mathbb{C}$ and fourth-order identity tensor $\mathbb{I}$, and together with (A.105), we then have

$$\mathbf{M}^e_{m+1} = \mathbf{M}^{e\,\text{trial}}_{m+1} - J^i_{m+1}\mathbb{C}[\Delta t\mathbf{D}^i_{m+1}], \tag{A.110}$$

where

$$\mathbf{M}^{e\,\text{trial}}_{m+1} = J^i_{m+1}\mathbb{C}[\mathbf{E}^{e\,\text{trial}}_{m+1}] - 3J^i_{m+1}K\alpha(\vartheta_{m+1} - \vartheta_0)\mathbf{1} \tag{A.111}$$

is the trial Mandel stress. Note that ϑ_{m+1} is known (supplied by Abaqus through subroutine UEL), and so is J^i_{m+1}; the latter is known from the integration described in Section A.4,

where ξ_{m+1} is determined, which in turn gives J^i_{m+1} through (3.34),

$$J^i_{m+1} = \exp(3\beta\xi_{m+1}). \tag{A.112}$$

For ease of display of the ensuing discussion, we introduce the modified elastic constants

$$\tilde{K} = J^i_{m+1}K, \qquad \tilde{G} = J^i_{m+1}G, \tag{A.113}$$

which allows us to write the thermoelastic relation (A.109) as

$$\mathbf{M}^e = 2\tilde{G}\mathbf{E}^e + (\tilde{K} - \tfrac{2}{3}\tilde{G})(\mathrm{tr}\,\mathbf{E}^e) - 3\tilde{K}\alpha(\vartheta - \vartheta_0)\mathbf{1}, \tag{A.114}$$

which for the trial Mandel stress from (A.111) gives

$$\mathbf{M}^{e\,\mathrm{trial}}_{m+1} = 2\tilde{G}\mathbf{E}^{e\,\mathrm{trial}}_{m+1} + (\tilde{K} - \tfrac{2}{3}\tilde{G})(\mathrm{tr}\,\mathbf{E}^{e\,\mathrm{trial}}_{m+1})\mathbf{1} - 3\tilde{K}\alpha(\vartheta - \vartheta_0)\mathbf{1}. \tag{A.115}$$

Now, for the inelastic stretching, we have from (A.82) that

$$\mathbf{D}^i = \sqrt{\tfrac{3}{2}}\dot{\bar{\epsilon}}^p\mathbf{N}^p + \dot{\xi}\mathbb{S}, \tag{A.116}$$

with $\mathbb{S}$ given by

$$\mathbb{S} = \beta_p\mathbf{m}\otimes\mathbf{m} + \beta_l(\mathbf{1} - \mathbf{m}\otimes\mathbf{m}), \tag{A.117}$$

where $\mathbf{m}$ is described by (3.139),

$$\mathbf{m} = \frac{\mathbf{F}^{i-\mathsf{T}}\mathbf{m}_{\mathrm{R}}}{|\mathbf{F}^{i-\mathsf{T}}\mathbf{m}_{\mathrm{R}}|}.$$

Also, with (A.113), (A.110) may be written as

$$\mathbf{M}^e_{m+1} = \mathbf{M}^{e\,\mathrm{trial}}_{m+1} - 2\tilde{G}\Delta t\mathbf{D}^i_{m+1} - \Delta t(\tilde{K} - \tfrac{2}{3}\tilde{G})(\mathrm{tr}\,\mathbf{D}^i_{m+1})\mathbf{1}. \tag{A.118}$$

Noting that

$$\mathrm{tr}\,\mathbf{D}^i = \dot{\xi}(\beta_p + 2\beta_l), \tag{A.119}$$

we can write (A.118) as

$$\mathbf{M}^e_{m+1} = \mathbf{M}^{e\,\mathrm{trial}}_{m+1} - 2\tilde{G}\Delta t(\sqrt{\tfrac{3}{2}}\dot{\bar{\epsilon}}^p_{m+1}\mathbf{N}^p_{m+1} + \dot{\xi}_{m+1}\mathbb{S}_{m+1}) - \Delta t(\tilde{K} - \tfrac{2}{3}\tilde{G})\dot{\xi}_{m+1}(\beta_p + 2\beta_l)\mathbf{1}. \tag{A.120}$$

The tensor $\mathbb{S}_{m+1}$ can be split up into spherical and deviatoric parts as

$$\mathbb{S}_{m+1} = \tfrac{1}{3}(\beta_p + 2\beta_l)\mathbf{1} + \mathbb{S}_{m+1,0} \quad \text{with} \quad \mathbb{S}_{m+1,0} = (\beta_p - \beta_l)(\mathbf{m}_{m+1}\otimes\mathbf{m}_{m+1} - \tfrac{1}{3}\mathbf{1}), \tag{A.121}$$

and we thus have that

$$\mathbf{M}^e_{m+1} = \mathbf{M}^{e\,\mathrm{trial}}_{m+1} - 2\tilde{G}\Delta t[\sqrt{\tfrac{3}{2}}\dot{\bar{\epsilon}}^p_{m+1}\mathbf{N}^p_{m+1} + \dot{\xi}_{m+1}\mathbb{S}_{m+1,0}] - \tilde{K}\Delta t\dot{\xi}_{m+1}(\beta_p + 2\beta_l)\mathbf{1}. \tag{A.122}$$

The deviator of $\mathbf{M}^e_{m+1}$ can be found from (A.122) as

$$\mathbf{M}^e_{m+1,0} = \mathbf{M}^{e\,\text{trial}}_{m+1,0} - 2\tilde{G}\Delta t[\sqrt{\tfrac{3}{2}}\dot{\bar{\epsilon}}^p_{m+1}\mathbf{N}^p_{m+1} + \dot{\xi}_{m+1}\mathbb{S}_{m+1,0}]. \tag{A.123}$$

Noting that

$$\mathbf{N}^p = \sqrt{\tfrac{3}{2}}\frac{\mathbf{M}^e_0}{\bar{\sigma}}, \tag{A.124}$$

we can write (A.123) as

$$\mathbf{M}^{e\,\text{trial}}_{m+1,0} = (\sqrt{\tfrac{2}{3}}\bar{\sigma}_{m+1} + \sqrt{6}\tilde{G}\Delta t\dot{\bar{\epsilon}}^p_{m+1})\mathbf{N}^p_{m+1} + 2\dot{\xi}_{m+1}\mathbb{S}_{m+1,0}. \tag{A.125}$$

We now introduce the direction of the trial Mandel stress

$$\mathbf{N}^{p\,\text{trial}}_{m+1} = \sqrt{\tfrac{3}{2}}\frac{\mathbf{M}^{e\,\text{trial}}_{m+1,0}}{\bar{\sigma}^{\,\text{trial}}_{m+1}} \tag{A.126}$$

$$\bar{\sigma}^{\,\text{trial}}_{m+1} = \sqrt{\tfrac{3}{2}}|\mathbf{M}^{e\,\text{trial}}_{m+1,0}|, \tag{A.127}$$

so that

$$\mathbf{M}^{e\,\text{trial}}_{m+1,0} = \sqrt{\tfrac{2}{3}}\bar{\sigma}^{\,\text{trial}}_{m+1}\mathbf{N}^{p\,\text{trial}}_{m+1}. \tag{A.128}$$

Then (A.125) may be written as

$$\sqrt{\tfrac{2}{3}}\bar{\sigma}^{\,\text{trial}}_{m+1}\mathbf{N}^{p\,\text{trial}}_{m+1} = (\sqrt{\tfrac{2}{3}}\bar{\sigma}_{m+1} + \sqrt{6}\tilde{G}\Delta t\dot{\bar{\epsilon}}^p_{m+1})\mathbf{N}^p_{m+1} + 2\tilde{G}\Delta t\dot{\xi}_{m+1}\mathbb{S}_{m+1,0}. \tag{A.129}$$

In the above tensorial equation, $\dot{\bar{\epsilon}}^p_{m+1}$, $\mathbf{N}^p_{m+1}$, and $\mathbb{S}_{m+1}$ are unknown. To proceed further, we note from (A.121) that knowledge of $\mathbf{m}_{m+1}$ immediately yields $\mathbb{S}_{m+1}$. We rewrite (3.139) at time t_{m+1} as

$$\mathbf{m}_{m+1} = \frac{\mathbf{U}^{e\mathsf{T}}_{m+1}\mathbf{R}^{e\mathsf{T}}_{m+1}\mathbf{F}^{-\mathsf{T}}_{m+1}\mathbf{m}_{\mathrm{R}}}{|\mathbf{U}^{e\mathsf{T}}_{m+1}\mathbf{R}^{e\mathsf{T}}_{m+1}\mathbf{F}^{-\mathsf{T}}_{m+1}\mathbf{m}_{\mathrm{R}}|}, \tag{A.130}$$

where we have made use of the multiplicative decomposition of $\mathbf{F}$, and the polar decomposition of $\mathbf{F}^e$. In expression (A.130) for $\mathbf{m}_{m+1}$, the only unknown is $\mathbf{U}^e_{m+1}$ since $\mathbf{R}^e_{m+1}$ is given from (A.108) (and $\mathbf{F}_{m+1}$ is known from the outset). Taking into consideration the approximation of small time steps (A1), we assume that $\mathbf{U}^e_{m+1}$ may be approximated by its value at the beginning of the step, $\mathbf{U}^e_m$. In this case, we can calculate $\mathbf{m}_{m+1}$ from (A.130) and with (A.108) as

$$\mathbf{m}_{m+1} \doteq \frac{\mathbf{U}^{e\mathsf{T}}_m(\mathbf{R}^{e\,\text{trial}}_{m+1})^{\mathsf{T}}\mathbf{F}^{-\mathsf{T}}_{m+1}\mathbf{m}_{\mathrm{R}}}{|\mathbf{U}^{e\mathsf{T}}_m(\mathbf{R}^{e\,\text{trial}}_{m+1})^{\mathsf{T}}\mathbf{F}^{-\mathsf{T}}_{m+1}\mathbf{m}_{\mathrm{R}}|}, \tag{A.131}$$

which we may substitute into (A.121) to obtain $\mathbb{S}_{m+1,0}$. (The approximation of using $\mathbf{U}^e_m$ instead of $\mathbf{U}^e_{m+1}$ in (A.131) is further legitimized by noting the earlier approximation of small elastic strains (A2); in this case, the tensor U^e is only slightly different from the identity tensor $\mathbf{1}$, and thus has only limited influence on $\mathbf{m}$.)

With $\mathbb{S}_{m+1,0}$ known, two unknowns remain in (A.129), viz. $\dot{\bar{\epsilon}}^p_{m+1}$ and $\mathbf{N}^p_{m+1}$. We now proceed to reduce (A.129) to a scalar equation in which only $\dot{\bar{\epsilon}}^p_{m+1}$ occurs as an unknown.

To this end, we introduce the definitions

$$\begin{aligned} a_0 &= \mathbf{N}^{p\,\text{trial}}_{m+1} : \mathbb{S}_{m+1,0}, \\ a_1 &= \mathbf{N}^{p\,\text{trial}}_{m+1} : \mathbf{N}^{p}_{m+1}, \\ a_2 &= \mathbf{N}^{p}_{m+1} : \mathbb{S}_{m+1,0}. \end{aligned} \tag{A.132}$$

Next, we contract (A.129) with $\mathbf{N}^{p\,\text{trial}}_{m+1}$, which gives

$$\sqrt{\tfrac{2}{3}}\bar{\sigma}^{\,\text{trial}}_{m+1} = (\sqrt{\tfrac{2}{3}}\bar{\sigma}_{m+1} + \sqrt{6}\tilde{G}\Delta t\dot{\bar{\epsilon}}^{p}_{m+1})a_1 + 2\tilde{G}\Delta t\dot{\xi}_{m+1}a_0, \tag{A.133}$$

and solving for a_1, we obtain

$$a_1 = \frac{\sqrt{\frac{2}{3}}\bar{\sigma}^{\,\text{trial}}_{m+1} - 2\tilde{G}\Delta t\dot{\xi}_{m+1}a_0}{\sqrt{\frac{2}{3}}\bar{\sigma}_{m+1} + \sqrt{6}\tilde{G}\Delta t\dot{\bar{\epsilon}}^{p}_{m+1}}.. \tag{A.134}$$

Similarly, we now contract (A.129) with $\mathbf{N}^{p}_{m+1}$; the resulting expression can then be solved for a_2, yielding

$$a_2 = \frac{\bar{\sigma}^{\,\text{trial}}_{m+1}a_1 - \bar{\sigma}_{m+1} - \sqrt{3}\tilde{G}\Delta t\dot{\bar{\epsilon}}^{p}_{m+1}}{\sqrt{6}\tilde{G}\Delta t\dot{\xi}_{m+1}}. \tag{A.135}$$

Finally we also contract (A.129) with $\mathbb{S}_{m+1,0}$. With

$$\mathbb{S}_{m+1,0} : \mathbb{S}_{m+1,0} = \tfrac{2}{3}(\beta_p - \beta_l) \tag{A.136}$$

and using relations (A.134) and (A.135), after some algebra we obtain the expression

$$(\bar{\sigma}_{m+1} + 3\tilde{G}\Delta t\dot{\bar{\epsilon}}^{p}_{m+1})^2 - (\bar{\sigma}^{\,\text{trial}}_{m+1})^2 + 2\tilde{G}\Delta t\dot{\xi}_{m+1}(\sqrt{6}\bar{\sigma}^{\,\text{trial}}_{m+1}a_0 - 2\tilde{G}\Delta t\dot{\xi}_{m+1}(\beta_p - \beta_l)) = 0, \tag{A.137}$$

which can be rewritten as

$$\bar{\sigma}_{m+1} + 3\tilde{G}\Delta t\dot{\bar{\epsilon}}^{p}_{m+1} - \sqrt{(\bar{\sigma}^{\,\text{trial}}_{m+1})^2 - 2\tilde{G}\Delta t\dot{\xi}_{m+1}(\sqrt{6}\bar{\sigma}^{\,\text{trial}}_{m+1}a_0 - 2\tilde{G}\Delta t\dot{\xi}_{m+1}(\beta_p - \beta_l))} = 0. \tag{A.138}$$

Now, from (3.167) and (3.143), $\dot{\bar{\epsilon}}^{p}_{m+1}$ in (A.138) is given by

$$\dot{\bar{\epsilon}}^{p}_{m+1} = \begin{cases} (\dot{\bar{\epsilon}}^{p}_{\text{bc}})_{m+1} & \text{if} \quad \xi_{m+1} = 0, \\ (\dot{\bar{\epsilon}}^{p}_{\text{ox}})_{m+1} & \text{otherwise.} \end{cases} \tag{A.139}$$

If we substitute (A.139) into (A.138) and use the appropriate one of the flow functions (3.164) and (3.165) solved for $\bar{\sigma}$, we obtain an expression that contains only one unknown: $(\dot{\bar{\epsilon}}^{p}_{\text{bc}})_{m+1}$ or $(\dot{\bar{\epsilon}}^{p}_{\text{ox}})_{m+1}$ (depending on the value of ξ_{m+1}). Equation (A.138) then needs to be solved implicitly for this unknown. Once we have this result, $\dot{\bar{\epsilon}}^{p}_{m+1}$ is determined from (A.139).

The direction $\mathbf{N}^{p}_{m+1}$ can now easily be determined by solving (A.129) for the desired quantity, taking into account that from (A.84), $\mathbf{N}^{p}_{m+1} = \mathbf{0}$

The direction $\mathbf{N}^p_{m+1}$ can now easily be determined by solving (A.129) for the desired quantity, giving

$$\mathbf{N}^p_{m+1} = \left(\frac{1}{\bar{\sigma}_{m+1} + 3\tilde{G}\Delta t \dot{\bar{\epsilon}}^p_{m+1}} \right) (\bar{\sigma}^{\text{trial}}_{m+1} \mathbf{N}^{p\,\text{trial}}_{m+1} - \sqrt{6}\tilde{G}\Delta t \dot{\xi}_{m+1} \mathbb{S}_0) \qquad \text{for} \qquad \dot{\bar{\epsilon}}^p_{m+1} > 0. \tag{A.140}$$

(In the case of $\dot{\bar{\epsilon}}^p_{m+1} = 0$, $\mathbf{N}^p_{m+1}$ is not needed for the calculation of $\mathbf{D}^i_{m+1}$, cf. (A.82).)

$\mathbf{F}^i_m$ may now readily be updated using the mapping $(A.85)_1$. With $\mathbf{F}^i_{m+1}$ known, the Kroner-Lee decomposition of $\mathbf{F}$,

$$\mathbf{F} = \mathbf{F}^e \mathbf{F}^i,$$

gives the elastic deformation gradient at t_{m+1}, which can be used to compute $\mathbf{M}^e_{m+1}$. This completes the integration procedure for $\mathbf{F}^i$.

A.6 Estimate for derivatives $\partial \mathbf{T}/\partial \mathbf{F}$ and $\partial \mathbf{T}/\partial \vartheta$

Apart from the above integration procedure, we also need to compute an estimate of the tensors $\frac{\partial \mathbf{T}}{\partial \mathbf{F}}$ and $\frac{\partial \mathbf{T}}{\partial \vartheta}$ at time t_{m+1} for the stiffnesses K^u_{AiBk} and $K^{u\vartheta}_{AiB}$ in (A.19) and (A.23), respectively.

A.6.1 $\partial \mathbf{T}/\partial \mathbf{F}$

Based on experience with plasticity theories, we assume that $\frac{\partial \mathbf{T}_{m+1}}{\partial \mathbf{F}_{m+1}}$ can be reasonably well approximated by taking the derivative of the updated Mandel stress $\mathbf{M}^e_{m+1}$ from (A.120) with respect to the trial elastic strain $\mathbf{E}^{e\,\text{trial}}_{m+1}$:

$$\frac{\partial \mathbf{T}_{m+1}}{\partial \mathbf{F}_{m+1}} \doteq \frac{\partial \mathbf{M}^e_{m+1}}{\partial \mathbf{E}^{e\,\text{trial}}_{m+1}}. \tag{A.141}$$

An approximation to the derivative $\frac{\partial \mathbf{M}^e_{m+1}}{\partial \mathbf{E}^{e\,\text{trial}}_{m+1}}$ has been worked out in Weber and Anand (1990); we follow their work closely in the following.[1]

We start by denoting the sought-after expression by

$$\bar{\mathbb{C}} = \frac{\partial \mathbf{M}^e_{m+1}}{\partial \mathbf{E}^{e\,\text{trial}}_{m+1}}. \tag{A.142}$$

As discussed in Section A.4, the rate $\dot{\xi}_{m+1}$ (and updated value ξ_{m+1}) is computed without knowledge of $\mathbf{E}^e_{m+1}$, or equivalently, $\mathbf{E}^{e\,\text{trial}}_{m+1}$; and since all other factors in the terms in (A.120)

[1] It is important to note that any approximations in the expression for the global tangent matrix, which is computed by Abaqus using the stiffnesses provided by the subroutine UEL, *do not affect the accuracy of the solution*, but only the rate of convergence.

containing $\dot{\xi}_{m+1}$ are constants, these terms do not appear in $\bar{\mathbb{C}}$.[2] We thus have

$$\bar{\mathbb{C}} = \frac{\partial \mathbf{M}_{m+1}^{e\ \text{trial}}}{\partial \mathbf{E}_{m+1}^{e\ \text{trial}}} - \sqrt{2}\tilde{G}\Delta t \left[\tfrac{3}{2}\dot{\bar{\epsilon}}^p \frac{\partial \mathbf{N}_{m+1}^p}{\partial \mathbf{E}_{m+1}^{e\ \text{trial}}} + \mathbf{N}_{m+1}^p \otimes \frac{\partial \dot{\bar{\epsilon}}_{m+1}^p}{\partial \mathbf{E}_{m+1}^{e\ \text{trial}}} \right]. \tag{A.143}$$

The first term in (A.143) is simply equal to the fourth-order elasticity tensor:

$$\frac{\partial \mathbf{M}_{m+1}^{e\ \text{trial}}}{\partial \mathbf{E}_{m+1}^{e\ \text{trial}}} = \mathbb{C}. \tag{A.144}$$

Next, taking derivatives of (A.126) and (A.127) (with (A.111)) gives

$$\frac{\partial \mathbf{N}_{m+1}^{p\ \text{trial}}}{\partial \mathbf{E}_{m+1}^{e\ \text{trial}}} = \frac{\sqrt{6}\tilde{G}}{\bar{\sigma}_{m+1}^{\text{trial}}} \left[(\mathbb{I} - \tfrac{1}{3}\mathbf{I} \otimes \mathbf{I}) - \mathbf{N}_{m+1}^{p\ \text{trial}} \otimes \mathbf{N}_{m+1}^{p\ \text{trial}} \right] \tag{A.145}$$

and

$$\frac{\partial \bar{\sigma}_{m+1}^{\text{trial}}}{\partial \mathbf{E}_{m+1}^{e\ \text{trial}}} = \sqrt{6}\tilde{G}\mathbf{N}_{m+1}^{p\ \text{trial}}, \tag{A.146}$$

respectively. In that case, we can find the derivative $\partial \mathbf{N}_{m+1}^p / \partial \mathbf{E}_{m+1}^{e\ \text{trial}}$ from (A.140) by making use of (A.145) and (A.146), and the chain and product rules. After some algebra, we obtain

$$\frac{\partial \mathbf{N}_{m+1}^p}{\partial \mathbf{E}_{m+1}^{e\ \text{trial}}} = \frac{\sqrt{6}\tilde{G}}{\sqrt{(\bar{\sigma}_{m+1}^{\text{trial}})^2 - \tilde{B}\bar{\sigma}_{m+1}^{\text{trial}} + \tilde{C}}} \left[(\mathbb{I} - \tfrac{1}{3}\mathbf{I} \otimes \mathbf{I}) - \frac{2\bar{\sigma}_{m+1}^{\text{trial}} - \tilde{B}}{2\sqrt{(\bar{\sigma}_{m+1}^{\text{trial}})^2 - \tilde{B}\bar{\sigma}_{m+1}^{\text{trial}} + \tilde{C}}} \left(\mathbf{N}_{m+1}^p \otimes \mathbf{N}_{m+1}^{p\ \text{trial}} \right) \right], \tag{A.147}$$

with $\tilde{B}$ and $\tilde{C}$ given by

$$\tilde{B} = 2\sqrt{6}\tilde{G}\Delta t \dot{\xi}_{m+1} a_0, \quad \tilde{C} = 4(\tilde{G}\Delta t \dot{\xi}_{m+1})^2 (\beta_p - \beta_l), \tag{A.148}$$

respectively. Finally, we need to determine $\partial \dot{\bar{\epsilon}}_{m+1}^p / \partial \mathbf{E}_{m+1}^{e\ \text{trial}}$. For this, we first linearize (A.138), which with (A.148) gives

$$d\bar{\sigma}_{m+1} + 3\tilde{G}\Delta t\, d\dot{\bar{\epsilon}}_{m+1}^p - \frac{2\bar{\sigma}_{m+1}^{\text{trial}} - \tilde{B}}{2\sqrt{(\bar{\sigma}_{m+1}^{\text{trial}})^2 - \tilde{B}\bar{\sigma}_{m+1}^{\text{trial}} + \tilde{C}}} d\bar{\sigma}_{m+1}^{\text{trial}} = 0. \tag{A.149}$$

Noting that

$$d\dot{\bar{\epsilon}}_{m+1}^p = \frac{\partial \dot{\bar{\epsilon}}_{m+1}^p}{\partial \bar{\sigma}_{m+1}} d\bar{\sigma}_{m+1}, \tag{A.150}$$

[2] The modified elastic moduli $\tilde{G}$ and $\tilde{K}$ depend on J_{m+1}^i, which is determined by ξ_{m+1} through (A.112). Since ξ_{m+1} does not depend on $\mathbf{E}_{m+1}^{e\ \text{trial}}$ (cf. Section A.4), neither do the modified elastic moduli.

where $\partial\dot{\bar{\epsilon}}^p_{m+1}/\partial\bar{\sigma}_{m+1}$ can be found by taking the derivative of the combination of (3.143) with (3.164) and (3.165), we can solve (A.149) for $d\bar{\sigma}_{m+1}$ in terms of $d\bar{\sigma}^{\text{trial}}_{m+1}$, which yields

$$d\bar{\sigma}_{m+1} = \frac{c_{m+1}(2\bar{\sigma}^{\text{trial}}_{m+1} - \tilde{B})}{2\sqrt{(\bar{\sigma}^{\text{trial}}_{m+1})^2 - \tilde{B}\bar{\sigma}^{\text{trial}}_{m+1} + \tilde{C}}}\, d\bar{\sigma}^{\text{trial}}_{m+1} \tag{A.151}$$

with

$$c_{m+1} = \frac{1}{1 + 3\tilde{G}\Delta t \dfrac{\partial\dot{\bar{\epsilon}}^p_{m+1}}{\partial\bar{\sigma}_{m+1}}}. \tag{A.152}$$

Substituting (A.151) back into (A.149) then gives $d\dot{\bar{\epsilon}}^p_{m+1}$ in terms of $d\bar{\sigma}^{\text{trial}}_{m+1}$:

$$d\dot{\bar{\epsilon}}^p_{m+1} = (1 - c_{m+1})\frac{(2\bar{\sigma}^{\text{trial}}_{m+1} - \tilde{B})}{6\tilde{G}\Delta t\sqrt{(\bar{\sigma}^{\text{trial}}_{m+1})^2 - \tilde{B}\bar{\sigma}^{\text{trial}}_{m+1} + \tilde{C}}}\, d\bar{\sigma}^{\text{trial}}_{m+1}. \tag{A.153}$$

From this expression and with (A.146), we finally obtain

$$\frac{\partial\dot{\bar{\epsilon}}^p_{m+1}}{\partial\mathbf{E}^{e\,\text{trial}}_{m+1}} = \frac{\sqrt{6}}{6}\frac{1 - c_{m+1}}{\Delta t}\frac{2\bar{\sigma}^{\text{trial}}_{m+1} - \tilde{B}}{\sqrt{(\bar{\sigma}^{\text{trial}}_{m+1})^2 - \tilde{B}\bar{\sigma}^{\text{trial}}_{m+1} + \tilde{C}}}\mathbf{N}^{p\,\text{trial}}_{m+1}. \tag{A.154}$$

We can now substitute the expressions (A.144), (A.147), and (A.154) into (A.143). After rearranging, we then arrive at the final result

$$\bar{\mathbb{C}} = \mathbb{A} - \alpha_J \mathbf{N}^p_{m+1} \otimes \mathbf{N}^{p\,\text{trial}}_{m+1}, \tag{A.155}$$

with

$$\mathbb{A} = 2\tilde{G}\frac{\bar{\sigma}_{m+1}}{\sqrt{(\bar{\sigma}^{\text{trial}}_{m+1})^2 - \tilde{B}\bar{\sigma}^{\text{trial}}_{m+1} + \tilde{C}}}(\mathbb{I} - \mathbf{I}\otimes\mathbf{I}) + \tilde{K}(\mathbf{I}\otimes\mathbf{I}) \tag{A.156}$$

and

$$\alpha_J = \tilde{G}\frac{2\bar{\sigma}^{\text{trial}}_{m+1} - \tilde{B}}{\sqrt{(\bar{\sigma}^{\text{trial}}_{m+1})^2 - \tilde{B}\bar{\sigma}^{\text{trial}}_{m+1} + \tilde{C}}}\left[\frac{\bar{\sigma}_{m+1}}{\sqrt{(\bar{\sigma}^{\text{trial}}_{m+1})^2 - \tilde{B}\bar{\sigma}^{\text{trial}}_{m+1} + \tilde{C}}} - c_{m+1}\right], \tag{A.157}$$

where we have from (A.141) that

$$\frac{\partial\mathbf{T}_{m+1}}{\partial\mathbf{F}_{m+1}} \doteq \bar{\mathbb{C}}. \tag{A.158}$$

Remark: In the approximation (A.141), note that the Cauchy stress $\mathbf{T}_{m+1}$ is a quantity in the *current configuration*, while the Mandel stress $\mathbf{M}^e_{m+1}$ is a quantity in the *intermediate space*; therefore, if there are *large rotations* between the intermediate and current configurations, convergence may be affected negatively. In our simulations, we have found the heuristic remedy for this issue of simply *rotating the plastic directions* $\mathbf{N}^{p\,\text{trial}}_{m+1}$ and $\mathbf{N}^p_{m+1}$ by the elastic rotation $\mathbf{R}^e_{m+1}$ and calculating a modified Jacobian with these *directions of*

plastic flow in the current configuration. This modified Jacobian $\bar{\mathbb{C}}_{\text{mod}}$ can be calculated by computing the rotated plastic directions,

$$\tilde{\mathbf{N}}^p_{m+1} = \mathbf{R}^e_{m+1}\mathbf{N}^p_{m+1}\mathbf{R}^{e\mathsf{T}}_{m+1}, \qquad \tilde{\mathbf{N}}^{p\,\text{trial}}_{m+1} = \mathbf{R}^e_{m+1}\mathbf{N}^{p\,\text{trial}}_{m+1}\mathbf{R}^{e\mathsf{T}}_{m+1}; \tag{A.159}$$

in analogy to (A.155), $\bar{\mathbb{C}}_{\text{mod}}$ is then given by

$$\bar{\mathbb{C}}_{\text{mod}} = \mathbb{A} - \alpha_J \tilde{\mathbf{N}}^p_{m+1} \otimes \tilde{\mathbf{N}}^{p\,\text{trial}}_{m+1}, \tag{A.160}$$

with $\mathbb{A}$ and α_J calculated as before from (A.156) and (A.157), respectively. Where suitable, this modified Jacobian $\bar{\mathbb{C}}_{\text{mod}}$ was used in place of $\bar{\mathbb{C}}$.

A.6.2 $\partial\mathbf{T}/\partial\vartheta$

For the derivative $\partial\mathbf{T}/\partial\vartheta$ at time t_{m+1}, we make the approximation that

$$\frac{\partial\mathbf{T}_{m+1}}{\partial\vartheta_{m+1}} \doteq \frac{\partial\mathbf{M}^{e\,\text{trial}}_{m+1}}{\partial\vartheta_{m+1}}. \tag{A.161}$$

In this case, with (A.115) and neglecting the dependence of the thermoelastic material properties on temperature, we have that

$$\frac{\partial\mathbf{T}_{m+1}}{\partial\vartheta_{m+1}} \doteq -3\tilde{K}\alpha\mathbf{1}. \tag{A.162}$$

A.7 Description of the element

A linear, reduced-integration, two-dimensional, four-noded element was implemented; it is shown in Fig A-3. The corresponding shape functions in natural coordinates ξ_e, η_e are given by

$$N_1 = \tfrac{1}{4}(1-\xi_e)(1-\eta_e), \tag{A.163}$$
$$N_2 = \tfrac{1}{4}(1+\xi_e)(1-\eta_e), \tag{A.164}$$
$$N_3 = \tfrac{1}{4}(1+\xi_e)(1+\eta_e), \tag{A.165}$$
$$N_4 = \tfrac{1}{4}(1-\xi_e)(1+\eta_e). \tag{A.166}$$

There are three types of elements:

(i) Plane strain;

(ii) Generalized plane strain;

(iii) Axisymmetry.

Details for these cases are given in the following Sections. We then also discuss hourglass control.

A.7.1 Plane strain

We take the 3-direction to be the out-of-plane direction. Then, in the present case, the following restrictions apply to the deformation gradient $\mathbf{F}$:

$$F_{33} = 1, \quad F_{13} = F_{23} = F_{31} = F_{32} = 0. \tag{A.167}$$

A.7.2 Generalized plane strain

Again with the 3-direction as the out-of-plane direction, as before we have

$$F_{13} = F_{23} = F_{31} = F_{32} = 0. \tag{A.168}$$

The component F_{33}, however, is allowed to vary *in time*, but *not in space*:

$$F_{33} = \hat{F}_{33}(t), \tag{A.169}$$

where the function $\hat{F}_{33}(t)$ is *prescribed at all times.*

This assumption is useful when modeling an out-of-plane expansion or contraction that is imposed on a two-dimensional structure, such as, e.g., two-dimensional surface features that follow the thermal contraction of a substrate.

A.7.3 Axisymmetry

For this case, we take the radial, axial, and circumferential directions to be the 1-direction, 2-direction, and 3-direction, respectively. We again have

$$F_{13} = F_{23} = F_{31} = F_{32} = 0, \tag{A.170}$$

and, denoting the referential and current radial positions of a material point by R and r, respectively, for F_{33} we have that

$$F_{33} = \frac{r}{R}. \tag{A.171}$$

These radial positions can be calculated as

$$R = N_A X_1^A, \quad r = N_A x_1^A \tag{A.172}$$

with X_1^A and x_1^A the referential and current positions of node A in the 1-direction, respectively.

Further, we denote the referential and current axial position of a material point by Z and z, respectively. With this nomenclature, volume integrals for the present case are evaluated as follows:

$$\int ()\, dV_{\mathrm{R}} = \int ()\, 2\pi R\, dR\, dZ, \qquad \int ()\, dV = \int ()\, 2\pi r\, dr\, dz. \tag{A.173}$$

A.7.4 Hourglass control

Hourglass control was achieved in the following way: since Abaqus does not support graphical output of user element simulations, in order to obtain such graphical output the simulation needs to be run with an additional mock mesh of Abaqus built-in elements whose motion is constrained to be the same as the one of the real mesh (consisting of user elements). The mock mesh is given almost zero stiffness so as not to influence the motion of the real mesh; however, the elements of the mock mesh are given a suitable hourglass stiffness in order to prevent this phenomenon on both the real and the mock mesh.

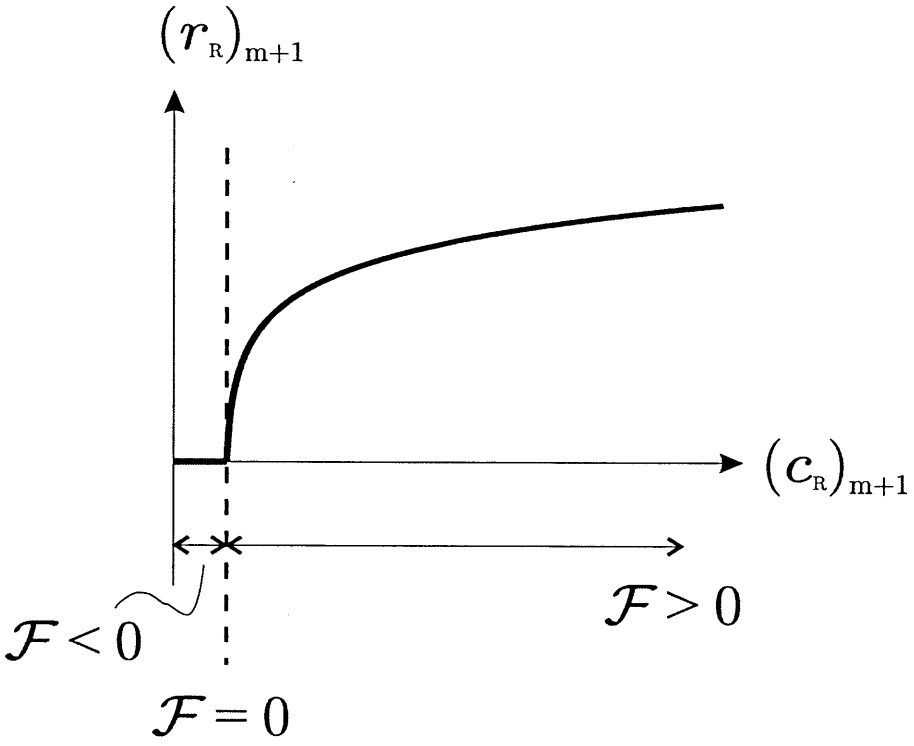

Figure A-1: Dependence of $(r_R)_{m+1}$ on $(c_R)_{m+1}$ from theory.

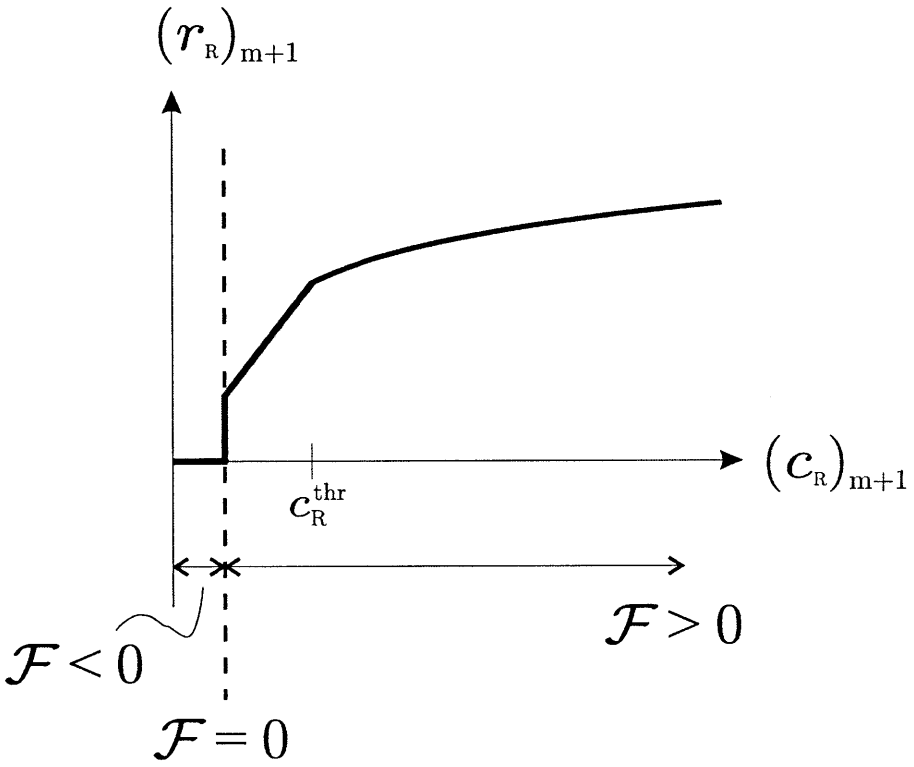

Figure A-2: Dependence of $(r_R)_{m+1}$ on $(c_R)_{m+1}$ as implemented, with a linear relationship for the region where $\mathcal{F}_{m+1} > 0$ and $(c_R)_{m+1} < c_R^{thr}$.

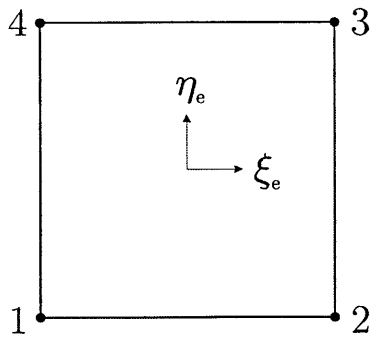

Figure A-3: Schematic of linear finite element with natural coordinates.

Appendix B

Material parameter estimation for coupled theory

In this Appendix we bricfly discuss our procedure for estimating the material parameters appearing in our theory for the FeCrAlY heat-resistant alloy studied by Tolpygo et al. [102, 103]. As stated in Section 4.2, where possible we have used direct literature data, but for those parameters which are not readily available we have used numerical predictions from our theory to approximately match the experimental results for oxide thickness, residual stresses, and specimen elongation from five of the plate-oxidation experiments reported on by Tolpygo et al. [102, 103]. To the best of our knowledge, data for all desired material parameters for FeCrAlY are not available in the literature; under these circumstances data for a similar alloy — in most cases a MCrAlY alloy (where M stands for one or more of the elements Fe, Ni, Co) — was used.

The final set of material parameters are given in Tables 4.1 and 4.2; cf. page 65. In these tables we list the appropriate literature source or whether the parameters were calibrated using the procedures described below. We point out that due to the highly coupled nature of the constitutive theory, our calibration procedure is iterative in nature, and that the final parameter values *are approximate, and most likely not unique.*

B.1 Elastic and thermal properties

We assume linear temperature dependence for the following material parameters: the elastic moduli G_{bc}, K_{bc}, G_{ox}, K_{ox}, and the thermal conductivities κ_{bc}, κ_{ox}:

$$\left.\begin{aligned} G_{\text{bc}} &= G^0_{\text{bc}} + M_1(\vartheta - \vartheta_{\text{ref}}),\\ K_{\text{bc}} &= K^0_{\text{bc}} + M_2(\vartheta - \vartheta_{\text{ref}}),\\ G_{\text{ox}} &= G^0_{\text{ox}} + M_3(\vartheta - \vartheta_{\text{ref}}),\\ K_{\text{ox}} &= K^0_{\text{ox}} + M_4(\vartheta - \vartheta_{\text{ref}}),\\ \kappa_{\text{bc}} &= \kappa^0_{\text{bc}} + M_5(\vartheta - \vartheta_{\text{ref}}),\\ \kappa_{\text{ox}} &= \kappa^0_{\text{ox}} + M_6(\vartheta - \vartheta_{\text{ref}}), \end{aligned}\right\} \tag{B.1}$$

with constants G^0_{bc}, K^0_{bc}, G^0_{ox}, K^0_{ox}, κ^0_{bc}, κ^0_{ox}, and M_1 through M_6. The reference temperature ϑ_{ref} was introduced in (3.166); we choose its value as $\vartheta_{\text{ref}} = 1473\,\text{K}$ ($\equiv 1200°\,\text{C}$). Values for the elastic and thermal properties were taken from literature, and are listed in Table 4.1.

B.2 Properties for diffusion, oxidation, and viscoplasticity

The final values of the material parameters relating to diffusion, oxidation, and viscoplasticity are given in Table 4.2. The parameter estimation procedure is discussed below.

B.2.1 The parameters $\Delta\mu^0, \mathcal{R}, c_{\max}$, and H

We begin by estimating values for the four properties $\Delta\mu^0$, $\mathcal{R}$, $c_{\max}$, and H related to the diffusion boundary conditions and the oxidation reaction.

Estimate for $\Delta\mu^0$:

Expression (3.194) describes the relation between the oxygen concentration at a boundary, $\breve{c}_{\text{R}}$, and the applied oxygen partial pressure p_{O_2}. An experimental measurement of $\breve{\tilde{c}}_{\text{R}} = \breve{c}/c_{\max}$ at a given temperature and oxygen partial pressure thus allows us to determine $\Delta\mu^0$ via (3.194).

Prot and Monty [82] provide such experimental measurements of of $\breve{\tilde{c}}_{\text{R}}$ for Al_2O_3 at various temperatures for $p_{\text{O}_2} = 0.2 - 0.5$ bar. At a temperature of $\vartheta = 1473\,\text{K}$, an upper bound to their estimate is $\breve{\tilde{c}}_{\text{R}} = 5 \times 10^{-5}$. Using $p_{\text{O}_2} = 0.2$ bar ($= 0.02$ MPa)[1] and $\breve{\tilde{c}}_{\text{R}} = 5 \times 10^{-5}$ in (3.194), we can solve for $\Delta\mu^0$ to obtain

$$\Delta\mu^0 \;(\equiv \mu^0_{\text{O}_i}) \;= 112\ \text{kJ/mol}. \tag{B.2}$$

Estimate for $\mathcal{R}$ in the reaction-diffusion equation (3.181):

Our aim here is to determine $\mathcal{R}$ for the oxidation of the *alloy* FeCrAlY. However, it is instructive to first determine $\mathcal{R}$ for a generic *pure metal* M in the oxidation reaction

$$a\text{M} + b\text{O} \rightarrow \text{M}_a\text{O}_b, \tag{B.3}$$

where a and b are stoichiometric coefficients. Consider an infinitesimal referential volume dv_{R} at the beginning of the reaction when $\xi = 0$. Let ρ_M and $\mathcal{M}_M$ denote the the mass density and molar mass of M. Then the total number of moles of M in dv_{R} is

$$n_{\text{M}} = \frac{\rho_{\text{M}}}{\mathcal{M}_{\text{M}}}\, dv_{\text{R}}. \tag{B.4}$$

[1] While Prot and Monty [82] do mention that their experiments were conducted at $p_{\text{O}_2} = 0.2 - 0.5$ bar, they don't specify the *exact* p_{O_2} at which the experiments were performed. For lack of better information, we thus assume their estimate of $\breve{\tilde{c}}_{\text{R}}$ to be valid at $p_{\text{O}_2} = 0.2$ bar.

Once the reaction has completed, that is when $\xi = 1$, from the reaction equation (B.3) we see that an amount b of species O has combined with an amount a of species M to form M_aO_b. Thus, the number of moles n_O of species O consumed in the complete chemical reaction is

$$n_O = \frac{b}{a} n_M = \frac{b}{a} \frac{\rho_M}{\mathcal{M}_M} dv_R. \tag{B.5}$$

Thus,

$$\mathcal{R} \stackrel{\text{def}}{=} \frac{n_O}{dv_R} = \frac{b}{a} \frac{\rho_M}{\mathcal{M}_M}. \tag{B.6}$$

Hence, denoting by

$$c_{R,M} \stackrel{\text{def}}{=} \frac{n_M}{dv_R} = \frac{\rho_M}{\mathcal{M}_M}, \tag{B.7}$$

the *number of moles of M per unit reference volume*, the expression (B.6) for $\mathcal{R}$ may equivalently be written as

$$\mathcal{R} = \frac{b}{a} c_{R,M}. \tag{B.8}$$

Specifically, in the case of oxidation of pure aluminum to aluminum oxide,

$$2Al + \tfrac{3}{2}O_2 \rightarrow Al_2O_3 \tag{B.9}$$

we have

$$\mathcal{R} = \frac{3}{2} c_{R,Al}. \tag{B.10}$$

This completes our discussion for the generic pure metal M.

For our specific purposes, we now need to determine $\mathcal{R}$ for the oxidation of the FeCrAlY alloy. The metallic element which takes part in the oxidation, Al, is one of many components of this alloy; however, the oxide scale that forms consists essentially of pure Al_2O_3 [cf., e.g., 16]. The process that enables this pure Al_2O_3 scale to form is known as *interdiffusion*: Fe and Cr, the other main components of the alloy, diffuse away from the oxidizing region, while additional Al diffuses toward it. Here, we make the simple assumption that

- *the only manner in which interdiffusion manifests itself is that every non-Al atom in the transforming region is replaced by an Al atom.*

Let $c_{R,bc}$ denote the initial number of moles of the bond-coat material per unit reference volume. Our assumption above requires that the number of moles of Al atoms per unit reference volume *after interdiffusion*, $c^*_{R,Al}$, is given by

$$c^*_{R,Al} = c_{R,bc}. \tag{B.11}$$

Next, after the interdiffusion, since all other atoms have diffused away, one may consider the material to now consist of "pure Al." Then, in analogy with our previous expression (B.10), we obtain

$$\mathcal{R} = \tfrac{3}{2} c^*_{R,Al} = \tfrac{3}{2} c_{R,bc} = 0.24 \times 10^6 \text{ mol/m}^3, \tag{B.12}$$

where $c_{R,bc} = 0.16 \times 10^6$ mol/m^3 was taken from Quested et al. [84].

Estimate for $c_{\max}$ in (3.187):

Recall from (3.187) that $c_{\max}$ denotes the number of moles of interstitial sites available to oxygen per unit reference volume. Consider first the possibility of interstitial oxygen, O_i, in a "solid solution" with an unoxidized metal. Such a situation seldom occurs in unoxidized metals because if any oxygen is present in the metal, it will usually immediately form small precipitates of a metal oxide. For this reason it is not suitable to determine $c_{\max}$ by considering the unoxidized bond coat. However, interstitial sites available to oxygen in the *aluminum oxide* scale are easily identified. For Al_2O_3 there is one interstitial site for every three lattice oxygen ions [69]. We assume that $c_{\max}$ is given at all times by its value in the pure Al_2O_3. Since $\mathcal{R}$ reprents the total amount of oxygen consumed per unit reference volume by the oxidation reaction, it also represents the total amount of oxygen per unit reference volume in the fully reacted oxide. Thus, using (B.12), we estimate that

$$c_{\max} = \tfrac{1}{3}\mathcal{R} = \tfrac{1}{2}c_{\mathrm{R,bc}} = 0.08 \times 10^6 \text{ mol/m}^3. \tag{B.13}$$

Estimate for the chemistry modulus H in (3.158):

In order to determine the chemistry modulus H we first introduce the *Gibbs free energy per unit reference volume*

$$\phi_{\mathrm{R}} \stackrel{\text{def}}{=} \psi_{\mathrm{R}} - \tfrac{1}{2}\mathbf{T}^e : \mathbf{C}^e. \tag{B.14}$$

The change in Gibbs free energy *per mole* (here taken to be moles of Al) for the oxidation reaction at a given temperature and atmospheric pressure in air, denoted $\Delta\phi$, may be found tabulated in literature, e.g. from Chase et al. (1985). Converting $\Delta\phi$ which is in units of energy per mol to an energy per unit volume, we obtain

$$\Delta\phi_{\mathrm{R}} = c_{\mathrm{R,bc}}\,\Delta\phi, \tag{B.15}$$

where, as before, we have neglected a change in the amount of moles of bond-coat due to interdiffusion. Since there are no external forces applied to the solid during experimental measurements of $\Delta\phi$, we may set the term $\frac{1}{2}\mathbf{T}^e : \mathbf{C}^e$ in (B.14) to zero, and thus the change in Helmholtz free energy $\Delta\psi_{\mathrm{R}}$ is given by

$$\Delta\psi_{\mathrm{R}} = \Delta\phi_{\mathrm{R}} = c_{\mathrm{R,bc}}\,\Delta\phi\,. \tag{B.16}$$

Next, from (3.158) we see that as ξ varies from 0 to 1 the change in the free energy is

$$\Delta\psi_{\mathrm{R}} = -\tfrac{1}{2}H\,. \tag{B.17}$$

Thus, using (B.17) and (B.16), we may estimate H as

$$H = -2c_{\mathrm{R,bc}}\,\Delta\phi = 387 \text{ GJ/m}^3, \tag{B.18}$$

where the energy $\Delta\phi = -1208$ kJ/mol was taken from Chase Jr. et al. [22].

B.2.2 Calibration procedure for the remaining material parameters for diffusion, oxidation, and plastic deformation of the bond-coat and the oxide

We now turn our attention to a procedure for estimating the remaining material parameters. In order to contain the complexity of the calibration procedure, we first make some simplifying assumptions:

(A1) Recall that the oxygen diffusivities in the bond coat and oxide are given by (3.179), viz.

$$D_{\mathrm{bc}}(\vartheta) = D_{0,\mathrm{bc}} \exp\left(-\frac{Q_{d,\mathrm{bc}}}{R\vartheta}\right), \quad D_{\mathrm{ox}}(\vartheta) = D_{0,\mathrm{ox}} \exp\left(-\frac{Q_{d,\mathrm{ox}}}{R\vartheta}\right).$$

Since the diffusing oxygen, once it has traveled through the oxide to the oxide/bond-coat transition zone, reacts very quickly with the bond coat to form new oxide, it is only the diffusion of oxygen in the *oxide* which is of primary concern. Thus, for our purposes the precise value of the diffusivity of oxygen in the *bond coat* is not of central importance. Here, for simplicity, we assume that these diffusivities are *equal*:

$$D_{0,\mathrm{bc}} = D_{0,\mathrm{ox}}, \qquad Q_{d,\mathrm{bc}} = Q_{d,\mathrm{ox}}. \tag{B.19}$$

(A2) We assume further that the the activation energy for the swelling reaction Q_s (cf. (3.168)) is the same as the one for diffusion of the free oxygen:

$$Q_s = Q_{d,\mathrm{bc}} = Q_{d,\mathrm{ox}}. \tag{B.20}$$

In addition:

- For the viscoplasticity of bond coat we set the reference strength value S_{bc} in (3.164) at $S_{\mathrm{bc}} = 20\,\mathrm{MPa}$.
- For the inelastic response of the oxide described by (3.165), we choose $\dot{\bar{\epsilon}}^0_{\mathrm{ox}} = 0.001\mathrm{s}^{-1}$ as the reference strain rate, and take $m_{\mathrm{ox}} = 0.005$ to approximate an essentially rate-independent plastic response for the oxide.

The material parameters that remain to be calibrated are:

- The oxygen diffusivities and material parameters for the evolution of ξ in (3.168), as specified in the list

$$\Xi_1 = (D_{0,\mathrm{ox}}, Q_{d,\mathrm{ox}}, C_\xi). \tag{B.21}$$

These are calibrated by matching the experimentally-measured oxide thickness evolution given in Tolpygo et al. [103].

- Material parameters related to viscoplastic properties of the bond-coat and the oxide, as well as those related to inelastic swelling, as specified in the list

$$\Xi_2 = (A_{\mathrm{bc}}, Q_{\mathrm{bc}}, m_{\mathrm{bc}}, S^0_{\mathrm{ox}}, M_{\mathrm{ox}}, \beta_l). \tag{B.22}$$

These are calibrated by matching the experimentally-measured residual stresses and specimen elongations given in Tolpygo et al. [103].

Regarding the swelling due to oxidation, we know that the total amount will be given by J_{PB}, which for aluminum oxide is $J_{\mathrm{PB}} = 1.28$ [81]. However, we still need to quantify how much of it will be in the in-plane direction, that is, we need to calibrate β_l; once this is done, β_p can then be determined from $(3.138)_2$.

Our procedure for estimating the material parameter lists Ξ_1 and Ξ_2 is *iterative* in nature and discussed below.

Step 1: Preliminary calibration of the parameter list Ξ_1

The evolution of the oxide thickness depends on the continuous supply of oxygen diffusing to the reaction zone between the oxide/bond-coat interface and on the kinetics of the reaction that takes place there. These two processes are described by equations (3.181) and (3.168), respectively.

We now aim to determine a preliminary set of the parameters in Ξ_1 by calibrating them against experimental data of oxide thickness evolution as a function of temperature and time from Tolpygo et al. [103]. In order to perform this calibration we need approximate values for the parameters in Ξ_2. Based on experience with metal creep, and existing data in the literature [43], we make the following guess:

$$A_{\mathrm{bc}} = 1.4 \times 10^8 \text{ 1/s}, \quad Q_{\mathrm{bc}} = 282 \text{ kJ/mol}, \quad m_{\mathrm{bc}} = 0.25. \tag{B.23}$$

The plastic flow resistance of the oxide and its temperature-dependence is estimated using hardness data from Krell and Bakun [66], which gives

$$S^0_{\mathrm{ox}} = 1850 \text{ MPa}, \quad M_{\mathrm{ox}} = -3.63 \text{ MPa/K}. \tag{B.24}$$

Also, Tolpygo et al. [103] show that β_l is roughly between 0 and 5 per cent, and we accordingly use $\beta_l = 0.02$ as a first estimate.

For a first estimate of values for Ξ_1, it is easiest to guess a value for the total diffusivity $D_{\mathrm{ox},1}$ for a certain temperature, say $\vartheta_1 = 1473\,\mathrm{K}$, and choose a suitably large value of C_ξ.[2] Once there is approximate agreement of oxide thickness evolution between simulations and experiment at $\vartheta_1 = 1473\,\mathrm{K}$, we consider oxide thickness evolution at a second temperature $\vartheta_2 = 1373\,\mathrm{K}$. and estimate the total diffusivity $D_{\mathrm{ox},2}$ at this temperature. With D_{ox} known at two temperatures, it is straightforward to calculate the reference value $D_{0,\mathrm{ox}}$ and the activation energy for diffusion $Q_{d,\mathrm{ox}}$, using

$$Q_{d,\mathrm{ox}} = R\left(\frac{1}{\vartheta_2} - \frac{1}{\vartheta_1}\right)^{-1} \ln\left(\frac{D_{\mathrm{ox},1}}{D_{\mathrm{ox},2}}\right), \quad D_{0,\mathrm{ox}} = D_{\mathrm{ox},1} \exp\left(\frac{Q_{d,\mathrm{ox}}}{R\vartheta_1}\right). \tag{B.25}$$

[2]The precise value of C_ξ at this stage does not matter greatly as long as it is chosen large enough so that the oxidation process is "diffusion-limited" — as observed in experiment.

Reasonable agreement between simulation and experiment for oxide thickness evolution is found with the material parameters

$$D_{0,\text{ox}} = 7.5 \times 10^{-9}\ \text{m}^2/\text{s}, \quad Q_{d,\text{ox}} = 100\ \text{kJ/mol}, \quad \text{and} \quad C_\xi = 1.8 \times 10^{-6}\ 1/(\text{MPa}\times\text{s}). \tag{B.26}$$

We note that our estimates above were arrived at by conducting simulations for a plate thickness of $2h = 0.90\,\text{mm}$ at 1473 K, and $2h = 0.89\,\text{mm}$ at 1373 K. However, other plate thicknesses give nearly identical results.

Step 2: Preliminary calibration of parameter list $\Xi_{2a} = (\beta_l, S^0_{\text{ox}}, M_{\text{ox}})$

We next perform a preliminary calibration of the material parameters

$$\Xi_{2a} = (\beta_l, S^0_{\text{ox}}, M_{\text{ox}}), \tag{B.27}$$

which govern the swelling due to oxidation and the plastic flow of the oxide. In this step, we will retain the assumptions (B.23).

First, we also retain the previous assumption $M_{\text{ox}} = -3.63$ MPa/K for the temperature-dependence of the plastic flow resistance of the oxide, and consider the permanent elongational strains after cool-down for plates of thickness $2h = 0.43\,\text{mm}$ and $2h = 4.04\,\text{mm}$ for a dwell temperature of 1473 K. The oxide flow resistance S^0_{ox} mainly governs the absolute amount of strain developed for both plate thicknesses, while the lateral growth strain parameter β_l governs how big the strain difference is between the thicker and the thinner plate. Therefore, S^0_{ox} and β_l can be adjusted in a trial-and-error fashion until the simulations and experiments for the elongational strains after cool-down match. Reasonable agreement is obtained for

$$\beta_l = 0.03 \quad \text{and} \quad S^0_{\text{ox}} = 2010\ \text{MPa}. \tag{B.28}$$

Next, to determine M_{ox}, we consider strain after cool-down for $2h = 0.61\,\text{mm}$ at a dwell temperature of 1373 K. There is close agreement between simulation and experiment for the previously assumed value of $M_{\text{ox}} = -3.63$ MPa/K, and therefore this value is kept. If, however, there were a need to adjust the simulation results at this lower dwell temperature, this could be achieved by changing M_{ox}.

In summary, in the preliminary calibrations of Step 1 and Step 2 we have thus obtained the following estimates:

$$\begin{aligned} \Xi_1 &: \quad D_{0,\text{ox}} = 7.5 \times 10^{-9}\ \text{m}^2/\text{s}, \quad Q_{d,\text{ox}} = 100\ \text{kJ/mol}, C_\xi = 1.8 \times 10^{-6}\ 1/(\text{MPa}\times\text{s}); \\ \Xi_{2a} &: \quad \beta_l = 0.03, \quad S^0_{\text{ox}} = 2010\ \text{MPa/K}, \quad M_{\text{ox}} = -3.63\ \text{MPa/K}. \end{aligned} \tag{B.29}$$

Step 3: Calibration of the parameter list $\Xi_{2b} = (A_{\text{bc}}, m_{\text{bc}}, Q_{\text{bc}})$. Final calibration

Our next step is to calibrate the bond-coat creep properties

$$\Xi_{2b} = (A_{\text{bc}}, m_{\text{bc}}, Q_{\text{bc}}). \tag{B.30}$$

First, we will keep the previously assumed values $m_{\text{bc}} = 0.25$ and $Q_{\text{bc}} = 282$ kJ/mol in (B.23), and attempt to estimate A_{bc}. For this purpose, we take the experimental measurement of residual stress after cool-down from a dwell temperature of 1473 K for a plate-thickness of $2h = 4.04$ mm. When changing the value of A_{bc} during the calibration, care has to be exerted because of the following fact: in Step 2, we had obtained agreement between simulated and experimental results for plate elongation; however, if the bond-coat creep rate is now changed, this agreement will no longer hold. This issue can be resolved by not only adjusting A_{bc}, but also (again) S^0_{ox}. For example, if the propensity for plastic deformation in both the bond-coat and oxide is increased at the same time, the stresses in the oxide scale will decrease while approximately keeping the elongation constant. Performing the calibration in this fashion, we obtain reasonable agreement of the stress values for

$$A_{\text{bc}} = 48 \times 10^3 \text{ 1/s}, \quad S^0_{\text{ox}} = 2405 \text{ MPa/K}. \tag{B.31}$$

Next, we again simulate the two other conditions considered in Step 2 (0.43 mm at 1473 K; 0.61 mm at 1373 K) to check if simulations and experiments match satisfactorily for the chosen values of A_{bc} and S^0_{ox}. This is the case here; however, if it were not, these two other conditions would need to be considered here as well when choosing A_{bc} and S^0_{ox}.

The parameters m_{ox} and Q_{bc} have so far not been adjusted, yet we have found reasonable correspondence between simulation and experiment. We therefore keep their values permanently. (Again, if agreement cannot be obtained with such guesses, they would also have to be adjusted during calibration).

At this point, all parameters in the lists Ξ_1 and Ξ_2 have been determined. For completeness, we again check if the oxide thickness evolutions from simulation (as discussed in Step 1) still match the experiments since the mechanical parameters have been adjusted after Step 1. Since the influence of these parameters on oxide thickness evolution is small, agreement is still satisfactory.

The calibration procedure for Ξ_1 and Ξ_2 is thus complete. In summary, the lists Ξ_1 and Ξ_2 contain the following values:

$$\begin{aligned}
\Xi_1: &\quad D_{0,\text{ox}} = 7.5 \times 10^{-9} \text{ m}^2/\text{s}, \quad Q_{d,\text{ox}} = 100 \text{ kJ/mol}, C_\xi = 1.8 \times 10^{-6} \text{ 1/(MPa×s)}; \\
\Xi_2: &\quad A_{\text{bc}} = 48 \times 10^3 \text{ 1/s}, \quad Q_{\text{bc}} = 282 \text{ kJ/mol}, \quad m_{\text{bc}} = 0.25, \\
&\quad S^0_{\text{ox}} = 2405 \text{ MPa/K}, \quad M_{\text{ox}} = -3.63 \text{ MPa/K}, \quad \beta_l = 0.03.
\end{aligned} \tag{B.32}$$

We now examine more closely some of the calibrated material parameters (see Table 4.2). In the temperature range 1373 K to 1573 K:

- The calibrated diffusivity of free oxygen in the oxide, D_{ox}, ranges from $1.2 - 3.6 \times 10^{-12}$ m^2/s. This compares with a value of $2.3 \times 10^{-14} - 1.6 \times 10^{-12}$ m^2/s reported by Frost and Ashby [44] for oxygen diffusivity via grain boundaries in alumina.

- We have calibrated the activation energy for oxygen diffusion in the oxide as $Q_{d,\text{ox}} = 100$ kJ/mol. Reports on this value in literature vary: Frost and Ashby [44] estimate 380 kJ/mol for grain-boundary transport, while the experiments of Oishi and Kingery [79] on polycrystalline alumina between 1473 K and 1573 K indicate it as 119 kJ/mol.

- The bond-coat viscoplasticity parameters at a stress level of $\bar{\sigma} = 20$ MPa in this temperature range predict an equivalent tensile plastic strain rate of $\dot{\epsilon}_{bc} = 0.9 - 21 \times 10^{-6}$ 1/s, which represents a reasonable value for a high-temperature alloy.

- For the oxide plasticity in the same temperature range, we calibrated a flow resistance S_{ox} which varies between 2.0 to 2.8 GPa. This compares with an estimate for S_{ox} between 1.5 and 2.2 GPa obtained by Krell and Bakun [66] (we have converted their original hardness data into a tensile flow resistance).

- Finally, the calibrated lateral swelling strain of $\beta_l = 0.03$ agrees with Tolpygo et al. [103], who estimate it to lie between zero and 0.05.

Appendix C

FeCrAlY oxidation: relative contributions of individual phenomena to the overall response – a parametric study

The theory formulated here is highly non-linear and involves strong coupling between many mechanisms. One of the major benefits of a numerical implementation of a coupled theory is that one can identify the relative contribution of a particular mechanism to the overall response by just switching it on or off, or by varying the numerical parameters representing a particular mechanism in the simulations. In what follows we conduct a brief parametric study to assess the relative importance of the major ingredients of the coupled theory. Specifically, we examine the effects of:

(a) Neglecting transient heat transfer.

(b) Neglecting in-plane swelling by setting $\beta_l = 0$. Or, assuming completely isotropic swelling by setting $\beta_l = \beta_p = \frac{1}{3}J_{\text{PB}} = 0.082$.

(c) Assuming that the oxide only deforms elastically, by switching off oxide plasticity, i.e. by setting the value of the tensile flow resistance of the oxide, S_{ox}, to a very large value.

(d) Assuming that oxide can readily creep at high temperatures by increasing the value of the strain rate sensitivity parameter of the oxide, m_{ox}.

(e) Assuming that bond-coat only deforms elastically, by switching off bond-coat viscoplasticity, i.e. by setting the pre-exponential parameter A_{bc} to zero.

(f) Changing the parameter $D_{0,\text{ox}}$, which controls the diffusion of oxygen in the alumina scale.

We examine the effects of items (a) through (f) on the results of the flat-plate simulations discussed in Section 4.3. Unless otherwise noted, we examine the particular case of plate thickness of $2h = 3970$ microns for temperature $\vartheta_{\text{hot}} = 1573$ K. The main simulation results, the changes in which are examined below, are:

(i) the oxide thickness;

(ii) the in-plane strain after cool-down; and

(iii) the in-plane compressive residual stress after cool-down.

Henceforth, the in-plane strain after cool-down and the compressive in-plane stress in the oxide after cool-down, will be simply referred to as "strain" and "stress", respectively. In our discussion, we refer to the calibrated material parameters as given in Tables 4.1 and 4.2 as the "benchmark values". Apart from the specific parameter which is being changed in the simulation results below, all other material parameters were kept constant at their values listed in Tables 4.1 and 4.2.

C.1 Neglect of transient heat transfer

With κ_{char}, c_{char}, and l_{char} representing characteristic values of the thermal conductivity, specific heat, and a geometric length scale, a characteristic time scale for thermal diffusion is[1]

$$t_{\text{char}} \stackrel{\text{def}}{=} \frac{l_{\text{char}}^2}{\kappa_{\text{char}}/c_{\text{char}}}.$$

For the range of temperatures and values of the volume fraction of oxide, the thermal conductivity κ has values in the range 5 to 32 W/(m×K). Thus, choosing

$$\kappa_{\text{char}} = 15 \text{ W/(m}\times\text{K)},$$

using the presumed constant value for specific heat from Table 4.1,

$$c_{\text{char}} = 5 \text{ MJ/(m}^3\times\text{K)},$$

and using the half-thickness of the plate as the characteristic length

$$l_{\text{char}} = h/2 = 1985\,\mu\text{m},$$

we obtain

$$t_{\text{char}} = 1.3\,\text{s}.$$

Thus, the characteristic time for a change in temperature at the boundary of the plate to propagate throughout the entire plate is on the order of one second. Indeed, if one applies a sudden temperature change at the surface of the plate, after about 3 seconds the temperature at the plate mid-plane is within one percent of the newly applied temperature at the boundary. *Heat transfer therefore occurs much faster than the tens of hours that are characteristic of oxidation, and clearly even faster than the 120 s during which the temperature is ramped down form the high temperature to its ambient value during thermal cycling.* For this reason,

[1]Note that in our theory the specific heat c_{char} is measured per unit (reference) *volume*, and not per unit mass; cf. (3.154).

- For the problem of oxidation of the thin plates under consideration, one may *safely neglect transient heat transfer*, and simply prescribe the desired temperature history *at the nodes* of the finite element mesh.

Nevertheless, since in eventual applications of the theory to turbine blades and other high-temperature components one will encounter more complex geometries and boundary conditions than those examined in this paper, in the main body of the paper — *for completeness* — we have explicitly modeled the transient heat transfer.

C.2 Neglect of in-plane swelling. Assumption of isotropic swelling

Next, we examine the effects of two limiting cases for the in-plane swelling:

(i) neglect of in-plane swelling by setting $\beta_l = 0$; and

(ii) assuming completely isotropic swelling by setting $\beta_l = \beta_p = \frac{1}{3} J_{\text{PB}} = 0.082$.

The calibrated benchmark value is $\beta_l = 0.03$. The simulation results for $\beta_l \in [0.000, 0.030, 0.082]$ are shown in Fig. C-1: subfigures (a), (b) and (c) show the oxide thickness, the stress, and the strain for a plate of thickness $2h = 3970$ microns, while the subfigure (d) shows the strain for a plate of thickness $2h = 450$ microns.

- **Oxidation depth**: Fig. C-1(a) shows that the value of β_l has no discernible effect on oxide thickness.

- **Compressive stress in oxide**: Since there is no in-plane swelling for $\beta_l = 0$, no growth stresses are generated at the high temperature. Hence, the compressive stress levels for $\beta_l = 0$ shown in Fig. C-1(b) represent the stress purely due to the thermal expansion mismatch.[2]

  For isotropic swelling, $\beta_l = 0.0832$, the stress level is almost the same as that for $\beta_l = 0.030$. The reason for this result is that the level of growth stress is *capped by plastic flow strength of the oxide.*

- **Lateral strain after cool-down**: As shown in Fig. 2-2(c) the lateral strain is strongly dependent on the plate thickness. We examine the effects of variation of β_l for two plate thicknesses $2h = 3970$ and $2h = 450$ microns in Fig. C-1(c) and Fig. C-1(d), respectively.

  These figures show, as expected, that if there is no in-plane swelling, $\beta_l = 0$, there is *almost no lateral strain.*[3]

[2]For $\beta_l = 0$, the stress level after 2 hours of oxidation is lower than the stress levels for 10 hours and 50 hours of oxidation, since after 2 hours the oxidation reaction has not reached its final value of 0.93 (even in the uppermost parts of the specimen), and consequently the thermal mismatch stress is not yet fully-developed.

[3]The small amount of lateral strain in Fig. C-1(c) is again due to the thermal expansion mismatch.

Fig. C-1(c) shows that isotropic swelling does not significantly increase the in-plane strain for the thick plate $2h = 3970$ microns, since the additional in-plane swelling is strongly resisted by the thick bond coat. However, Fig. C-1(d) shows that for the thinner plate $2h = 450$ microns, the in-plane strains after cool-down are clearly higher in the isotropic $\beta_l = 0.082$ case than for the benchmark case of $\beta_l = 0.03$.

These calculations show that it is important to model the swelling of the oxide, including its anisotropic nature.

C.3 Oxide plasticity switched off

The results for the situation if one assumes that the oxide only deforms elastically, obtained by setting $S_{ox} \to \infty$, are shown in Fig. C-2. The calibrated benchmark value is $S_{ox} = 2405$ MPa.

- **Oxidation depth**: As in the case of changes in β_l discussed in the previous subsection, switching off oxide plasticity has a very limited effect on the oxide thickness. For brevity we do not show the corresponding plot.

- **Compressive stress in oxide**: When oxide plasticity is turned off, the plate is deprived of one of the two mechanisms by which the compressive growth stresses can be relaxed (the other one being permanent elongation of the entire plate due to *bond-coat* viscoplasticity). The resulting stress levels are therefore much larger than the ones in the benchmark case. In fact, as can be seen in Fig. C-2a, the stress levels reach almost 20 GPa for small oxidation times, which is an unrealistically high value, and much larger than what is measured experimentally.

- **Lateral strain after cool-down**: The very large stresses in the oxide correspondingly increase the driving stress for viscoplastic deformation in the bond coat, and the overall specimen elongation progresses much more rapidly when there is no oxide plasticity.

These calculations show that it is important to account for the plastic deformation of the oxide.

C.4 Significantly rate-sensitive plastic response of oxide

In our calibration for the inelastic response of the oxide, we have chosen a very low value for the strain rate sensitivity parameter $m_{ox} = 0.005$. As discussed in Appendix B, this very low value of m_{ox} approximates an *essentially rate-independent plastic response.* In this section, we examine the effect of *significantly increasing* the value of this parameter to $m_{ox} = 0.2$, which represents a rate-sensitivity similar to that of the underlying bond-coat. The results are shown in Fig. C-3.

- **Oxidation depth**: Again, there is almost no change in the oxidation depth and the plot is omitted.

- **Compressive stress in oxide**: Fig. C-3(a) shows the compressive stress in the oxide. For $m_{ox} = 0.2$ the oxide shows a significant rate-sensitive plastic response, and it exhibits significant creep strains at all non-zero values of stress. As a consequence, any growth stresses that are generated at the high temperature are quickly "relaxed" by the inelastic deformation of the oxide. Accordingly, the stress levels observed after cool down to room temperature are the ones due to thermal expansion mismatch.

- **Lateral strain after cool-down**: Since there are no compressive growth stresses in the oxide which can cause corresponding tensile stresses which drive elongation of the bond coat, Fig. C-3(b) shows that for $m_{ox} = 0.2$ there is essentially no strain after cool-down, except for the one due to thermal expansion mismatch.

These calculations show that in the temperature range studied in this paper, it is important to to model the plastic deformation of the oxide as essentially *rate-independent.*

C.5 Bond-coat viscoplasticity switched off

Next, we examine the consequences of assuming that bond-coat only deforms elastically by switching off bond-coat viscoplasticity, i.e. by setting the pre-exponential parameter A_{bc} to zero. The results are shown in Fig. C-4.

- **Oxidation depth**: Again, there is almost no change in the oxidation depth and the plot is omitted.

- **Compressive stress in oxide**: As mentioned earlier, viscoplastic deformation of the bond coat — which gives rise to a permanent elongation of the plate — is one of the mechanisms that relaxes the stress in the oxide. When there is no viscoplastic deformation in the bond coat, such a permanent elongation is not possible. Consequently the stresses in the oxide can only be relaxed due to *oxide* plasticity, and as soon as they fall below the flow strength for the oxide (recall that the benchmark case represents an essentially *rate-independent plastic response of the oxide*), they are not reduced any further. Thus, as seen in Fig. C-4(a), aside from the very early stage of oxidation, the compressive stress in the oxide is essentially constant.

- **Lateral strain after cool-down**: Again, when there is no viscoplastic deformation in the bond coat, there is no overall permanent elongation. Therefore, the strain after cool-down shown in Fig. C-4(b), is purely due to the thermal expansion mismatch.

Remark: Having discussed oxide and bond-coat plasticity in Sections C.3 through C.5, we point out that the assumption (3.167) regarding the relative amount of *plastic flow during the oxidation reaction* also has a *significant effect* on the magnitudes of the stresses and strains that develop. As discussed in the paragraph leading up to (3.167), the simplest

choice, i.e. $\omega = \xi$, would lead to an *absence of compressive stress development at high temperature*, leading only to room-temperature stresses that are essentially those due to the thermal expansion mismatch, which disagrees with experiment. Thus, within the framework of our theory, the assumption (3.167), viz.

$$\omega = \begin{cases} 0 & \text{if} \quad \xi = 0, \\ 1 & \text{otherwise}, \end{cases}$$

is important in obtaining predictions for the stress and strain which are in accordance with the experiments of Tolpygo et al. [102, 103].

C.6 Change of oxygen diffusivity in the oxide

Finally, we discuss the effects of change in how fast *oxygen diffusion* occurs in the oxide layer. Such a change is caused by a variation in the material parameter $D_{0,\text{ox}}$ (for a fixed value of the activation energy $Q_{d,\text{ox}}$, cf. (3.179)). We examine the effects of three values

$$D_{0,\text{ox}} \in [1 \times 10^{-9}\ \text{m}^2/\text{s},\ \underline{7.5 \times 10^{-9}\ \text{m}^2/\text{s}},\ 20 \times 10^{-9}\ \text{m}^2/\text{s}], \tag{C.1}$$

where the calibrated benchmark value is underlined. The results for the oxide thickness, in-plane strain after cool-down, and the in-plane compressive stress in the oxide after cool-down are shown in Fig. C-5.

- **Oxidation depth**: Fig. C-5(a) shows that unlike for the cases examined previously in this Appendix, a change in the value of $D_{0,\text{ox}}$ has a *very large effect* on the oxide thickness as a function of oxidation time. It is the oxygen diffusivity in the alumina, D_{ox}, that dictates the evolution of oxide thickness. The lower value $D_{0,\text{ox}} = 1 \times 10^{-9}$ m^2/s results in a lower growth rate than the benchmark value $D_{0,\text{ox}} = 7.5 \times 10^{-9}$ m^2/s, while the higher value $D_{0,\text{ox}} = 20 \times 10^{-9}$ m^2/s results in a much faster growth rate.

- **Compressive stress in oxide**: The change in the stress versus oxidation time shown in Fig. C-5(b) is simply a consequence of this change in the *oxidation rate*. For the lower value of $D_{0,\text{ox}} = 1 \times 10^{-9}$ m^2/s, oxidation progresses more slowly. Then at a given time, say 50 hours, the oxide thickness is smaller than that for the benchmark case. This results in a smaller tensile stress in the bond-coat to drive permanent elongation. There is thus less permanent elongation in the bond-coat that can relax the compressive stress in the oxide — the compressive stress in the oxide is therefore *higher* than that for the benchmark case of $D_{0,\text{ox}} = 7.5 \times 10^{-9}$ m^2/s.

  By a similar argument, for the higher value $D_{0,\text{ox}} = 20 \times 10^{-9}$ m^2/s the compressive stress in the oxide is *lower* than that for the benchmark case.

- **Lateral strain after cool-down**: As just discussed, Fig. C-5(c) shows that for the lower value of $D_{0,\text{ox}} = 1 \times 10^{-9}$ m^2/s the lateral elongation progresses more slowly then

the benchmark value, while for the higher value $D_{0,ox} = 20 \times 10^{-9}$ m^2/s it progresses more quickly.

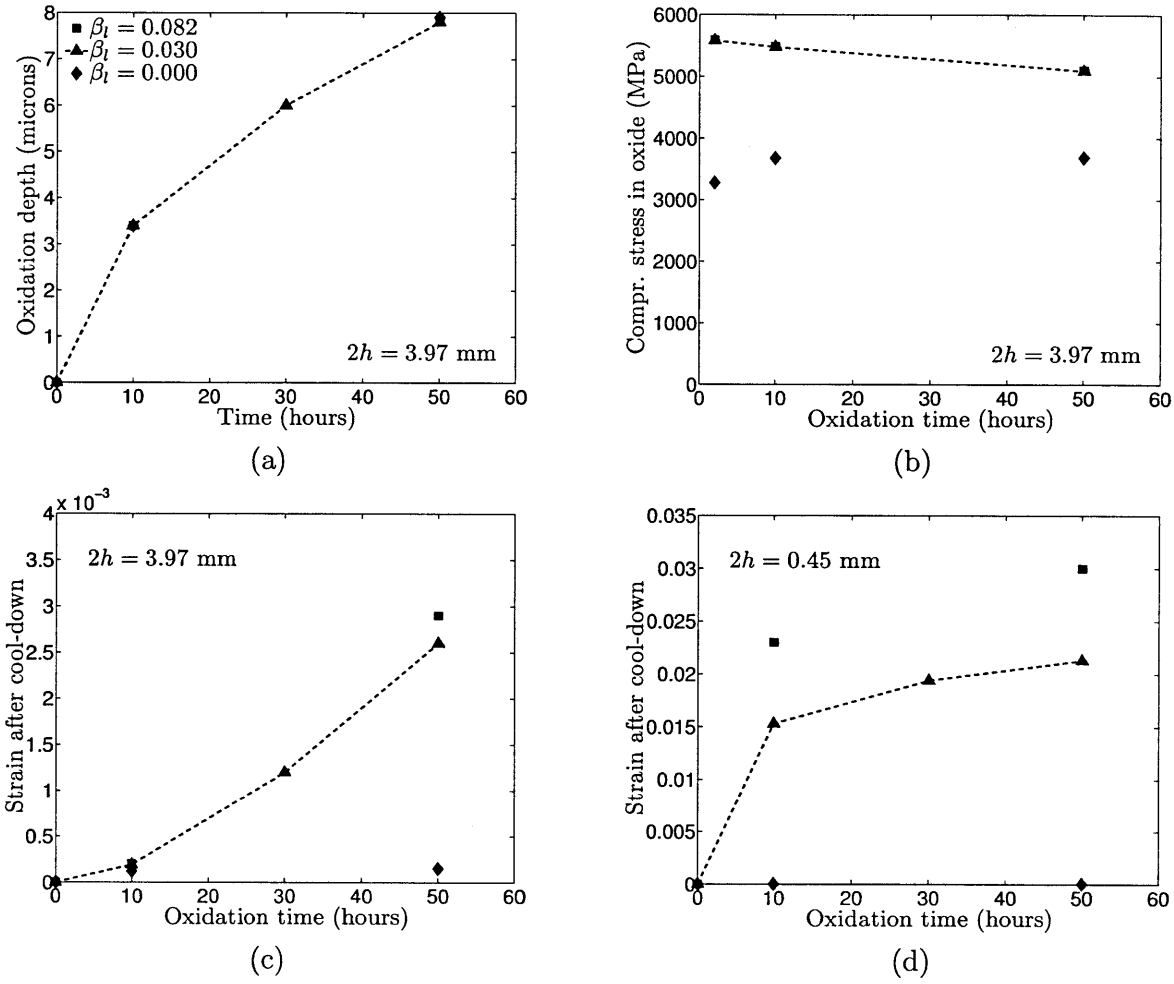

Figure C-1: Results of plate oxidation simulations for different values of β_l. The legend in (a) also applies to (b)-(d). Note that in all figures, the upward-pointing triangles connected by the dashed lines represent the calibrated "benchmark" case. (Relevant benchmark value for this figure: $\beta_l = 0.03$.)

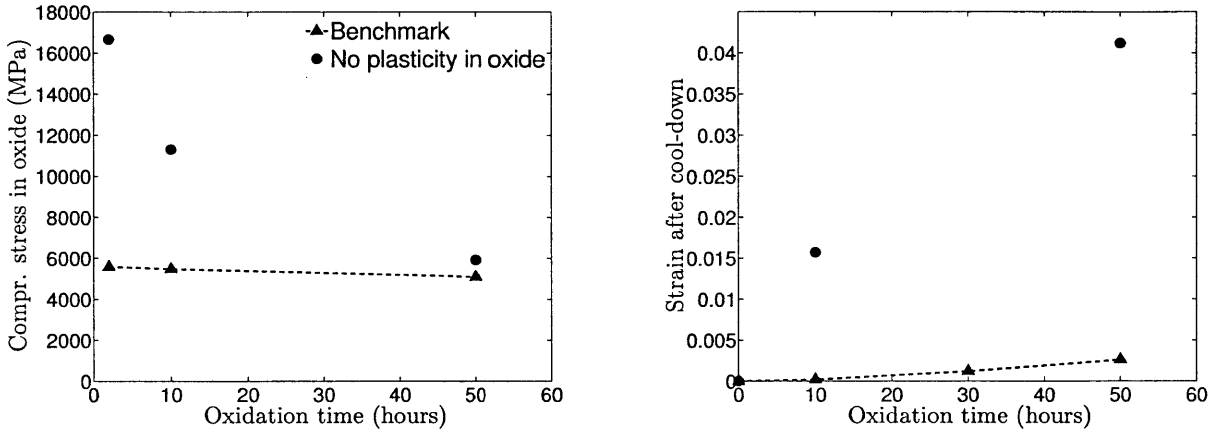

(a) (b)

Figure C-2: Results of plate oxidation simulations if there is no plasticity in the oxide; $2h = 3.97$ mm; benchmark. The legend in (a) also applies to (b). (Relevant benchmark value for this figure: $S^0_{ox} = 2405$ MPa.)

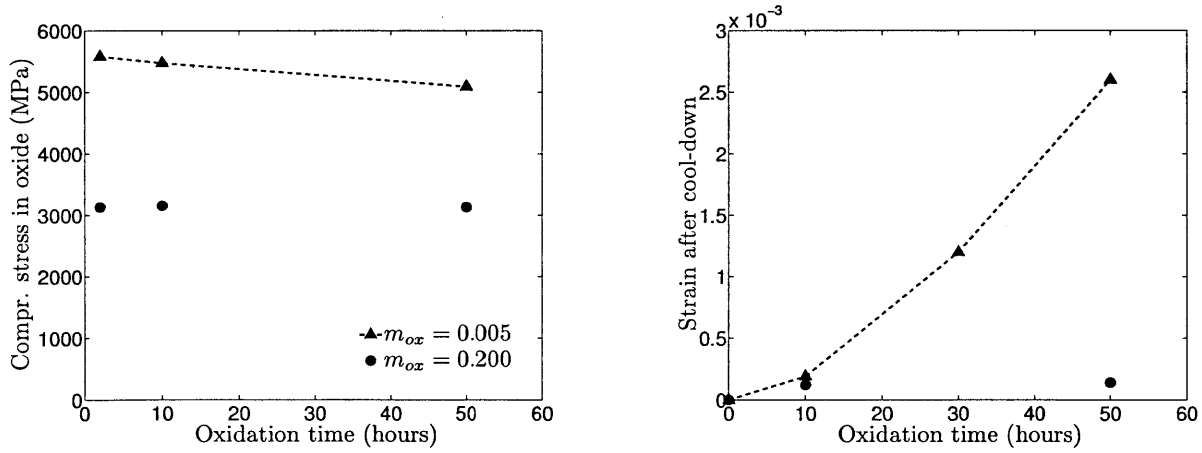

(a) (b)

Figure C-3: Results of plate oxidation simulations if oxide plasticity is rate-sensitive; $2h = 3.97$ mm. The legend in (a) also applies to (b).

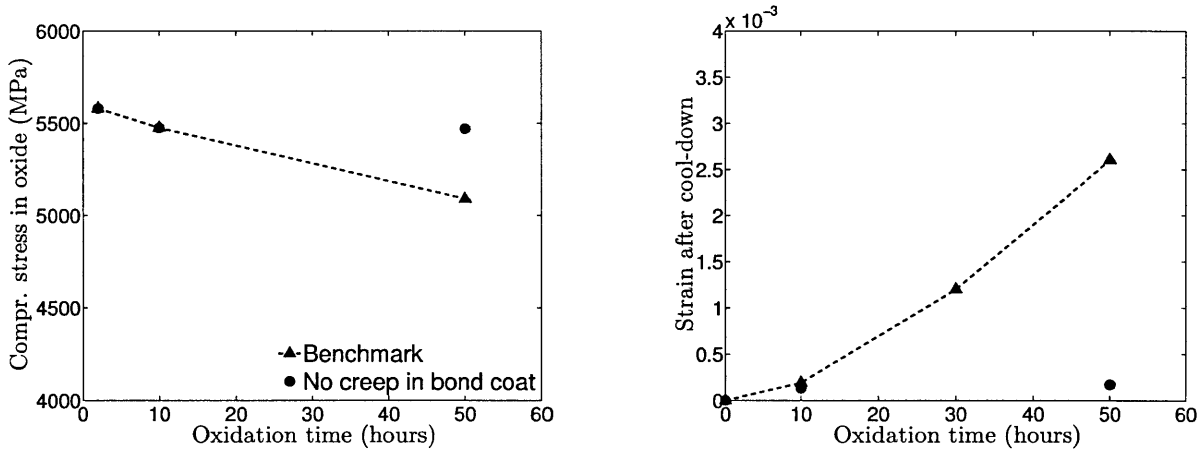

Figure C-4: Results of plate oxidation simulations if there is no creep in bond coat; $2h = 3.97$ mm. The legend in (a) also applies to (b). (Relevant benchmark value for this figure: $A_{bc} = 48 \times 10^3$ 1/s.)

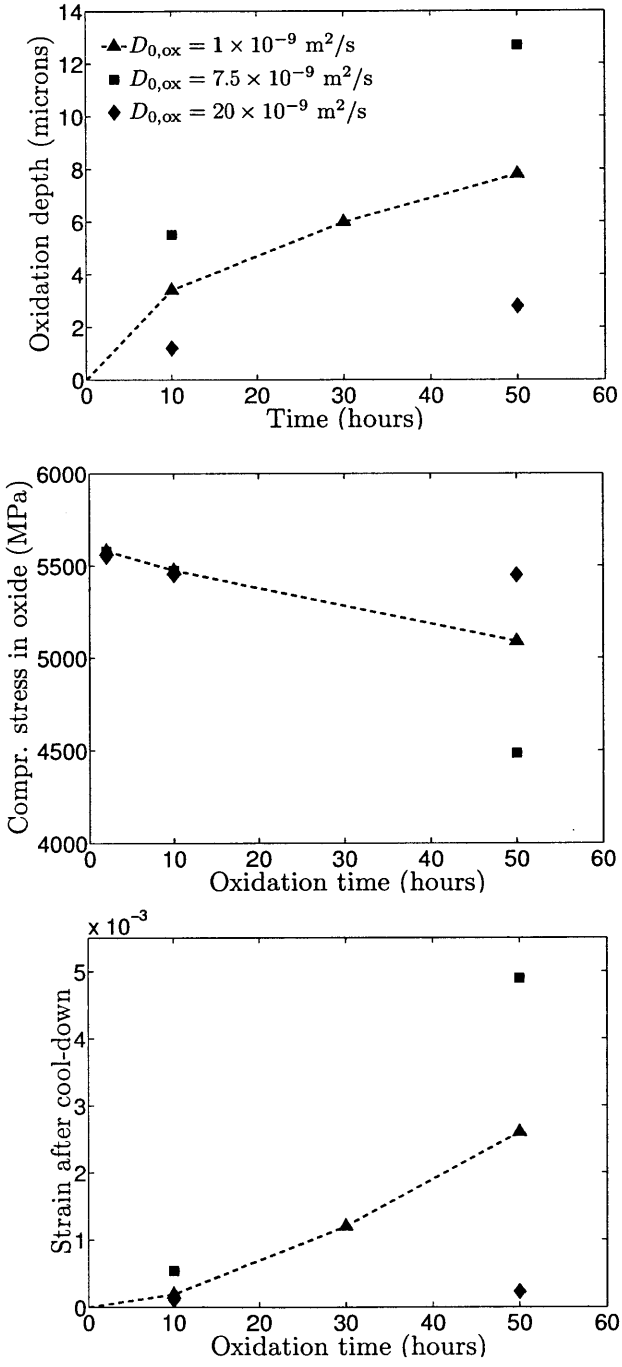

Figure C-5: Parametric study on $D_{0,ox}$. The legend in (a) also applies to (b) and (c).

Part V

Appendices related to Part II

Appendix D

Brief overview of the experimental literature on degradation and failure of plasma-sprayed TBC systems

D.1 Introduction

Because of the immense technological significance of TBC systems, their failure behavior has garnered considerable attention in the Mechanics and Materials community, and much experimental work has been done; it is the goal of this Appendix to give an overview and summary of these experimental efforts for the plasma-sprayed type.

Historically, the experimental characterization of TBC systems can be tracked to the early 1990s [34]. TBC systems tend to spall "spontaneously" (i.e. without an externally applied mechanical load) after they have undergone prolonged high-temperature exposure; therefore, many studies (especially the early ones) mainly focussed on *thermally exposing TBC system specimens*, and keeping track of exactly what thermal history it takes to bring about failure.[1] We discuss these experiments with purely thermal loading in Section D.2.

More recently, the TBC research community became interested in how a TBC system reacts if there is a *mechanical load.* Accordingly, such tests were either devised from scratch or adopted from related fields like material property determination in *composite materials.* Due to the irreversible processes of oxidation and viscoplasticity which take place at high temperature, it is expected that the mechanical properties of the TBC system change over the course of thermal exposure. For this reason, these mechanical tests were performed after the experimental specimens had been exposed to different thermal histories. We discuss such *purely mechanical* experiments (which may have been performed on specimens thermally exposed *before* the mechanical test) in Section D.3.

Finally, recently various groups have performed tests under *combined thermal and mechanical loading*, i.e. where thermal and mechanical loading took place at the same time. Such experiments are described in Section D.4.

[1] It is the oxidation and the thermal mismatch as discussed in the main body of this work that give rise to this spontaneous failure.

We point out that we do not attempt in this Appendix to give an exhaustive list of papers on the experimental characterization of TBC system failure. Rather, we discuss a number of investigations that we deem particularly substantial and which we believe capture the essence of the field.

D.2 Purely thermal loading

When a TBC system is exposed to high temperature, as discussed in the main body, the bond coat will oxidize, and because of the associated volumetric expansion, *large local stresses and strains* will be induced within and/or in the vicinity of this slowly-growing thermally grown oxide. These stresses and strains are further exacerbated when the TBC system is cooled down to room temperature due to the thermal mismatch of the different materials that are involved: while the metallic bond coat and substrate have coefficients of thermal expansion on the order of 15×10^{-6} 1/K, the ones of the TGO and the YSZ top coat are only about 50 to 70 percent of this value. Such local stress peaks are the driving force for the generation of local *microcracks* that start forming in and around the TGO. Such microcracks are themselves not detrimental to the TBC system, especially since for plasma-sprayed TBC systems the porous YSZ top coat already contains a multitude of interfaces between the individual splats from plasma-spraying, and those "inter-splat boundaries" are intrinsic weak regions similar to microcracks. However, as the thermal exposure or cycling continues, the number and length of such microcracks continue to increase, and eventually they coalesce to form larger cracks. When these larger cracks have grown large enough, there need not be any external mechanical load to cause the top coat to completely debond from the bond coat and substrate; it is this failure mode that is observed in *purely thermal* experiments.

The morphology of a TBC system that spalled after several cycles at 1394 K is shown in Fig. D-1. (This image was taken from Sridharan et al. [97], who performed experiments on an EBPVD TBC system; however, a spalled plasma-sprayed TBC system is expected to look very similar.) Trunova et al. [104] recently performed thermal exposure experiments on a plasma-sprayed TBC system; in their study the primary interest was to quantify the relation of the time the TBC system spends at high temperature in every cycle, the *dwell time*, to specimen lifetime, i.e. the overall time it takes for the specimen to spall. (The answer to the related question of how the high temperature to which the TBC system is exposed, the *dwell temperature*, affects the lifetime, is straightforward: since a *higher* dwell temperature leads to accelerated oxidation and hence to quicker generation of large local stresses, it will *decrease* the lifetime.)

As might be intuitively expected, Trunova et al. [104] found that *shorter dwell times* lead to a *lower lifetime*. If the dwell time is short, for a given *total time* for the experiment, a specimen will have undergone *more cycles* than one that had a higher dwell time; and in every cycle, when the specimen is cooled to room temperature, the thermal mismatch stresses are superposed on the previously existing stress state, thereby furthering the propagation and coalescence of microcracks.

Another part of the experimental work of Trunova et al. [104] was the microstructural characterization of the failed specimens. A completely failed TBC system from their ex-

periments is shown in Fig. D-2. It can be seen that *failure occurred close to or at the top-coat/TGO interface*, which is an observation that has been widely reported for plasma-sprayed TBC systems; cf., e.g., Hutchinson and Hutchinson [59], Yamazaki et al. [112], Yanar et al. [116], Zhao et al. [121].

It is clear that much valuable information can be gathered from such *purely thermal tests*. However, they are limited in that one depends on oxidation and thermal mismatch to induce any stress and strain; *mechanical tests*, which do not have this limitation, will be discussed next.

D.3 Purely mechanical loading

Our discussion of purely mechanical testing starts out in Section D.3.1 with different versions of *bend tests*, which recently seem to have become the most popular choice for investigation of TBC system failure. Another option is to perform some type of *indentation*, or to load the TBC system directly *in tension*, which can be achieved by gluing a connector on top of the top coat. (Gluing stiffeners onto the top coat is also required for bend tests, as will be discussed.) These variants are examined in Sections D.3.2 and D.3.3, respectively. Two more tests, a *pushout test* and a *shear delamination test*, are discussed in Sections D.3.4 and D.3.5, respectively.

D.3.1 Bend tests

For illustration of a bend test on a TBC system, we first examine the recent paper by Zhao et al. [121]. The failure mode of interest, as discussed above, is the *delamination* of the top coat from the rest of the TBC system. In bending, this can be achieved by taking a beam consisting of a metallic substrate and a TBC system, carefully introducing a notch at the center of the beam by locally removing the top coat (e.g. by a wire saw), and then gluing two *stiffeners* onto the top coat on both sides of the notch.[2] The "composite beam" is then put into bending with the notch on the tension side. A sketch of the set-up by Zhao et al. [121] along with a photograph of the experiment is shown in Fig. D-3. At a certain critical load, cracks will initiate near the top-coat/TGO interface: this moment represents the *initiation of delamination*. In the corresponding curve of load versus roller displacement, the beginning of delamination is characterized by a local peak, as is shown in Fig. D-4. As the beam is then deformed further, the two nominally symmetric cracks continue to propagate out, continually disconnecting more of the stiffener/top-coat composites from the rest of the specimen. As long as the substrate remains elastic, the load will continue to increase due to the stiffness of the partially cracked specimen, of which the substrate stiffness now forms the major component. (Unfortunately such further loading is not shown in the work of Zhao et al. [121], but can be observed, e.g., in Yamazaki et al. [112].)

It is now straightforward to imagine other implementations of such bend tests. Most notably, a different version is the *asymmetric bend test* performed by Zhao et al. [119]; a sketch of their specimen, their experimental set-up, and a cracked specimen are shown

[2]If no stiffeners were used, the top coat would quickly develop *vertical cracks* (also called *segmentation cracks* or *mud cracks*), which is not the intent of the test.

in Figs. D-5, D-6, and D-7, respectively. (Note that unlike in the case of the symmetric bend test, here there is *only one continuous stiffener*, and *two sets of TBC system plus substrate* are glued to it.) A typical resulting curve of load versus roller displacement is shown in Fig. D-8, where again initiation and initial propagation of delamination can clearly be discerned, here between the points B and D. Finally, while the investigation by Zhao et al. [119] was only on as-sprayed specimens, they later also performed the corresponding studies on thermally-exposed samples, which are documented in Zhao et al. [120].

D.3.2 Indentation tests

Indentation testing is another method that has been used to assess the failure behavior of TBC systems. In order to bring about delamination, the indentation is often performed on a *cross-section* of a TBC system, usually on the top coat in proximity to the TGO, i.e. in the weak top-coat/TGO interface region. A micrograph of a residual indent from Rabiei and Evans [85] is shown in Fig. D-9.

While the discussion in Rabiei and Evans [85] regarding interface strength is more qualitative in nature, in the recent work of Yamazaki et al. [113] and Mao et al. [73] there are results for the *mode-I fracture toughness* K_{Ic} of the top coat near the top-coat/TGO interface. Values for K_{Ic} can readily be converted to the related *interface fracture energy* in tension G_{Ic} (also known as a *critical mode-I energy release rate*; the term "rate" implies a measurement per unit surface) via

$$G_{\mathrm{Ic}} = \frac{(K_{\mathrm{Ic}})^2}{E}, \tag{D.1}$$

where E is the Young's modulus of the material under consideration [113]. Note that a characteristic value of $K_{\mathrm{Ic}} = 1$ MPa$\times$m$^{0.5}$ corresponds to a fracture energy of $G_{\mathrm{Ic}} = 27$ J/m^2 when using $E = 37$ GPa [16].

Results for K_{Ic} from Yamazaki et al. [113] and Mao et al. [73] are given in Figs. D-10 and D-11. (In Fig. D-11, measurements for fracture toughness on the top-coat *surface* are also mentioned.) Since in both those publications, tests were performed on specimens that had been exposed at high temperature with different dwell times, Figs. D-10 and D-11 give the interface fracture energy *as a function of dwell time.* The results in Fig. D-10 for indentation indicate that fracture toughness (or equivalently, fracture energy) seems to *increase* as a function of dwell time, which might at first be counterintuitive since the generation and propagation of microcracks as discussed in Section D.2 surely tends to lower toughness. However, such an increase in fracture energy has also been observed elsewhere [112], and the explanation is believed to be the considerable *sintering* of the plasma-sprayed top coat, which increases the top-coat strength.

For completeness, we note that in top coats deposited by EBPVD, this initial increase in fracture energy is *not observed*; rather, it decreases as a function of dwell time right from the start, as documented by Thery et al. [101]. This can be seen in Fig. D-12 from Thery et al. [101], where the calculated interface fracture energy in shear, G_{IIc}, is plotted as a function of thermal cycles (or equivalently, dwell time).

D.3.3 Tension tests

The simple concept of gluing a connector on top of the top coat and then testing the TBC system in tension has been explored with some interest over the past 15 years; cf., e.g., Eriksson et al. [37], Kim et al. [63], Qian et al. [83].

We specifically examine the results by Eriksson et al. [37], who, in addition to performing the tension tests, also carried out a detailed microstructural study of their samples. In Fig. D-13, their results for adhesion strength of the top coat is given as a function of TGO thickness (which is a monotonous function of dwell time). Some of their tests were performed on specimens that had been isothermally or cyclically exposed at high temperature, and they also performed some tests in a "burner rig", which is an experimental set-up that *includes combustion* as opposed to just exposing the specimens in air.

It can be seen in Fig. D-13 that the isothermally exposed samples again increase in bond strength with increasing dwell time (or, as shown here, with increasing TGO thickness); this increase was already discussed above for the bend tests by Yamazaki et al. [112]. However, when the specimens are cycled between dwell and room temperature, the additional micro-crack generation and propagation during cool-down again cause a direct decrease in bond strength. Fig. D-14 shows a micrograph from Eriksson et al. [37]; it shows the failure to have occurred right at the top-coat/TGO interface, with some remnant top coat still adhering to the TGO. (As Eriksson et al. [37] point out, such failure where the TGO becomes visible is termed "black fracture" in industry due to the dark appearance of the TGO, while failure in the top coat is known as "white fracture".)

D.3.4 Pushout tests

Another experiment on failure of a TBC system is the "push-out test", which is depicted in Fig. D-15, taken from Tanaka et al. [100]. As can be seen, a specimen with a TBC system applied on two opposite sides is pushed through a fixture, inducing top-coat delamination. The test is discussed in detail in Kim et al. [64] and Tanaka et al. [100], but in both cases EBPVD TBC systems are considered. To the knowledge of the authors, there is no literature on pushout tests on plasma-sprayed TBC systems. However, it has been found in preliminary experiments in our group at MIT that the alignment of fixture and specimen in the testing machine can be rather difficult, and certainly increases the scatter in results further than the already large inherent one from the inhomogeneous material structure. Other testing methods may thus be more favorable than the pushout test.

D.3.5 Shear-delamination tests

In 2010, Xu et al. [111] proposed a simple "shear-delamination test" on a *flame-sprayed* TBC system,[3] where the top coat is removed everywhere on a coupon except on a small "island". This island is subsequently sheared off with a tool on which the horizontal force is measured, as shown in Fig. D-16.

[3]The *flame-spray* deposition process is different from plasma-spraying in that the particle velocities in flame-spraying are much lower than in plasma-spraying [99].

While this test also induces delamination mainly in shear like the pushout test, due to the simpler set-up we believe that this test is more promising and quicker to perform.

D.4 Thermo-mechanical loading

Recently, Kitazawa et al. [65] and Chen et al. [23] have performed *combined thermo-mechanical tests* in which the thermal and mechanical loads were applied at the same time. Both these publications investigate classical metal tension specimens (dogbone or cylindrical) that consist of a superalloy and an applied TBC system.

Chen et al. [23], note that, as expected, the TBC systems do not contribute to the load-carrying capacity of the specimens in a discernible way, and that the TBC systems accommodate the plastic deformation of the metallic substrate by developing *segmentation cracks* (cf. Footnote 2) perpendicular to the applied load (in the top coat, and sometimes also in the bond coat). There was also a limited amount of spallation of the TBC system which was observed both close to the eventual substrate failure surface and also elsewhere, as can be seen in Fig. D-17.

D.5 Summary

Over the past two decades, there has been a considerable effort in the Mechanics and Materials community to experimentally characterize the degradation and failure of plasma-sprayed TBC systems. This effort started with purely thermally exposing specimens and observing how long the dwell time was until spontaneous failure was reached. As a next step such thermally exposed specimens were then mechanically tested to determine the failure-related material properties as a function of dwell time. Most recently, some thermo-mechanical tests have been performed in which the mechanical testing also took place at high temperature. However, as pointed out by Hutchinson and Hutchinson [59], this is likely *not necessary* since it is the *additional stresses associated with the cool-down process* that usually bring about the eventual failure of a TBC system, and therefore the room-temperature material properties are the ones of interest.

The procedure of first thermally exposing a specimen and then testing it mechanically has thus become somewhat standard in the field. However, what exists to date is a collection of "isolated" experiments that determine *one* specific property such as a tensile or shear fracture energy, and which were performed on specimens that were manufactured using a wide range of specific manufacturing conditions (such as spraying parameters). What is needed is therefore a *coherent suite* of experiments on specimens that were all manufactured by the same entity and in the same fashion. These experiments need to be performed by a single research group, and will together determine *all of the failure-related material properties* of a plasma-sprayed TBC system. The specific types of experiments for this suite can be chosen freely from the above-discussed, or any newly-designed ones. (An example of such a suite of experiments for the case of *adhesive joints* can be found in [98].)

Once the material properties are determined in this fashion, they can serve as an *input* into a *model for failure of plasma-sprayed TBC systems.* The overarching ultimate goal is

then to be able to use a numerical implementation of the calibrated model to *predict the degradation and failure behavior of plasma-sprayed TBC systems.*

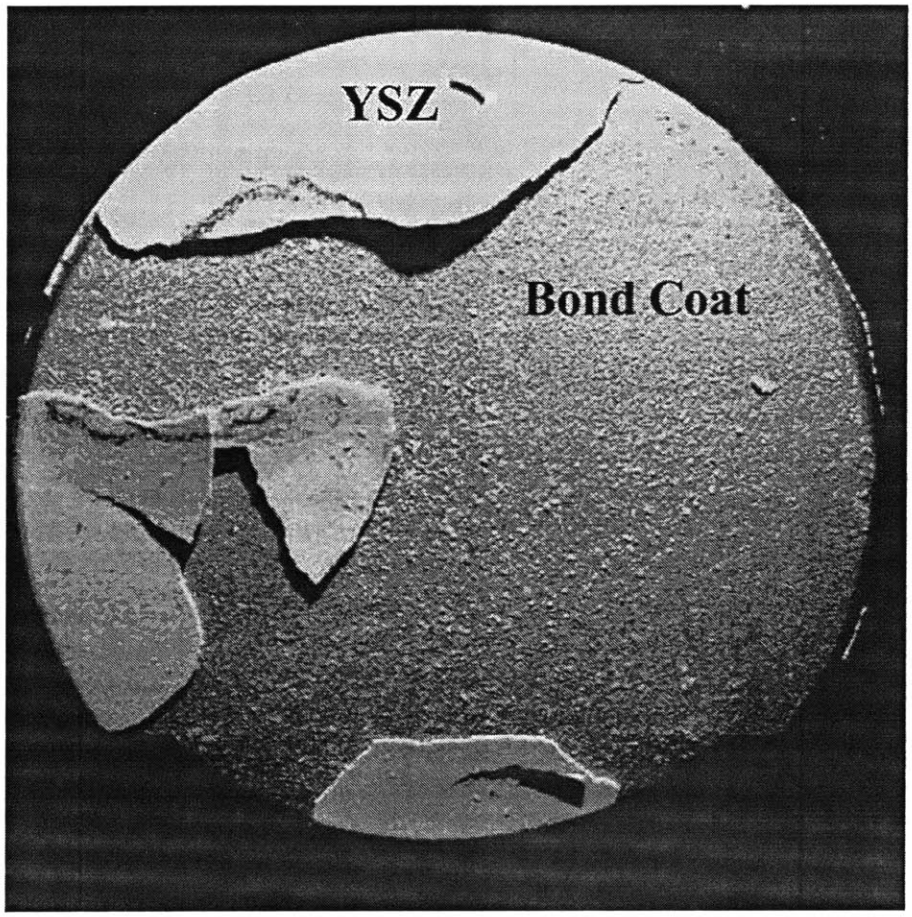

Figure D-1: Top view of a failed TBC system after thermal exposure. (Note that this is an EBPVD TBC system; however, a spalled plasma-sprayed TBC system is expected to look very similar.) From Sridharan et al. [97].

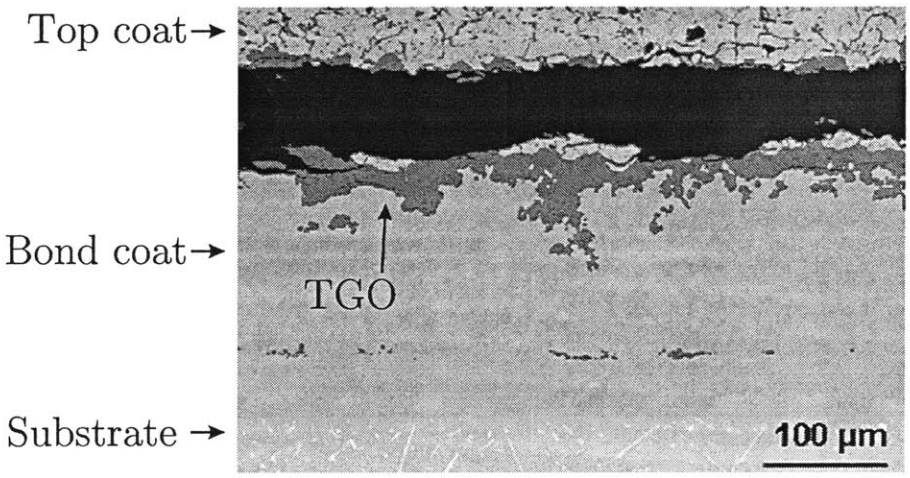

Figure D-2: Failure of a plasma-sprayed top coat near the top-coat/TGO interface. Adapted from Trunova et al. [104].

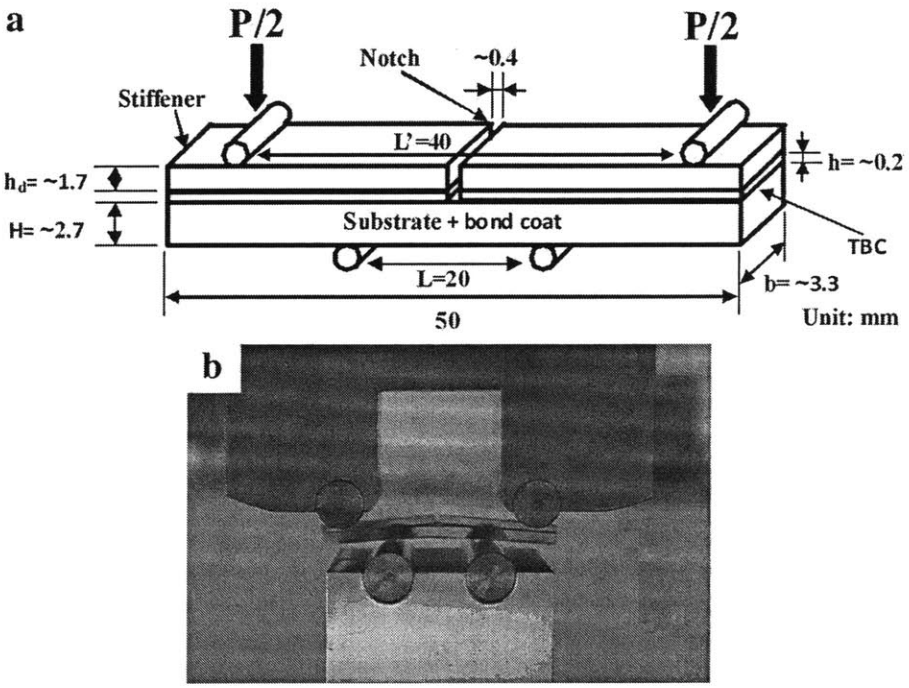

Figure D-3: Dimensions of the notched four-point bend test by Zhao et al. [121] (a), and photograph of their test set-up (b). From Zhao et al. [121]. (The label "TBC" indicates the top coat.)

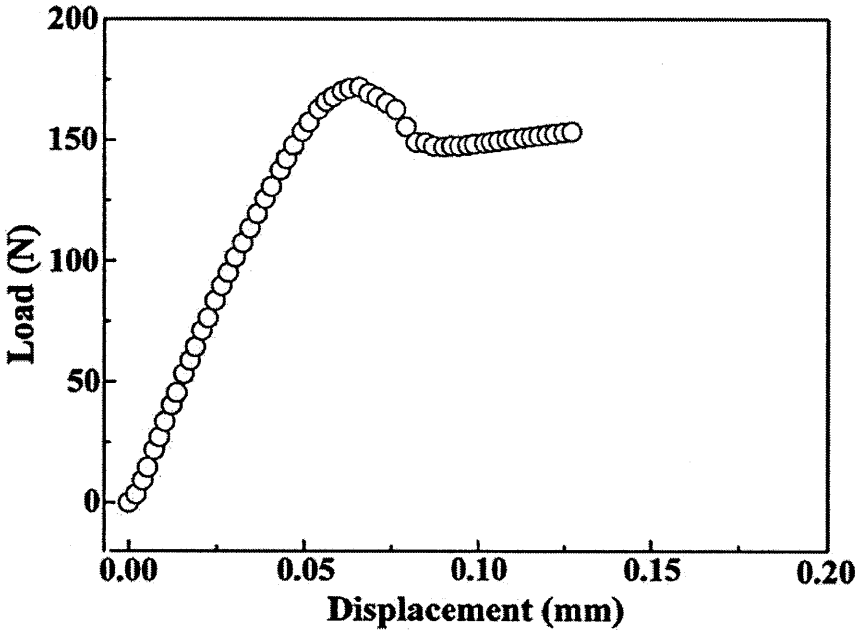

Figure D-4: Load vs. displacement of the roller in the experiment of Zhao et al. [121]; image from the same reference.

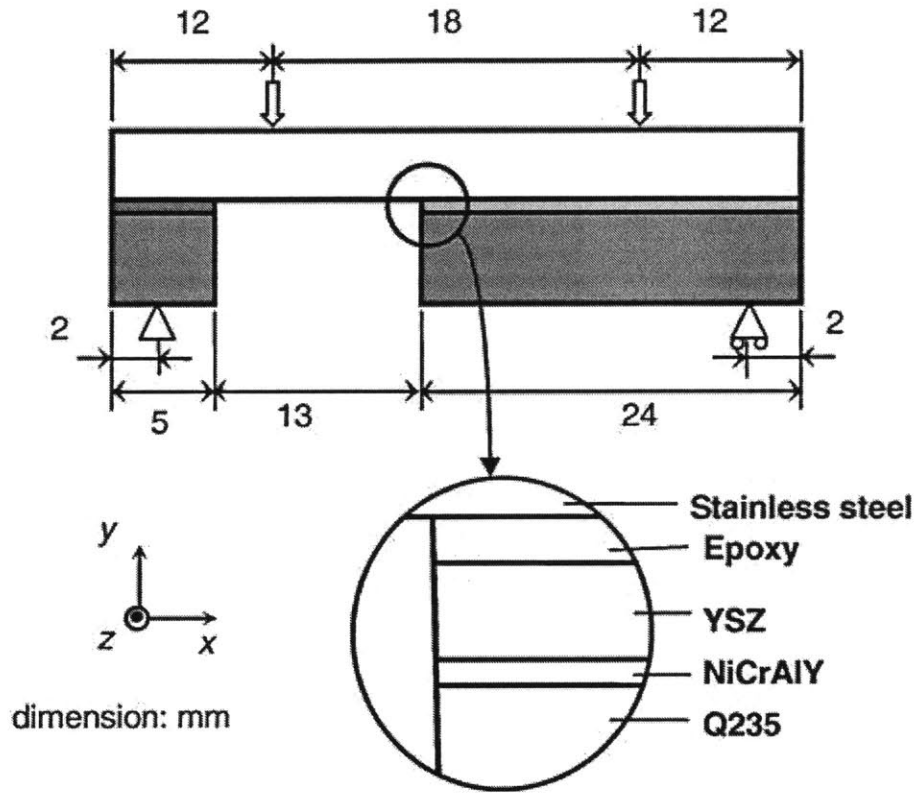

Figure D-5: Dimensions of the specimens used by Zhao et al. [119]; image from the same reference.

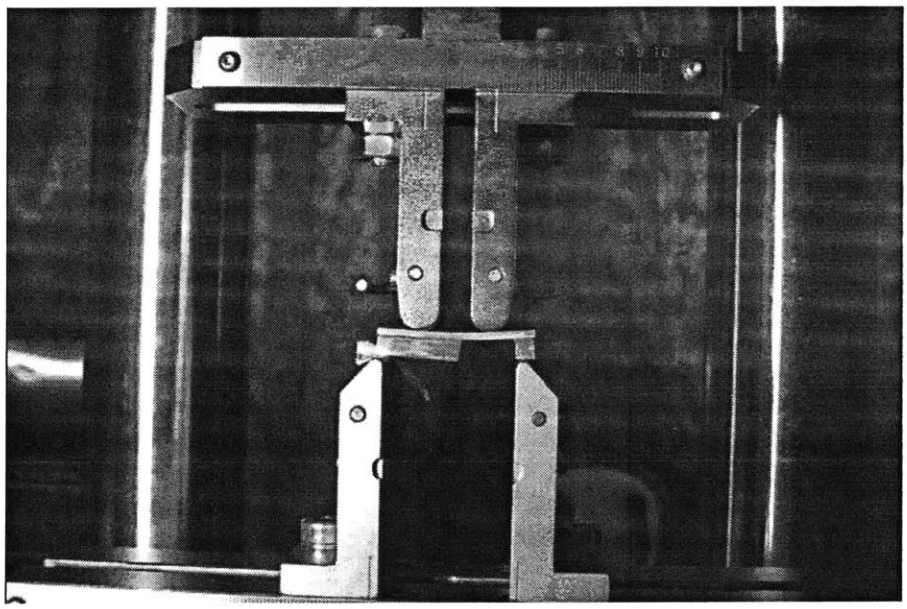

Figure D-6: Test set-up used by Zhao et al. [119]; image from the same reference.

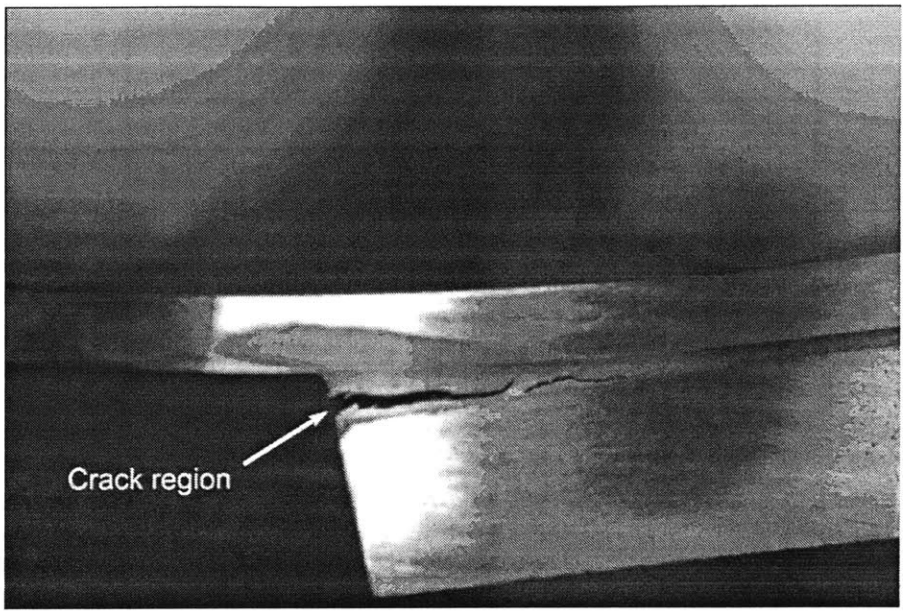

Figure D-7: Cracked specimen in the experiment by Zhao et al. [119]; image from the same reference.

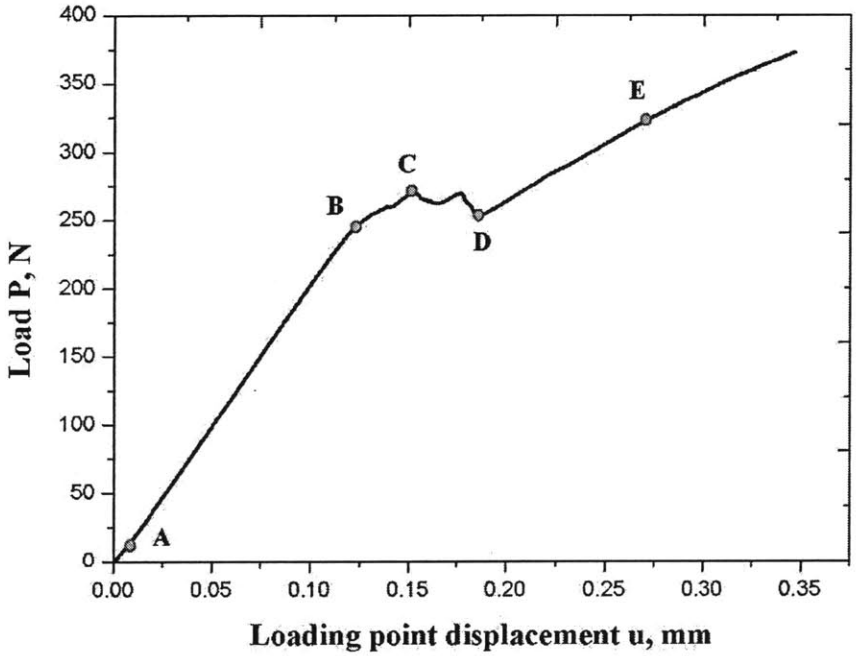

Figure D-8: Typical load-displacement curve from the experiments by Zhao et al. [119]; image from the same reference.

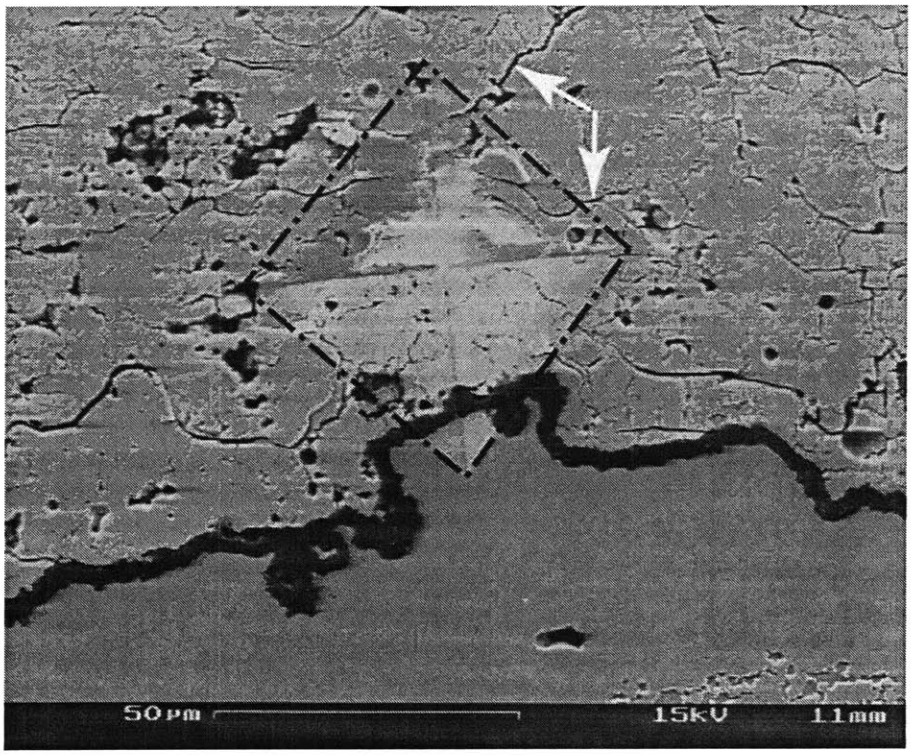

Figure D-9: Residual indentation near the top-coat/TGO interface; arrows indicate additional cracking due to indentation. From Rabiei and Evans [85].

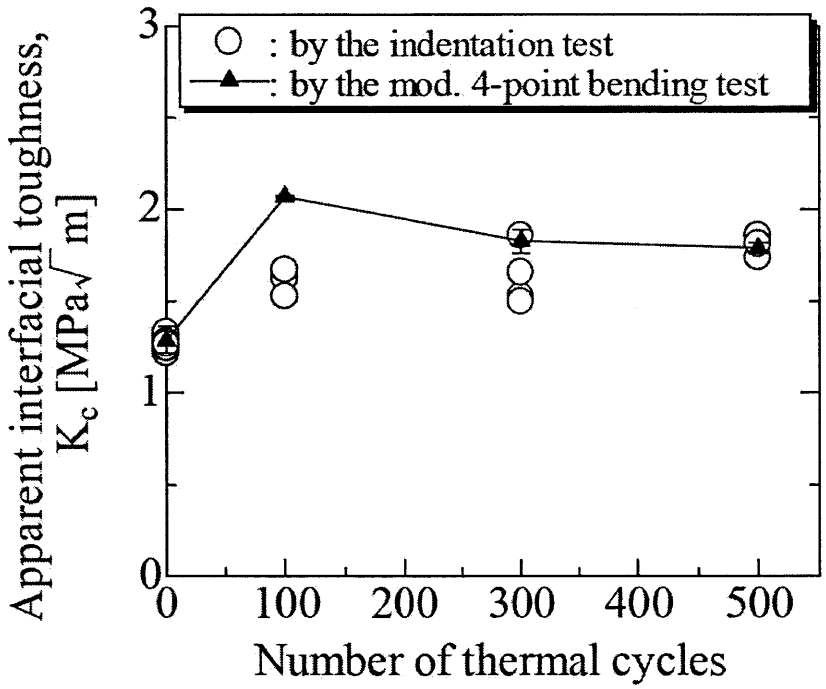

Figure D-10: Fracture toughness as a function of thermal cycles, as measured by indentation and four-point bending. From Yamazaki et al. [113].

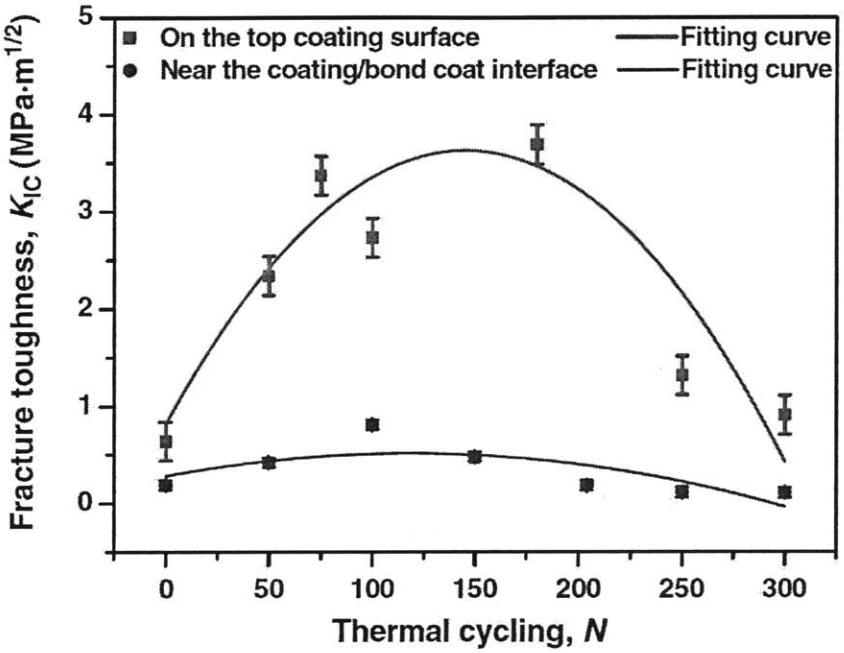

Figure D-11: Fracture toughness as a function of thermal cycles, as measured by indentation, in different regions of the TBC system. From Mao et al. [73].

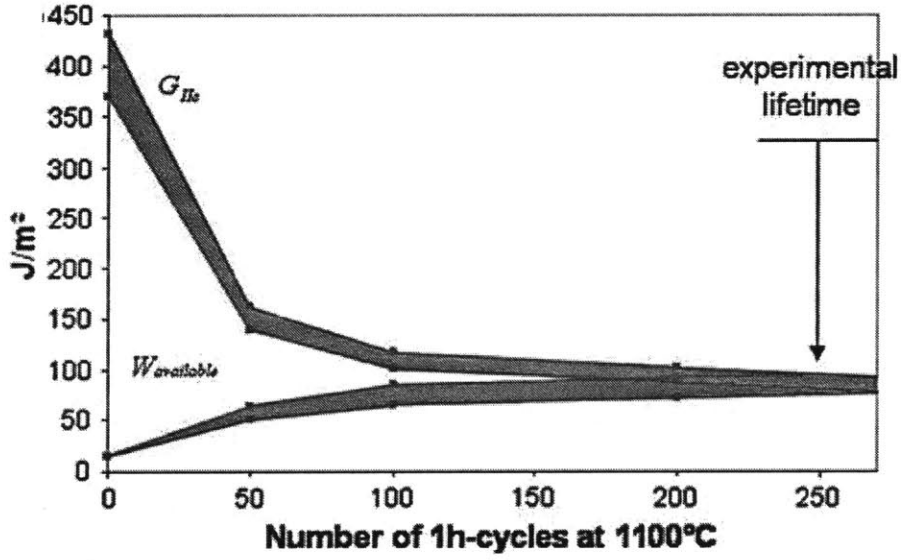

Figure D-12: Interface fracture energy in shear G_{IIc} as a function of thermal cycles in the experiment of Thery et al. [101] (image from the same reference); also plotted is $W_{\mathrm{available}}$, the strain energy which is stored in the specimen.

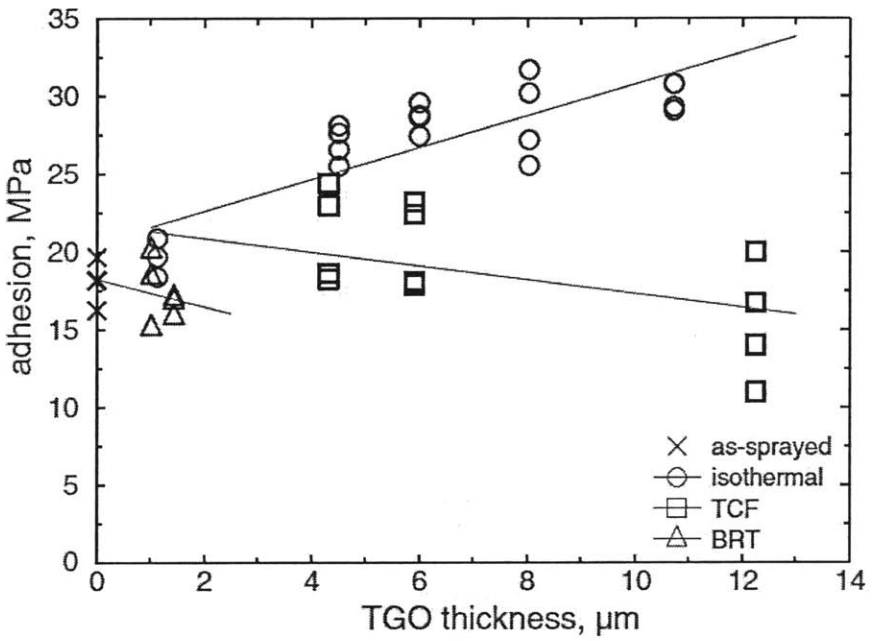

Figure D-13: Adhesion strength of the top coat measured in a tensile test. From Eriksson et al. [37].

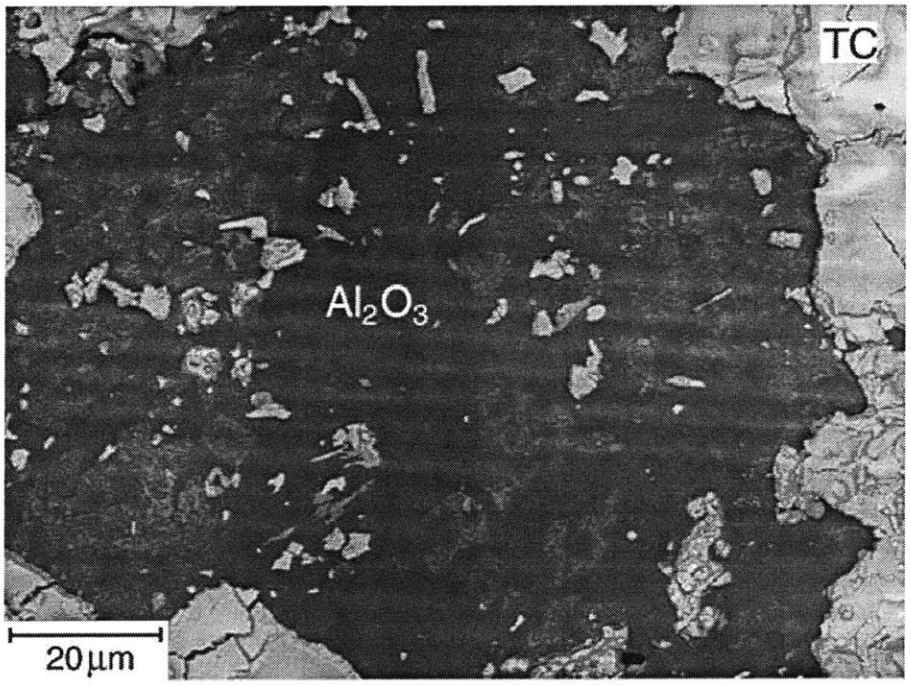

Figure D-14: Fracture at the top-coat/TGO interface in a tension test. From Eriksson et al. [37].

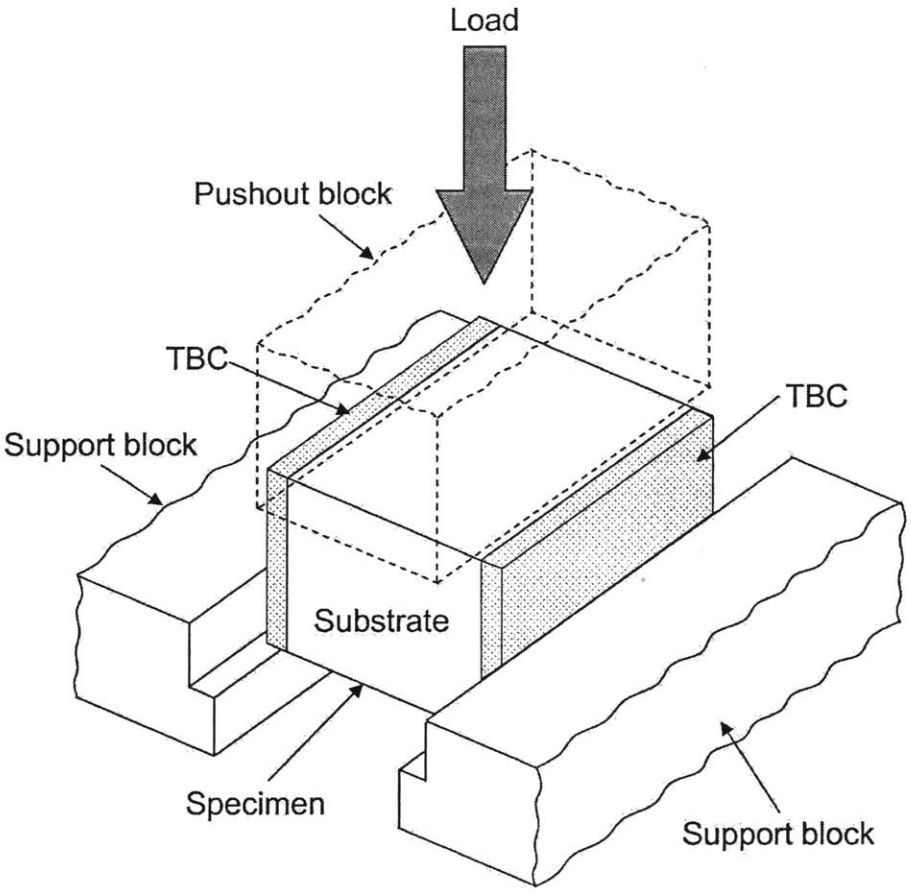

Figure D-15: Schematic of the pushout test. From Tanaka et al. [100].

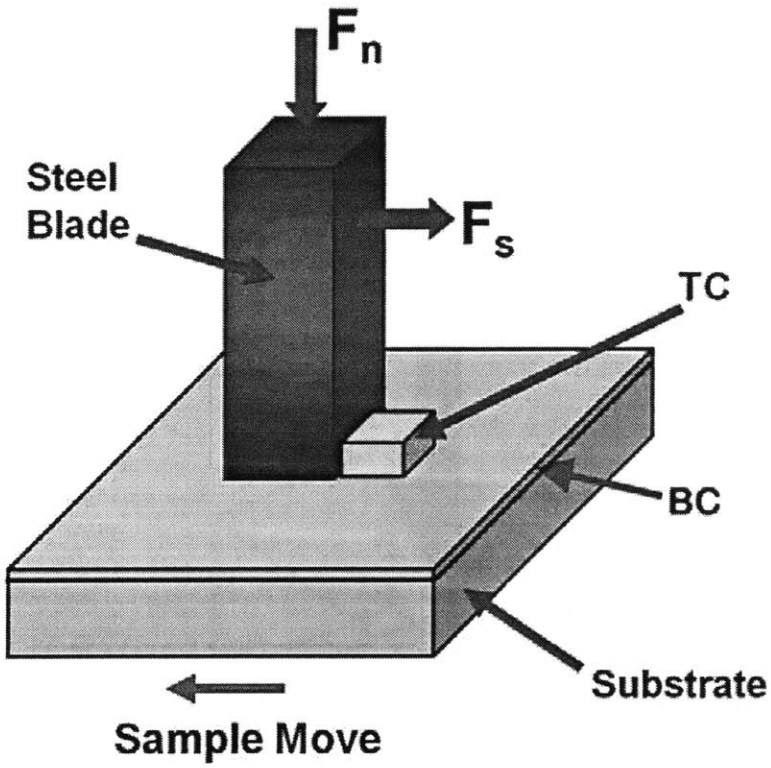

Figure D-16: Schematic of the shear-delamination test. From Xu et al. [111].

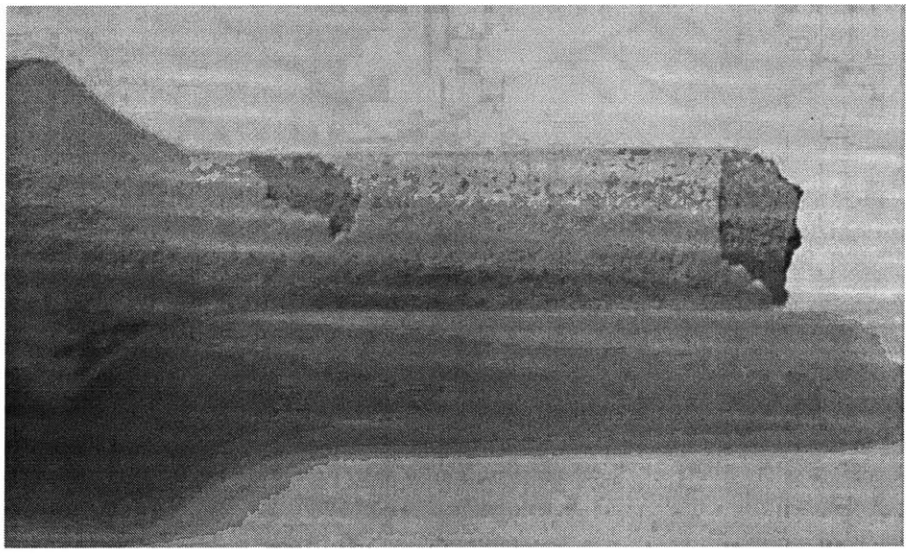

Figure D-17: Failed superalloy specimen with an applied TBC system after thermomechanical testing. From Chen et al. [23].

Appendix E

Summary of time-integration procedure for interface constitutive model

Note that as pointed out earlier, this integration procedure was devised in the work of Su et al. [98].

Let $\{\hat{\mathbf{e}}_1(0), \hat{\mathbf{e}}_2(0), \hat{\mathbf{e}}_3(0)\}$ be an orthonormal triad, with $\hat{\mathbf{e}}_1(0) = \mathbf{n}$ aligned with the normal to the interface in the reference configuration, and $\{\hat{\mathbf{e}}_2(0), \hat{\mathbf{e}}_3(0)\}$ be in the tangent plane at the point of the interface under consideration. Let $\{\hat{\mathbf{e}}_1(t), \hat{\mathbf{e}}_2(t), \hat{\mathbf{e}}_3(t)\}$ be the same basis in the current configuration, with $\mathbf{e}_i(t) = \mathbf{R}(t)\mathbf{e}_i(0)$, where $\mathbf{R}(t)$ is the rotation that determines $\mathbf{e}_i(t)$. Then, the traction and the total relative displacement

$$\mathbf{t}(t) = \sum_i t_i(t)\hat{\mathbf{e}}_i(0), \quad \boldsymbol{\delta}(t) = \sum_i \delta_i(t)\hat{\mathbf{e}}_i(0), \tag{E.1}$$

may be transformed into the current configuration as

$$\tilde{\mathbf{t}}(t) = \mathbf{R}(t)\mathbf{t}(t) = \sum_i t_i(t)\hat{\mathbf{e}}_i(t), \tag{E.2}$$

$$\tilde{\boldsymbol{\delta}}(t) = \mathbf{R}(t)\boldsymbol{\delta}(t) = \sum_i \delta_i(t)\hat{\mathbf{e}}_i(t), \tag{E.3}$$

We consider that we are given

1. $\tilde{\mathbf{t}}(t) = t_1(t)\hat{\mathbf{e}}_1(t) + t_2(t)\hat{\mathbf{e}}_2(t) + t_2(t)\hat{\mathbf{e}}_3(t)$,
2. $s^{(i)}(t)$,
3. $\gamma^{(1)}(t)$, $\gamma^{(2)}(t)$
4. $\Delta\tilde{\boldsymbol{\delta}} = \Delta\delta_1\hat{\mathbf{e}}_1(t) + \Delta\delta_2\hat{\mathbf{e}}_2(t) + \Delta\delta_3\hat{\mathbf{e}}_3(t)$,
5. $\Delta t = \tau - t$, and
6. $\mathbf{R}(t)$ which determines $\hat{\mathbf{e}}_i(t) = \mathbf{R}(t)\hat{\mathbf{e}}_i(0)$.

We need to calculate $\{\mathbf{t}(\tau), s^{(i)}(\tau), \gamma^{(1)}(\tau), \gamma^{(2)}(\tau), \}$, and march forward in time.

Step 1. Calculate the trial stress at the end of the step (components with respect to $\hat{\mathbf{e}}_i(t)$)

$$t_1^*(\tau) = t_1(t) + K_N \Delta\delta_1 \tag{E.4}$$
$$t_2^*(\tau) = t_2(t) + K_T \Delta\delta_2 \tag{E.5}$$
$$t_3^*(\tau) = t_3(t) + K_T \Delta\delta_3 \tag{E.6}$$
$$\tilde{\mathbf{t}}_T^*(\tau) = t_2^*(\tau)\hat{\mathbf{e}}_2(t) + t_3^*(\tau)\hat{\mathbf{e}}_3(t) \tag{E.7}$$
$$\bar{\tau}^*(\tau) = \sqrt{\tilde{\mathbf{t}}_T^*(\tau) \cdot \tilde{\mathbf{t}}_T^*(\tau)} = \sqrt{(t_2^*(\tau))^2 + (t_3^*(\tau))^2} \tag{E.8}$$

Step 2. Calculate $b^{(i)}$

$$b^{(1)} = \left\{t_1^*(\tau) - s^{(1)}(t)\right\} \tag{E.9}$$
$$b^{(2)} = \left(\bar{\tau}^*(\tau) + \mu t_1^*(\tau) - s^{(2)}(t)\right) \tag{E.10}$$

Step 3. Calculate $A^{(ij)}$

$$A^{(11)} = \left[K_N + h^{(11)}(t)\right] > 0 \tag{E.11}$$
$$A^{(12)} = 0 \tag{E.12}$$
$$A^{(21)} = K_N \mu \tag{E.13}$$
$$A^{(22)} = \left[K_T + h^{(22)}(t)\right] > 0 \tag{E.14}$$

Step 4. Calculate the plastic relative displacement increments

(a) If $b^{(1)} > 0$ and $b^{(2)} \leq 0$ then

$$x^{(1)} = \frac{b^{(1)}}{A^{(11)}} \tag{E.15}$$
$$x^{(2)} = 0 \tag{E.16}$$

(b) If $b^{(1)} \leq 0$ and $b^{(2)} > 0$ then

$$x^{(1)} = 0 \tag{E.17}$$
$$x^{(2)} = \frac{b^{(2)}}{A^{(22)}} \tag{E.18}$$

(c) If $b^{(1)} > 0$ and $b^{(2)} > 0$ then first calculate A^{-1}; recall that we have assumed that the matrix A is invertible. Then solve for the plastic strain increments

$$x^{(i)} = \sum_j (A^{-1})^{(ij)} b^{(j)} \tag{E.19}$$

Check if $x^{(i)} > 0$ then accept this solution. However, if $x^{(1)} > 0$ and $x^{(2)} < 0$ then

$$x^{(1)} = \frac{b^{(1)}}{A^{(11)}}, \qquad x^{(2)} = 0, \tag{E.20}$$

or if $x^{(2)} > 0$ and $x^{(1)} < 0$ then

$$x^{(2)} = \frac{b^{(2)}}{A^{(22)}}, \qquad x^{(1)} = 0. \tag{E.21}$$

Step 5. Update the traction

$$t_1(\tau) = t_1^*(\tau) - K_N\, x^{(1)} \tag{E.22}$$

$$\bar{\tau}(\tau) = \bar{\tau}^*(\tau) - K_T\, x^{(2)} \tag{E.23}$$

$$\tilde{\mathbf{t}}_T(\tau) = \frac{\bar{\tau}(\tau)}{\bar{\tau}^*(\tau)}\, \tilde{\mathbf{t}}_T^*(\tau) = \frac{\bar{\tau}(\tau)}{\bar{\tau}^*(\tau)}\, \{t_2^*(\tau)\hat{\mathbf{e}}_2(t) + t_3^*(\tau)\hat{\mathbf{e}}_3(t)\} \tag{E.24}$$

$$t_2(\tau) = \frac{\bar{\tau}(\tau)}{\bar{\tau}^*(\tau)}\, t_2^*(\tau) \tag{E.25}$$

$$t_3(\tau) = \frac{\bar{\tau}(\tau)}{\bar{\tau}^*(\tau)}\, t_3^*(\tau) \tag{E.26}$$

$$\tilde{\mathbf{t}}(\tau) = t_1(\tau)\hat{\mathbf{e}}_1(t) + t_2(\tau)\hat{\mathbf{e}}_2(t) + t_3(\tau)\hat{\mathbf{e}}_3(t) \tag{E.27}$$

$$\mathbf{t}(\tau) = \mathbf{R}(t)^\top\, \tilde{\mathbf{t}}(\tau) = t_1(\tau)\hat{\mathbf{e}}_1(0) + t_2(\tau)\hat{\mathbf{e}}_2(0) + t_3(\tau)\hat{\mathbf{e}}_3(0) \tag{E.28}$$

Step 6. Update the state variables

$$s^{(1)}(\tau) = s^{(1)}(t) + h^{(11)}(t)x^{(1)} \tag{E.29}$$

$$s^{(2)}(\tau) = s^{(2)}(t) + h^{(21)}(t)x^{(1)} + h^{(22)}(t)x^{(2)} \tag{E.30}$$

Step 7. Update $\gamma^{(1)}$ and $\gamma^{(2)}$:

$$\gamma^{(1)}(\tau) = \gamma^{(1)}(t) + x^{(1)} \tag{E.31}$$

$$\gamma^{(2)}(\tau) = \gamma^{(2)}(t) + x^{(2)} \tag{E.32}$$

Appendix F

A simple model for top-coat creep at elevated temperatures

As pointed out before, plasma-sprayed top coats show considerable creep at elevated temperatures. This has been investigated by Heckmann et al. [52] and Echsler et al. [36].[1]

Our goal in this Appendix is to briefly characterize this creep behavior in a simple manner *for a fixed elevated temperature.* For simplicity, we consider a one-dimensional setting in compression.[2] We assume that the compressive *plastic* or *creep strain rate* $\dot{\epsilon}^p \geqslant 0$ can be described by [2]

$$\dot{\epsilon}^p = \dot{\epsilon}_0^p \left(\frac{\sigma}{s}\right)^{1/m} \tag{F.1}$$

with $\sigma \geqslant 0$ the compressive stress, $\dot{\epsilon}_0^p$ a reference strain rate, and m a rate-sensitivity parameter. s denotes the *deformation resistance*, which is taken to evolve according to [14]

$$\dot{s} = h_0 \left(1 - \frac{s}{s_{\text{sat}}}\right)^q \dot{\epsilon}^p, \tag{F.2}$$

with a hardening modulus h_0, saturation value for the deformation resistance s_{sat}, and a further material parameter q. The evolution equation (F.2) is subject to an initial condition $s(t=0) = s_0$. In summary, the material parameters are thus

$$\dot{\epsilon}_0^p, \qquad m, \qquad h_0, \qquad , s_0, \qquad s_{\text{sat}}, \qquad q. \tag{F.3}$$

To calibrate the above set of material parameters, we use the experimental data by Echsler et al. [36] for uniaxial compression at a temperature of 1323 K. Guided by experience with plasticity theories, we make the following initial guesses for the material parameters:

$$\dot{\epsilon}_0^p = 1 \times 10^{-7}\ 1/\text{s},\ \ 1/m = 10,\ \ h_0 = 1000\ \text{MPa},\ \ s_0 = 50\ \text{MPa},\ \ s_{\text{sat}} = 75\ \text{MPa},\ \ q = 1. \tag{F.4}$$

[1] Such high-temperature creep data is difficult to obtain experimentally; accordingly, to the knowledge of the authors, the amount of data available in the literature is limited to the two above publications.

[2] This case can easily be generalized to arbitrary deformations in 3 dimensions; cf., e.g., Gurtin et al. [48].

Using a trial-and-error procedure comparing the model results[3] with the experiments, we adjust these values until reasonable agreement is reached. This is the case for the parameters given in Table F.1. The corresponding simulated and experimental curves are shown in Fig. F-1.

[3]For computation of the model prediction, a simple explicit MATLAB algorithm was used that was originally written by Dr. Nicoli Ames.

Table F.1: Calibrated top-coat creep parameters at a temperature of 1323 K.

$\dot{\epsilon}_0^p$ (1/s)	$1/m$	h_0	s_0	s_{sat}	q
2×10^{-11}	3.1	1800	1.3	70	1.3

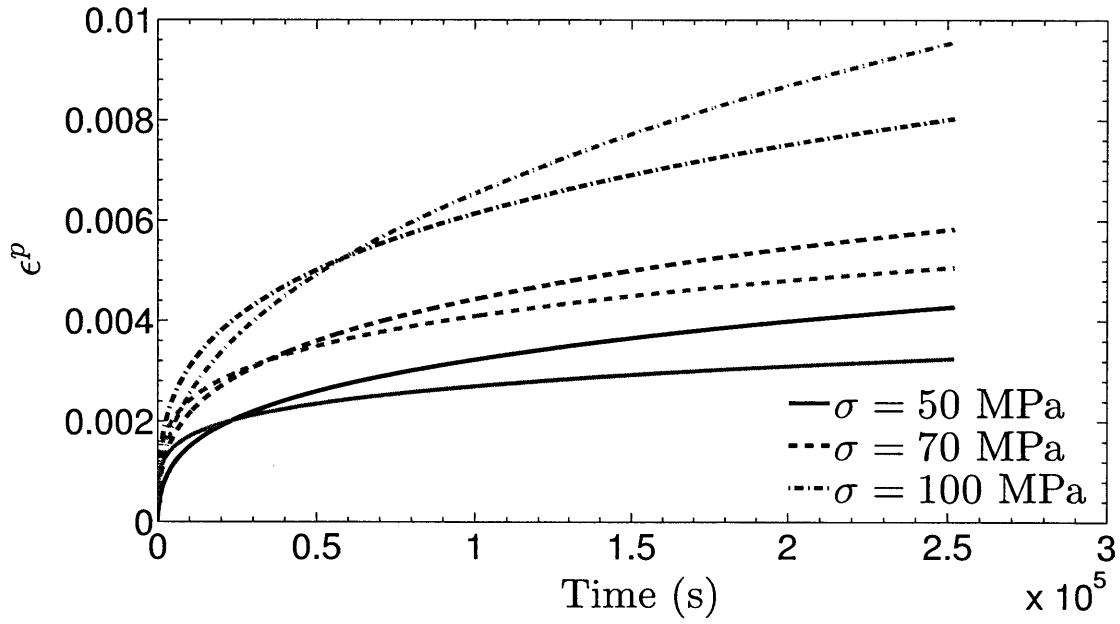

Figure F-1: Top-coat creep at 1323 K: experimental data from Echsler et al. [36] (grey curves) and calibrated model (black curves).